N° d'ordre : **42475**

UNIVERSITE DE LILLE 1

THÈSE

présentée par

Stephania KOSSMAN

pour l'obtention du

TITRE DE DOCTEUR EN MECANIQUE DES SOLIDES,
DES MATERIAUX, DES STRUCTURES ET DES SURFACES

intitulée

Indentation instrumentée multi-échelles de matériaux homogènes et multi-matériaux

---

Soutenue le ***8 Décembre 2017*** devant le jury d'examen :

Directeurs :	**Didier CHICOT**, Professeur, Université de Lille 1
	Alain IOST, Professeur, ENSAM CER Lille
Rapporteurs :	**Stéphane BENAYOUN**, Professeur, Ecole Centrale de Lyon
	Corinne NOUVEAU, Maître de Conférences HDR, ENSAM CER Cluny
Membres :	**Éric LE BOURHIS**, Professeur, Université de Poitiers
	Hervé PELLETIER, Professeur, Université de Strasbourg
	Mariana STAIA, Professeur, Université de Caracas (Venezuela)
	Philippe DUFRENOY, Professeur, Université de Lille 1
Invités :	**Francine ROUDET**, Maître de Conférences HDR, Université de Lille 1
	Thierry COOREVITS, Maître de Conférences, ENSAM CER Lille

Région
Hauts-de-France

DOCTORAT DE L'UNIVERSITE DE LILLE 1 SCIENCES ET TECHNOLOGIES

Doctoral School: SPI Sciences pour l'Ingénieur

Laboratory: Laboratoire de Mécanique de Lille – FRE 3723

Discipline: Mécanique des solides, des matériaux, des structures et des surfaces

TITLE OF THE THESIS:

Multiscale instrumented indentation of homogeneous materials and multimaterials

ABSTRACT:

The mechanical properties (hardness and elastic modulus) can be studied at different scales as a function of the composition and microstructure of materials (number of phases, constituent distribution, grain size…). In this work, we studied this mechanical response at the nano, micro and macroscopic scales, through different instruments that allow to apply loads ranging from 10 mN up to 2 kN generating penetrations depths between 50 nm and 250 µm.

The first stage consisted in the improvement of the experimental conditions, developing and interpreting the experimental data, following a rigorous metrological methodology, in order to achieve the connection between the results obtained at the three studied scales. These tests were performed in metallic industrial materials, which are sufficiently homogeneous at the tested penetration depths (steels and aluminum alloy). For example, we had proposed an alternative approach to the Oliver and Pharr method to fit the unloading curve to estimate the elastic modulus.

Afterwards, this methodology is applied to the study of the response obtained by indentation in a composite material, which is highly heterogeneous, used in the fabrication of brake pads in the railway industry. The obtained results (spatial distribution on the surface and through the volume of hardness and elastic modulus) are going to be valuables in the applications of models to study the squeal noise during braking, looking to reduce its effects.

Keywords:

Multiscale indentation; multicyclic indentation; grid indentation; metrological procedure; heterogeneous materials; brake pads.

DOCTORAT DE L'UNIVERSITE DE LILLE 1 SCIENCES ET TECHNOLOGIES

Ecole doctorale : SPI Sciences pour l'Ingénieur

Laboratoire : Laboratoire de Mécanique de Lille – FRE 3723

Discipline : Mécanique des solides, des matériaux, des structures et des surfaces

TITRE DE LA THÈSE :

Indentation instrumentée multi-échelles de matériaux homogènes et multi-matériaux.

RÉSUMÉ :

Les propriétés mécaniques (dureté et module d'élasticité) peuvent s'étudier à différentes échelles en fonction de la composition et de la microstructure des matériaux (nombre de phases, répartition des constituants, diamètre des grains…). Dans ce travail nous étudions ces comportements aux échelles nano, micro et macroscopiques, grâce à une gamme d'appareils expérimentaux en indentation instrumentée qui permettent d'appliquer des forces variant de 10 mN à 2 kN et de provoquer des enfoncements mesurables de 50 nm à 250 µm.

Une première partie consiste à optimiser les conditions expérimentales, dépouiller et interpréter les données en suivant une démarche métrologique rigoureuse, dans le but d'effectuer le raccordement entre les résultats obtenus aux trois échelles de mesure étudiées. Ces essais sont effectués sur des matériaux métalliques industriels mais suffisamment homogènes (aciers et alliage d'aluminium). Nous proposons par exemple une méthode alternative à celle d'Oliver et Pharr pour estimer le module d'élasticité à partir de la courbe de décharge en indentation.

Cette méthodologie est ensuite appliquée à l'étude du comportement sous indentation d'un matériau composite, hautement hétérogène, utilisé pour la fabrication de plaquettes de freinage dans le domaine ferroviaire. Les données obtenues (répartition spatiale en surface et en volume de la dureté et des modules d'élasticité) sont destinées à être utilisées dans les modèles simulant le bruit de crissement au freinage, afin d'en atténuer les effets.

Mots-clefs :

Indentation instrumentée multi-échelles ; indentation multi-cyclique ; cartographie ; démarche métrologique ; matériaux hétérogènes ; plaquettes de freinage.

Acknowledgments

The success of a PhD principally depends on the PhD candidate, and of course on other factors such as the work environment, supervisors, colleagues, etc. I was not the exception it depended mainly on me, but I was very lucky in other aspects, especially regarding the people around me, and here starts my long list.

Firstly, I thank God for this great opportunity in my professional career and life, for all the lived experiences, and for giving me the strength to finish it successfully.

Then, certainly in the top of the list are my two supervisors, Prof. Chicot and Prof. Iost, they become like dads for me, they were excellent in the human and scientific sense, they are incredible persons with a great sense of humor. I express my eternal gratitude to them because no matter what they always found the time for me, for their patience to response my thousands of “petites questions”, to deal with my personality, and their willingness to help me always. Both had very different mindsets but with the same purpose encouraging and helping me to achieve my goals. They teach me so many things, I was very lucky to share with them that have 30 years in the field of indentation (or even more), we definitely made a great team together. They were the best chefs that I could ever imagine, they were beyond any expectation. I thank them for trusting in me since the beginning, for their continuous motivation, and forging my character.

I worked in two laboratories, we were not very numerous but gladly I met great people. I’m grateful to all of them, they become part of my everyday routine, they help me a lot and made my days better, thanks to Isabel, Philemon, Alex, Mohammad, Alberto, Thierry, Francine, Adrien and Cosmin. But I specially thank to: Isabel, because of her contagious spirit and joy, she encourages me many times when I needed, it was like and older sister with a huge heart; Philemon, because of his support, complicity and genuineness, always available to help. Alberto, as Venezuelan compatriot, he remembers me my Venezuelan people. Mohammad, because of his authenticity and deep conversations. Alex, because of his peculiar and funny personality, making me laugh so many times. Thierry, because of his kindness, all his scientific help, all the work together, the teachings hours and coffees with great conversions.

I would like to thank to Prof. Mariana, she became like a mother for me, I will be eternally grateful for introduce me to Prof. Chicot and Prof. Iost during my master internship. I express my sincere gratitude for being so special with me, give me her support and put me under

pressure when it was necessary. I also thank to the Prof. Eli and Meme for being so kind with me.

I thank to my roommate and special friend Krystel, she taught me so many things about life and gave me her support during difficult times.

I express my gratitude to Maggie and Paul, for being so kind and care about me.

I appreciate all the help that gave me Prof. Philippe and his team, Itziar, Vincent and Anne-Lise, providing me the samples for the research and the required information.

I thank to David for all his scientific help and being so kind.

My sincere thanks to Mr. Luis Pérez (my father in law), for his unconditional help, all invested hours in helping me, his gentleness and love.

Besides, I express my gratitude to all the members of the evaluation committee present at the dissertation day, and specially to the reviewers of the manuscript Prof. Benayoun and Prof. Nouveau, for their dedication and constructive critics.

I specially thank to the *Région Hauts-de-France* for the financial support to pursue my PhD studies, without their support it would not have been possible to achieve this goal.

The top of the list is shared by many persons, I cannot forget to thank to my mother, sisters, and husband. Being so far away from here, their spiritual support and unconditional love were essential for me. I specially thank to my hubby for clear my mind, for pushing me to be better in every sense and showing me a solution for everything, I thank him for being that person that can change my mood.

Index

List of figures

List of tables

Introduction

Nowadays composite materials are used in several applications since they provide advantages combining very dissimilar properties, with respect to the homogeneous ones. Brake pads for any kind of transport applications, from bikes to airplanes, are known to be heterogeneous materials that overcome critical conditions of temperature, wear, corrosion, etc., during service.

Particularly for railway applications, brake pad materials undergo extreme conditions of temperature and wear. In order to predict their service life and their behavior during braking, it is mandatory to know their mechanical properties. The mechanical characterization of these materials has been a challenge for the industry; during many years, the brake pads were produced by trial and error due to their complex structures and characteristics. Today the requirements in service are superior, consequently the actual knowledge of the properties is desired; this last decade many works have been done to accomplish this objective [1–4].

This work is focused on the determination of elastic modulus and hardness of highly heterogeneous brake pads for railway applications; at the macro scale, these materials are typically characterized by classic methods like uniaxial compression performed with a cumbersome procedure to obtain accurate properties [1], which leads to the global properties of the material. In order to achieve the mechanical properties of individual phases or constituents of brake pads, we propose the use of the multiscale instrumented indentation testing (IIT) allowing a very localized response at very small loads, or an overall response at elevated loads.

The technique is based on the penetration of an indenter of known geometry and properties into a material of unknown properties, recording a load-displacement curve that allows to obtain the mechanical properties such as hardness and elastic modulus. This technique is very powerful for mechanical characterization because of its experimental simplicity and, as we mentioned before, the possibility to work among different scales of loading, from pico to kilo Newtons and consequently from nano to micrometers of indentation depths [5,6]. Brake pads were studied from the nano range to identify the local intrinsic properties, to the macro range to get their overall properties at different penetration depths, necessary in the squeal noise simulations. Due to the complexity of the characterization of these materials, we previously study the performance and applicability of multiscale indentation in metallic homogeneous materials. In this sense, the investigation was divided in five chapters briefly described below in order to contribute to the understanding of this test at different scales of measurement:

- *Chapter I* reports some of the basis of instrumented indentation testing that are fundamental in the analysis and understanding of the load-displacement curves, as well as the calculation of the elastic modulus and hardness, focusing on the study of sharp indentation (pyramidal indenters). We pointed out some of the most important aspects of this method applied to homogeneous materials, that corresponds to the fundamentals of the technique; also, the description of principal parameters affecting the test and the correction of the data are given (frame compliance, deformation mode, tip defect, alignment, etc.), since the reliability of instrumented indentation testing depends on them.
- *Chapter II* presents the description of the three instruments used in this research that allow us to perform the indentation tests for loads of 10 mN up to 2 kN: Nanoindenter XP (10 mN-10 N), Microindenter CSM2-107 (0.1-20 N) and Macroindenter ZHU 2.5 (5 N-2 kN), located at two different laboratories (ENSAM Lille and IUT A Lille). As well as the microstructure and references values of the mechanical properties of the metallic materials (aluminum, ferritic and austenitic steel). Different complementary testing methodologies were applied:
    - Classic test using only one loading-unloading cycle and subsequently allowing the determination of one couple of hardness and elastic modulus values.
    - Continuous stiffness measurement (CSM) mode which allows the plot of the two mechanical properties versus the indenter displacement (a great number of hardness and elastic modulus couples).
    - Multicyclic tests applied when CSM mode is not available in order to locally obtain additional information compared to the classic tests.

  The specifications of these indentation tests for the calculations of the elastic modulus and hardness are described in this chapter

- *Chapter III* consists in the development of a new approach proposed to improve the power law model of Oliver and Pharr to fit the unloading curve used to calculate stiffness and elastic modulus of the material. This new approach was developed because the convergence of the power law method was difficult to achieve for materials with significant plastic deformation like most of the metals (almost vertical unloading curve). The methodology relies on two main aspects: the interchange of the load-displacement variables (*e.g.* displacement dependent variable) since it is a better conditioning problem, and the rewriting of the approach as a dimensionless expression in order to get comparable fitting parameters at different loads and scales. The robustness of both methods was tested through Monte Carlo simulations, introducing a Gaussian noise to the displacement data to evaluate the effect on calculation of the mechanical properties. The inverted approach was then used to fit the unloading curves of the performed tests.

- *Chapter IV* is addressed to answer a main interrogative: do the obtained mechanical properties change with the scale of measurement in indentation?

  It first presents the results obtained by multiscale indentation performed on the metallic materials, for loads ranging from 10 mN up to 2 kN and for penetrations depths ranging from 50 nm up to 250 µm with the three instruments using pyramidal indenters (Berkovich or Vickers). To establish relations among the scales of indentation in heterogeneous materials, we need to understand the phenomenon that happens at each scale of measurement, the data, the similarities in the analysis, the uncertainties, and the limits of the instruments and experiments. This chapter points out the difficulties of the technique, the correction of different parameters such as frame compliance, tip defect, etc., and highlight the importance of considering the deformation mode (sink-in or pile-up) for the calculation of the elastic modulus and hardness. We present the similarities and discrepancies across scales and instruments, validating the methods of analysis and the strategies to be considered in the study of heterogeneous materials.

- *Chapter V* should respond to the following question: Highly heterogeneous materials can be mechanically characterized by instrumented indentation? Do the mechanical properties can be compared with the overall response obtained by uniaxial compression?

  A summary of the background of some pioneering works in instrumented indentation testing on heterogeneous materials from nano to macro scales is firstly presented. At nano scale characterization is focused on grid indentation methodology that consists in performing numerous indentation tests in an organized configuration (mapping) and analyzing them by statistical means. Then, this chapter presents the microstructural characterization and the experimental methodology for the indentation tests; at the nano scale we used CSM tests applied as grid indentation and at the macro scale multicyclic tests with increasing load.

  The results at the nano scale are based on a statistical interpretation of the properties extracted at shallow penetrations to obtain the individual properties of each component; at this scale, a multilayer model was used for the analysis of the curve following the analogy that multiple stacked phases are equivalent to multilayer systems.

  The analysis at the macro scale was intended to develop the global mechanical properties and the variation with the penetration depth and test position on the sample by means of multicyclic indentation.

In the conclusion, we present some outlooks for further works, particularly a metrological study of the tests to elucidate the real uncertainties for a better interpretation of the results, and consequently an improvement in the understanding of the indentation technique.

Through this research work we achieved the publication of four papers (and one more in submission) and the participation at two conferences listed below:

Papers

- Kossman S., Iost A., Chicot D., Mercier D., Roudet F., Serrano I., Dufrenoy P., Magnier V., Cristol A. Mechanical characterization by multiscale instrumented indentation in highly heterogeneous material. Materials and Design. Submission in Oct 2017
- Kazamer N., Kossman S., Baranyi I., Chicot D., Serban V., Rajnai Z. et Voda M. « Effet de l'addition de TiB2 sur les propriétés mécaniques et tribologiques de revêtements NiCrBSi déposés par projection à la flamme ». Matériaux et Techniques. Submmited Sept 2017. (Article written in the framework of a convention with the *Association Universitaire de la Francophonie* (AUF 2016) between the University of Oboda (Budapest, Hungary), the University of Timisoara (Timisoara, Romania) and the University of Lille I (Lille, France), where I participated).
- Kossman S., Coorevits T., Iost A., and Chicot D., "A new approach of the Oliver and Pharr model to fit the unloading curve from instrumented indentation testing," Journal of Materials Research, vol. 32, no. 12, pp. 2230–2240, 2017.
- Bentoumi M., Bouzid D., Benzaama H., Mejias A., Kossman S., A. Montagne, Iost A., and Chicot D., "Multiscale and multicycle instrumented indentation to determine mechanical properties: Application to the BK7 crown borosilicate," Journal of Materials Research, vol. 32, no. 8, pp. 1444–1455, 2017.
- Kossman S., Chicot D., and Iost A., « Indentation instrumentée multi-échelles appliquée à l'étude des matériaux massifs métalliques ». Matériaux et Techniques, vol. 105, no. 1, pp. 104, 2017.

Conferences

- European Congress and Exhibition on Advanced Materials and Processes (EUROMAT), September 2017 (Thessaloniki, Greece).

Oral presentation: "A new approach of the Oliver and Pharr model to fit the unloading curve from instrumented indentation testing". Kossman S., Coorevits T., Iost A., and Chicot D.

Poster: "Mechanical characterization by multiscale instrumented indentation in highly heterogeneous material". Kossman S., Iost A., Chicot D., Mercier D., Roudet F., Serrano I., Dufrenoy P., Magnier V., and Cristol A.

- Indentation 2016, October 2016 (Lille, France).

Oral presentation: « Indentation instrumentée multi-échelles appliquée à l'étude des matériaux massifs métalliques ». Kossman S., Chicot D., and Iost A.

Poster: "A new approach of the Oliver and Pharr model to fit the unloading curve from instrumented indentation testing". Kossman S., Coorevits T., Iost A. and Chicot D.

CHAPTER I

Theoretical background of instrumented indentation testing

I.1. Introduction

From almost two hundred years ago, hardness measurements have been a valuable technique for material characterization, initially founded in Mohs hardness scale in 1822, which measures the capability of different minerals to lead a permanent scratch into the others, classifying diamond as the maximum value of the scale. Decades later, the interpretation of hardness as the resistance to plastic deformation induced by a stiffer material of known geometry was developed by Brinell in 1900, the tests consist in indenting a flat surface with a spherical indenter made of hardened steel, then the diameter of the indentation was measured. Meyer hardness scale in 1908, was founded in a similar concept but using the projected contact area. Later in 1922 was developed Vickers hardness using a pyramidal square based indenter. Simultaneously Rockwell scale was established, it was given by the measurement of the indentation while the application of the load, the technique used different indenters and procedures according to the indented material [6–9]. These techniques have been very valuable in engineering as a measurement of the mechanical properties and quality control of materials. One of the constrain of these methods is the measurement of the residual imprint by optical devices, particularly to characterize materials at small scales, promoting the development of the instrumented indentation testing (IIT).

Since the early 1970's until now instrumented indention testing has become a first-rate technique for quality control of materials, that allows to quickly characterize them obtaining their mechanical properties. In instrumented indentation testing, load and penetration depth are continuously and simultaneously recorded during the loading-unloading process, typically with a precise control of both parameters.

The main advantages of this technique regarding the conventional testing methods, such as traction or compression, are that it is less time consuming, it does not require a special shape of the samples, and it is considered as a non-destructive technique. Through the years, a huge improvement has been done in the instruments design to obtain reliable results with less uncertainty, also new techniques have been developed as the ultra-fast indentation, the coupled instruments with atomic force microscopes (AFM) or scanning electron microscope (SEM) [6,10–14].

IIT is applied in a wide variety of materials such as metals, ceramics, polymers, and composites. Thus, their application areas are broad including microelectronics [15,16], aeronautics [17,18], dental materials [19,20], fracture rocks [21,22], tribological coatings [23–26], biological materials [27–29], food products [30,31], etc.

IIT can be accurately performed from a few pico to kilo Newtons that means penetration depths of some nanometers to hundreds of micrometers, allowing the investigation of the materials across the length scales. At the micro and macro scales it can be compared with conventional hardness tests such as Rockwell, Vickers and Brinell. The investigation of the material behavior through different scales of measurement has become an attractive field of research [32–34]. Theoretical models have emerged to describe material behavior using quantum mechanics, molecular dynamics, dislocation dynamics, and continuum mechanics, *i.e.* from few atoms to the macroscopic scale [35].

I.2. Basis of the test

I.2.1. Instrumented indentation tests: load-displacement curve

The instrumented indentation test consists in the application of a load with an indenter of known properties and geometry into the surface material of unknown properties, recording a load-displacement curve during the entire test, which allows to extract the information needed to estimate the mechanical properties, an example is given in Fig. I.1.

The most important quantities extracted from the test for the later calculation of the mechanical properties are listed below:

$h_{\mathrm{max}}, P_{\mathrm{max}}$: maximum displacement and load, respectively, after dwell time.

h_{f}: residual depth obtained after the indenter withdrawal.

h_{r}: intercept of the tangent of the unloading curve.

h_{c}: contact penetration depth.

S: slope of the unloading curve, tangent at h_{max}.

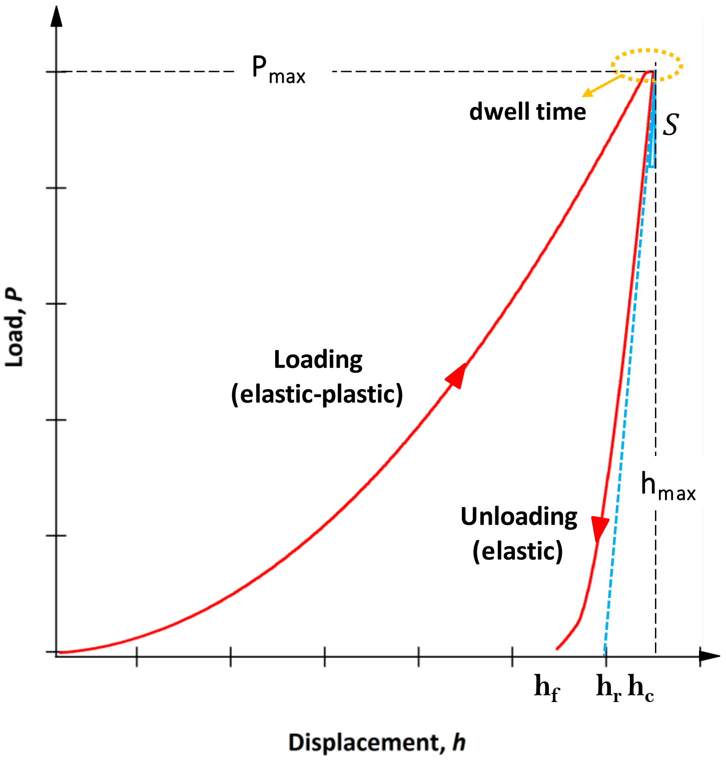

Fig. I.1. Load displacement curve, showing important quantities and parameters for the analysis to get the elastic modulus and hardness.

In the subsequent sections we describe different elements related to the application of the test, and some principles involved in the calculation of the mechanical properties of the materials. Since, the test and material response depend directly on the indenter geometry, we first give a brief explanation of the most used indenters and some elements related to them to help in the understanding of the further information, which correspond to the shape and functions describing of the loading and unloading curves.

I.2.2. Indenters types

Instrumented indentation tests are typically performed with pyramidal or spherical indenters in a broad range of materials. The more frequently used pyramidal indenters are Vickers and Berkovich, nevertheless Knoop and cube corner exhibit some advantageous applications [36,37]. Spherical indenters allow the direct application of Hertz equations and the relation with stress-strain curves [38,39]. Nowadays flat punch geometry is widely used in the study of biological tissues and food, because it facilitates the estimation of the contact area during penetration [40].

Vickers indenter consists in a base square pyramid with a semi-angle between the opposing faces of $\psi = 68°$ (Fig. I.2). Berkovich indenter is a triangular base pyramid fabricate with an angle of $\psi = 65.27°$ that gives the same projected area to depth ratio than Vickers pyramid (Fig. I.2). Vickers is usually employed at the industrial macro range, instead Berkovich is preferred at the nano and micro scales because the pyramid construction easily converges in a single point, rather than in a line in the four-sided Vickers pyramid. These two indenters are commonly fabricated in diamond [41].

Vickers indenter angle was chosen based in the optimum condition for Brinell hardness (spherical indenter), which must achieve a ratio between the diameter of the residual indentation and the diameter of the spherical indenter equal to 0.375, corresponding to the angle $\psi = 68°$ [8,42].

From geometrical consideration, the ratio of the length of one side of the residual impression is related by a factor of ~7.5 for Berkovich indenter. For Vickers indenter, the length of diagonal is 7 times the total penetration depth. The representative strain within the specimen material is approximately 8% for both indenters [6].

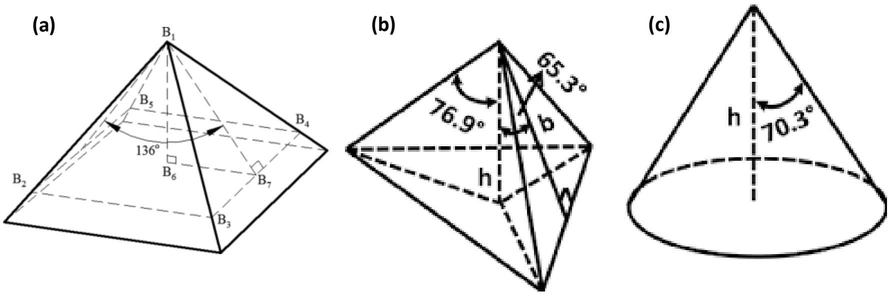

Fig. I.2. Schematic representation of the indenter geometries, a) Vickers, b) Berkovich, and c) equivalent axisymmetric cone.

Knoop indenter is a four-sided pyramid with two face angles 172.5° and 130° (Fig. I.3). The impression has one diagonal which length is approximately seven times the shorter diagonal. It is particularly used in the study of hard materials due to the longer diagonal in comparison with Vickers indenter; it is also useful in the study of material presenting anisotropy [6,36,43,44].

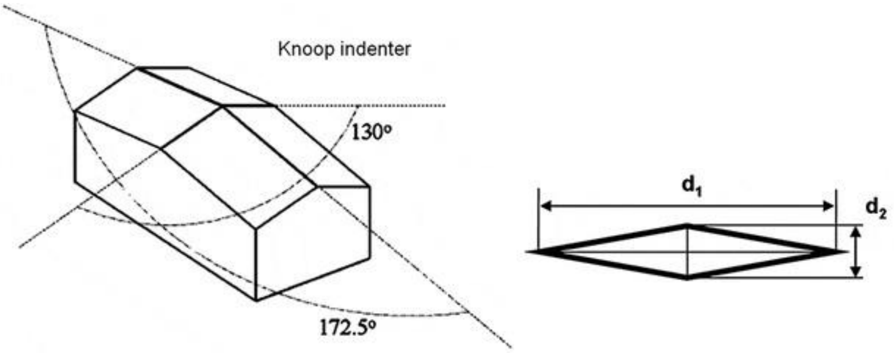

Fig. I.3. Schematic illustration of Knoop indenter, showing the angles between faces and residual impression of diagonals $d1$ and $d2$.

Cube corner is a three face-sided pyramid with a semi-angle of 35.26°. It uses is convenient to create a cutting action rather than a compressive state like that given by Vickers and Berkovich indenters, allowing to produce intentional cracks to study fracture toughness, but also the plastic properties [6,37,45].

Spherical indenters are valuable to study the transition from elastic to plastic contact. It is used from nano to the macrometric scale. It can be made of different materials (*e.g.* tungsten carbide, diamond or steel) and diverse radius.

I.2.3. Axisymmetric indenters

Important efforts have been done during many years to understand the behavior of the materials under indentation, especially by finite element simulations (FEM) that is a powerful tool in this subject. FEM simulations and indentation data analysis are usually based in axisymmetric indenters, which principle have been used by several authors to describe models explaining the material response, *e.g.* Nix and Gao [46] established an axisymmetric model of sharp and conical indentation to relate micro hardness to the indenter displacement.

For Berkovich indenter the equivalent angle θ of the axisymmetric conical indenter is determined assuming the same base area of contact at any penetration depth. In Fig. I.4 the projected area of a triangular base pyramid indenter with an angle ψ ($\psi = 65.3°$ for Berkovich indenter, $\psi = 68°$ for Vickers indenter) is equal to the projected area of the equivalent conical indenter, then, the angle θ for the conical indenter is given by Eq. I.1. In the case of Berkovich or Vickers indenters $\theta = 70.3°$ for the equivalent conical indenter [6,47].

$$\theta = \tan^{-1}\left(\sqrt{\frac{3\sqrt{3}}{\pi}}\tan\psi\right) \tag{I.1}$$

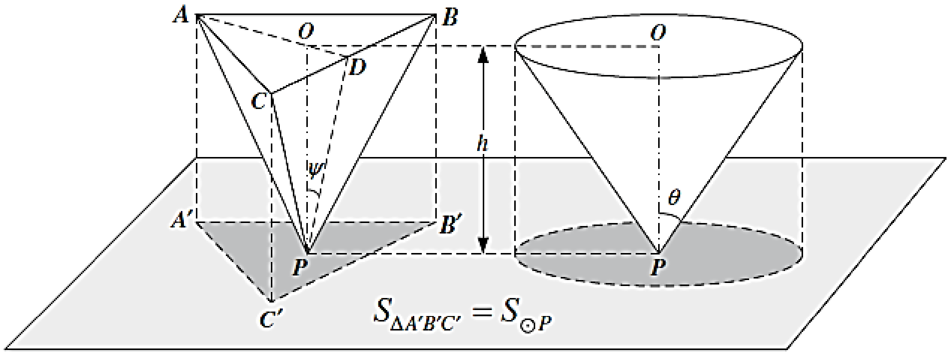

(i) triangular pyramid indenter (ii) conicalindenter

base area equivalence

Fig. I.4. Schematic diagram of triangular pyramid indenter of angle ψ, and its equivalent axisymmetric conical indenter of angle θ based on the equivalence of equal base area [47].

The equivalent projected areas of contact between conical and pyramidal indenters is obtained by Eq. I.2,

$$A = \pi {h_c}^2 \tan^2\theta \qquad \text{(I.2)}$$

where h_c is the depth of penetration measured from the edge of the circle or area of contact.

The equivalent cone of angle $\theta = 70.3°$ for the analysis of Berkovich and Vickers indentation gives a projected contact area $A = 24.5{h_c}^2$ [6]. Table I.1 summarizes the expressions for the contact areas of different pyramidal indenters.

Table I.1. Projected contact areas and intercept factor for various types of indenters. For pyramidal indenters, the semi-angles are the face angles with the central axis.

Indenter type	Projected contact area	Semi-angle ψ	Effective cone angle	Intercept factor ε
Berkovich	$A_c = 3\sqrt{3}{h_c}^2\tan^2\psi$	65.27°	70.30°	0.75
Vickers	$A_c = 4{h_c}^2\tan^2\psi$	68°	70.30°	0.75
Knoop	$A_c = 2{h_c}^2\tan\psi_1\tan\psi_2$	$\psi_1 = 86.25°$ $\psi_2 = 65°$	77.64°	0.75
Cube corner	$A_c = 3\sqrt{3}{h_c}^2\tan^2\psi$	35.26°	42.28°	0.75
Cone	$A_c = \pi{h_c}^2\tan^2\theta$	θ	θ	0.727

The axisymmetric assumption deviates in part from the reality since actual testing is conducted with non-axisymmetric indenters (Berkovich, Vickers, cube corner, etc.) that involve large strains in the material and complex elastic-plastic deformations, which lead to modifications in the analysis of the data [47,48], *e.g.* the addition of the parameter β (Eq. I.15) introduced in the relation between the reduced modulus and the contact stiffness.

Min *et al.* [49] found using three-dimensional finite element analysis that the equivalence between the axisymmetric cone with Berkovich and Vickers indenter is applicable, the plastic strains fields and the load-displacement curves are equivalent. This analysis does not consider the type of deformation in the indentation, *i.e.* effects of pile-up (upward movement of the material) or sink-in (downward movement of the material) that lead to differences between the axisymmetric and pyramidal indenters.

Qin *et al.* [50] showed that the equivalence of equal base area between the conical indenter and Berkovich indenter leads to significant errors, especially at the microindentation scale. They proposed instead a new equivalence based on an equal angle cone for triangular pyramid indenters $\psi = \theta$, it was validated for a large range of indenters and angles and indentation depths in iridium. Later, Shi *et al.* [47] demonstrated that the relation stablished by Qin *et al.* based on equal angles was valid for a large range of work-hardening materials between Berkovich and the axisymmetric cone, but it was not applicable for Vickers indenter, leading to important errors in hardness calculation. They demonstrated that the equivalence by the base areas was not suitable at the micro indentation range.

I.2.4. Principle of self-similarity or geometric similarity

Conical and pyramidal indenters such as Vickers and Berkovich indenters are self-similar, according to Cheng and Cheng [35] the geometric similarity states that two geometric objects described by a group of finite number of length and angle parameters, are similar if length parameters are proportional to each other with the same proportional constant and identical angles, *i.e.* $\alpha = \alpha', \beta = \beta'$ … and $(a/a') = (b/b')$ …= constant (Fig. I.5).

Geometric similarity of indentation implies that the representative strain in the material depends only on the effective cone angle of the indenter, for smaller angles (*i.e.* sharper indenters) the induced strain is greater. Likewise, the mean contact pressure acting on a pyramidal or conical indenter is the same indifferently of the indentation size for homogeneous materials [51].

The geometric similarity indicates that the ratio h_f/h_{max} would be constant indifferently of the applied load.

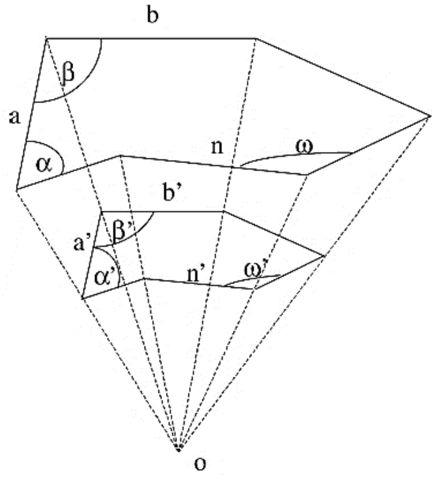

Fig. I.5. Object with geometric similarity [35].

Hill *et al.* [52] and Mesarovic *et al.* [53] demonstrated an overall solution for the self-similarity in spherical indenters, indicating that the geometry, stress and strain fields throughout the indentation process are derivable from a single solution by appropriate scaling (Eq. I.3). The similarity is defined for the fully plastic regime for relative small contact sizes; then, the non-dimensional contact size defined as contact radius over sphere radius a/R and contact pressure $P/(\pi a^2 \sigma_0)$ (σ_0 representative strength of the solid), will depend only on h/R and the strain-hardening exponent n.

$$\frac{P}{\pi a^2 \sigma_0} = \alpha \left(\frac{a}{\varepsilon_0 R}\right)^{1/n} \text{ and } a^2 = c^2 2hR \qquad \text{(I.3)}$$

where α and c^2 depend on the value of n and the friction assumption, ε_0 is the representative strain.

I.2.5. Loading curve

For elastic materials, the expression deduced by Love [54] and Sneddon [55] gives the relation between the load and the penetration depth given by the contact of a non-adhesive rigid conical indenter loaded into a flat specimen. For these materials load and unload are proportional to the square of the penetration depth by:

$$P = \frac{2Eh^2}{(1-\nu^2)\pi} \tan\theta = C_{\mathrm{e}} h^2 \qquad \text{(I.4)}$$

where the constant C_e depends on the indenter angle θ, and the elastic material parameters $E/(1-v^2)$.

For rigid plastic solids, the loading curve is also proportional to the square of the displacement (Eq. I.5), the expression is derived from Tabor analysis [56], which states that the mean contact pressure on a conical or pyramidal indenter is constant regardless the size of the imprint if the material is homogeneous, based on the geometric similarity principle. In the case of fully work-hardened metals, the relation for the contact pressure depends on the indenter geometry and the yield strength (σ_y) of the material (Eq. I.6), and it is independent of the penetration depth.

$$P = C_\mathrm{p} h^2 \tag{I.5}$$

$$P = C_\theta \sigma_y \tag{I.6}$$

In the case of elastic-plastic solids the same relation given by Eq. I.5 describes the loading curve, substituting C_p by C_ep that hinges on the indenter geometry and material properties represented by Eq. I.7 [6].

$$C_{ep} = \left[\frac{1}{\sqrt{\pi H \tan^2\theta}} + \left(\frac{2(\pi-2)}{\pi}\right)\sqrt{\frac{\pi}{4}\frac{\sqrt{H}}{E_\mathrm{R}}}\right]^{-2} \tag{I.7}$$

Larsson et *al.* [57] found other expressions for the constants C_e and C_{ep}, based on the Poisson's ratio and the yielding stress, respectively. Their equations were derived from an extensive finite element analysis inspired by the spherical cavity model.

In a general way, the loading curves can be represented by the Meyer's relation, where C depends on the material behavior (*e.g.* elastic elastic-plastic),

$$P = Ch^\alpha \tag{I.8}$$

where the exponent α could be rational numbers. Zeng *et al.* [58] found that the exponent on Eq. I.8 differs from 2 at the initial portion of the loading curves, while increasing the load the exponent is approximated to 2, suggesting that the load should be at least 30 mN for nanoindentation in bulk materials.

Gubicza *et al.* [59] differently from the relations above proposed a polynomial of 2nd degree of the form:

$$P = a_0 h + a_1 h^2 \tag{I.9}$$

where a_0 and a_1 are fitting parameters.

Many authors had studied the load-displacement relation [57,60,61], leading to different expressions depending on the assumptions of the analysis. Nevertheless, the approach of Eq. I.5 is typically used to describe the loading curve.

It is worth mentioning that most of the works that lead to these relations were performed based on classical indentation (not instrumented) leading to great contributions for the field of instrumented indentation.

The loading curve includes relevant information about the material behavior. From a dimensional analysis by finite element simulation in isotropic elastic-plastic materials with work hardening behavior, Cheng and Cheng [35] observed that work-hardening has a greater effect on the force required to move the indenter for smaller ratios of the yield strength to the elastic modulus (σ_y/E). At larger ratio σ_y/E, the ratio P/Eh^2 approaches that of pure elastic contact regardless the work hardening behavior. Another finding is that in the loading curves from conical indentation do not detect if the material work-hardens, since work-hardening does not modify the square-dependence, consequently σ_y/E and n cannot be determined uniquely using the loading curves. The same analysis was valid for pyramidal indenters based in the self-similarity principle.

I.2.6. Unloading curves

Unloading curves are different according to the material behavior, for elastic solids the unloading curve would superpose the loading curve. For elastic-plastic solids the curves contain information about the elastic modulus and hardness of the material, generally the initial loading slope gives the necessary information to determine the elastic modulus.

Two main approaches have been largely applied for the analysis of unloading curves. Firstly, the approach of Doerner and Nix [62] based in the flat punch approximation assumes that at the beginning of the unloading curve the contact area is constant, considering that the pyramidal geometry has a small effect on the final result. They modified the definition of the indenter function using the concept of contact depth as a substitute of the diagonal lengths, maximum depth or plastic depth [11]. The contact depth is obtained by fitting the first third of the unloading curve by a straight line, which coincides with the tangent to the unloading curve, therefore, the intercept gives the contact depth h_c by the expression,

$$h_{\mathrm{c}} = h_{\max} - \frac{P_{\max}}{S} \tag{I.10}$$

Furthermore, Doerner and Nix stated the next relation related to the unloading slope,

$$\frac{dh}{dP} = \frac{1}{h_c}\sqrt{\frac{\pi}{24.5}}\frac{1}{E_{\mathrm{R}}} \tag{I.11}$$

Nowadays this method is validated by the standard ISO 14577, denominated linear extrapolation method that implies that the unloading curve is described by,

$$P - P_{\max} = q + z(h - h_{\max}) \tag{I.12}$$

where q, z are fitting parameters, the linear extrapolation is performed with the initial 30% of the unloading curve. The cylindrical punch approximation made by Doerner and Nix is good when the unloading response is initially linear, *i.e.* for materials that do not show significant elastic recovery, or presenting large ratio E/σ_y.

The second approach used in the analysis of unloading curves, was proposed in the early 90's by Oliver and Pharr [48,63], opposite to Doerner and Nix, they stated that the unloading curve obtained with a Berkovich indenter is described by the non-linear power law relation in Eq. I.13 and it is not a straight line, implying that the contact area is modified upon unloading. They found that this method could be applied to any axisymmetric indenter.

$$P = B'(h - h_{\mathrm{f}})^m \tag{I.13}$$

where B', h_f and m, are fitting parameters. B' and m sometimes are believed to be constants related to the material behavior. Through the analysis of the elastic reloading Pharr *et al.* [64] found that the exponent m is related to the shape of the deformed surface. Cheng and Cheng [35] by dimensional analysis identified that B' is not a material constant since it depends on the indentation depth, Eq. I.13 is interpreted as an interpolation formula for a specific $h_{\max}$.

In this case the standard ISO 14577 suggests that the unloading curve should be fitted with the upper 50 to 80% part of the curve. The m exponent is an indicator of the pressure distribution [65], the expected value for m was 2, corresponding to the axisymmetric equivalent conical indenter. Nevertheless, the value of m varies between 1.25 to 1.6 for a large range of materials that is more alike to a paraboloid of revolution ($m = 1.5$). This discrepancy was explained by the concept of the effective indenter shape, discussed below.

Oliver and Pharr [48,63] determined that the contact depth calculation is based on models of indentation into a flat elastic half space by rigid punches of simple geometry [54,55], assuming sink in of the contact periphery and that pile up is negligible, the process is schematized in Fig. I.6 and the expression is described by,

$$h_c = h_{\max} - \varepsilon \frac{P_{\max}}{S} \tag{I.14}$$

where ε is a constant related to the indenter geometry, that takes different values $\varepsilon = 0.72$ for a conical indenter, $\varepsilon = 0.75$ for a paraboloid of revolution, and $\varepsilon = 1$ for a flat punch. Through the analysis of the experimental curves the approach of a paraboloid of revolution ($\varepsilon = 0.75$) seems more suitable to the actual unloading curve; this value is generally used in the literature.

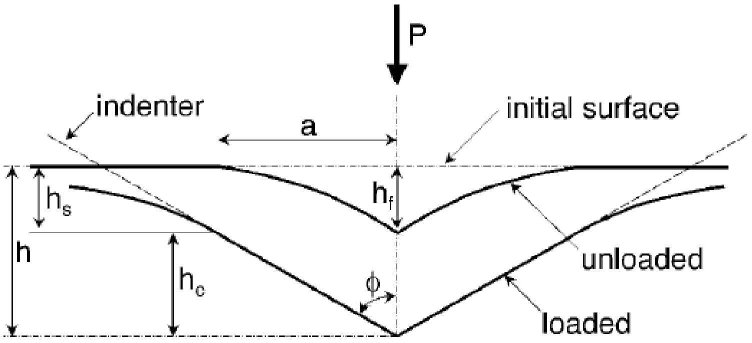

Fig. I.6. Schematic representation of an impression after unloading according to Eq. I.14.

For Oliver and Pharr, the reduced elastic modulus and the contact stiffness are connected by the next relation,

$$S = \left(\frac{dP}{dh}\right)_{h_{\max}} = \beta E_R \frac{2\sqrt{A}}{\sqrt{\pi}} \tag{I.15}$$

where S is the derivative of Eq. I.13 evaluated at the maximum displacement.

Two main simplifications are done upon unloading in the analysis above, namely no reverse plasticity occurs since the unloading is only elastic; and the shape of the impression is equivalent to a flat-sided cone and leads to an impression of depth h_f. Nevertheless, the elastic recovery upon unloading leads to significant deviations in the expected shape of the unloading curve, exhibiting a subtle convex curvature in the surface instead of a perfect conical or pyramidal shape, consequently the measured stiffness should be multiplied by a geometric factor $1/\beta$.

The value of β has been determined by several authors with different approaches, it ranges from 1.02 to 1.08. Generally, the correction considers the difference between the geometry of the axisymmetric conical indenter and the pyramidal indenter, however even for indentation of an elastic half-space by axisymmetric conic punch the value of β deviates from the unity [66]. King [67] suggested $\beta = 1.034$ from finite element analysis of indentations with flat punch of triangular cross-section, this value is frequently adopted in nanoindentation analysis. Gong *et al.* [68] determined $\beta = 1.032$ considering the presence of residual stresses in the response of the material during the unloading part. Hay *et al.* [66] found $\beta = 1.067$ ($\theta = 70.3°, \nu = 0.3$), according to the radial displacements within the circle of contact of the conical indenter, they proposed an expression based on the Poisson's ratio of the specimen and on the indenter angle. Dao *et al.* [69] based on three-dimensional FEM calculated $\beta = 1.096$ for Berkovich indenter and $\beta = 1.0595$ for the equivalent cone. The slightly modifications between these values do not change significantly the calculation of the elastic modulus [6].

I.3. Determination of the mechanical properties

I.3.1. Determination of the hardness from IIT

The simplest definition of hardness states the relation between the applied normal force and the area of indentation:

$$H = \frac{P}{A} \tag{I.16}$$

Therefore, according to the area definition used in its computation, different hardness numbers are obtained. The area could be determined by observation of the residual imprint or by analytical models from the load-displacement curves.

For classical indentation (not instrumented), the hardness number can be calculated considering the true or the projected contact area. Vickers hardness (*HV*) is calculated with the actual surface area of the impression considering the measuring diagonals of the residual imprint (*d*); instead Meyer hardness (*HMeyer*) uses the projected contact area. *HV* is ~7% lower than the mean contact pressure [6,70]. The corresponding relations are presented in Table I.2.

In instrumented indentation, it is possible to calculate different hardness numbers as well, the main definitions are Martens and instrumented hardnesses. Martens hardness (*HM*) is measured at the maximum load and reached penetration depth, using the superficial or actual area (Table I.2); in the macro range of test force the standard ISO 14577-1 reported the spectrum of values for steels between 2 to 7 GPa. Martens hardness also can be calculated by linear regression of the loading curve (from 50% to 90% of $P_{\max}$):

$$h = m\sqrt{P};\ HM = \frac{h^2}{m^2 A_\mathrm{r}} \tag{I.17}$$

where m is the slope from the linear regression of the loading curve.

The instrumented hardness *HIT* denotes the mean contact pressure between the load and the projected contact area A_c calculated at h_c. Both hardness definitions are summarized in Table I.2. Note that the area function depends on the scale of measurement, here we present the relations for a perfect pyramid shape, nevertheless the relation suitable for each scale considering the tip blunting and other defects in the indenter should be replaced.

It is worth mentioning that *HM* and *HIT* are mainly used in micro and nanoindentation. *HM* is equivalent to the *HV* when pile-up is not important [71], considering $d = 7h_{max}$. For hardness evaluation is mandatory to denote clearly the considerations for its calculation to guarantee that the values are comparable.

Table I.2. Hardness numbers for classical indentation tests and instrumented indentation tests, considering the true or the projected contact area.

Hardness [MPa]	**Comments**
$HV = \frac{2P}{d^2}\sin\left(\frac{136°}{2}\right) = 1.8544\frac{P}{d^2}$	P in N and h in mm, true contact area
$HMeyer = 2\frac{P}{d^2}$	P in N and h in mm, projected contact area
$HM = \frac{P}{A_r} = \frac{P}{26.43{h_{max}}^2}$	P in N and h in mm, true contact area
$HIT = \frac{P}{A_c} = \frac{P}{24.5\ {h_c}^2}$	P in N and h in mm, true contact area

Hardness is not considered as intrinsic property of the material but instead a property that depends on the geometry of the indenter and the friction between the indenter and the specimen [51,72,73]. Cheng and Cheng [35] found that a specific hardness value can be obtained by controlling the elastic modulus E, yield stress σ_y and work hardening coefficient n.

On the other hand, hardness should be measured at the regime of fully plastic deformation otherwise the quantity measured is the mean contact pressure and it is not load independent. Typically using pyramidal indenters due to the complex state of stress-strain, full plasticity is quickly achieved.

Tabor [74] demonstrated that hardness can be related to yield stress by $H = 3\sigma_y$, based on experimental observations in metals with elastic-perfectly plastic behavior and on the slip-line field solution for indentation rigid-plastic solids with a frictionless rigid indenter.

In metals with work-hardening the indentation process increases the yield or flow stress of the materials. Hence, the plastic strain varies over the deformed region and the amount of work hardening changes from point to point. Despite the complex strain distribution underneath the indenter Tabor proposed that representative or mean plastic strain is related to the hardness by:

$$H = 3\sigma_0 \tag{I.18}$$

where σ_0 is the uniaxial flow stress at a specific strain value. For Vickers indentation on metals Tabor found that representative strain varies from 0.08 to 0.1 and that the ratio of Vickers hardness to the yield stress is 3 at this strain value.

Cheng and Cheng found by finite element analysis that this relation is modified according to the ratio σ_y/E. For $\sigma_y/E < 0.02$, H/σ_0 varies between 2.4 and 2.8. For $\sigma_y/E > 0.06$, H/σ_y is approximately 1.7.

I.3.2. Elastic modulus calculation

Young's modulus or elastic modulus is an intrinsic material directly related to the atomic bonds. Usually this property is measured by tensile tests or by ultrasonic methods. The elastic modulus obtained from instrumented indentation tests gives a correct estimation of this intrinsic property that is comparable with the traditional methodologies. Elastic modulus is a size independent property.

In instrumented indentation, the analysis relies on the assumption of an elastic-plastic loading and an elastic unloading, without reverse plasticity. Hence, the elastic modulus is related to the initial slope of the unloading curve, as we mentioned previously, the measured elastic modulus would be directly linked to the methodology used for the analysis of the unloading curve, the contact area, the deformation mode, the axisymmetric assumption for the analysis, etc.

In this section, we summarize the principal methodology for the calculation of the elastic modulus that is based in the Oliver and Pharr model [48,63] and we mention some methods proposed in the literature. It is worth nothing that elastic modulus can be obtained from the work of indentation (areas under the load-displacement curve), this methodology will be described in section I.3.6.

From the Oliver and Pharr method the reduced elastic modulus E_{R} is obtained by Eq. I.19. The correction parameter β in the relation was previously explained.

$$E_{\mathrm{R}} = \frac{S\sqrt{\pi}}{2\beta\sqrt{A_c}};\ \text{with}\ S = \left(\frac{dP}{dh}\right)_{h_{\max}} \tag{I.19}$$

The deformation of the indenter becomes significant and the contact stiffness (S) decreases while it penetrates a hard material. This effect is corrected considering the effective or reduced modulus E_{R} of the system. Then the elastic modulus of the material is calculated by the next relation:

$$\frac{1}{E_{\mathrm{R}}} = \frac{1-{\nu_{\mathrm{i}}}^2}{E_{\mathrm{i}}} + \frac{1-\nu^2}{E} \tag{I.20}$$

where E_i and ν_i are the elastic modulus and the Poisson's ratio of the diamond indenter, 1140 GPa and 0.07, respectively. E and ν correspond to the elastic modulus and Poisson's ratio of the specimen material. The reduced modulus approaches the specimen elastic modulus if the indenter is rigid. The difference between E_{R} and $E/(1-\nu^2)$ increases as the modulus of the tested material approximates that of the indenter [58,75].

Other methodologies rely in the relation between hardness and elastic modulus [76–80]. Page *et al.* [79] demonstrated that the ratio of the load to square contact stiffness is related to the material properties as follow:

$$\frac{P}{S^2} = \frac{\pi H}{4{E_{\mathrm{R}}}^2} \tag{I.21}$$

Later, Oliver and Pharr [48] proposed to link this relation to the ratio of the plastic work to the total work measured, without the necessity of calculating the contact area.

Zeng and Chiu [58] determined a methodology based on experimental results and finite element analysis that does not require knowledge of the contact area, and allows the calculation of the elastic modulus and yielding stress; it was corroborated in a large range of materials. The two principal relations of the method are presented below:

$$P = (1-\vartheta)f(\nu)Eh^2 + 2\vartheta\sqrt{\frac{24.56}{\pi}\frac{E}{1-\nu^2}}h_0(h-h_0) \tag{I.22}$$

$$f(\nu)=\frac{2.1891(1-0.21\nu-0.01\nu^{2}-0.41\nu^{3})}{1-\nu^{2}} \tag{I.23}$$

where the parameter ϑ is the ratio between the yielding stress and the strain hardening parameter, which is 1 for elastic-perfect plastic and 0 for elastic materials. h_0 is a constant referring to the plastic depth for an elastic-perfect plastic material.

Malzbender and de With [80] proposed an approach to calculate the elastic modulus to the hardness ratio by the relation between the slopes of the loading (S_L) and the unloading (S) curves evaluated at the point of maximum load:

$$\frac{S_{\mathrm{L}}}{S}=\frac{\pi\tan\theta}{\beta}\cdot\frac{H}{E_{\mathrm{R}}}\cdot\frac{h_{\mathrm{c}}}{h_{\max}};\ \text{with}\ h_{\mathrm{c}}=h_{\max}\left[1+\frac{\pi\tan\theta}{2}\frac{\varepsilon}{\beta}\frac{H}{E_{\mathrm{R}}}\right]^{-1}f(n) \tag{I.24}$$

$$E_{\mathrm{R}}=\frac{S_L S^2}{2f(n)S-\varepsilon S_L}\cdot\frac{1}{2\beta\tan\theta P};\ f(n)\approx(1.28-0.8n)(1-14.78\sigma_y/E_{\mathrm{R}}) \tag{I.25}$$

I.3.3. Contact areas

The contact area is a main element on the analysis of the instrumented indentation data, its calculation is modified according to the scale of measurement. Different approaches exist in the literature to take into account the defects of the indenter, specifically the tip blunting [81–87].

In nanoindentation since the early 90's the polynomial expression determined by Oliver and Pharr has been largely used (Eq. I.26).

$$A_{\mathrm{c}}=C_0\,{h_c}^{2}+C_1\,{h_c}^{1}+C_2\,{h_c}^{1/2}+C_3\,{h_c}^{1/4}+\ldots+C_8\,{h_c}^{1/128} \tag{I.26}$$

where C_0 to C_8 are constants determined by the curves fitting. The eight coefficients are used just because they fit well the data but they do not have a physical meaning. The expression can be adapted to different indenter geometries. The first term ($C_0=\pi\tan^2\theta$; θ is the indenter angle) represents the perfect pyramid; the second a paraboloid of revolution, which is approximated to the sphere at small penetrations. The third term could be linked to the tip defect [88]. The higher order terms may describe deviations from the perfect geometry and give a function that could be suitable over different orders of magnitude in the displacement [48,63].

To obtain the area coefficients the calibration is generally performed into a material of known properties such as the fused silica using the continuous stiffness measurement mode.

The method consists in obtaining the coefficients that lead to a constant elastic modulus over a determined depth range [48].

Herrmann *et al.* [89] proposed to plot the square root of the theoretical contact area as a linear function, where the coefficients are fitting parameters. Similarly, Thurn and Cook [82] suggested the same relation but assigning a physical meaning to the coefficients presented below:

$$\sqrt{A_\mathrm{c}} = \frac{h_\mathrm{c}}{C_1} + \frac{C_1}{C_2}\ ;\ C_1 = \frac{1}{\sqrt{\pi}\tan\theta}\ \text{and}\ C_2 = \frac{1}{2\pi R} \qquad \text{(I.27)}$$

where R is the tip radius.

Chicot *et al.* [90] obtained a contact area only dependent on the truncated length of the indenter tip (h_b) determined by high resolution microscopy, the relation was proposed as reliable alternative when the instrument does not account with the continuous stiffness measurement mode that renders impossible the calibration described above (Eq. I.28). They proved the validity of the expression from 10 nm up to the microindentation range, measuring the elastic modulus and hardness in the characterization of TiHfCN film of 2.6 μm of thickness.

$$A_\mathrm{c} = \pi\tan^2\theta\left(h_\mathrm{c} + h_\mathrm{b}\left(1 - exp\left(-\frac{2\,h_\mathrm{c}}{h_\mathrm{b}}\right)\right)^{3/2}\right)^2 \qquad \text{(I.28)}$$

With a similar approach, Troyon et Huang [84] proposed a relation for the micro range just considering the tip defect:

$$A_\mathrm{c} = \pi\tan^2\theta\ (h_\mathrm{c} + h_\mathrm{b})^2 \qquad \text{(I.29)}$$

At the macro scale Cagliero *et al.* [41] suggested that for Vickers indentation it is needed to add an extra parameter based on the length of the non-convergent faces of the pyramid, *i.e.* the four faces intercept in a segment of length t and not in a vertex point.

$$A_\mathrm{c} = \pi\tan^2\theta\ {h_\mathrm{c}}^2 + 2\tan\theta\, h_\mathrm{c}t \qquad \text{(I.30)}$$

All the previous relations are conveniently expressed in terms of θ that is the semi-angle of the equivalent axisymmetric cone equal to 70.3° for Vickers and Berkovich indenters that give the same projected contact area.

I.3.4. Effective indenter shape

The initial idea is that the behavior of an axisymmetric indenter into a previously indented surface specimen, is equal to an equivalent rigid tip of modified shape against a flat surface [91]. In other words, the effective indenter produces the same normal surface displacements on a flat surface than that created by a conical indenter in the previously deformed surface, for indenters with relatively large angles. The shape is described by $z = u(r)$, where r is the radial distance from the center of contact and $u(r)$ is the distance between the tip and the curve surface [48,91]. Fig. I.7 schematizes the effective indenter shape.

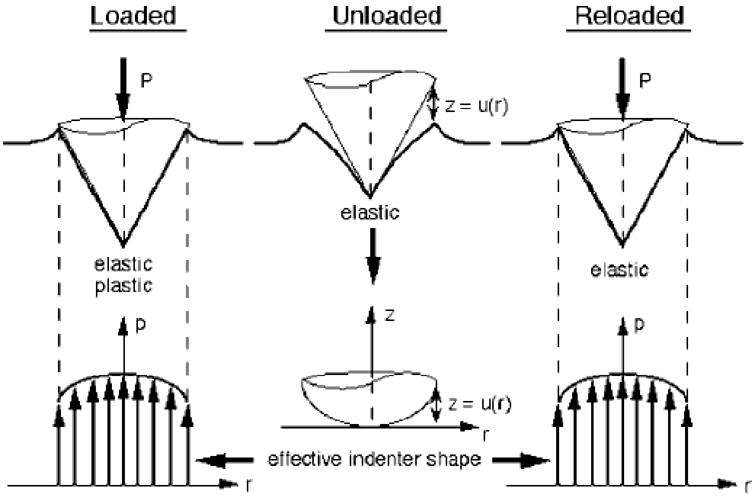

Fig. I.7. Schematic representation of pressure distributions under the indenter during loading, unloading and reloading and effective indenter shape [64].

Sneddon's integral transform method is applied to axisymmetric distributions of normal pressures corresponding to many indenters. This method describes that the contact mechanics for an axisymmetric indenter of arbitrary profile is given by a power law, this relation is approximated the effective indenter shape (Eq. I.31) [55].

$$z = Br^n \qquad \text{(I.31)}$$

where B and n are constants, for conical indenter n=1 and $B = \cot\theta$, and for spherical indenters $n = 2$, $\sim B = 1/2R$ according to Fischer [6]. Pharr and Bolshakov [64] assigned as the best fitting parameters, $B = 4.34 \cdot 10^{-8} nm^{-1.63}$ and $n = 2.63$.

Pharr and Bolshakov [64] used Sneddon's solution to give the relation between load and displacement for indenters of arbitrary profile:

$$P = \frac{2E_{\mathrm{R}}}{\left(\sqrt{\pi}B\right)^{1/n}} \frac{n}{n+1} \left(\frac{\Gamma(n/2+1/2)}{\Gamma(n/2+1)} \right)^{1/n} h^{1+1/n} \tag{I.32}$$

where Γ is the gamma function, n varies from 2 to 6, and it is related to the exponent in Eq. I.13 by $m = 1 + 1/n$.

The effective indenter shape must produce the same pressure distribution by elastic deformation of a flat elastic half-space. During the initial loading, the pressure is obtained by a complex elastic-plastic deformation; then, at the unloading stage the pressure decreases by elastic recovery leading to a curved surface; finally, during reloading stage the pressure distribution is recovered by elastic processes only. Therefore, the initial pressure distribution due to elastic-plastic deformations can be linked to the pressure distribution upon unloading and reloading due to elastic processes [48,64].

The effective indenter concept is not applicable if the reverse plasticity is important to modify the unloading curve from elastic behavior [64].

From the effective indenter concept, it is possible to estimate the ε parameter from the Oliver and Pharr contact depth (Eq. I.33) [91],

$$\varepsilon = m(1 - \varphi) \tag{I.33}$$

where φ is expressed by,

$$\varphi = \frac{1}{\sqrt{\pi}} \left(\frac{\Gamma(n/2+1/2)}{\Gamma(n/2+1)} \right) \tag{I.34}$$

These expressions lead to values of ε between 0.74 to 0.79, which is coherent to the approximation frequently used in the analysis of the indentation data $\varepsilon = 0.75$. Determining the coefficient m from the fitting of the unloading curve ε can be calculated [48,64].

I.3.5. Deformation mode sink-in and pile-up

Two principal deformation modes may be developed during indentation tests. In elastic materials, the surface drawn inwards and downwards underneath the indenter, that is known as sink-in. For elastic-plastic materials, the surface can deform by sink-in and pile-up; pile-up is known as the upward flow of the material surface. In the regime of fully plastic deformation, the behavior depends on the ratio σ_y/E and on the work hardening properties.

There exist many mechanisms for plastic deformation. For metals, a good approximation is the power law work-hardening and the conventional stress-strain relation described by,

$$\sigma = E\varepsilon \text{ for } \varepsilon \leq \frac{\sigma_y}{E} \tag{I.35}$$

$$\sigma = C\varepsilon^n \text{ for } \varepsilon \geq \frac{\sigma_y}{E} \tag{I.36}$$

where σ_y is the initial yield strength, C the strength coefficient, n the work hardening exponent, E is the elastic modulus, and ε is the strain. For perfectly plastic solids $n = 0$ and for most of the metals n varies between 0.1 to 0.5 [42].

The pile-up or sink-in formation depends on the ratio σ_y/E and on work hardening exponent n. When pile-up predominates, the contact depth is greater than the maximum penetration depth. Fig. I.8 shows schematically the two deformations modes.

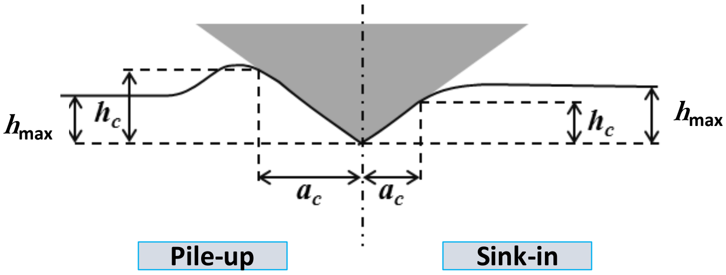

Fig. I.8. Schematic representation of an impression showing pile-up and sink-in. a_c indicates the contact radius.

The shape of the plastic zones relies on the material properties, for materials without work-hardening and large ratio σ_y/E the plastic zone has a hemispherical shape well extended beyond the circle of contact, this lead to extensive pile-up and the measurements of the contact depth according to Oliver and Pharr methodology is underestimated (Eq. I.14) [6,92]. In materials with a small ratio σ_y/E the plastic zone is limited to the boundary of the contact circle; hence, sink-in probably dominates. Johnson [93] noted that a large capacity for work hardening yields in the extension of the plastic zone to greater depths and diminution of the pile-up around the indenter, *i.e.* the work hardening tends to reduce the radius of the plastic zone in the surface pile-up. Bolshakov and Pharr [92] suggested that the Oliver and Pharr method provides a good estimation for a large amount of materials with work-hardening behavior, but more accurately for materials presenting sink-in.

The effect of pile-up and sink-in is crucial for the correct estimation of the contact area, and consequently the elastic modulus and hardness. The Oliver and Pharr method could lead to underestimations up to 60% of the actual contact surface. Many authors have proposed diverse methodologies to take into account pile-up effect [71,92,94–97], which is not a simple task. The standard ISO 14577 does not account this deformation mode. Frequently, the authors suggest that the best way to consider pile-up is by imaging the residual imprints [35,71,94,98].

Loubet *et al.* [88] and Hochstetter *et al.* [99] developed a relation to estimate the contact height (h_c) for pile-up or sink-in deformation of the material, the relation considers a plastic depth added to the indenter tip defect (h_b, also called h_0) multiplied by a factor $\alpha = 1.2$ for a Berkovich indenter:

$$h_c = \alpha\left(h_{\max} - \frac{P_{\max}}{S} + h_b\right) \tag{I.37}$$

Choi *et al.* [95] proposed that the contact depth is determined by considering the elastic deflection h_d, plastic pile-up height h_{pile}, the correction depth for the tip blunting Δh_b and the maximum indentation depth:

$$h_c = h_{\max} + h_{\text{pile}} - h_d + \Delta h_b \tag{I.38}$$

Zhou *et al.* [94] found by AFM/SEM images that for Berkovich indentation, pile-up only occurs along the edges of the triangle indent and not in the corners. They suggested that the contact depth or contact area can be corrected by two methods. First, the pile-up area measured by AFM must be added to the contact area of Oliver and Pharr [63]. The second method, consists in a relation between the actual properties and the apparent measured ones, based on the ratio of the contact depth of the Oliver and Pharr analysis to the pile-up height, for which they estimated geometrically an expression presented in the following equation,

$$h_{\text{pile}} = (2\sqrt{3} - 3)h_c \tag{I.39}$$

Then, Zhou *et al.* [94] proposed the next relations for the relation between the actual (H_0, E_0) and apparent (H_a, E_a) properties values in the case of monolithic materials,

$$H_0 = \left(2\sqrt{3} - 2\right)^{-2} H_a \tag{I.40}$$

$$E_0 = \left(2\sqrt{3} - 2\right)^{-1} E_a \tag{I.41}$$

On the other hand, the ratios such as $h_f/h_{\max}$ or W_e/W_t are used as an indication of the deformation mode; Oliver and Pharr [48] identified that generally for $h_f/h_{\max} > 0.7$ the material shows pile-up, Yetna *et al.* [100] demonstrated that this limit was higher $h_f/h_{max} > 0.83$ for a large number of materials. Choi *et al.* [95] found that the material preferably sinks-in when $W_e/W_t < 0.15$.

I.3.6. Work of indentation approach

The work of indentation defined as the area under the load-displacement curve, can be obtained by integrating the loading and unloading curves, which corresponds to the total work W_t and the elastic work W_e, respectively. Hence, the plastic or also called irreversible work, W_p, is the difference between the total and the elastic work that corresponds to the enclosed area between the loading and unloading curves, *i.e.* $W_t = W_e + W_p$ [6,35,101]. The schematic representation is presented in Fig. I.9. Many authors [6,35,101–104] had determined relationships between these quantities and the mechanical properties.

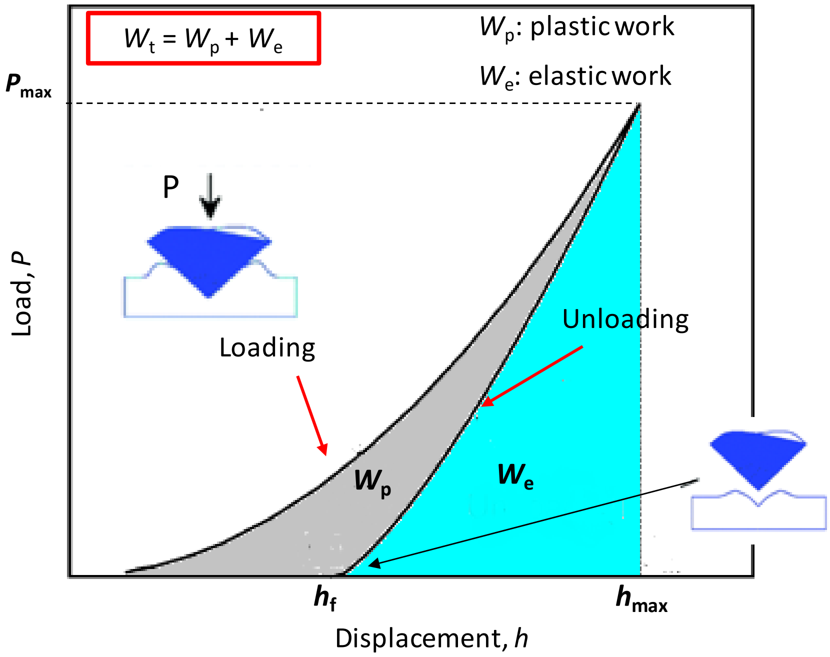

Fig. I.9. Load-displacement curves pointing out the areas under the curve considered as the work of indentation [105].

The total work is obtained by determining the integral of the relation of the loading curve described previously:

$$W_t = \int_0^{h_{max}} Ch^{\alpha}\, dh = \frac{C{h_{max}}^{\alpha+1}}{\alpha+1}; \text{with } \alpha = 2, W_t = \frac{C{h_{max}}^3}{3} \quad (I.42)$$

where C depends on the material behavior, and α could be rational numbers (Meyer's relation).

Similarly, the elastic work is calculated by integrating the power law relation,

$$W_{\mathrm{e}} = \int_0^{h_{\max}} B'(h - h_{\mathrm{f}})^m \, dh = \frac{B'(h_{\max} - h_{\mathrm{f}})^{m+1}}{m+1} \tag{I.43}$$

Both areas can also be calculated by numerical integration that does not require the fitting of the loading and unloading curves [104]. From dimensional analysis, total and elastic works are proportional to $h_{\max}{}^3$[35].

The ratio of the plastic or elastic work to the total work is related to the elastic modulus and hardness of the material by:

$$\frac{W_{\mathrm{p}}}{W_{\mathrm{t}}} = 1 - \kappa \frac{H}{E_{\mathrm{R}}}; \text{ or } \frac{W_{\mathrm{e}}}{W_{\mathrm{t}}} = \kappa \frac{H}{E_{\mathrm{R}}} \tag{I.44}$$

where κ is a constant initially set to ~5, some authors mentioned that it was not dependent on the work hardening behavior of the material [48,80,106]. Then, Choi *et al.* [95] found that this constant could take different values depending on the work hardening behavior and on the relation H/E_{R}, leading to two values, 5.17 for $W_{\mathrm{e}}/W_{\mathrm{t}} < 0.15$, and 7.30 for $W_{\mathrm{e}}/W_{\mathrm{t}} > 0.25$ as showed in Fig. I.10. Afterwards, Yetna *et al.* [103] suggested the value of 6.6 for the range $0.15 < W_{\mathrm{e}}/W_{\mathrm{t}} < 0.25$.

The ratio $W_{\mathrm{p}}/W_{\mathrm{t}}$ has been also correlated with the ratio of the residual depth to the maximum penetration depth $h_{\mathrm{f}}/h_{\max}$, there exists different approaches in the literature to relate both quantities based on finite element analysis and experimental data [35,107–109].

In general, the ratios $W_{\mathrm{p}}/W_{\mathrm{t}}$, $h_{\mathrm{f}}/h_{\max}$ and H/E_{R} are function of σ_y/E, n, and θ [35].

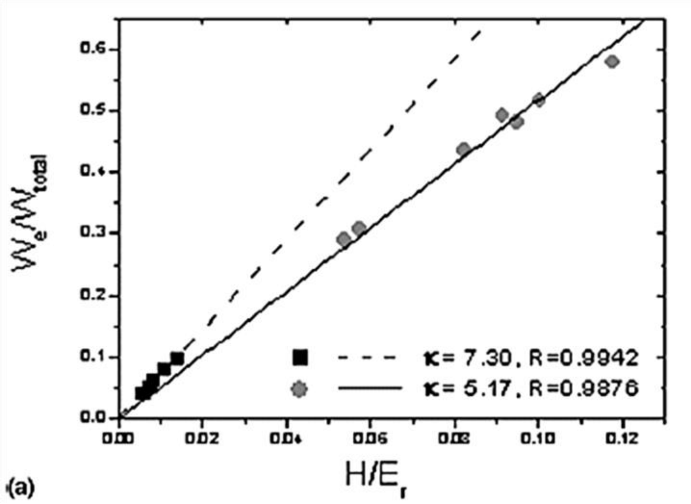

Fig. I.10. Relation between $W_{\mathrm{e}}/W_{\mathrm{total}}$ and H/E_{R} by FEA results [95].

Eq. I.44 shows that the ratio H/E_{R} can be calculated directly from the work of indentation, prior knowledge of one of the two properties allows the calculation of the other without determination of the contact area. When both properties are unknown, there are some approaches in the literature useful for their calculation. Tan [101] developed a relation for the elastic modulus that depends on the contact area, the maximum load and displacement, the residual depth and the elastic work, determined as:

$$E_{\mathrm{R}} = \frac{1}{2}\sqrt{\frac{\pi}{A_{\mathrm{c}}}}\left(\frac{{P_{\mathrm{max}}}^{2}}{W_{\mathrm{e}}} - \frac{P_{\mathrm{max}}}{h_{\mathrm{max}} - h_{\mathrm{f}}}\right) \tag{I.45}$$

where the contact area is determined by the Oliver and Pharr method (Eq. I.26). The values of the elastic modulus obtained by this method in different materials were comparable to those calculated by the contact stiffness mode.

Yetna *et al.* [103] proposed a methodology that does not need the computation of the contact area, but rather in the constant κ, the contact stiffness and the ratio $W_{\mathrm{e}}/W_{\mathrm{t}}$, resulting attractive since pile-up or sink-in do not interfere directly in the calculation:

$$E_R = \frac{W_{\mathrm{e}}/W_{\mathrm{t}}}{\kappa \frac{4\beta^2}{\pi} P_{\mathrm{max}} (C_{\mathrm{t}} - C_{\mathrm{f}})^2} \tag{I.46}$$

C_{t} and C_{f} are the total and load frame compliances of the system, respectively. β is the correction factor. In this case, the values of E_{R} calculated by the work of indentation resulted closer to the theoretical values, than the elastic modulus obtained by the area and stiffness relation.

On the other hand, hardness obtained by the work of indentation, is the relation between the work and the indented volume, which change significantly according to the approach used for its calculation, leading to different results, not necessarily comparable with the typical hardness numbers (*HM*, *HIT*). Some common definitions are the total hardness (*HT*) and the plastic hardness (*HP*) in Eqs. I.47-48 that consider the total and plastic work, respectively. *HP* is known as the irreversible work required to create a unit of volume of permanent deformation [60,101,103,104,110].

$$HT = \frac{W_{\mathrm{t}}}{V_{\mathrm{c}}} \text{ or } HT = \frac{W_{\mathrm{t}}}{V_{\mathrm{t}}} \tag{I.47}$$

$$HP = \frac{W_{\mathrm{p}}}{V_{\mathrm{p}}} \tag{I.48}$$

The definitions of V_c, V_t and V_p change according to the assumptions made for their calculation. V_t can be obtained by Eq. I.49, considering the maximum displacement and the equivalent axisymmetric cone (θ = 70.3°) [104]. Malzbender *et al.* [61] proposed instead the use of the contact depth considering the tip defect (h_b) (Eq. I.50). A similar approach was given by Tan [101] using a polynomial expression for the volume obtained from the expression of the contact area of Oliver and Pharr that takes into account the correction of the indenter tip (Eq. I.51), the coefficients C_0 to C_8 are fitting parameters. Chicot *et al.* [104] suggested the use of the maximum penetration depth correcting the tip defect (Eq. I.52).

$$V_t = \frac{\pi}{3}\tan^2\theta\, {h_{max}}^3 \tag{I.49}$$

$$V_t{}^M = \frac{\pi}{3}\tan^2\theta\,(h_c + h_b)^3 \tag{I.50}$$

$$V_c{}^T = C_0\, {h_c}^3 + C_1\, {h_c}^2 + C_2\, h_c + \ldots + C_8\, {h_c}^{1/64} \tag{I.51}$$

$$V_t{}^C = \frac{\pi}{3}\tan^2\theta\,(h_{max} + h_b)^3 - {h_b}^3 \tag{I.52}$$

For the plastic volume Sakai *et al.* [60] determined a simple relation of proportionality between the total volume and the plastic volume given by the ratio h_f/h_{max}. Chicot *et al.* [104] found a similar relation according to its total volume. As an alternative Tan [101] proposed the same function area that for contact volume (Eq. I.51) but replacing h_c by h_f.

The hardness definitions of Chicot *et al.* [104] are equivalent between them and comparable to the Meyer hardness. Similarly, the values obtained by Tan [101] were alike and overestimate the *HIT* hardness calculated from the load-displacement data.

I.4. Correction of the data

The load-displacement data from instrumented indentation testing allow to estimate the mechanical properties of the materials. However, the recorded data are affected by numerous errors disturbing the calculation of the desired properties. The most important errors are related to displacement differences, environmental changes and non-ideal shape of the indenter and usually the measurements at nanoindentation scale are more sensitive to those errors. In this section, we describe the main corrections for the experimental data in order to obtain more reliable results.

I.4.1. Frame compliance

Prior to the calibration of the frame compliance, C_f is an unknown parameter of the system. The measured total compliance C_t is the sum of the contact compliance C_c of the sample (the inverse of the stiffness), and the load frame compliance, C_f. The system is usually represented by two springs in series model, which lead to a constant frame compliance with load. [48,110]:

$$C_{\mathrm{t}} = C_{\mathrm{f}} + C_{\mathrm{c}} = C_{\mathrm{f}} + \frac{\sqrt{\pi}}{2E_{\mathrm{R}}\sqrt{A_c}} \tag{I.53}$$

where A_c is the projected contact area, and E_R the reduced elastic modulus. In this equation, the hypothesis is a constant elastic modulus and a known area function.

A similar relation is given if the instrumented hardness is considered as a constant with load, leading to a constant relation of $\sqrt{HIT}/E_R$:

$$C_t = C_{\mathrm{f}} + C_{\mathrm{c}} = C_{\mathrm{f}} + \frac{\sqrt{\pi}\sqrt{HIT}}{2E_{\mathrm{R}}\sqrt{P_{\mathrm{max}}}} \tag{I.54}$$

The measured displacement, h^* is directly affected by C_f, thus the penetration depth is usually higher than the actual value because it includes the frame deformation. Consequently, the contact stiffness, *S,* decreases and leads to an underestimation of the elastic modulus. The correction of displacement data is given by Eq. I.55:

$$h = h^* - C_{\mathrm{f}}\, P \tag{I.55}$$

where h is the actual displacement on the sample.

It is worth mentioning that the value of C_f should be positive if any previous calibration of this parameter has been performed. Nevertheless, typically the value is already included in the instrument from a previous calibration by the manufacturer, in this case a further calculation of the frame compliance could lead to a negative or positive value.

Various methods exist to determine C_f, usually implying the use of homogeneous and isotropic samples, with E and ν known. Table I.3 summarizes three methods frequently used to perform this calibration procedure, included in the ISO 14577-4.

Table I.3. Summary of methods used in the frame compliance determination.

Method	Hypothesis/Test	Plot	C_f determination
1	E_R and HIT = const. / standard at different loads or multicyclic tests.	C_t vs. $1/P_{max}^{0.5}$ (Eq. I.54)	Intercept with y axis (extrapolation) C_f = const.
2	E_R = const. Area function (A) known or determined by high resolution imaging techniques/ standard at different loads or multicyclic tests.	C_t vs. $1/A_c^{0.5}$ (Eq. I.53)	Intercept with y axis (extrapolation) C_f = const.
3	E_R and HIT = const. Continuous stiffness measurement method.	P/S^2 vs. h (Eq. I.56)	Iteration until obtaining a flat curve at high penetrations

The two first methods presented in Table I.3 are the most used in indentation and the calibration protocol can be found in some of the software's instruments (*e.g.* Zwick Universal Hardness Machine). Both methods are easy to perform because the data are taken directly from the results without any iteration procedure. Usually, it is highly recommended to use the data at higher loads or displacements to avoid imperfections of the indenter, a possible existence of the indentation size effect with a variation of hardness with penetration depth, noise and vibrations affecting the data of load-displacement at low loads.

Method 3 was suggested by Oliver and Pharr [48] as an improvement for a previous calibration procedure proposed by them. This new method uses the continuous stiffness measurement mode to perform the tests; this method includes different steps: first, the determination of the contact point identified as the slope change in the plot of the harmonic stiffness as function of the displacement into the surface, second, the procedure is based on the plot of P/S^2 versus the displacement, at depths greater than a few hundred nanometers where the hardness and modulus are constant, the ratio P/S^2 should be constant (Eq. I.56). Finally, C_f is obtained by changing its value to have a flat P/S^2 versus h at large displacements. This procedure is interesting because it does not require prior knowledge of the area function. [48]

$$\frac{P}{S^2} = \frac{\pi}{(2\beta)^2}\frac{H}{E^2} \qquad \text{(I.56)}$$

where β is the correction factor between the axisymmetric conical indenter and the pyramidal indenter.

The previous methodology of Oliver and Pharr was based on an iterative procedure to calibrate the area function and the frame compliance with one set of data from a single reference sample without requiring independent measurements of the indent areas; nevertheless, the method was limited due to time consuming.

The frame compliance is a very critical parameter to correctly determine the mechanical properties by indentation tests. For example, if C_f is smaller than the actual one value, the corrected displacement is higher than the real one, thus elastic modulus and hardness will be underestimated. The accurate determination of the frame compliance becomes more important at high loads or displacements, where C_f is the dominant factor or has the same order of magnitude than the contact compliance, C_s [48,110,111]. Likewise, C_f affects significantly affects the determination of elastic modulus more than hardness, because the correction modifies the stiffness and the area in the modulus and just the area in the hardness.

To improve the accuracy on the estimation of C_f, Van Vliet *et al.* [112], proposed a direct measurement of the frame compliance, and the identification of the effects of the load, loading direction and loading rate on its determination. The proposed system replaced the indenter holder and indenter, by an indenter holder with a flat punch shape of several millimeters of diameter, called platen. The platen is mounted to the load train with a pin-nut arrangement (Fig. I.11) and covered with cyanoacrylate. Then, the platen makes a firmly contact with the sample holder ($P > 10$ N) until cyanoacrylate is fully polymerized. A standard load-displacement cycle is performed and registered. For each loading cycle, the loading and unloading data are fitted to a straight line whose slope represents the direct measurement of C_f in each direction. Some of the advantages of the method are that it does not require the estimation of the contact areas, extrapolation of results or fitting of the unloading curve; therefore, the method reduce the uncertainties on C_f. It is worth mentioning that even that the method leads to very accurate values, the procedure is time consuming and difficult to be performed as regular calibration practice.

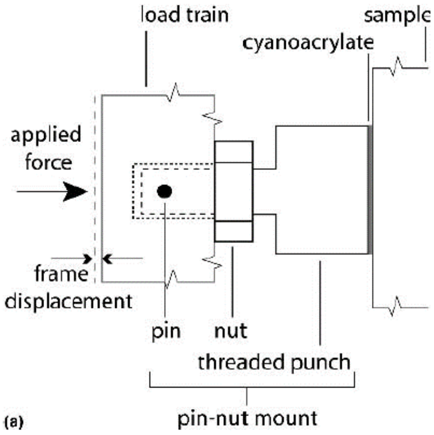

Fig. I.11. Schematic flat punch mounting for the determination of the direct frame compliance. The pin locks the punch when the nut is tightened against the threaded post. After the test, the nut is released manually and the pin is removed to allow full retraction of the bunded punch sample [112].

In the literature many other methods exist to consider the frame compliance correction [41,113–115], however the methods listed in Table I.3 are the most common practices in indentation.

I.4.2. Indenter area function or tip defect

The contact area given at the penetration depth h_c, should be corrected since the geometry of the indenters are not perfect in practice. At the nanoindentation scale this correction is more critical because penetrations depths are small. In the literature two principal methodologies are adopted to perform this correction and are described below.

Method 1: consists in performing the indentation test into a material of known properties (E_R and ν) at different loads or using the continuous stiffness measurement mode (CSM). Then the actual area is found by:

$$A = \pi\left(S\frac{1}{\beta E_R}\right)^2 \tag{I.57}$$

Then, it is usually recommended express the correction as the ratio of the actual to the ideal area function. The area function could be given by different expressions such as that proposed by Oliver and Pharr [63]. At the nano scale the instruments usually account with the CSM mode where the modulus is set constant up to a specific penetration depth to find the correction of the area function, the calibration is frequently performed in fused silica.

Method 2: is based on the determination of the tip rounding or tip defect (h_b) by means of high resolution microscopy or by analytical methods, then, the tip defect is added to the displacement measurements [84,90,110]. An example of the analytical method is given by

Fischer-Cripps [6] who proposed to plot dP/dh evaluated at the maximum displacement versus h_c (considering sink-in, Eq. I.14) that should be a straight line as follow:

$$\frac{dP}{dh} = Ch_c + D; \text{then } h_\mathrm{b} = \frac{D}{C} \tag{I.58}$$

I.4.3. Thermal drift

The thermal drift is related to dimensions changes in the components of the instrument due to thermal contraction, or creep in the specimen material; both effects modify the register of the displacement and are virtually independent [6,110]. In nanoindentation tests, generally the thermal drift is measured fixing the load at a certain point before the total load, for a specific time (few seconds); then the displacement variation is measured and the rate at which the material is deformed is calculated in nm/s, to subsequently correct the data. For example, during unloading the load is held constant at 10% of P_max and the indenter continues to penetrate the material at a rate of 0.05 nm/s, therefore the displacement measurement acquired for 10 seconds is corrected by 0.5 nm [116].

The thermal drift correction is specific for each test. The displacements should be corrected according to the time at which they were acquired. Generally, thermal drift could affect significantly at the nano scale, but it is less important at the micro and macro scale where the change of the displacement is too small in comparison with the order of magnitude of the recorded displacements [34].

I.4.4. Initial penetration depth or zero-contact point

The standard ISO14577-1 treats the zero-point determination, which represents the first contact of the indenter with the surface, this determination should be performed individually for each curve. The standard states two principal methods for its determination:

Method 1: extrapolation of a fitted function, for example a polynomial of 2nd degree, within the range from zero up to 10 % of the maximum indentation depth. The fitting should be performed below the depth at which plastic yielding is achieved.

Method 2: determination at the first increase of the force or contact stiffness. This methodology is well adopted in most of the instruments software. In nanoindentation for continuous stiffness measurement mode the contact stiffness leads to an abrupt change of slope, making easier the identification of the zero-contact point.

In the literature exists different methods to deal with the correction of the position at the first contact, but most of them are found in the two previous methodologies described. For example, Chudoba *et al.* [117] suggested to fit the first nanometers of the data (about 30 nm) by a power law, similarly to the principle of fitting the curve with a 2nd order polynomial [6,118]. Kalidindi and Pathak [119], instead modified the definition of the zero point by a Hertzian approach in spherical indentation. Marteau *et al.* [120] proposed to correct the zero-point errors using the evolution predicted by macroscopic behavior laws.

I.5. Uncertainties in instrumented indentation testing

I.5.1. Force uncertainties

In nanoindentation instruments usually the force resolution is ranged from 1 nN to 1 μN. Nevertheless, in some metrology laboratories the minimum traceable force is ~5 μN [12,121]; however, the national laboratories as the National Institute of Standards and Technology (NIST) has done efforts to improve the available force standards to the micro and nano Newton range, *i.e.* Electrostatic Force Balance [75,122].

A common assumption in indentation is that the models for force detection represent the real interaction between the indenter and the sample [122]. In practice, differences may exist between the measured force by the load cell in the instrument and the forces experienced by the sample, these differences are related to forces such as Van der Waals, electrostatic, chemical adhesion, etc.

The misalignment between the drive and measurement axes, produce a cosine error or a linear component from Abbe errors, contributing to the force uncertainties [122,123].

I.5.2. Displacement uncertainties

The uncertainties in the penetration depth related to the displacement sensor in the instrument, is typically obtained using a displacement interferometer or capacitance sensor with uncertainties in the sub-nanometer range, usually this procedure is performed by the instrument manufacturer. The uncertainties associated to the effects of Abbe offset and misalignments between the drive and the measuring axis are in the nanometer range [122].

On the other hand, the displacement data is affected by several factors such as initial depth of penetration, thermal drift, mechanical vibrations, frame stiffness, roughness, and fluctuations of voltage [110,122,124].

I.5.3. Indenter area function uncertainties

The geometric errors of the indenter are expected to be in the order of the manufacturing tolerances. For pyramidal tips as Vickers and Berkovich, the main errors are tip rounding, face and base angle errors, and additionally for Vickers indenter, a non-unique point of intersection. Moreover, the spherical indenters can show deviations from the perfectly spherical shape, particularly for indenters in the nanometer scale [75,122,125].

The errors sources of the area function are extensible known, however the uncertainties in the area function are not broadly quantified in the literature, due to the limitations and complications measuring the tip shape by advanced techniques, such as atomic force microscopy [122,126].

Besides, rotational misalignments between the indenter axis and the sample surface normal vector, produces errors in the area function.

The elastic modulus and the hardness are connected to the indented area, consequently, the area function of the indenter affects importantly the calculation of both properties [75].

The errors on the apex angle should not exceed 0.3° (ISO 14577) that is approximately $\pm$ 0.8 of the geometric parameter $\phi = 24.5$, the indenter tip defect must be measured continuously or calibrated through the function area calibration in rigid materials of a known elastic modulus as fused silica.

I.5.4. Frame compliance

During the indentation test the applied force produces the indenter penetration into the sample, and the deformation of various components in the system such as the indenter shaft, the sample holder and other components of the instrument, this deformation is denoted as the instrument frame compliance. Various techniques and approaches exist to measure the instrument frame compliance and to perform its calibration, discussed in section I.4.1 [41,112,113,127,128].

In mechanical systems, the separation of force and metrology loops entails to displacement measurements less affected by the instrument stiffness. On the contrary, usually in instrumented indentation systems the force and metrology loops are coincident, creating a direct coupling between the force and penetration depth measurements; consequently, the displacement measurements are highly dependent to the uncertainties of the frame distortions. [75,122]

Some sources of uncertainties due to the computation methods of the frame compliance are listed below:

- Restriction of the analysis to the unloading data, which is usually approximated to a power law function (Oliver and Pharr model), that depends strongly on the portion of the curve be fitted [41,112].

- Extrapolation of the experimental data using the Eqs. I.53-54, whichever the used method, assuming constant hardness and elastic modulus, known function area, etc. This procedure, assigns significant uncertainties to the x variable, leading to bias in the estimated value of C_f, being different to the actual one [75].

- Inaccurate calculation of E and A_c in the iterative method of Oliver and Pharr, the assumption that the material sinks-in and the value of ε [63,112].

These issues, can result in a large uncertainty of the frame compliance, affecting all the subsequent calculations. [41,75,112,129,130]

1.5.5. Uncertainty perpendicularity and alignment

Misalignment could be defined as the state where the sample surface is not perpendicular to the symmetry axis of the tip. There are different elements affecting the perpendicularity and alignment during the indentation test, such as mounting of the indenter and the sample; bending in the instrument frame; and the sample form [122,131]. Principally, two types of misalignment could happen; first, due to the sample surface, when it is not perpendicular to the axis of the tip and force application; and second, when the symmetry axis of the tip is not aligned with the load application axis [131].

Errors in the area function of the indenter should be less than 1% maintaining the central axis within 1° (limit specified by ISO 14577) and do not lead to important changes in the determination of the mechanical properties for indenters such as Berkovich, Vickers and spherical. If the angular misalignment is more than 1°, the errors in the area show a significant increase. These errors are not symmetric, for bigger misalignments, about 5°, the errors can range from 10 to 30 %. The flat punch indenter is more susceptible to effects of misalignments, and Berkovich when comparing with the Vickers indenter [122,127,131].

A tilt in the Y-axis of rotation leads to slightly bigger errors in the hardness measurements than in the elastic modulus. The hardness and the elastic modulus showed an increase with the tilt angle, since the contact area increases, creating a physical contact larger than the calculated assuming orthogonal alignment, *e.g.* hardness and modulus are approximated 10%

bigger for a tilt angle of 5°. This error is related to lateral forces caused by the contact of the indenter with a tilted surface [132].

I.5.6. Surface roughness

The presence of a roughness degree in the surface samples is unavoidable, it can introduce errors in the first contact detection and in the estimation of the contact areas. For a well-polished sample, the surface has undulations from several nanometers to tens of nanometers, therefore, when the indenter touches the surface, it penetrates the higher asperities, in this case the effective contact is smaller than the supposed by the theoretical models. Gradually with the increasing load, the indenter penetrates deeper and the contact approximates the perfect contact and the specimen response correspond to its real properties [125,133].

The ISO14577 stipulates that surface roughness should be maximum 5% of the required maximum penetration depth. For depth inferiors to this requirement the scatter of hardness and elastic modulus is more than 25% and the properties are not reliable [132]; similarly, the scatter degree on the load-displacement curves increases with the roughness and the first contact detection is highly affected. On the other hand, the contact stiffness is not affected by the surface roughness or the work hardening due to mechanical polishing [120,134].

The importance of surface roughness is directly related with the scale of measurement, due to the different ranges of penetration. In nanoindentation and microindentation tests, the condition of roughness < $5\%h_{\max}$ could be violated, in such case the number of tests should be increased [135].

The hardness is more affected than the elastic modulus for the roughness, because the area is used directly to its calculation, instead in the computation of the elastic modulus the square root of the area is used. In nanoindentation tests the surface roughness is considered an important issue to understand the indentation size effect [120,132,134,136].

Marteau *et al.* [136] and Xia *et al.* [134] presented an interesting model to treat simultaneously and statistically the nanoindentation loading curves identifying the first contact error defined as the gap between the experimental curves and the simulated one using Bernhardt's model to circumvent the roughness problems. They found that scatter of the first contact error is reduced diminishing the surface roughness. The application of this correction to the data leads to an almost constant modulus no matter the surface roughness. The zero-point correction through this statistical method is adequate to estimate the mechanical properties on rough surfaces without bias related to the roughness. It is worth mentioning, that the experimental elastic modulus computed without this approach present a large scatter with the surface roughness.

I.5.7. Zero contact point

In instrumented indentation tests the indenter makes contact with the surface before starting the test, this initial contact is usually performed at very small loads (*e.g.* 1 μN), nevertheless, there is always a small penetration into the material that will carry an error in the displacement data. Consequently, this initial depth should be added to the data to correct it.

In the previous section we mentioned the two principal methods for the correction of the zero point, by extrapolation of the data or by recognition of a force peak or contact stiffness change. According to the standard ISO 14577 the uncertainty related to this method should be not greater than 1% of the maximum displacement for the micro and macro scales; at the nano scale it is accepted to have greater uncertainties.

It is clear that the uncertainties in the zero-point determination depend on the external conditions such as noise and vibrations, roughness of the specimen, material properties, instrument settings; *e.g.* the recognition of the zero-contact point would be more difficult in very soft materials like polymers, which at a very small force could penetrate quickly into the material surface.

I.6. Conclusions

This chapter gives some of the most important basis for the analysis of instrumented indentation testing, this information would be useful in the study of homogeneous and heterogeneous materials with three different instruments, in order to validate and understand the fundamentals of the technique on industrial materials with non-ideal behavior.

CHAPTER II

Materials and experimental methodology

The main objective of this research is the study of the instrumented indentation technique from the nanometric to the macrometric scales in order to stablish relationships and the connection between them. To accomplish this purpose, we performed different tests in industrial metallic materials using three instruments encompassing a broad spectrum of load-displacement scales, searching the understanding of the instrument functioning and dissimilarities according to the scale of measurement. Afterward, this analysis was helpful in the investigation of a highly heterogeneous material used as a brake pad in railway applications.

This chapter includes the main characteristics of the instruments and indenters; subsequently, a presentation of the bulk metallic materials and their mechanical properties. Finally, we present the testing procedure and the methodology of calculation. Any change in these conditions will be pointed out in the subsequent results and discussion chapters. The description of brake pad material and the experimental methodology applied on it is presented in Chapter V to facilitate the comprehension and reading of this work.

II.1. Characteristics of the instruments

II.1.1. Nanoindenter XP

Nano Indenter XP made by MTS, currently Keysight (Fig. II.1), is a depth-sensing indentation instrument, which force is imposed by passing a current through a coil that sits within a circular magnet; the imposed force is proportional to the current passing through the coil. The instrument can be operated by displacement control in the system software, but it is fundamentally a load-controlled instrument. The displacement sensing system consists of a three-circular plate capacitive arrangement. The two outside plates are fixed to the head and have holes to accommodate the indenter shaft. The indenter position is determined by the difference in voltage between the center plate and the outside plates. The assembly is supported by two leaf springs with very low stiffness in the vertical direction and very high stiffness in the horizontal direction. The working mode is XP which has the following specifications: displacement resolution <0.01 nm, load theoretical resolution 50 nN, maximum load ~750 mN, maximum penetration depth ~10 µm.

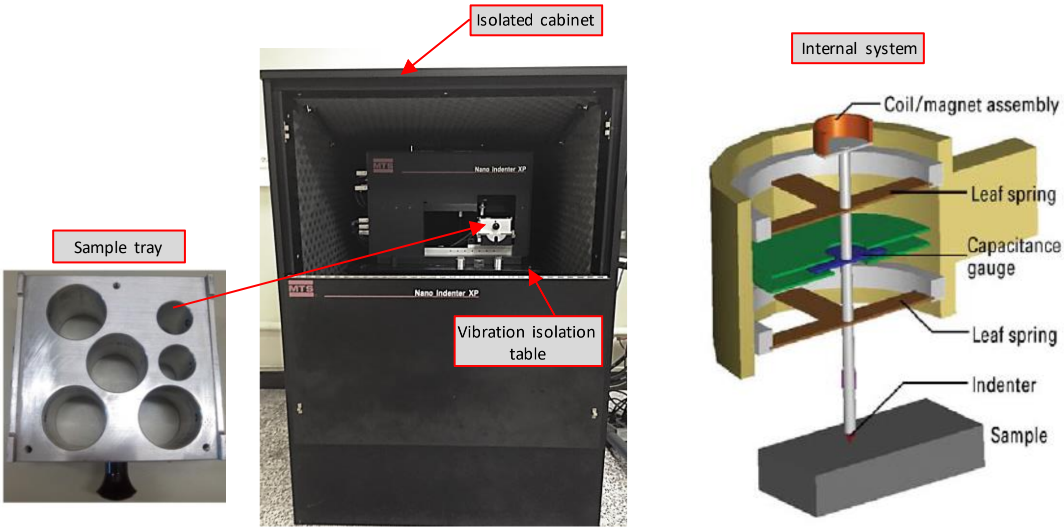

Fig. II.1. Nano Indenter XP by MTS with the operation internal system and the sample tray.

The nanoindenter includes a high load working mode, based in a motor-driven cantilever for load application (Fig. II.2). In this system, contact points are added to the end of the torsion bar, cantilever and loading element; after contact between the torsion bar and the loading elements, the load is applied by torsion to the bar and finally the unloading consists in releasing the torque. The high load mode works up to 1 kg (~10 N). The change between the low loads range and high loads range is achieved close to 1 N.

The instrument is located inside of an isolated cabinet to retard environmental temperature changes and acoustic disturbance from vibrations, and it is placed on a vibration isolation table to avoid mechanical vibrations from the floor. It has a platform for the sample tray that can be moved in the x and y directions. The sample mounting system consists in two steps, first the sample is glued with Crystalbond adhesive to a cylindrical support [115]; second it is mounted in a sample tray with a clamping mechanism by screws (Fig. II.1), six samples can be mounted at the same time.

The instrument comprises the continuous stiffness measurement (CSM) mode that allows the continuous measurement of hardness and elastic moduli with the penetration into the material. The methodology is accomplished by superimposing a small oscillation on the primary loading signal and analyzing the resulting response of the system by means of a frequency-specific amplifier [116].

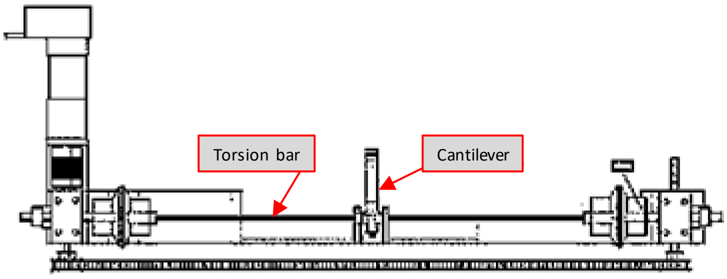

Fig. II.2. High load system in the Nanoindenter XP.

Nanoindentation tests are performed up to 10% of $P_{\max}$, at this load the indenter is held at a small constant load for 50 s. The change of displacement measured during this period is attributed to thermal expansion or contraction of the specimen or instrument, then the drift rate is calculated as the slope of the plot of the displacement as a function of time, subsequently the displacement data are corrected automatically by the software.

The Nano Indenter XP will be called in this work as nanoindenter and the tests performed on it as nanoindentation tests, even if the instrument works as well in the micro and macro range. Note that the nano range is defined in the standard ISO 14577 [135] for displacements up to 0.2 µm, this limit is exceeded in the instrument.

II.1.2. Microindenter CSM2-107

The CSM2-107 microindenter (Fig. II.3) made by CSM-Instruments (currently Anton Paar) works between 0.05 to 30 N. The force and displacement resolutions are 100 µN and 0.3 nm, respectively (range of 100 µm maximum depth limit). The loading and unloading rates vary between 0 and 300 N/min. The displacement measurement is determined by the difference of voltage in the capacitive sensor. A coil localized in the upper part of the load column drives the displacement into the sample. The imposed force is controlled by the current variation in the magnetic coil, the schematic representation of the measuring head assembly is presented in Fig. II.3. A reference fork (touch probe) serves as reference to the indenter before it touches the surface (Fig. II.4). A motorized table is integrated to the system to change the sample position in (x direction) and between the measuring head and the microscope. To perform the tests, initially the indenter approaches the specimen (speed 10-25% min^{-1}) until contact with the surface at the contact force (2.5-10 mN), then the speed changes to the selected loading rate [137]. The specimen is fixed by a sample holder or vice tool (Fig. II.3).

The instrument was used with two different reference forks, the first one called reference 1 corresponds to the original machine design, which is a stiff reference fixed at the same position for all the tests after calibration of the optimum set up distance (called dz) between the surface sample and the indenter. Through the years, the reference system has been improved by the company to encompass the indenter and provides a constant reference during penetration in order to reduce the frame distance to a minimum value. This was achieved through the mobility of the system that allows to make small changes in the reference according to the testing position, this new system has been installed recently in the instrument and it would be called as reference 2. We will discuss in Chapter IV (section IV.1) the influence of reference 1 and 2 on the tests results. Fig. II.4 shows the details of both references systems.

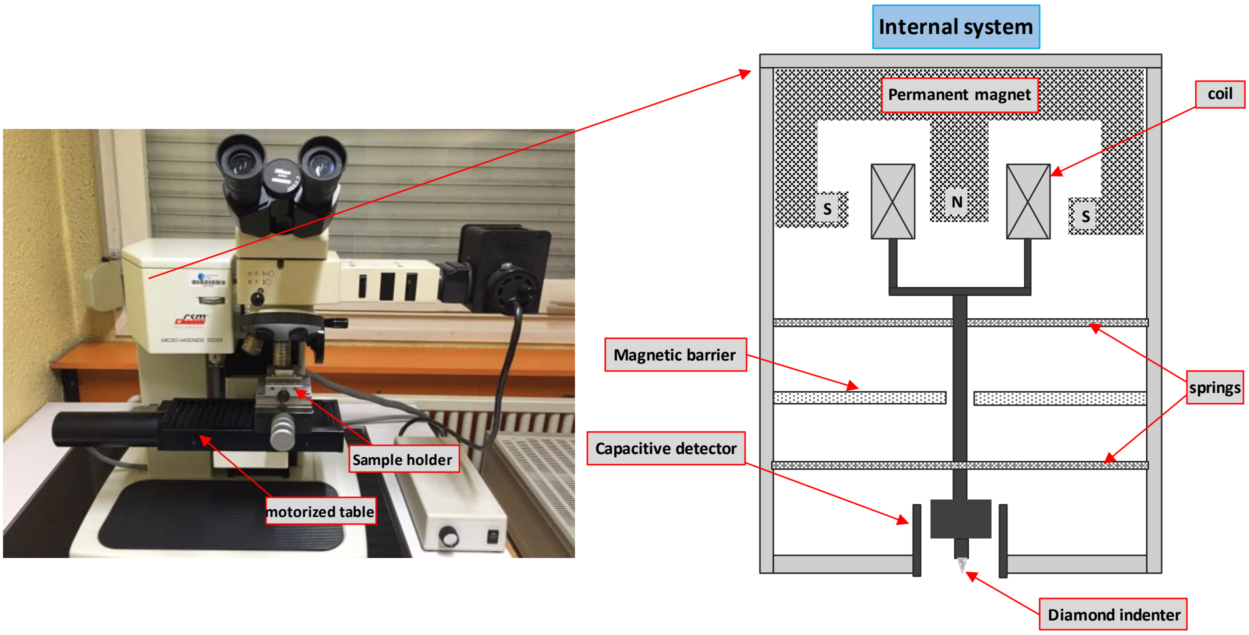

Fig. II.3. Microindenter CSM2-107 showing the internal working system.

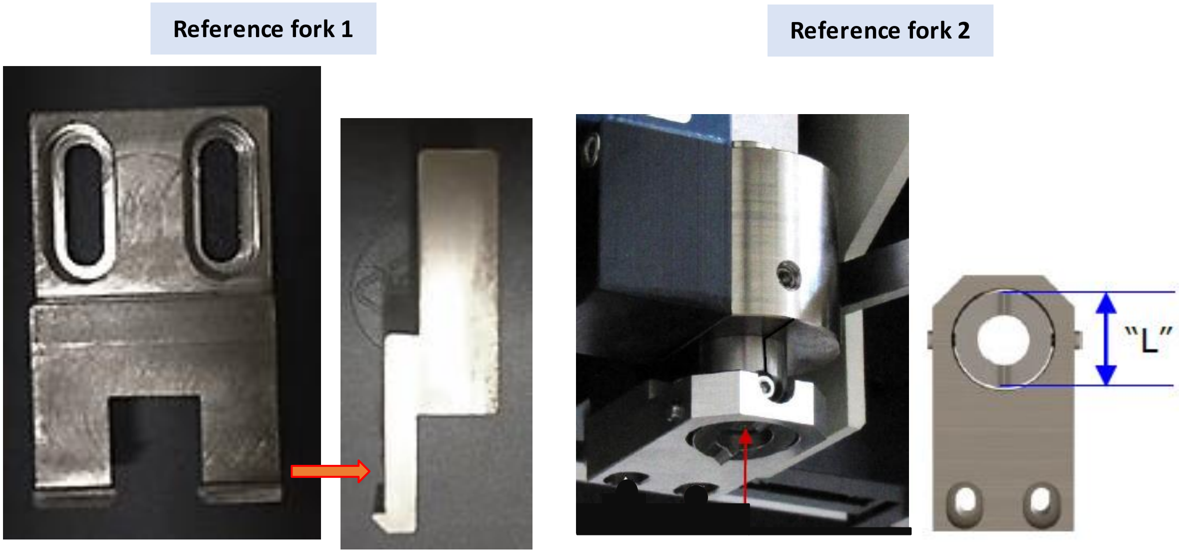

Fig. II.4. References forks 1 and 2 used at the microindenter.

The CSM2-107 instrument will be named during this work as microindenter and the tests performed on it as microindentation tests, although that the instrument works also in the macro range, at loads higher than 2 N according to ISO 14577.

II.1.3. Macroindenter ZHU 2.5

The universal hardness testing machine ZHU 2.5 fabricated by Zwick Roell Group, works in the loads range between 5 N to 2.5 kN. The measuring head contents a load cell, a high-resolution travel measurement system, a sensor foot in complete accordance with the Abbe measurement principle, and an indenter which can be easily interchanged [138]. A detailed schematic representation of the system is presented in Fig. II.5. The accuracy of load cell is grade 1 (standard DIN EN ISO 7500-1) and the displacement resolution is 0.02 µm. The loading and unloading rates can be controlled by force or displacement, similarly to the holding mode during the dwell time.

The machine is coupled with a microscope and a motorized table. The table allows to change the sample position (x and y) and to displace it between measuring head and the microscope, it is designed to support the maximum working load of the instrument (2.5 kN). The measuring procedure is schematized in Fig. II.6.

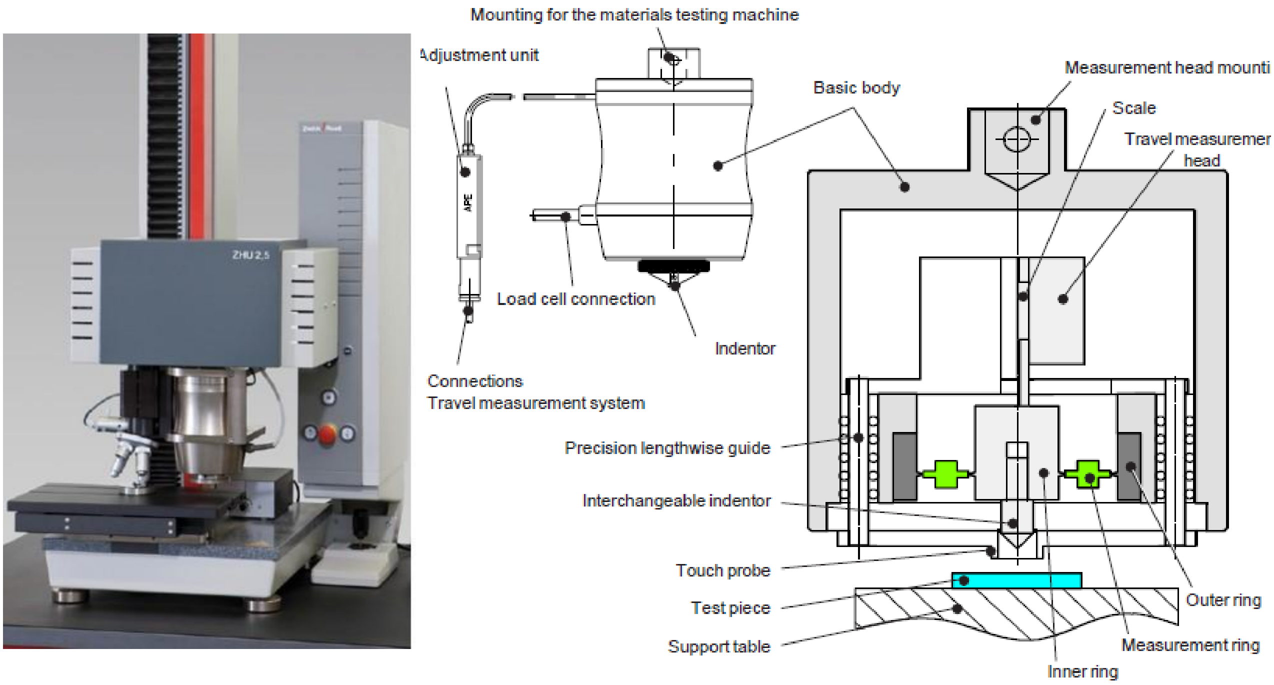

Fig. II.5. Macro indenter Zwick ZHU 2.5 and scheme of the operating system.

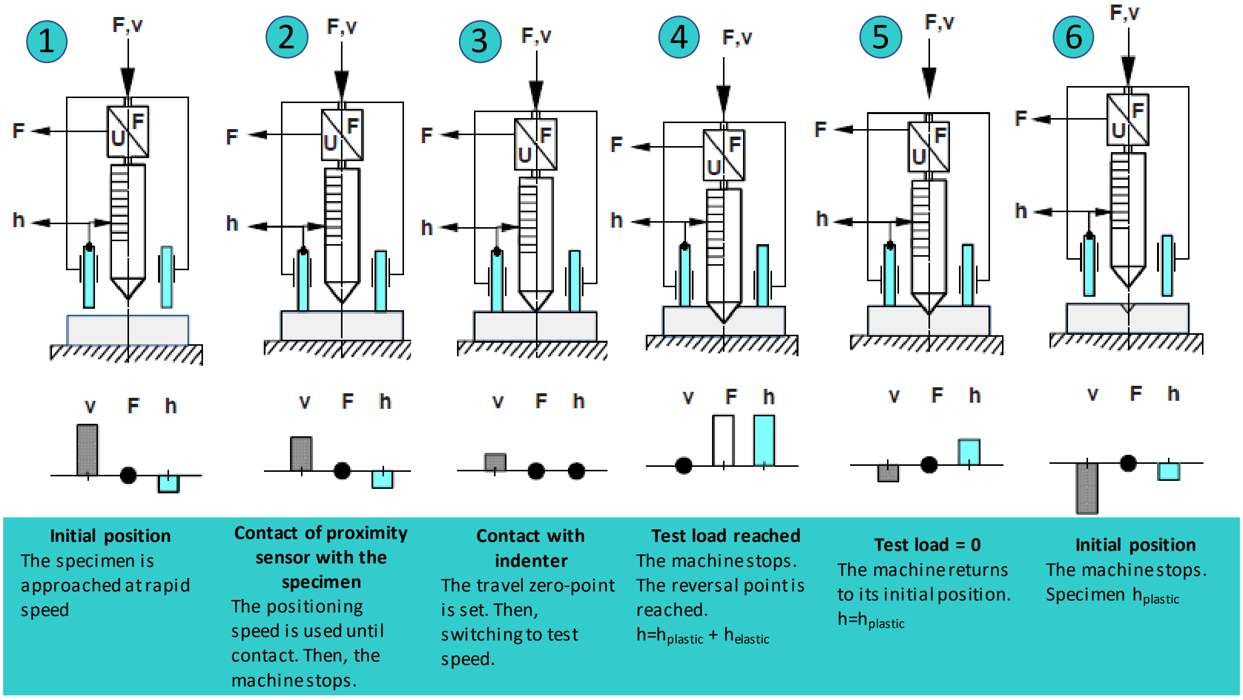

Initial position The specimen is approached at rapid speed	**Contact of proximity sensor with the specimen** The positioning speed is used until contact. Then, the machine stops.	**Contact with indenter** The travel zero-point is set. Then, switching to test speed.	**Test load reached** The machine stops. The reversal point is reached. $h=h_{plastic} + h_{elastic}$	**Test load = 0** The machine returns to its initial position. $h=h_{plastic}$	**Initial position** The machine stops. Specimen $h_{plastic}$

F= Force, v= speed, h= indenter position

Fig. II.6. Evolution of the measuring procedure for the macroindenter ZHU2.5. h_{plastic} corresponds to the residual depth after the indenter retreat and h_{elastic} corresponds to the penetration depth recovered upon unloading.

In the instrument ZHU 2.5, the sample is not fixed with a vice or glue, it is just placed on the motorized table. The instrument will be called in this work as macroindenter and the tests performed on it as macroindentation tests, to distinguish it from the other two instruments.

II.2. Indenters

In nanoindentation a Berkovich indenter was used to perform the tests, the calibration is accomplished in fused silica using the continuous stiffness measurement method, usually the tests are performed up to $h_{\max} = 2000$ nm, an example of the calibration curves (up to 250 nm) is presented in Fig. II.7, the function area is obtained by the Oliver and Pharr method (Eq. II.1) [48] which is integrated in the instrument software. This calibration procedure was done several times because the samples were tested at different dates. Usually, the calibration is performed every three months, according to the frequency of use of the instrument (approximately 4 nights per week).

$$A_c = C_0\, h_c{}^2 + C_1\, h_c{}^1 + C_2\, h_c{}^{1/2} + C_3\, h_c{}^{1/4} + \ldots + C_8\, h_c{}^{1/128} \qquad \text{(II.1)}$$

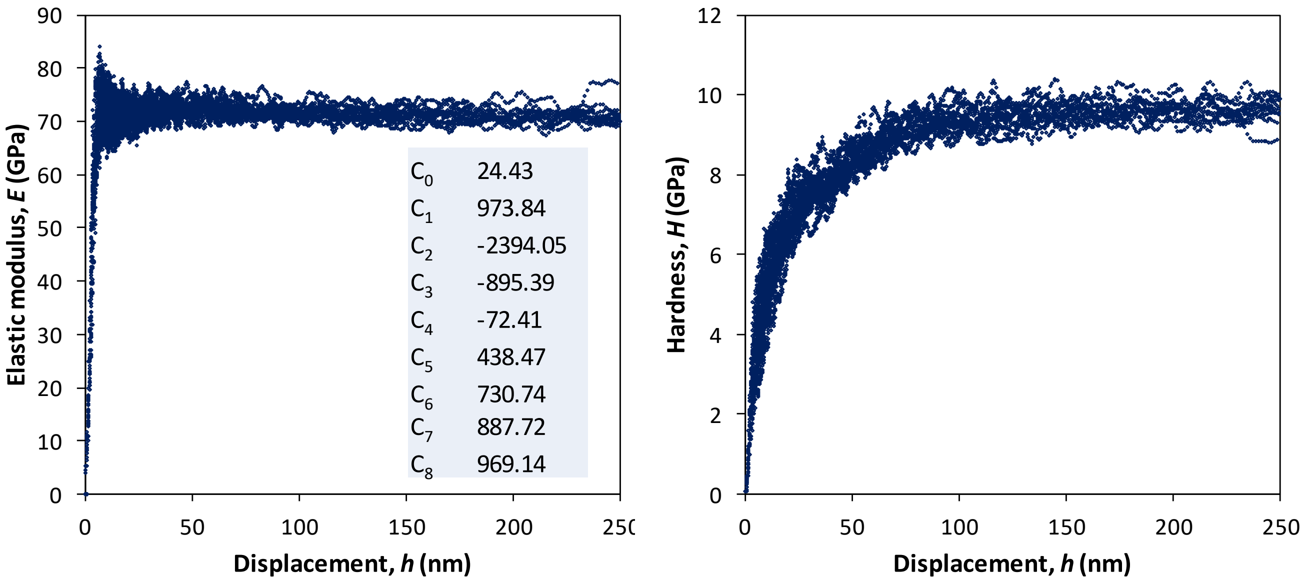

Fig. II.7. Calibration curves performed in fused silica by CSM nanoindentation tests. The validity of the function area starts at the displacement where elastic moduli is constant.

In microindentation and macroindentation, we used Berkovich and Vickers indenters, respectively. The tip defect (h_b) in both cases was estimated through scanning electron microscopy (SEM) (Fig. II.8), obtaining 100 nm for Berkovich indenter and 185 nm for Vickers indenter. It is worth mentioning that these values were estimated at greater magnifications in the microscope, but the quality of the pictures was not good, because of that we presented the analogous at smaller magnifications.

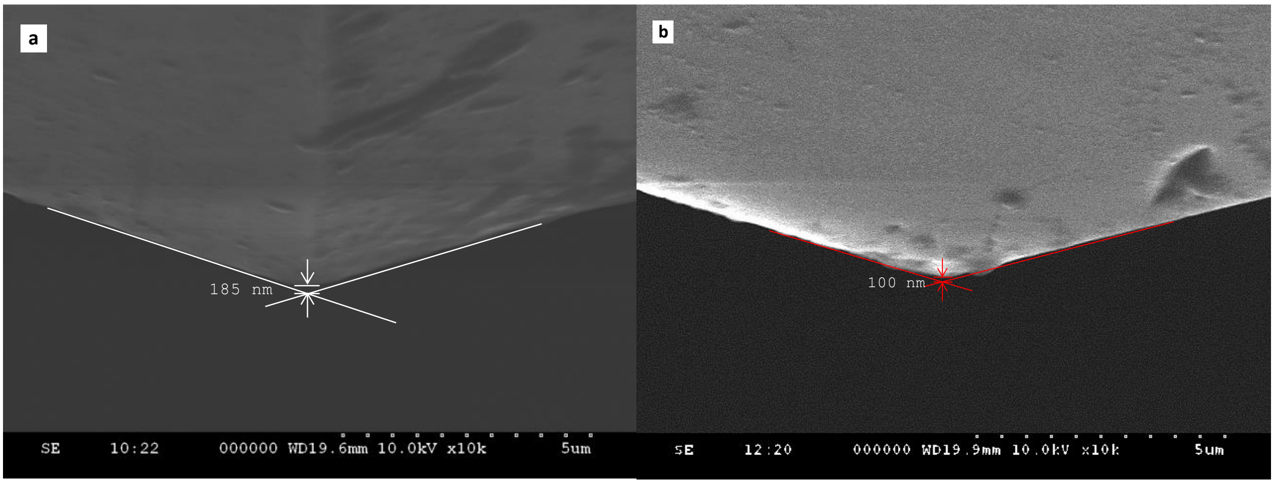

Fig. II.8. SEM micrographs of the used indenters: (a) Vickers indenter used in macroindentation with a tip defect of ~185 nm. (b) Berkovich indenter used in microindentation with a tip defect of ~100 nm.

The area functions at both scales depend on the tip defect, they are described by Eq. II.2 [90] and Eq. II.3 [84]. The approximation of h_b obtained by SEM is suitable since it is small in comparison with thousands of nanometers of penetration depth reached in both instruments, obviously special attention should be given at smaller loads < 1 N, specially at the microindenter.

$$A_c = 24.5\left(h_c + h_b\left(1 - exp\left(-\frac{2\,h_c}{h_b}\right)\right)^{3/2}\right)^2 \tag{II.2}$$

$$A_c = 24.5\,(h_c + h_b)^2 \tag{II.3}$$

In practice, it is difficult to get a perfect intersection of the four faces in a single point in a Vickers indenter [133], in some cases an additional parameter is added to the function area to take into account this element [41], but usually at the macro scale the diamond pyramid is considered to have a perfect shape. For the further calculations, we only considered the tip defect.

The three indenters have a penetration depth limit according to the height of the diamond pyramids, at greater penetrations than this limit, the material is penetrated with the cylinder at which the diamond pyramids are attached; usually this cylinder is made of steel [113]. The limits are ~12 µm for Berkovich indenter nanoindentation, ~25 µm for Berkovich indenter in microindentation, and ~250 µm for Vickers indenter in macroindentation.

II.3. Metallic materials

The first stage of the research was focus on the study of four bulk metallic industrial materials by multiscale indentation whose main characteristics and microstructure are described below. The interest of studying industrial materials is to deal with the heterogeneities of these materials and observe how they can affect the response by indentation.

II.3.1. Steel hardness blocks (39HRC and 63.4HRC)

The specimens correspond to two reference hardness blocks of known hardnesses, 39HRC (3.7 GPa) and 63.4HRC (7.8 GPa), typically these samples are used in the calibration of hardness testing machines (not instrumented). These names 39HRC and 63.4HRC, are kept during presentation results of this work. To observe their microstructure (Fig. II.9) they were polished until mirror finish and etched with Nital at 2%.

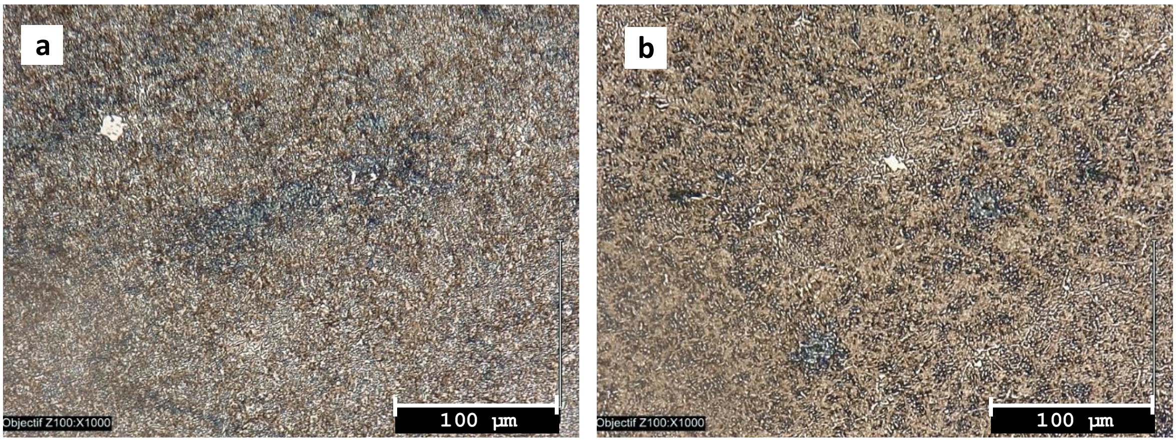

Fig. II.9. Microstructure of hardness block samples etched with Nital at 2%, a) 39HRCand b) 63.4HRC.

Both samples present a fine microstructure composed by islands of proeutectoid cementite (white regions) and the dark regions of very fine perlite. Elastic modulus of steels usually varies between 190 to 210 GPa and the Poisson's ratio is ~0.3, those values are taken as reference for the further analysis of the mechanical properties obtained by indentation [139].

II.3.2. Aluminum alloy (Al)

The sample belongs to series 7000 for aeronautical applications, it is a high strength alloy hardened by formation of precipitates. The main alloying elements are Zn, Mg and Cu. For the microstructural observation, the sample was polished until mirror finish, then it was etched by immersion with Keller reagent (95 ml water, 2.5 ml HNO_3, 1.5 ml HCl, 1 ml HF) for 5 s and subsequently by Weck's reagent (100 ml water, 1 g NaOH, 4 g $KMnO_4$) for 10 s.

The microstructure is presented in Fig. II.10, exhibiting elongated grains and precipitates [140]. Some of its mechanical properties are: hardness 0.6 -1 GPa, elastic modulus 70-74 GPa, yield strength 359-407 MPa, and Poisson's ratio 0.35 [139].

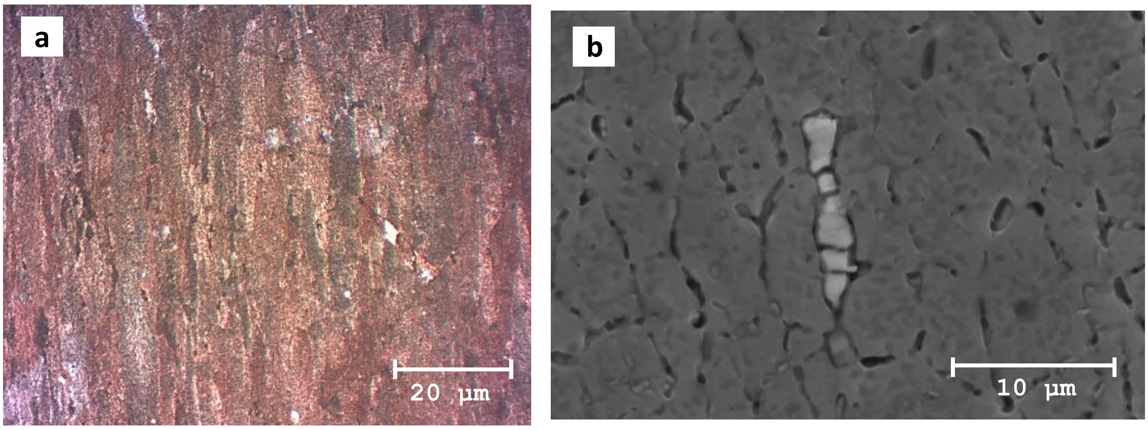

Fig. II.10. a) Microstructure of aluminum alloy (series 7000) showing elongated grains, observed by optical microscopy with polarized light b) precipitates observed by scanning electron microscopy.

II.3.3. Stainless steel grade 316L (SS316L)

The stainless steel 316L has an austenitic (face centered cubic fcc) structure, this material is easily work hardened, its typical composition is presented in Table II.1. The sample was polished until mirror finishing and etched with a solution composed by: 1 ml HNO_3 at 16 %, 1 ml HCl at 32% and 1 ml of glycerol; the sample was previously heated at 40 °C and then etched by 15 s.

Table II.1. Typical composition of stainless steel grade 316L (% by weight).

Alloy	C	N	Cr	Ni	Mo	Mn	Si	S	P	Cu
SS316L	0.02	0	16.4	10.5	2.1	1.8	0.5	0.010	0.03	0.4

The microstructure exhibit austenite grains with substantial presence of twinning and without evidence of precipitates in the grain boundaries (Fig. II.11). The mechanical properties are: hardness 1.4-1.8 GPa [141], elastic modulus 170-201 GPa [141–143], yield strength 205 MPa [141].

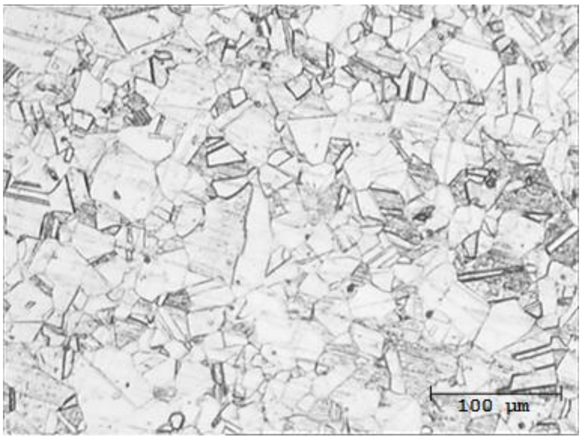

Fig. II.11. Microstructure of austenitic stainless steel 316L, etched with HNO_3 +HCl + glycerol.

Table II.2 summarizes the mechanical properties of the studied metallic samples found in the literature that will be used in the presentation of the results as reference values. In general, the values in this table are given as reference for the order of magnitude since the properties where unknown, particularly hardness that it is not an intrinsic material property.

Table II.2. Reference mechanical properties of bulk metallic materials. Hardness values are calculated with the actual contact area.

Material	Elastic modulus (GPa)	Hardness (GPa)	Poisson's ratio
Steel 39HRC	190 -210 [139]	3.7	0.3
Steel 63HRC	190 -210 [139]	7.8	0.3
Aluminum	70 -74 [139]	0.6 – 1 [139]	0.35
SS316L	170-201 [141–143]	1.4 - 1.8 [141]	0.3

II.3.4. Preparation of samples before to indentation tests

Previously to perform the indentation tests the samples were rectified (39HRC and 63.4HRC) or milled (SS316L and Al) to obtain parallel surfaces. Therefore, a chemical-mechanical polishing was performed, first with SiC papers (80-2000 grades), about 30-60 s on each paper according to the hardness of the sample; subsequently a final polishing with colloidal silica (OP-U from Struers). For aluminum, a similar procedure was performed; but the samples were submerged in an ultrasound bath with ethanol between each step (initial and final polishing), also a previous polishing with diamond suspension (3 µm) was done before the final step with colloidal silica.

II.4. Experimental procedure for multiscale indentation tests

II.4.1. Multiscale indentation tests

The general conditions for the indentation tests using the nano, micro and macro indenters are summarized in Table II.3. In the results presentation (Chapter IV) we will point out the type of test performed and in the case of variation from the following procedures it will be mentioned.

Table II.3. Test conditions for indentation tests in metallic samples using the nanoindenter, microindenter and macroindenter.

Parameters	**Nano classic**	**Nano CSM**	**Micro classic**	**Micro multicyclic**	**Macro classic**
Range of loads	20 - 700 mN	up to $h_{\max}$	0.1 – 20 N	0.1 – 20 N	5 – 2000 N
Loading/unloading rate	30 s	---	$2P_{\max}$ (N/min)	30 s	$2P_{\max}$ (N/min)
Dwell time at $P_{\max}$	15 s	15 s	15 s	15 s	15 s
Indenter	Berkovich		Berkovich		Vickers
Area function	Oliver and Pharr [48]		Chicot *et al.* [90]		Troyon and Huang [144]
Fixation	Glued to sample support and fixed to sample tray.		Sample holder (the sample remains suspended)		modeling clay around sample.
Other tests parameters		Frequency 45 Hz, strain rate 0.05 s^{-1}, surface approach sensitivity 40%		50 cycles, unload up to 20-30% $iP_{\max}$. Linear load increase.	

Classic tests performed at the three instruments (Fig. II.12), consist in a single load-unload cycle. The loading and unloading rates are set equal to $2P_{\max}$ N/min at the micro and macro indenters, which corresponds to 30 s for the nanoindenter. At the maximum load, the system is held at constant load during a dwell time (15 s) to avoid bulging effect, *i.e.* the indenter continues penetrating the material at the point where the load is removed.

The deflection at the end of the unloading curve at the microindenter is due to the machine functioning, specifically a shift between the displacement and force sensors at the end of the unloading part, note that is below 40% of $P_{\max}$ considered for the fitting (section II.5).

Continuous stiffness measurement tests are only performed at the nanoindenter, since is not available in the other instruments. For this method, we set a maximum displacement as parameter to stop the test, the reached load depends on the material properties.

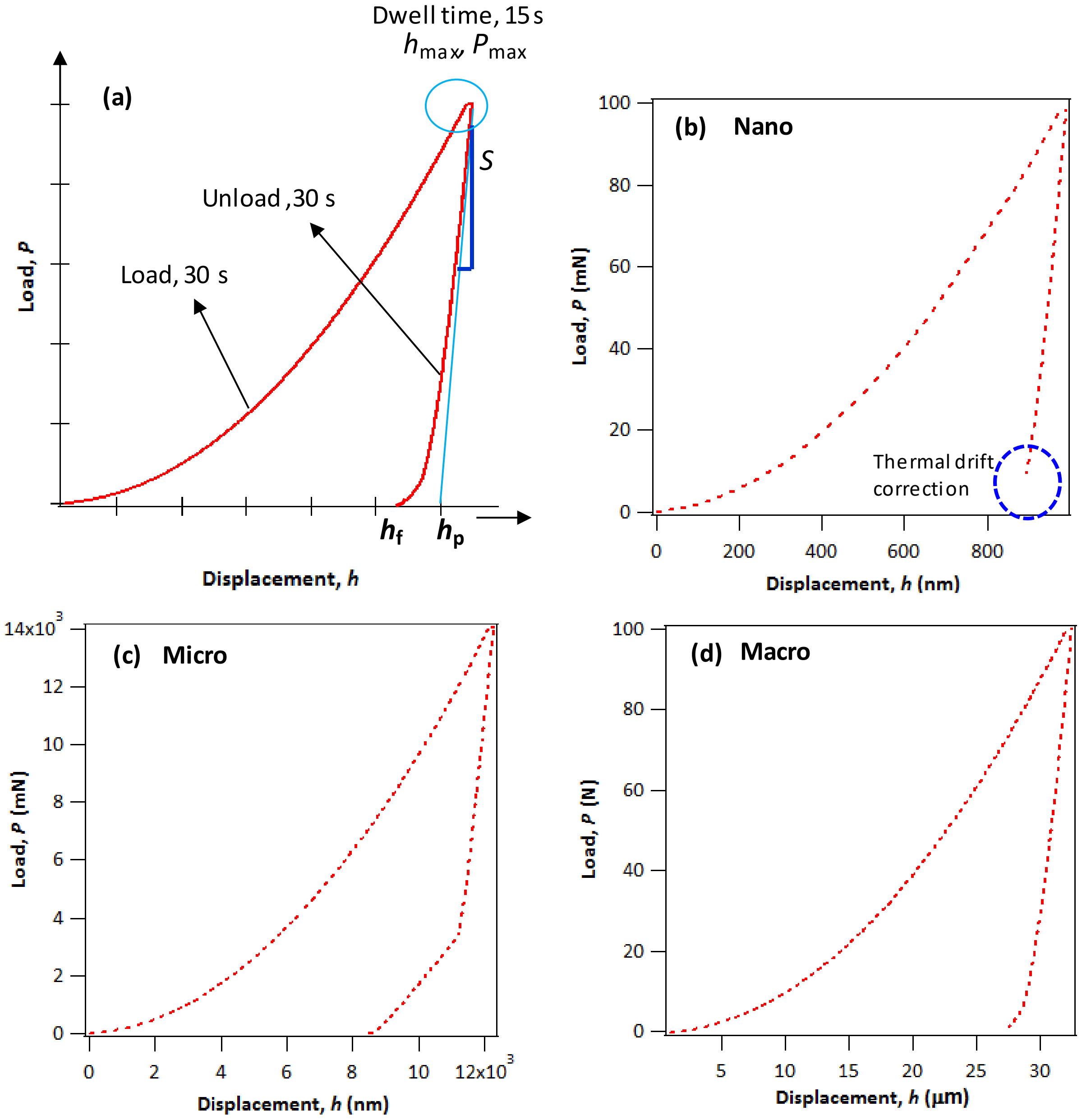

Fig. II.12. Load-displacement curves of classic tests: a) Presentation of the principal quantities needed in the analysis, h_f residual depth, S stiffness, h_p plastic depth. b) Test performed at the nanoindenter, the thermal drift is corrected at 10% of P_{max}. c) Test performed at the microindenter, the deflection at the end of the unloading curve is due to the instrument mechanism. d) Test performed at the macroindenter.

Multicyclic tests were performed at the microindenter (Fig. II.13) in order to obtain an equivalent response as the one obtained by the CSM tests, since both tests give the variation of the elastic modulus and hardness as a function of the penetration depth. The test consists in multiple load-unload cycles, at the maximum load of each cycle the force is held constant by 15 s, then the unload part is performed until 20-30% of the maximum load. If the unload part is done close to zero force, the appearance of the curves at the upper part is similar, leading to comparable results.

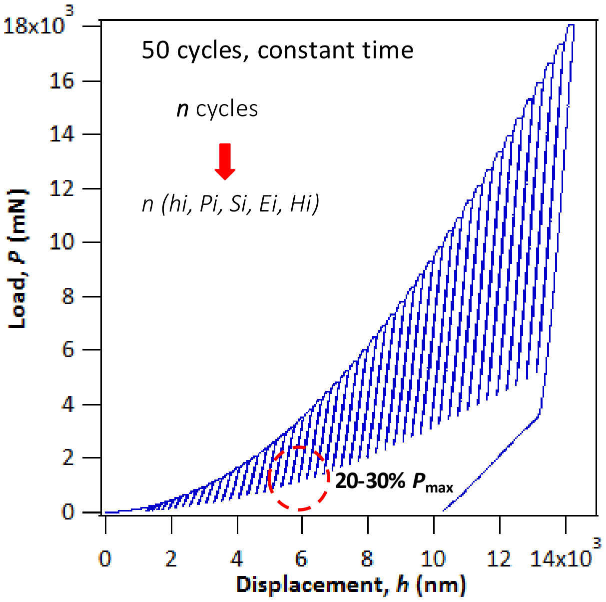

Fig. II.13. Load-displacement curve from multicyclic tests at the microindenter.

All the sequences of tests were performed at least 10 times. According to the obtained dispersion in each instrument and the characteristics of the sample the number of tests was increased in order to achieve a representative material-system response.

It is worth nothing that we did not work at the high load range at the nanoindenter since we got erroneous results, for example the unloading curves from classic tests presented an anomalous curvature leading to a wrong calculation of the mechanical properties; in the case of CSM tests a gap is observed in the curves of the evolution of elastic modulus or hardness versus penetration depth, an example is presented in Fig. II.14.

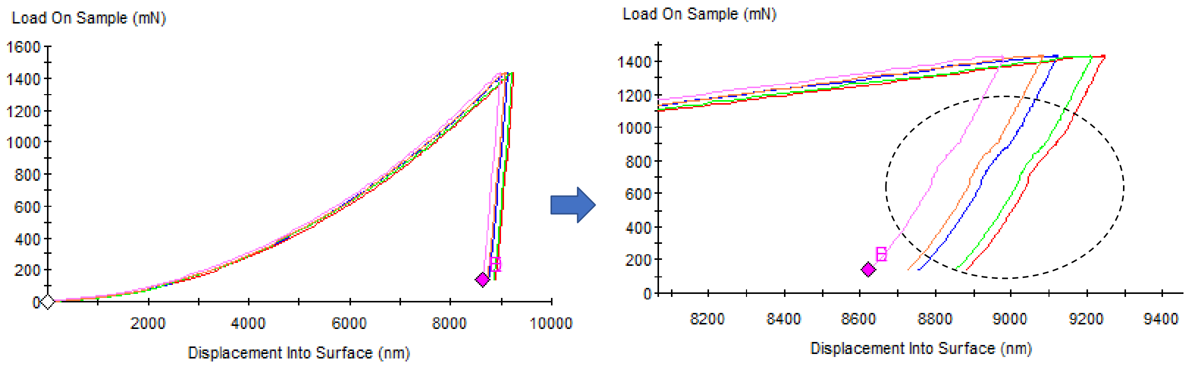

Fig. II.14. Load-displacement curve from classic tests at the nanoindenter in aluminum P_{max}=1400 mN corresponds with the high load range of the instrument. Note the deviation in the unloading curves.

II.4.2. Corrections of the data

According to the standard ISO 14577, the experimental data must be principally corrected by three factors: the frame compliance, the thermal drift, and the zero-contact point.

The methodology used for the frame compliance correction is discussed in Chapter IV, due to the important impact of this parameter in the experimental results.

Thermal drift

Thermal drift is typically corrected at the nano scale. The correction is performed automatically at the nanoindenter for each test. At this scale, variations of the penetration depth given by this phenomenon alter significantly the experimental data and consequently the results.

The penetration depths reached with the micro and macro indenters are greater than in the nanoindenter (> 2 μm up to 250 μm), therefore, changes of displacement related to the thermal drift (typically > 0.5 nm/s) were considered negligible. We corroborate this assumption at the microindenter performing multicyclic tests, at the end of each cycle at 20% P_{max}, we did not observe significant displacement changes, *e.g.* Δh < 10 nm for displacement of the order of thousands of nanometers.

Zero contact point

The corrections of the zero-contact point are performed directly with the software of each instrument. There are different methodologies according to the instrument or type of test described below.

At the nanoindenter, the zero-contact point is corrected for classic tests using the slope change in the load-displacement curve Fig. II.15a-b, *i.e.* it is done by the recognition of the force increase. For CSM tests (Fig. II.15c-d) the zero point is detected by the slope change in the plot of the harmonic contact stiffness versus displacement, which is a more sensitive method.

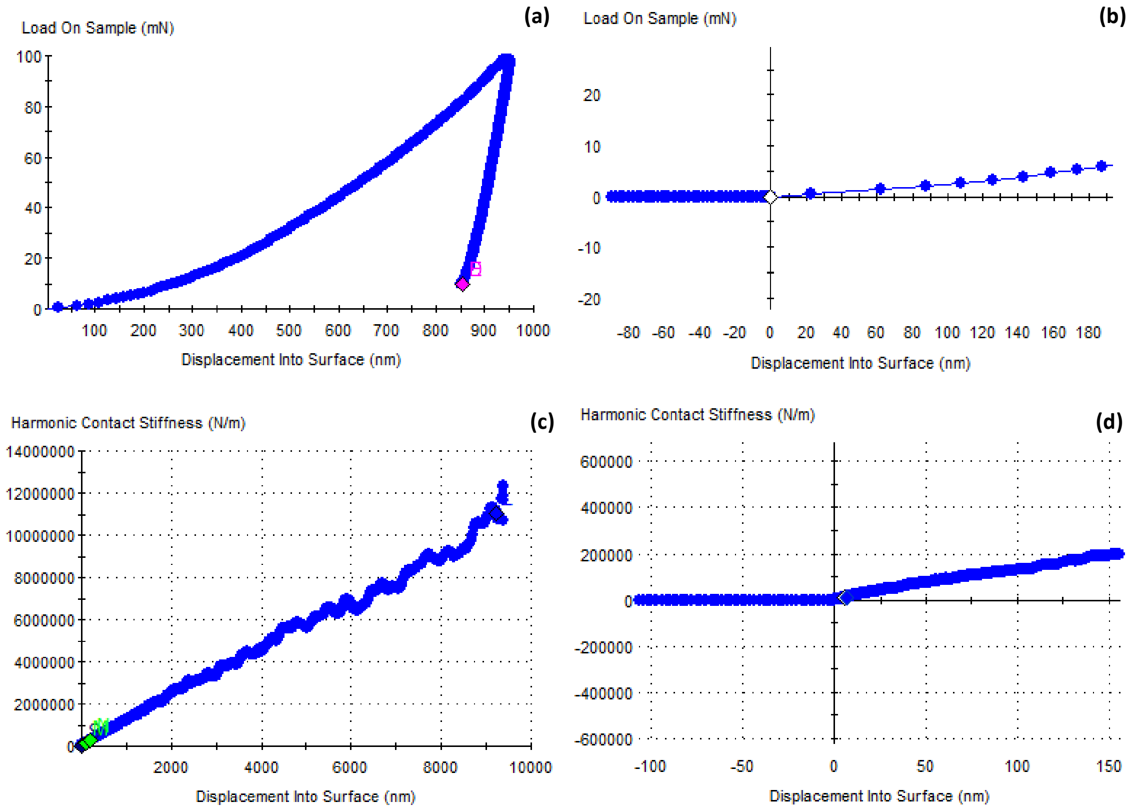

Fig. II.15. a) Load-displacement curve for classical test. b) Zoom of the region of the curve (a) where zero contact point is determined from the slope of the data change. c) Harmonic contact stiffness versus displacement into surface obtained by CSM tests taken from the instrument software. d) Zoom of the region used to determine zero contact point in CSM tests. Note that the change in the slope is more abrupt with the second methodology, which is usually more precise but is material dependent [48].

For the microindenter the zero point is detected by the slope change in the penetration or force curves versus time, usually it is easier to identify this brake point using the force data (Fig. II.16). This method is applied for classic and multicyclic tests.

In the nano and micro indenters we can select the zero-point in the curve using the software. With these two instruments, we did not have any problem after correction of the zero-point using the software of each instrument. At the nanoindenter the correction performed by default with the software is usually correct; similarly, at the microindenter it is generally well identified too; but it should be carefully observed and correct it manually for tests performed at the inferior load limit (0.1 -1 N) and in multicyclic tests, where generally the curve is shifted to the right (*i.e.* bigger displacements).

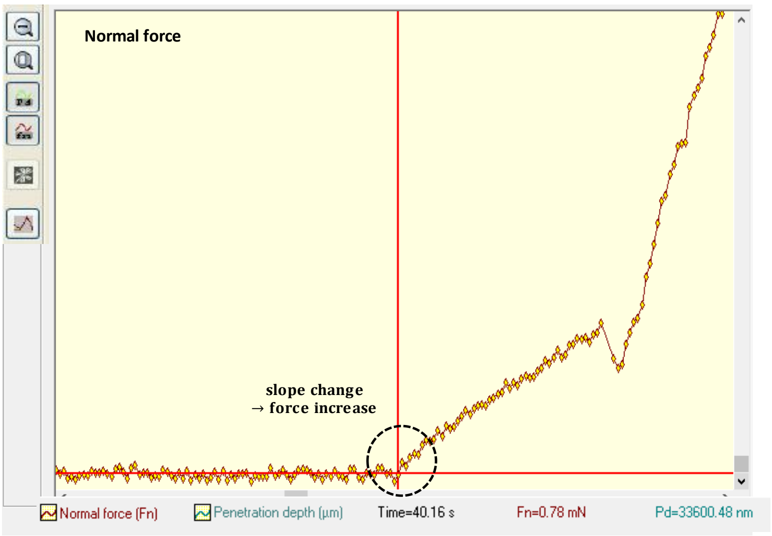

Fig. II.16. Example of zero contact point determination with the software of the microindenter using the curve force versus time.

For the macroindenter the software can make the correction of the zero-contact point by two methods: detection of the first peak force increase, or approaching the data with a 2nd degree polynomial up to 10% of the maximum displacement.

The detection with the first peak force is based in the same principle that the methodology applied with the nano and micro indenters for classic tests, but unfortunately the software sets the correction automatically without showing the data before correction and previous to the contact with the surface.

For the second method, using the approximation of the 2nd degree polynomial, the software makes the correction at the beginning of the curve and it is displayed in the screen (Fig. II.17a) but we do not have access to it when the data is exported.

The difference between both methods should not overpass a 1% uncertainty, nevertheless this value is difficult to achieve for loads below 50 N. Fig. II.17b shows an example of two exported curves corrected by the two methods with the software.

We realized that at this scale the zero-contact point determination is important, since it modifies strongly the results specially at loads under 50 N. Both methods were used for the correction in the different samples, usually at small loads the 2nd degree polynomial approaches better the real results. Apparently, the indenter starts to penetrate the sample before it recognizes the beginning of the tests, adding an extra displacement that is difficult to estimate because we do not have the entire data of the curve.

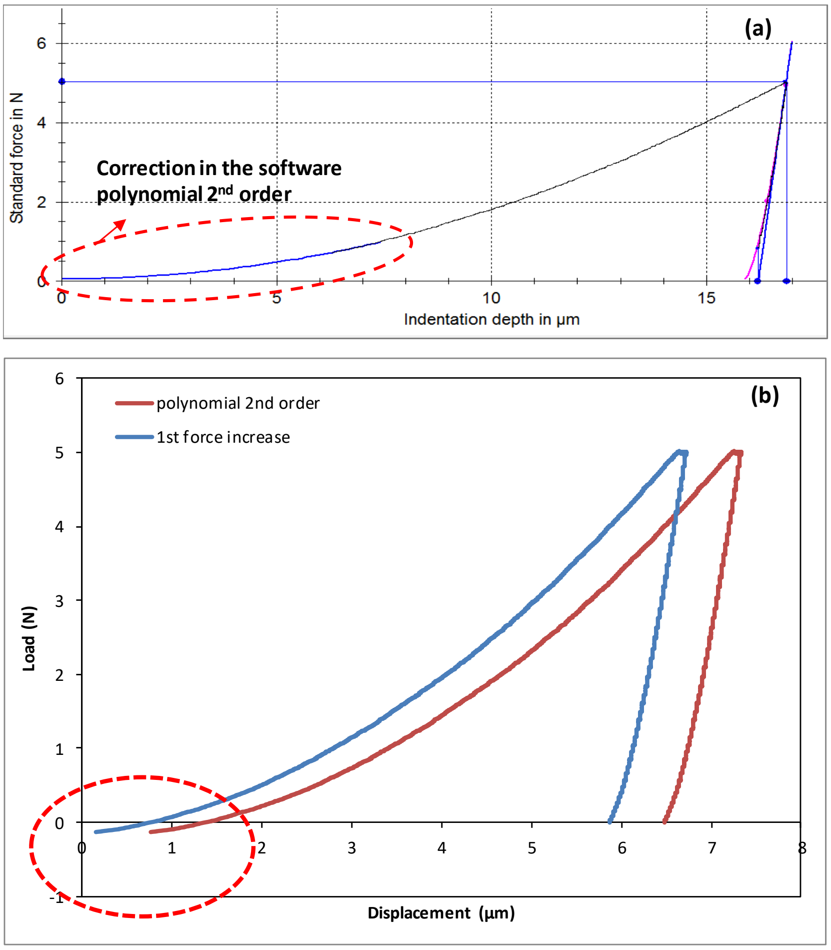

Fig. II.17. a) zero contact point correction of a load-displacement curve of aluminum, the enclosed region with the dotted line corresponds to the fitting performed by the software. b) exported load-displacement curves corrected with the zero-contact point with the method of first force increase and polynomial 2nd degree at 5N, exalting the differences between both methods.

To highlight these difficulties, we show in Fig. II.18 the differences between Vickers (measuring the diagonals of the imprints) and Martens hardness for aluminum and 39HRC samples. For sample 39HRC the estimation with the first force increase lead to an overestimation of Martens hardness and with the 2nd degree polynomial the values are underestimated but closer to the Vickers hardness measurements. In all the materials, the critical loads are below 50 N, generally it is better to use the 2nd order polynomial method at this range, consequently, this was the adopted methodology for the four studied materials.

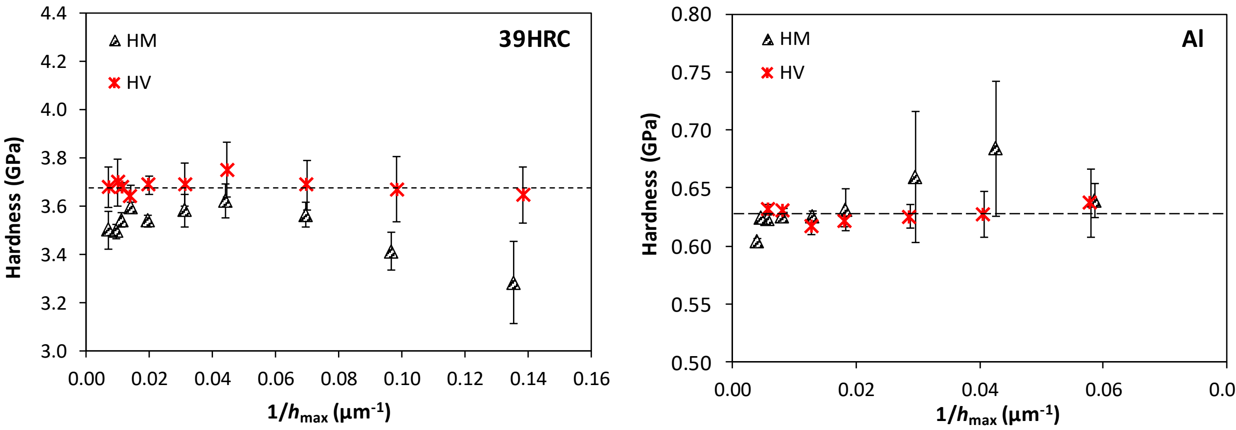

Fig. II.18. Vickers hardness (*HV*) and Martens hardness *(HM)* as a function of the reciprocal displacement. For both materials, the zero-contact point was determined by the 2nd degree polynomial for forces below 50 N.

It is worth mentioning that even if the zero-contact point is properly set, there is always a part of the results uncertainty related to this correction. The results obtained at the macroindenter machine must be observed carefully with respect to the estimation of the properties to avoid a wrong interpretation of the data.

II.5. Methodology of calculation

Elastic modulus and hardness, are the two properties principally calculated from the load-displacement curves. From the load-displacement curves estimate the elastic modulus and hardness. The elastic modulus was calculated by two methods: using the stiffness obtained from the unloading curve, and by the work of indentation method (areas under the curve). Similarly, hardness was calculated using the parameters from the load-displacement curve, and by the work of indentation methodology, the definitions of hardness from the work of indentation are presented in Chapter IV.

II.5.1. Methodology of calculation for *E* modulus and *H* from the data of the load-displacement curve

Fig. II.19 shows the steps performed to calculate elastic modulus and hardness using the load-displacement curves obtained with the three instruments. Each step is described below with the corresponding needed relations.

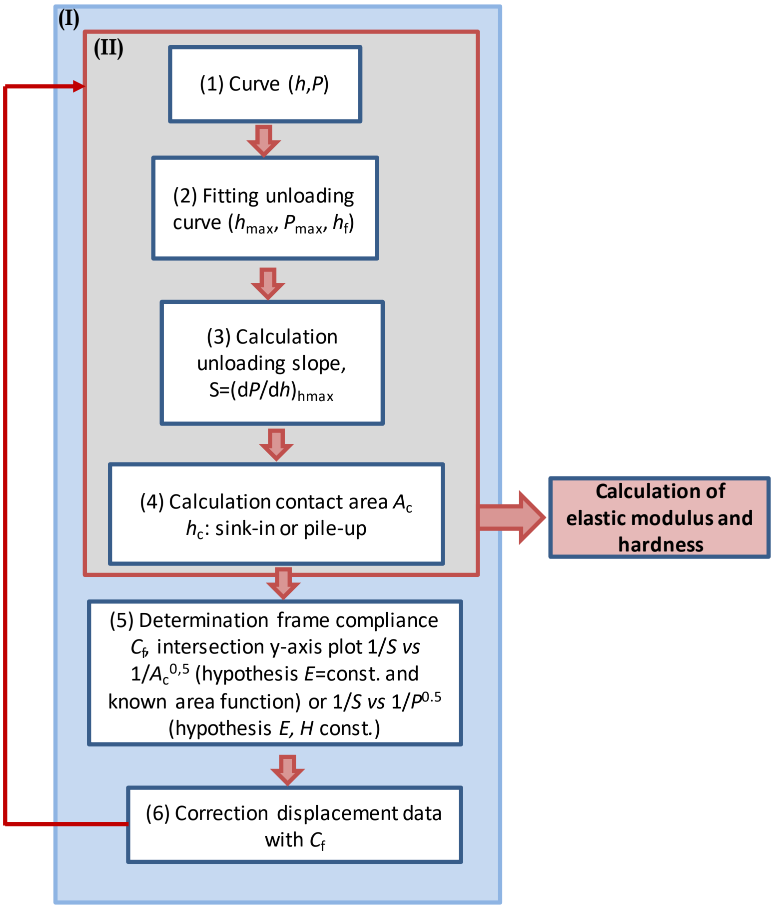

Fig. II.19. Schematic representation of the procedure used to compute elastic modulus and hardness using the data from instrumented indentation tests. The procedure I should be performed previously to the computation of the elastic modulus and hardness. After I, the steps included in II are performed again, followed by the calculation of the mechanical properties.

Step I.1: load-displacement from the instruments with correction of the zero-contact point, thermal drift (nanoindenter).

Step I.2: Fitting of the unloading curve by least-squares method using the data between 98 to 40% P_{max}, by the inverted method (Eq. II.5) described in detail Chapter III, which is equivalent to the power law of Oliver and Pharr (Eq. II.4) [63].

$$P = B'(h - h_f)^m \tag{II.4}$$

$$\frac{h}{h_{max}} = \frac{h_f}{h_{max}} + G\left(\frac{P}{P_{max}}\right)^n \tag{II.5}$$

where n, m, B', G, h_f and h_f/h_{max} are fitting parameters, h_{max} and P_{max} the maximum displacement and load, h, P the load displacement data.

All the load-displacement curves were fitted with the same methodology. Subsequently the stiffness (S) was calculated by Eq. II.6 equivalent to Eq. II.7 that corresponds to the Oliver and Pharr relation.

$$S_{\text{inv}} = \left(\frac{dP}{dh}\right)_{P_{max}} = \frac{1}{nG\frac{h_{\max}}{P_{\max}}(\frac{P}{P_{\max}})^{n-1}} = \frac{1}{nG\frac{h_{\max}}{P_{\max}}} \qquad \text{(II.6)}$$

$$S_{\text{O\&P}} = \left(\frac{dP}{dh}\right)_{h_{max}} = mB'(h_{\max} - h_f)^{m-1} \qquad \text{(II.7)}$$

Step I.3: calculation of the contact area A_c assuming pile-up or sink-in as deformation mode, according to definition of the contact depth h_c [63,88,99] (Eq. II.8-9), the relations for the areas for each scale were given previously but they are remembered here [63,90].

$$h_{\text{c\_sink-in}} = h_{\max} - 0.75\frac{P_{\max}}{S} \qquad \text{(II.8)}$$

$$h_{\text{c\_pile-up}} = 1.2(h_{\max} - \frac{P_{\max}}{S}) \qquad \text{(II.9)}$$

$$A_c nano = C_0\, h_c{}^2 + C_1\, h_c{}^1 + C_2\, h_c{}^{1/2} + C_3\, h_c{}^{1/4} + \ldots + C_8\, h_c{}^{1/128} \qquad \text{(II.10)}$$

$$A_c micro = 24.5\left(h_c + h_b\left(1 - exp\left(-\frac{2\,h_c}{h_b}\right)\right)^{3/2}\right)^2 \qquad \text{(II.2)}$$

$$A_c macro = 24.5\,(h_c + h_b)^2 \qquad \text{(II.3)}$$

Eq. II.9 corresponds to the relation presented in Chapter I (Eq. I.38) proposed by Loubet *et al.* [88] and Hochstetter *et al.* [99], the term h_b is not included in the relation, because it is considered trough the relations of the contact areas at the three scales, which lead to similar results.

Step I.4-5: determination of the frame compliance by two methods. The convenience of each method is described in Chapter IV.

- *Method 1*: C_s is the intercept with y axe given by extrapolation of the line in the plot by $1/S$ (C_t) versus $1/A_c^{0.5}$ (hypothesis constant elastic modulus and known area function).

$$C_t = C_s + C_c = C_s + \frac{\sqrt{\pi}}{2E_R\sqrt{A_c}} \tag{II.11}$$

- *Method 2*: C_s is the intercept determined given by extrapolation of the line given by the plot $1/S$ versus $1/P^{0.5}$ (hypothesis constant elastic modulus and hardness).

$$C_t = C_s + C_c = C_s + \frac{\sqrt{\pi}\,\sqrt{HIT}}{2E_R\sqrt{P_{max}}} \tag{II.12}$$

After calculation of the frame compliance the displacement data should be corrected by Eq. II.12:

$$h_{corrected} = h_{measured} - C_s P \tag{II.13}$$

After this correction of the displacement data, we repeat Steps I.1-3, corresponding to the second loop of calculation (II); at the end of Step II.3 the elastic modulus and hardness are obtained by the following relations.

The reduced elastic modulus, E_R, depends on the contact stiffness:

$$E_R = \frac{S\sqrt{\pi}}{2\gamma\sqrt{A_c}} \tag{II.14}$$

where γ is a factor related to the indenter angle and to the Poisson's ratio given by Eq. II.14 [66]. The correction factor γ can be replaced by the factor typically called β, we preferred to use γ instead because is given by a defined relation.

$$\gamma = \pi \frac{\frac{\pi}{4} + 0.15483073 \cot\theta \frac{(1-2v)}{4(1-v)}}{\left(\frac{\pi}{2} + 0.83119312 \cot\theta \frac{(1-2v)}{4(1-v)}\right)^2} \tag{II.15}$$

E_R contains the properties of the indenter (E_i, v_i) and of the material (E, v) described by Eq. II.15. For diamond indenters, E_i = 1140 GPa and v_i =0.07.

$$\frac{1}{E_R} = \frac{1 - {v_i}^2}{E_i} + \frac{1 - v^2}{E} \tag{II.16}$$

HIT is the instrumented hardness, A_c evaluated in $h_{c\ \text{pile-up}}$ or $h_{c\ \text{sink-in}}$, the A_c function is selected according to the scale.

$$HIT = \frac{P_{\max}}{A_c} \tag{II.17}$$

HM is the Martens hardness, A_r is the same function A_c but the constant 24.5 (C_0 in nano) changes to 26.43 that correspond to the real surface and it is evaluated at h_{max}.

$$HM = \frac{P_{\max}}{A_r} \tag{II.18}$$

HMeyer is the Meyer hardness; in this case A_c is evaluated at h_{max}.

$$HMeyer = \frac{P_{\max}}{A_c} \tag{II.19}$$

II.5.2. Methodology of calculation of the work of indentation

The areas under the curve are calculated numerically by the trapezoids method, using all the data points, given by Eq. II.19:

$$\sum_{i=1}^{N} \frac{f(x_{i-1}) + f(x_i)}{2} \Delta x_i \text{ or} \sum_{i=1}^{N} \frac{P_{i-1} + P_i}{2} (h_i - h_{i-1}) \tag{II.20}$$

where $f(x_i)$ and x_i, are the load and displacement data, respectively, using each point of the experimental data.

The areas under the loading and unloading curves are the total (W_t) and elastic (W_e) works, respectively; the plastic work (W_p) is the area enclosed by the load-displacement curve, *i.e.* the difference between W_t and W_e.

$$W_t = W_e + W_p \tag{II.21}$$

Before the estimation of the areas under the curves the curves should be corrected with the frame compliance, because the areas are modified after the correction as presented in Fig. II.20.

The unloading curves in microindentation show a point of deflection (Fig. II.12c) due to the functioning of the instrument that is not representative of the material response, this change in the slope modify the estimation of the area under the unloading curve corresponding to the elastic work. To avoid this problem the unloading curve is calculated theoretically using the fitting parameters that describe the curve; subsequently, the elastic work is calculated. The total work is determined directly with the experimental data. The same methodology was used for the curves obtained at the nano and macro indenters.

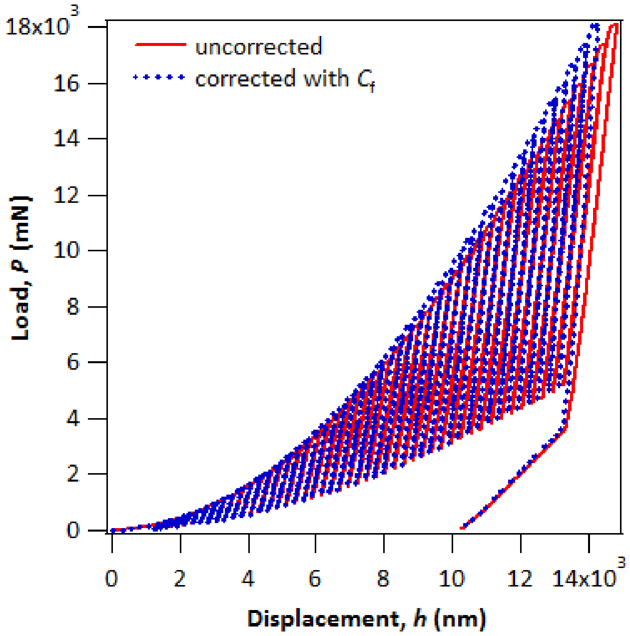

Fig. II.20. Load-displacement curve from multicyclic tests showing the difference between the uncorrected and the corrected curve with the frame compliance that affect the calculation of the areas under the curves.

Methodology for multicyclic tests after correction with the frame compliance:

1. Separation of cycles as individual tests
2. Fitting of the unloading curves
3. The data of the unloading curve (up to 20-30% of P_{max}) is completed using the fitting parameters until zero force ($P = 0$, $h = h_f$). Otherwise the elastic areas are underestimated (Fig. II.21)
4. The difference of the areas between the unloading curve up to 20-30% of P_{max}, and the total unloading curve until zero force is added to the total area of the following cycle, supposing that the unloading and reloading curves are approximately the same at the elastic region.

Therefore, the areas for multicyclic are calculated by the next relations, according to Fig. II.21, being i le number of cycle i-cycle:

$$W_{e\_i} = W_{e_i} + W_{e_i}{}^{*} \tag{II.22}$$

$$W_{t\_i} = W_{t_i} + W_{e_{i-1}}{}^{*} \tag{II.23}$$

$$W_{p\_i} = W_{t\_i} - W_{e\_i} \tag{II.24}$$

$$W_{t\ cumulative\_i} = W_{t\_i} + \sum_{1}^{i-1} W_{p\_i} \tag{II.25}$$

$W_{e\_i}/W_{t\ cumulative\_i}$ gives the relation W_e/W_t per cycle to calculate the mechanical properties.

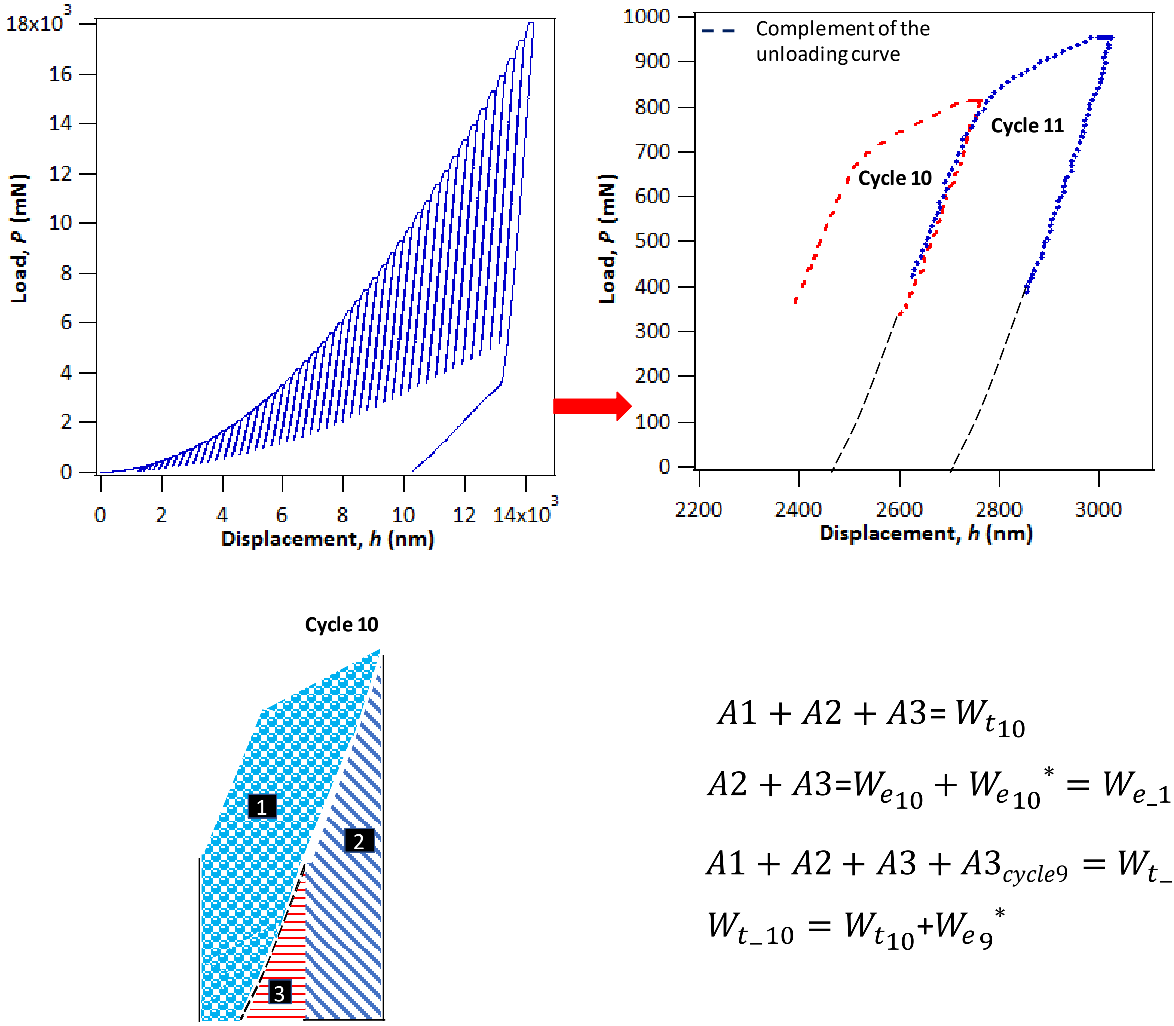

$$A1 + A2 + A3 = W_{t_{10}}$$

$$A2 + A3 = W_{e_{10}} + W_{e_{10}}{}^{*} = W_{e\_10}$$

$$A1 + A2 + A3 + A3_{cycle9} = W_{t\_10}$$

$$W_{t\_10} = W_{t_{10}} + W_{e_9}{}^{*}$$

Fig. II.21. Example of the method to calculate the areas under the curve in multicyclic tests. The example shows the corresponding areas for the total and elastic work corresponding to cycle 10 according to the expression II.22-II.25.

II.5.3. Calculation of elastic modulus by the work of indentation

After correction of the curves with the frame compliance we estimate the elastic modulus by the work of indentation approach (Eq. II.26) using the ratio W_e/W_t and the contact stiffness according to the relation proposed by Yetna *et al.* [103].

$$E_R = \frac{\frac{W_e}{W_t}}{k\frac{4\gamma^2}{\pi}\frac{P_{max}}{S^2}} \qquad \text{(II.26)}$$

where γ is a correction factor related to the indenter angle and to the Poisson's ratio; k is a constant that depends on the ratio W_e/W_t. For $W_e/W_t < 0.15$, $k = 7.3$; $W_e/W_t > 0.25$, $k = 5.17$; $0.25 > W_e/W_t > 0.15$ $k = 6.6$ [35,95,103,106].

Note the calculation does not depend on the contact area, that means that prior knowledge about the deformation mode is not needed. Nevertheless, the constant k obtained by different authors apparently depends on the deformation mode [35,95,103,106].

In summary, the procedures described in this chapter correspond to the tests performed for the study of multiscale indentation in bulk metallic materials (Chapter IV). The relations for the calculation of the elastic modulus and hardness are used as well for the study of heterogeneous materials (Chapter V).

CHAPTER III

A new approach of the Oliver and Pharr model to fit the unloading curve from instrumented indentation testing

The unloading part of a load-displacement curve from instrumented indentation tests (ITT) is usually approximated by a power law (Oliver and Pharr model), where the load is the dependent variable. This approach generally fits well the data. Nevertheless, the convergence is occasionally quite questionable. In this regard, we propose a different approach for the Oliver and Pharr model, called the inverted approach, since it assigns the displacement as the dependent variable. Both models were used to fit the unloading curves from nanoindentation tests on fused silica and aluminum, applying a general least squares procedure. Generally, the inverted methodology leads to similar results for the fitting parameters and the elastic modulus (E) when convergence is achieved. Nevertheless, this approach facilitates the convergence, because it is a better conditioned problem. Additionally, by Monte Carlo simulations we found that robustness is improved using the inverted approach, since the estimation of E is more accurate, especially for materials like aluminum.

III.1. Theoretical basis

Instrumented indentation testing (IIT) allows the estimation of the mechanical properties of materials from the load-displacement curve [10,111]. The principal properties calculated from the load-displacement data are elastic modulus and hardness. Some authors [145–149] calculate these properties from the loading part of the load-displacement curve. Nevertheless, most of the studies consider the unloading curve to compute them [58,62,63,150]. Besides, the properties can be calculated from the indentation work deduced from the area under the load-penetration curve [59,103,151].

The methodology proposed by Doerner and Nix [62] to determine the mechanical properties of materials represents the fundament of the Oliver and Pharr method [48,63]. Doerner and

Nix used a flat punch approximation that considers a constant contact area during the indenter withdrawn and consequently, the unloading curve is linear, therefore, the stiffness is calculated as the reciprocal of the compliance expressed by the next relation (Eq. III.1) [62].

$$\frac{dh}{dP} = \frac{1}{2h_p}\left(\frac{\pi}{24.5}\right)^{1/2}\frac{1}{E_R} \tag{III.1}$$

where h is the displacement, P the load, h_p the plastic depth obtained as the intercept with the displacement axis of the tangent line to the unloading curve at maximum load, and E_R the reduced elastic modulus.

Oliver and Pharr demonstrated that the Doerner and Nix approach presented some inconsistencies, *i.e.* the measured contact stiffness is highly dependent on the portion of the unloading curve taken for its calculation, the creep phenomenon at the beginning of the unloading curve and, the change in the area during the indenter removal [48,63].

On the other hand, the method of Oliver and Pharr is the model that has been mainly used by many researches related to IIT. In contrast to the method of Doerner and Nix, Oliver and Pharr demonstrated that unloading curves are not well represented by a linear fit. Instead, unloading curves are properly approximated by a power law relationship. This method can be extrapolated to a diversity of axisymmetric indenters geometries as sphere and pyramids [48,63].

The power law relation of Oliver and Pharr is given in the following relation, where B', m and h_f (residual depth) are fitting parameters determined by a least squares fitting procedure:

$$P = B'(h - h_f)^m \tag{III.2}$$

The previous relation is commonly used on the IIT analysis because it generally approximates well the unloading data. Oliver and Pharr did a broad study over different materials and proved that the variation of the power law exponent remains in the range of $1.2 \leq m \leq 1.6$, which discards the flat punch approximation ($m = 1$) and approaches instead to a paraboloid of revolution ($m = 1.5$). This result was unexpected to Oliver and Pharr, because the axisymmetric equivalent to Berkovich indenter is a cone ($m = 2$) [48]. The inconsistency was explained by the concept of “effective indenter shape”, explained in detail in Chapter I [64].

To compute the elastic modulus and hardness, it is necessary to calculate the contact stiffness, S (dP/dh) and the residual depth (h_f) by the fitting of the unloading curve.

The contact stiffness is calculated as the slope of the upper portion of the unloading curve, explicitly, is the derivative of load with respect to displacement evaluated at the maximum displacement (Eq. III.3) [48].

$$S_{O\&P} = \left(\frac{dP}{dh}\right)_{h_{\max}} = mB'(h_{\max} - h_f)^{m-1} \qquad \text{(III.3)}$$

The subscript O&P for the contact stiffness S denotes that the relation is derived from the Oliver and Pharr model.

Cagliero *et al.* [41] criticized the power law method because the model is constrained to pass through the point $P = 0$, $h = h_f$, which is not at the zone of interest and the value h_f used to compute the constant stiffness is affected by an important uncertainty. They proposed instead to fit the curve to next relation:

$$Y = S\,\frac{\sin(k_x X)}{k_x} \qquad \text{(III.4)}$$

Where $Y = P_{max} - P$ and $X = h_{max} - h$, being S and k_x fitting constants obtained by nonlinear regression.

The method of Cagliero *et al.* [41] gives a good approximation of the experimental data that change with the testing load. They highlight that their method allows the direct computation of S and its standard deviation by the nonlinear regression. The residuals between the fitting and the data are aleatory, instead results using the Oliver and Pharr, and Doerner and Nix methods presented a systematic trend in this study. Nevertheless, one disadvantage of the method is that it does not allow the computation of the residual depth which is usually used for the understanding of the deformation mode [48,100]. Two examples of the application of the Cagliero *et al.* [41] method for macroindentation tests performed at 5 N and 100 N are presented in Fig. III.1, we found that the method approaches well the experimental data up to certain load level according to the applied load.

Gong *et al.* [150] proposed another methodology supposing an initial stress state in the material described by Eq. III.5. They suggested that the power law coefficient should be quadratic to have a physical meaning based in the conical indenter approximation, which discards the analysis of the effective indenter shape.

$$P_{\text{eff}} = P + P_0 = B(h - h_f)^2 \qquad \text{(III.5)}$$

Where $P_0 = kh_0$, P_0 is a virtual load introduced assuming the action of the residual stress, h_0 is an initial displacement at the prospective contact point before the indenter is re-driven onto the indented surface, and B is a fitting constant dependent on the elastic properties of the material and the indenter geometry.

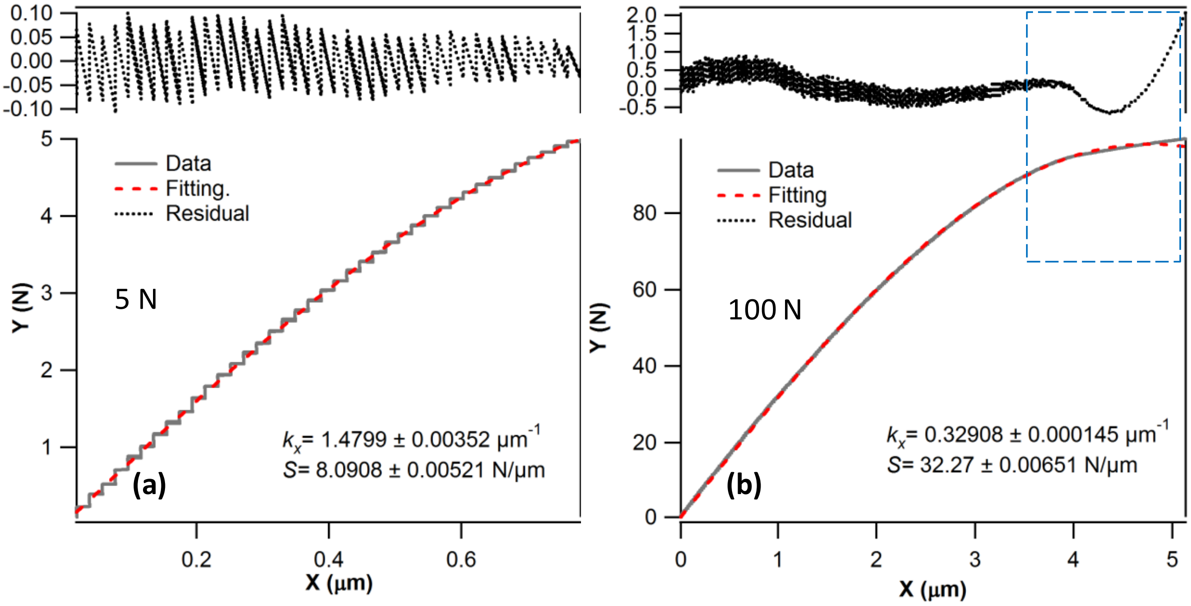

Fig. III.1. Examples of application of Cagliero *et al.* [41] model given by Eq. III.4. to fit the unloading curve (a) proper fitting of the unloading curve at 5N with random residuals. (b) fitting of the unloading curve at 100 N, the residuals are not random at the end of the unloading curve (upper region enclosed by dotted line).

The solution of Gong *et al.* [150] gives the same estimations of the contact stiffness as the Oliver and Pharr model, then both approximations are comparable, leading to similar results.

As a conclusion, usually if the fitting is correctly achieved, diverse methods are efficient to compute the contact stiffness, nevertheless the application of the methods would be conditioned by the data which is related to the instrument, *e.g.* some instruments can register erroneous data at the end of the unloading curve due to a malfunctioning of some internal components. Nevertheless, in this chapter our attention is focused in the power law of Oliver and Pharr model because it is standardized by ISO14577-1 [135], thus most of the investigations in instrumented indentation use this methodology because it is generally the analysis method included in the software of the instruments to compute the contact stiffness.

This chapter is concentrated on the study of a new approach of the Oliver and Pharr model to fit the unloading curve for pyramidal indenters (Vickers and Berkovich), which is intended to improve the robustness of the method. The detailed demonstration is based in nanoindentation tests on two materials with very different mechanical behavior such as fused silica and aluminum. Then at the end of this chapter some examples are presented at different scales to show the applicability and advantages of this approach.

III.2. A new approach of the Oliver and Pharr model to fit the unloading curve

The Oliver and Pharr model is rewritten as a dimensionless relation (Eq. III.6) in order to get comparable parameters for various tests and loads. Otherwise, the parameter *B'* that has units mN/nm^{m} (Eq. III.2) being a dimension dependent parameter, which is not comparable between tests if the power law coefficient, m, takes different values.

$$\frac{P}{P_{\max}} = B\left(\frac{h}{h_{\max}} - \frac{h_f}{h_{\max}}\right)^{m} \tag{III.6}$$

where B is given by the following relationship:

$$B = B' \frac{h_{\max}{}^{m}}{P_{\max}} \tag{III.7}$$

Consequently, the stiffness corresponding to the Oliver and Pharr model is described by the following relation:

$$S_{O\&P} = \frac{dP}{dh} = mB\frac{P_{\max}}{h_{\max}}\left(\frac{h}{h_{\max}} - \frac{h_f}{h_{\max}}\right)^{m-1} \tag{III.8}$$

The proposed method is intended to simplify the fitting by least squares procedure in order to compute easily the parameters that describe the unloading curve and to obtain more robust results. The new approach, called the inverted methodology is described by Eq. III.9 expressed by a dimensionless relation, where the displacement is estimated instead of the load.

$$\frac{h}{h_{\max}} = \frac{h_f}{h_{\max}} + G\left(\frac{P}{P_{\max}}\right)^{n} \tag{III.9}$$

where G, n and h_f are fitting parameters. These parameters can be arranged to get the equivalent ones of the Oliver and Pharr model, applying the next relationships:

$$m = \frac{1}{n}; B = \frac{1}{G^{1/n}} \tag{III.10}$$

The contact stiffness calculated by this method is obtained by the following relation:

$$S_{\text{inv}} = \frac{dP}{dh} = \frac{1}{nG\frac{h_{\max}}{P_{\max}}\left(\frac{P}{P_{\max}}\right)^{n-1}} \tag{III.11}$$

III.3. Least squares method to fit the unloading curve

The method most commonly used to fit an experimental data is the least squares regression (Eqs. III.12-13), due to the difficulties of solving equations with other methods, especially for complicated fitting functions [152]. The principle of this method consists in minimize the squares of the offsets between the data and the model, the squares are used instead of the absolute offset values because they can be treated as a continuous differentiable quantity [153].

$$\chi_{OP}{}^{2} = \sum_{i=1}^{z} (\widehat{P_i} - P_i)^2 \tag{III.12}$$

$$\chi_{inv.}{}^{2} = \sum_{i=1}^{z} (\widehat{h_i} - h_i)^2 \tag{III.13}$$

where $\widehat{P_i}$ and $\widehat{h_i}$ are the values of load and displacement respectively obtained by the fitting with the Oliver and Pharr and inverted models. These values depend on p number of parameters ($z \geq p$); P_i and h_i are the experimental values from each data point. This is the general expression for the least squares fitting, emphasizing that with the Oliver and Pharr model we minimize the differences between loads, and with the inverted methodology the differences between displacements.

The functions implemented to fit the unloading curve for both models are power law functions that can be linearize applying logarithm at both sides of the equations [152,154], in order to fit the data by a linear least squares fitting. However, this linearization commonly disrupts the implicit assumption of normal distributed errors [152]. Due to this reason, we suggest the use of a nonlinear least squares fitting which allows to compute the coefficients of the predicted model by means of an iterative process until achieve convergence, namely, the process ends when the difference between reduced chi-square values of two successive iterations is less than a fixed tolerance value [152,155]. The convergence principally depends on the type of fit (Newton, Gauss-Newton, Levenberg Marquardt, etc.), the initial parameters and the selected model [156,157].

The metrology loop in a measuring machine, is defined for the force and displacement. If the force sensor works properly, the Newton's third law of action-reaction guarantees that the force uncertainties are of order of magnitude of the sensor uncertainties. On the contrary, the displacement measure is more sensitive, any defect of stiffness in the metrology loop or any defect in the alignment of the sensor regarding the direction of the measurement, lead to notable uncertainties [158]. Thereby, also many factors as roughness, initial depth of penetration, contact point, thermal drift, mechanical vibrations, fluctuations of voltage, frame stiffness, etc., could affect the measured displacements in instrumented indentation tests [10,63,110,124,125].

The Oliver and Pharr model to fit the unloading curve, assigns the load as the dependent variable and the displacement as the independent variable. The least squares regression generally introduces errors in the dependent variable, y. Then, the error on the independent variable, x, should be negligible. In the real data from experimentation both variables are subject to uncertainties, therefore, the uncertainties on the dependent variable should be a sum of measured errors and the error propagated by the uncertainty in x [152,159]. However, in the case where one of the variables presents larger uncertainties respect to the other, this one should be assigned as the dependent variable and the uncertainties over the other one can be considered as negligible. Thus, the inverted methodology swaps the variables of displacement and load, since the uncertainties are more important in the displacement, assigned as the dependent variable.

III.4. Comparison between the Oliver and Pharr and the inverted models

To compare the Oliver and Pharr model and the inverted approach we studied two materials with very dissimilar behavior, fused silica (FQ) and aluminum (Al) tested in nanoindentation (Nano Indenter XP) with classical tests. Several standard tests at different loads between 20 mN up to 500 mN have been performed, the loading and unloading times were 30 s and the dwell time at maximum load 15 s. The calibration of the indenter tip was done on fused silica, using the continuous stiffness measurement method to compute the coefficients of the contact area according to the procedure of Oliver and Pharr [63], the details are given in chapter II.

The contact depth h_c is calculated assuming the main deformation mode as sink-in for fused silica, and pile-up for aluminum, according to previous studies [63,88,99]. The elastic modulus is calculated with the classical relations described in chapter II.

An example of the load-displacement dimensionless curves is presented in Fig. III.2 to highlight the dissimilar behavior between the two materials during unloading. The aluminum sample presents a quasi-vertical unloading curve.

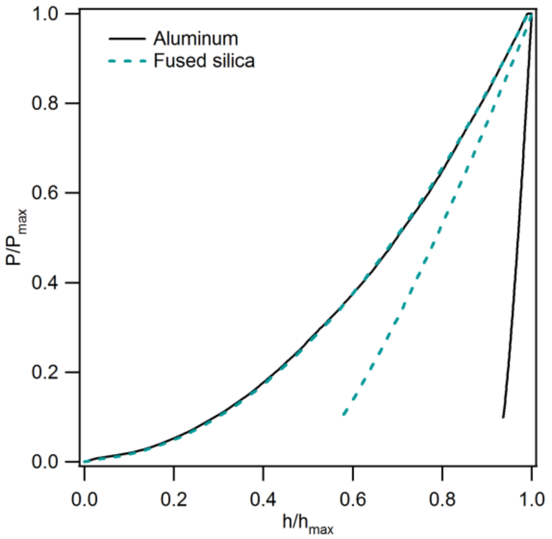

Fig. III.2. Load-displacement dimensionless curves for the fused silica and aluminum samples.

The fitting parameters of Oliver and Pharr and of inverted models were calculated for the two materials, to compare these two models.

The stiffness and elastic modulus were computed according to the relations previously described using the parameters obtained for each model. Both models were fitted until convergence. The results are presented in Table III.1, only three loads are represented for convenience in order to highlight the similitudes between the two methods. Nevertheless, five different loads were used to accomplish the analysis, the tendency related to the fit parameters and elastic moduli were comparable to the results in Table III.1.

Table III.1. Fitting parameters obtained by the Oliver and Pharr and by the inverted models using the dimensionless load-displacement curves.

Material	**Fused silica**			**Aluminum**		
Load *P* (mN)	98	245	490	98	245	491
$h_{\max}$ (nm)	910	1449	2049	1826	2941	4075
h_f (nm)	446	724	1032	1678	2715	3757
$h_f/h_{\max}$	0.49	0.50	0.50	0.92	0.92	0.92
G	0.51	0.50	0.50	0.08	0.08	0.08
n	0.81	0.81	0.80	0.74	0.73	0.73
B	2.29	2.35	2.39	30.17	33.15	32.98
m	1.24	1.24	1.25	1.36	1.36	1.37
R^2	0.99995	0.99997	0.99993	0.99996	0.99999	0.99997
*S*_inv. (mN/nm)	0.26	0.42	0.60	0.90	1.49	2.12
*E*_inv. (GPa)	72.8	72.6	73.4	70.7	72.5	75.0
*S*_O&P (mN/nm)	0.26	0.42	0.60	0.90	1.48	2.12
*E*_O&P (GPa)	72.8	72.5	73.3	70.7	72.3	74.8

R^2, coefficient of correlation. O&P: Oliver and Pharr model and inv.: inverted model.

Table III.1 shows that both models lead to a very similar estimation of the stiffness and consequently of the elastic modulus, which is conditioned to the convergence of the fitting of the unloading curves, a more detailed description of this subject is done in the next section. Besides, the two models represent excellently the experimental data since the coefficients of correlation, R^2, between the experimental values and the predicted values are very close to one [153]. In addition, the values obtained for m are comparable to the results obtained by Oliver and Pharr [48] for aluminum and fused silica.

In general, the inverted approach leads to approximate results to the Oliver and Pharr solution, validating the applicability of this methodology, at least for nanoindentation tests. Therefore, the interrogative is what are the advantages of the inverted approach? The following section gives some elements to answer this question.

III.4.1. Fitting the unloading curves with inverted and Oliver and Pharr models

The software in the instruments compute the stiffness derived from the unloading curve by an internal algorithm that usually approaches the curve to the Oliver and Pharr model. However, sometimes this algorithm fails, consequently, the value of the stiffness is incorrect and the elastic modulus as well. The algorithm can be programmed to a certain number of iterations; therefore, a local minimum can be found instead of a global minimum, obtaining an incorrect result. The evaluation of the results must be done cautiously, in the case that some values of the elastic modulus computed by the software were out of the range of coherent values according to the material, therefore the fitting parameters and the stiffness should be recalculated.

To exhibit the convenience of using the inverted approach to fit the unloading curve as a modified approach of the Oliver and Pharr model, the following assumptions were done in the data, all the measurements have the same standard deviation and the errors are normally distributed and independent.

Nonlinear least squares fitting needs starting values and step sizes. The rate of convergence of the approximation method can depend on these parameters and the selected method. An improper selection of the starting point may lead to the solution of a local minimum rather than an absolute one, also several local minimums can exist that render difficult the correct selection of the results. In this regard, the Oliver and Pharr model can lead to some problems to achieve convergence if the starting values are not correctly selected, obtaining a local minimum or any solution [150]. It is worth mentioning that these issues are mainly encountered in metallic samples that present high plastic deformation, rather than in materials with great elastic recovering upon unloading, like fused silica.

As an example of the analysis, the tests of aluminum and fused silica performed at 245 mN load were selected. The algorithm was built in the Mathematica® language to compute the fitting parameters of the unloading curve with both models.

The parameters were computed applying the two models for the fused silica sample. Several methods for the nonlinear fitting were tried, Newton, Quasi-Newton, Levenberg Marquardt and gradient. The initial values were not introduced in the algorithm, using the values that Mathematica takes by default that is one for all the parameters. The Levenberg Marquardt method leads to convergence with less iterations than the other methods. The Oliver and Pharr model does not achieve convergence with these setup values, the value of h_f/h_{max} should have the same order of magnitude to achieve the convergence (Table III.2). For the inverted approach, the convergence is reached after five iterations, with the setup initial values. The tolerance value to stop the algorithm is 0.002, as a default parameter in Mathematica ®.

In the case of the aluminum sample, the same settings stablished for the algorithm to fit the curve of the fused silica were applied. An equivalent behavior was obtained, *i.e.* without assigning initial values in the correct order of magnitude for the Oliver and Pharr model it is not possible to achieve the convergence (Table III.3). If the initial values are close to the solution values, the global minimum is easily found; nevertheless, if those are far from the solution, the number of iterations should be increased and in some cases the convergence is not achieved. The proposed methodology with the default setup values reaches the convergence after five iterations. Also, different sets of initials values lead to the same solution. As in the fused silica sample the best method to perform the least squares procedure is Levenberg Marquardt for both models.

Table III.2 and Table III.3 summarize the fitting procedure of the unloading curves for both samples at 245 mN using the Levenberg Marquardt method with a tolerance of 0.002 using Mathematica®. The fitting procedures were verified with Excel and Igor Pro finding the same trend than with Mathematica®.

Table III.2. Fitting results according to the initial values of parameters for the unloading curve of fused silica sample at 245 mN.

Model	Parameters	Initial values	Number of iterations	Fitting parameters	Standard errors
Inverted	G	1.00	5	0.50	3.04E-04
	h_f/h_{max}	1.00		0.50	2.77E-04
	n	1.00		0.81	8.31E-04
O&P	B	1.00	300	(nc)	(nc)
	h_f/h_{max}	1.00		(nc)	(nc)
	m	1.00		(nc)	(nc)
O&P	B	1.00	6	2.35	6.52E-04
	h_f/h_{max}	0.40		0.50	3.18E-04
	m	1.00		1.24	1.29E-03

nc: without convergence

Table III.3. Fitting results according to the initial values of parameters for the unloading curve of aluminum sample at 245 mN.

Model	Parameters	Initial values	Number of iterations	Fitting parameters	Standard errors
Inverted	G	1.00	5	0.08	1.19E-04
	$h_f/h_{\max}$	1.00		0.92	1.29E-04
	n	1.00		0.73	1.98E-03
O&P	B	1.00	300	(nc)	(nc)
	$h_f/h_{\max}$	1.00		(nc)	(nc)
	m	1.00		(nc)	(nc)
O&P	B	20.00	300	29.28	26.56 (nc)
	$h_f/h_{\max}$	0.85		0.99	2.91E-03(nc)
	m	1.20		0.86	1.54E-01 (nc)
O&P	B	20.00	6	33.04	2.64E-01
	$h_f/h_{\max}$	0.90		0.92	1.45E-04
	m	1.20		1.36	4.02E-03

nc: without convergence.

The values for the parameters G and n presented in Table III.2 and Table III.3 were recalculated with the Eq. III.10 to find the equivalent parameters of the Oliver and Pharr model, obtaining $B = 2.35$ and $m = 1.27$ for fused silica, and $B = 33.31$ and $m = 1.37$ for aluminum.

The results presented for the two materials stand out that the convergence is easily reached when the inverted approach is used.

In order to present some mathematical basis for the previous results, we evocate the conditioning concepts in numerical analysis. Regarding a function $f(x)$, a well-conditioned problem implies that the small perturbations of x lead to only small changes in $f(x)$. On the contrary, in an ill-conditioned problem a small perturbation of x leads to a large change in $f(x)$, that means that small relative errors in the inputs would lead to high errors in the outputs, opposite to a well-conditioned problem. To quantify the conditioning of a problem, the relative condition number (k) can be computed according the Eq. III.14. A lower number indicates a better conditioned problem [160–162].

$$k = \frac{||x|| \, ||J(x)||}{||f(x)||} \tag{III.14}$$

where $||J(x)||$ is the norm of the Jacobian matrix.

The condition numbers for the Oliver and Pharr and the inverted models were calculated using the experimental dimensionless curves at 245 mN for both materials (Table III.4). These results are related to the parameters of each model.

Table III.4. Condition number (Eq. III.14) of Oliver and Pharr and inverted models for fused silica and aluminum.

Model	Fused silica	Aluminum
O&P	27	207
Inverted	10	9

Table III.4 confirms the results regarding the convergence of the models presented in Table III.2 and Table III.3, indicating that the inverted approach leads to a better conditioned problem, *i.e.* small variations in the load data lead to small variations in the displacement data, due to a smaller slope. These results also demonstrate that for metallic samples with a large plastic deformation as aluminum, the inverted methodology is definitively an improved approach. It is worth mentioning that the relative condition number is only an evaluation of the superior limit of the relative error. Therefore, we evaluate the results in next section through Monte Carlo simulations.

III.4.2. Testing the robustness of the inverted and Oliver and Pharr models

In order to study the robustness of both models we used the Monte Carlo method defined by JCGM 101:2008 [163] as: "*the method used to determine the probability distribution for an output quantity from the probability distributions assigned to the input quantities on which the output quantity depends*". To apply this methodology, the constants of the Oliver and Pharr model computed from the load-displacement dimensionless curves found at 245 mN (Table III.1), were used to obtain the theoretical unloading curves to being perturbed by a random Gaussian noise. The resulting unloading curves from Monte Carlo (MC) simulations were fitted by the least squares method, collecting 10000 sets of fitting parameters. The schematic representation of Monte Carlo simulation is presented in Fig. III.3. The initial values to compute the fitting were set up to the approximated values of the solution of the curves without perturbation. The fitting was accomplished using the 80% of the unloading curve according to the standard ISO 14577-1 [135].

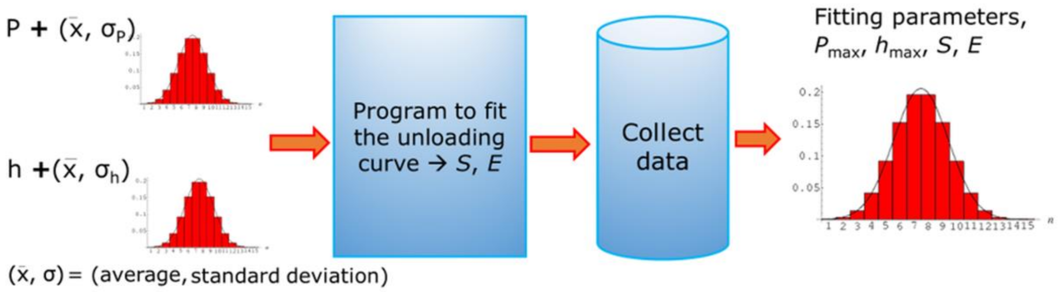

Fig. III.3. Schematic representation of Monte Carlo simulation, where P and h, are the load and displacement of the experimental data at which is added a Gaussian noise centered at zero (average) and standard deviation different to zero (σ).

The random Gaussian noise for the load data is centered at zero with a standard deviation of 0.001 mN. For the displacement, the Gaussian noise is also centered at zero but the standard deviations (stdv) were fixed at 2.5 nm (~0.2% $h_{\max}$) and 5 nm (~0.35% $h_{\max}$) for the fused silica sample, and 2.5 nm (~0.1% $h_{\max}$), 5 nm (~0.2% $h_{\max}$) and 10 nm (~0.35% $h_{\max}$) for the aluminum sample. The purpose is to reproduce a data with high dispersion between the different tests in order to evaluate the robustness of the Oliver and Pharr and inverted models. This procedure allows to corroborate the existence of correlations between the parameters of each model, presented in Fig. III.4, showing that the fit constants are highly correlated, as often reported for the power-law correlations [164,165].

Fig. III.4 clearly shows that increasing the perturbation of the indentation depth leads to a broader dispersion of parameters, which is higher for the aluminum sample.

When the algorithm fails to convergence another set of parameters can be identified in the plots of $h_f / h_{\max}$ versus B, and m versus B in the aluminum sample given by the Oliver and Pharr model. Nevertheless, the values that are outside of the white squares, under the striped areas also indicate that the fit performed with both models in the aluminum sample did not achieve the right minimum; the regions were delimited using the bounds of the power law exponent, m, $2 \geq m \geq 1$, considering that the values out of this range do not have a physical meaning [48]. It is consistent that both models sometimes did not achieve the convergence because the data is highly perturbed and the procedure of least squares can be easily stacked in a local minimum.

The correlation of fit parameters for the fused silica sample exhibits that both models give almost identical results, the region of valuable solutions is logically, amplified while increasing the standard deviation of the Gaussian noise on the displacement data. On the contrary, the results for the aluminum samples reveal that the two models do not follow the same trend, this is most notable when the standard deviation is increased. Subsequently, the main arising questions are: How these dissimilarities affect the estimation of the stiffness and elastic modulus? Which model would lead to a better approximation of the initial solution?

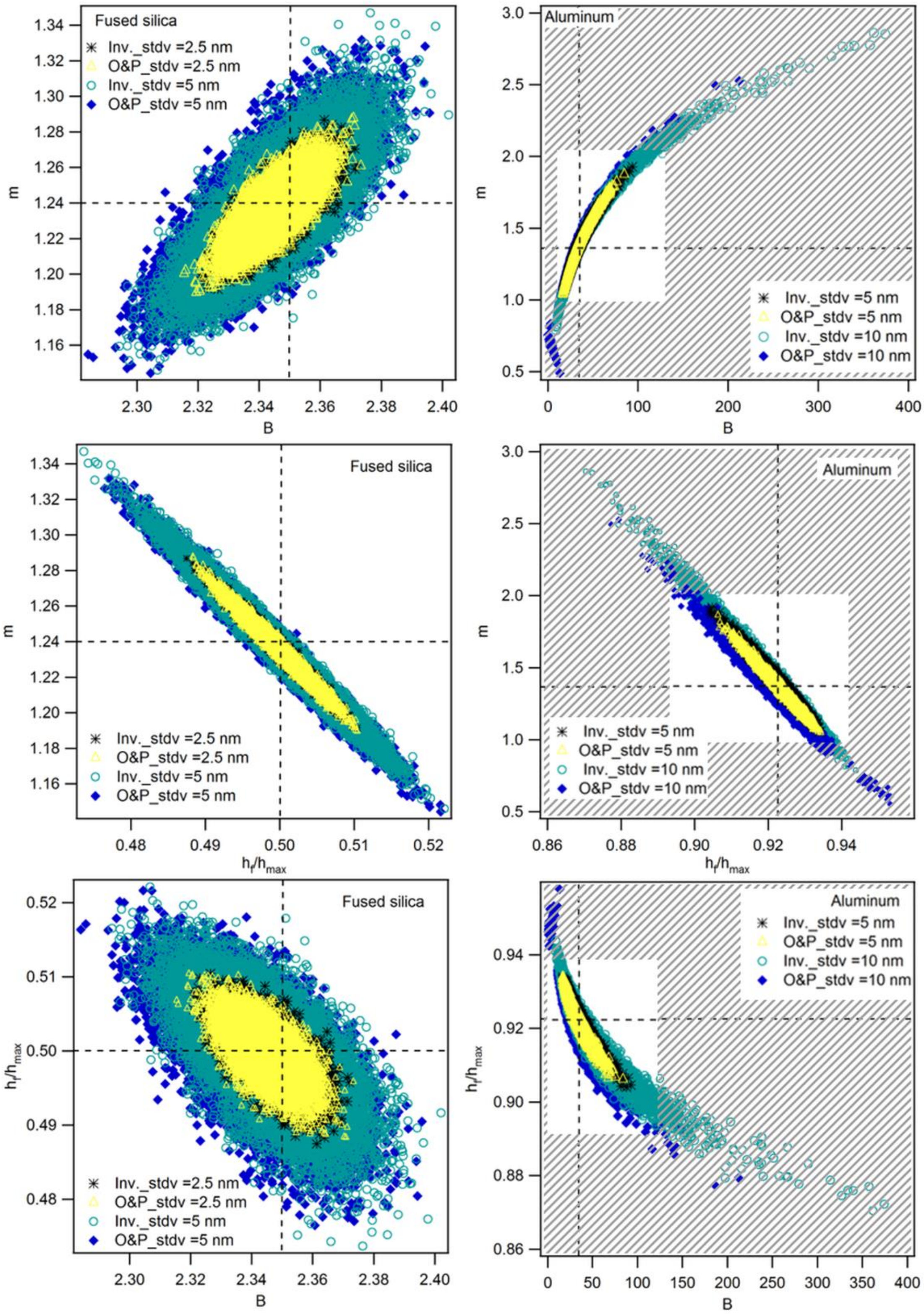

Fig. III.4. Correlation of fitting parameters obtained by the inverted and Oliver and Pharr models. The values are collected from 10000 load-displacement curves obtained from MC simulation.

To answer to these questions, we considered the histograms of the elastic modulus of both materials, dismissing the obtained values out of the correct order of magnitude (Fig. III.5 and Fig. III.6).

The unloading curves for the fused silica sample perturbed with a Gaussian noise with mean 0 and 5 nm standard deviation are perfectly overlapped, indicating that the models of Oliver and Pharr and inverted behave similarly. A smaller noise added to the displacement data results in similar behavior. Consequently, the estimated elastic modulus computed from the unloading curves using both models lead to similar values, as confirmed by the histograms in Fig. III.5.

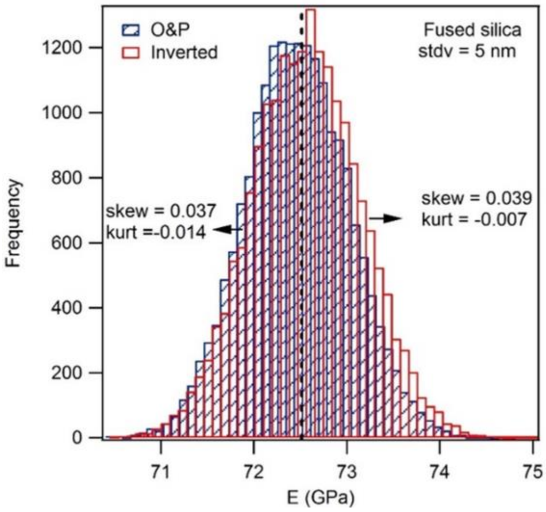

Fig. III.5. Histograms of the elastic modulus computed from the curves obtained by MC simulation for the fused silica. stdv represents the standard deviation of the Gaussian noise added to the displacement data. The unloading curves were fitted by the Oliver and Pharr and the inverted models.

The histograms representing the elastic modulus of fused silica sample (Fig. III.5) corroborate that both models lead to the same results, as observed for the fitting parameters represented in Fig. III.4. The average values obtained by the two models are the same as the reference value, 72.5 GPa, and they are well approximated to a normal distribution, *i.e.* the kurtosis and skewness are almost zero. The introduced noise to the data leads to a range of possible values for the elastic modulus of 72.5 ± 1.7 GPa with the 99.73 % of probability for the highest noise (5 nm).

The unloading curves of the aluminum sample are similar for both models with the smaller noise of 2.5 nm. However, increasing the standard deviation to 5 nm and 10 nm, causes some dissimilarities between both models, but they are not evident through the illustration of the curves. Nevertheless, the histograms of the elastic modulus obtained by Monte Carlo simulations (Fig. III.6) allow to differentiate between the inverted and the Oliver and Pharr models. There are represented for the Gaussian noise with 5 nm and 10 nm standard deviation.

The histograms plotted in Fig. III.6 confirm the existence of a gap between the results obtained by the two models for the aluminum sample; similarly, to the behavior observed for the fitting parameters in Fig. III.4. The mean values obtained by the inverted approach are equal to the reference value, 72.3 GPa. Instead, the average elastic modulus decreases when it is estimated by the Oliver and Pharr model. Likewise, the data obtained by the inverted approach are better approximated to a normal distribution due to the values of kurtosis and skewness are lower than for the Oliver and Pharr model as presented in the histograms. The values of elastic modulus are summarized in Table III.5, regarding the different Gaussian noises added to the displacement data.

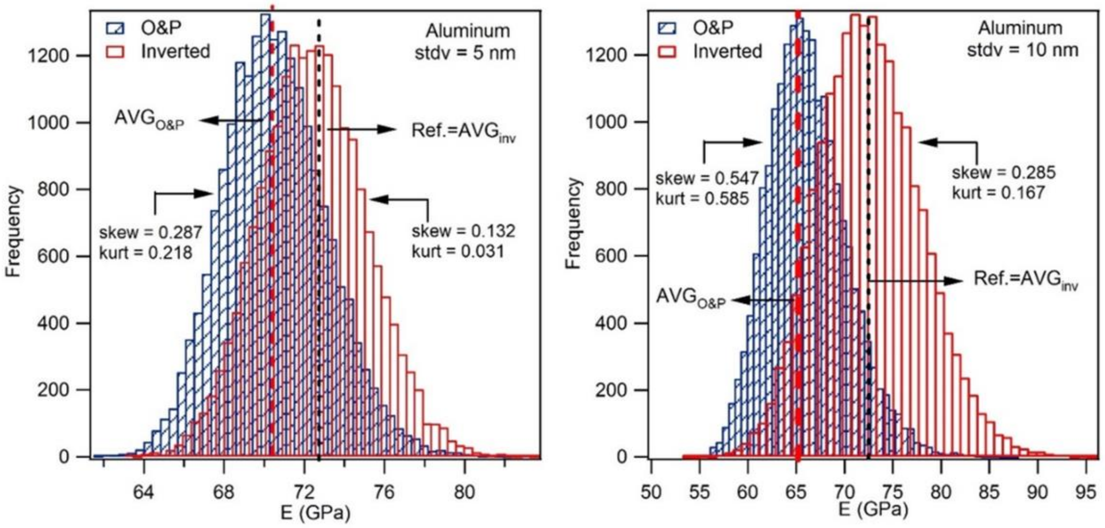

Fig. III.6. Histograms of the elastic modulus computed from the curves obtained by MC simulations for the aluminum sample using the Oliver and Pharr and the inverted models. stdv represents the standard deviation of the Gaussian noise added to the displacement data. The dotted lines represent the average elastic modulus of each data ($\mathrm{AVG}_{\mathrm{O\&P}}$, $\mathrm{AVG}_{\mathrm{inv}}$). For the inverted approach $\mathrm{AVG}_{\mathrm{inv}}$ the value match with the reference modulus (Ref.) computed without perturbation of the data.

Table III.5. Elastic moduli obtained by the Oliver and Pharr and inverted models, applying Monte Carlo simulations with different Gaussian noise added to the displacement data of the aluminum sample.

Parameters	**Inv. stdv=2.5 nm**	**O&P stdv= 2.5 nm**	**Inv. stdv=5 nm**	**O&P stdv=5 nm**	**Inv. stdv=10 nm**	**O&P stdv=10 nm**
E (GPa)	72.4	71.9	72.4	70.5	72.6	66.2
stdv (GPa)	1.3	1.4	2.6	2.6	5.3	4.1
Probability 95.45%	72.4 ± 2.7	71.9 ± 2.8	72.4 ± 5.3	70.5 ± 5.3	72.6 ± 10.6	66.2 ± 8.2
Kurtosis	-0.003	0.111	0.031	0.218	0.167	0.585
Skewness	0.105	0.158	0.132	0.287	0.285	0.547

Results in Table III.5 confirmed the previous statements, i.e. the modulus decreases respect to the reference value when the Oliver and Pharr model is used to compute it, while the standard deviation of the Gaussian noise added to the displacement data increases.

One of the differences in the estimation of the elastic modulus between the two models is related to the computation of the stiffness, that includes the residual depth in the Oliver and Pharr model (Eq. III.8), however, it is not considered in the inverted approach (Eq. III.11). The stiffness depends on the fitting parameters n, m, G, B, h_f/h_{max}; which exhibit differences between them. Generally, the parameters of the inverted approach (n, G and h_f/h_{max}) are closer to a normal distribution in comparison with the parameters of the Oliver and Pharr model (m, B and h_f/h_{max}). These dissimilarities lead to an underestimation of the stiffness when it is computed by the Oliver and Pharr model. The corresponding histograms for the contact stiffness for the aluminum sample are presented in Fig. III.7.

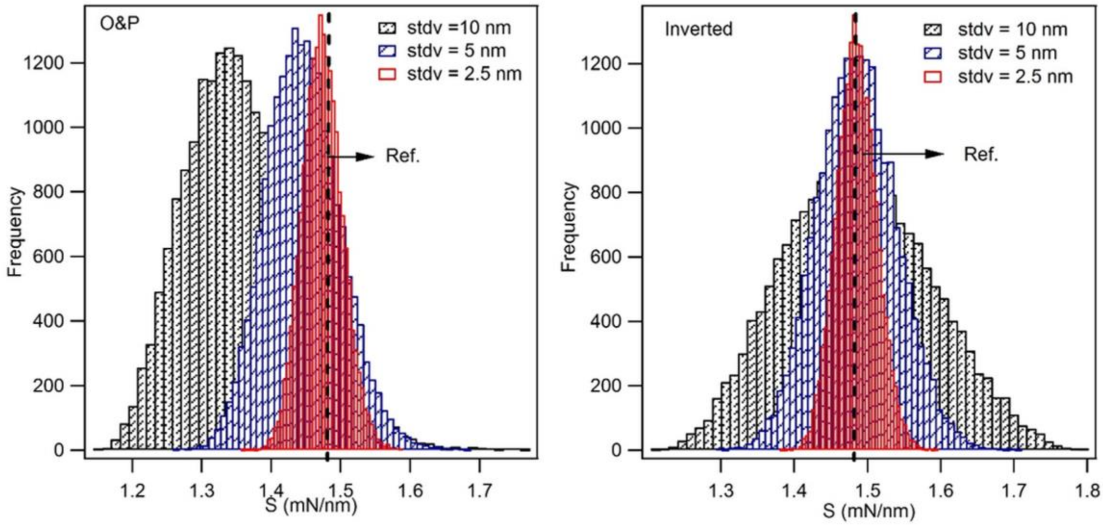

Fig. III.7. Histograms of the contact stiffness, S, computed from the fitting of the unloading curves of aluminum by the inverted and Oliver and Pharr models, for the curves obtained by Monte Carlo simulation with different Gaussian noises. Ref. is the reference value of S for the curve without perturbation.

Fig. III.7 shows the diminution of the stiffness computed from the Oliver and Pharr model while the standard deviation of the Gaussian noise increases, this variation of stiffness is directly related to the variation of the elastic modulus (Table III.5). On the contrary, the stiffness calculated by the inverted approach is centered almost at the same reference value for all the standard deviations, but the normality of the histograms is reduced when the noise increases.

Clearly the dispersion of the estimated elastic modulus is higher for the aluminum sample than for the fused silica sample, even if the Gaussian noise added to the displacement data is equivalent regarding $h_{\max}$. However, Fig. III.2 shows that the unloading curves for the two materials are dissimilar, the slope is higher for the aluminum sample and quasi vertical. The gap between the residual depth and the maximum depth that is related to the elastic recovery is 725 nm for the fused silica sample and 226 nm for the aluminum sample. Consequently, an equivalent perturbation of the displacement data would impact more the data of the unloading curve of the aluminum sample because it considers a smaller displacement difference for the fitting, leading to a higher dispersion on the elastic modulus.

According to the previous results the robustness of the inverted approach to compute the elastic modulus is improved compared to the Oliver and Pharr model, especially for the metallic samples with higher stiffness. For materials with a high elastic recovery, like the fused silica, both models lead to similar results. Nevertheless, if the standard deviation of the Gaussian noise is increased, fused silica will show a similar behavior to that of the aluminum sample. These results indicate that the designation of displacement as the dependent variable in the model to fit the unloading curve is going to enhance the robustness of the model.

III.4.3. Variation of fitting parameter with the fraction of the unloading curve

We performed the previous analysis with the 80% of the unloading curve (between 98% to 20 % of $P_{\max}$). Nevertheless, according to the instrument used and the level of load applied, the unloading curve deviates from the power law approximation (O&P or inverted), leading to important errors if this part of the data is considered. We evaluated the variation of the fitting parameters and their standard deviations according to the fraction of the unloading curve computed with both models presented in Fig. III.8. To do these calculations we used the theoretical load-displacement curves, obtained by the fitting constants of the Oliver and Pharr model from the experimental data of nanoindentation tests at a 245 mN of load in aluminum and fused silica samples (Table III.1). The theoretical load-displacement curves were perturbed by a random Gaussian noise centered at zero with a standard deviation of 1 nm added to the indentation depth data. For the load data, a random Gaussian noise centered at zero with a standard deviation of 0.001 mN was added. This procedure was repeated 10000 times by Monte Carlo (MC).

For the inverted model, the equivalent parameters, B and m, were computed in order to establish the comparison with the Oliver and Pharr model. The fraction of the curve is taken as a percentage of the maximum load, the upper value was fixed at 98 % of $P_{\max}$ to avoid creep effects (also commonly called bulging effect) and the lower value is moved within each test, the referred percentages on the *x* axis is an approximated percentage assuming the upper limit as 100 % of $P_{\max}$.

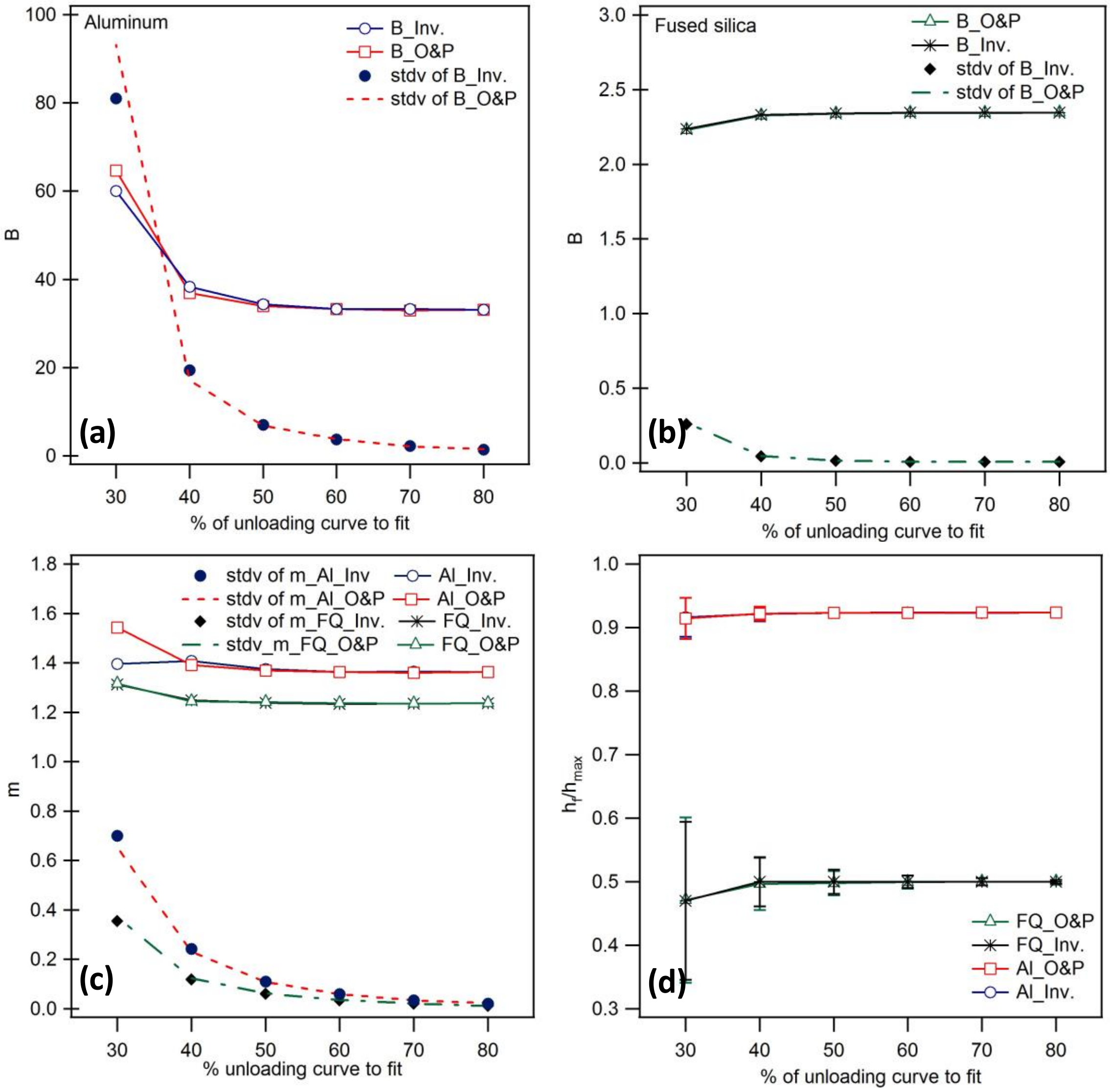

Fig. III.8. Variation of the fitting parameters with the fraction of the unloading considered to the fit, applying the Oliver and Pharr and the inverted models. The average and standard deviation values are computed from 10000 Monte Carlo simulations.

The parameters *B*, *m* and $h_f/h_{\max}$ do not change significantly between 80 to 40 % of the unloading curve for the two studied samples. However, the standard deviation increases while the fraction of the curve is reduced, thus, the models are less appropriate to fit the data. Suggesting that it is necessary to take as many points as possible to accomplish the fitting by the nonlinear least squares procedure, taking into account that there is going to be a compromise between the stabilization of the parameters and the randomness of the residuals. Nevertheless, using only the 30 % of the unloading curve for the fitting procedure would probably carry to an inaccurate computation of the parameters. It should be noted that the obtained parameters are very similar between the two models for the various fractions of the unloading curve.

These results were corroborated with the estimation of the stiffness and the elastic modulus (Fig. III.9). Remarkably, the computed values of elastic modulus are well approximated to the theoretical values of both materials (~72 GPa), independently of the fraction of the unloading curve taken to perform the least squares fit, and of the model to perform it. However, the standard deviation increases when the percentage of the curve decreases as was mentioned for the fitting parameters. Thus, the fitting of the unloading curve should be performing with the largest possible number of data, depending on each instrument, to improve the results reproducibility.

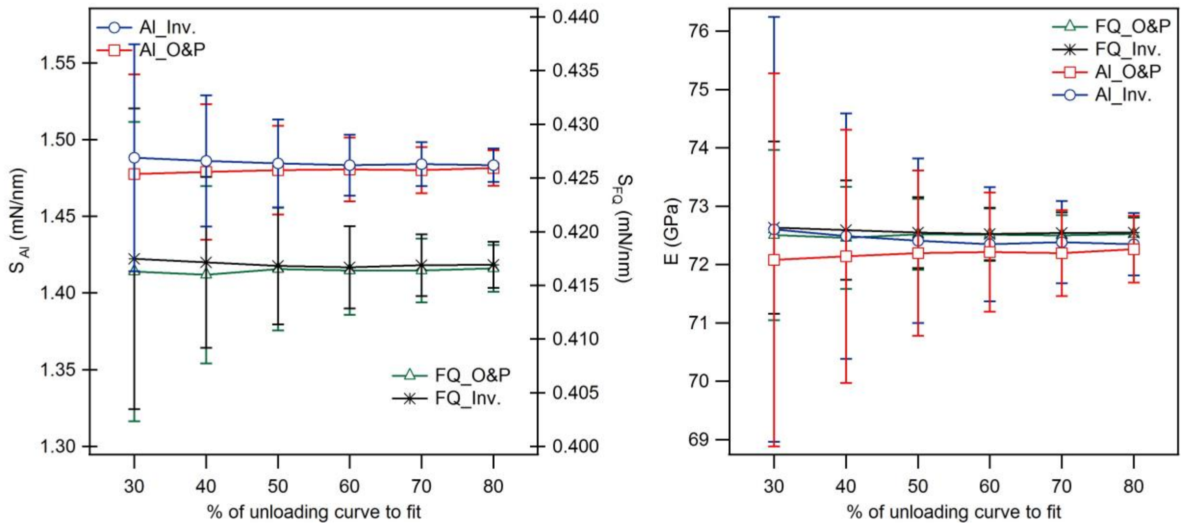

Fig. III.9. Variation of stiffness, *S*, and elastic modulus, *E*, with the percentage of the unloading curve considered to the fit applying the Oliver and Pharr and the inverted models. The average and standard deviation values are computed from 10000 Monte Carlo simulations.

III.5. Conclusions and applications

The new approach proposed in this chapter to fit the unloading curve approximates very well the experimental data and the results are comparable with the Oliver and Pharr model.

The inverted methodology is an approach of the Oliver and Pharr model that proposes the displacement as the dependent variable because this value is more sensitive to large uncertainties than the load, according to one principle of the least squares regression where uncertainties are attributed to the dependent variable.

Generally, the inverted approach facilitates the convergence by least squares fitting and leads to a better conditioned problem, mainly for metallic samples. If the experimental data is highly perturbed, particularly the indentation depths, the fitting procedure could give a wrong estimation of parameters, finding an incorrect minimum. In this regard, the Oliver and Pharr model is more sensitive. Consequently, by means of Monte Carlo simulations introducing a random Gaussian noise to the displacement data, we found that the inverted methodology improves the robustness, thus leading to a more accurate determination of the stiffness and the elastic modulus.

Regarding the interest of the methodology we demonstrated that the results are more robust using the inverted approach, because of this all the further study of multiscale indentation described in Chapter IV was performed applying the inverted method. Since we are interested in studying instrumented indentation tests at different scales, the dimensionless formulation to fit the unloading curve makes comparable the fitting parameters, and allows to stablish similitudes and differences among them, that could give supplementary information about the material behavior under indentation. The analysis should be performed cautiously because the fitting of the curve can lead to mathematical artifacts related to the register of the data or to the fitting itself (*e.g.* the portion of the unloading curve consider to the fitting). Another point to show is that the experimental data represents a complex behavior of the phenomena happening in the material, a model is an approximation that does not consider all the elements, *e.g.* upon unloading the material can experience a partial plastic retreat [64,166].

Fig. III.10a-c show the variation of the fitting parameters obtained with the inverted model for tests performed in the steel sample 39HRC at the nano, micro and macro scale (using the three instruments described in chapter II). The fitting was performed with the portion of the unloading curve between 98% to 40% $P_{\max}$. The ratio between the elastic work of indentation (W_e) given by the area under the unloading curve, to the total work (W_t) given by the area under the loading curve is presented in Fig. III.10d.

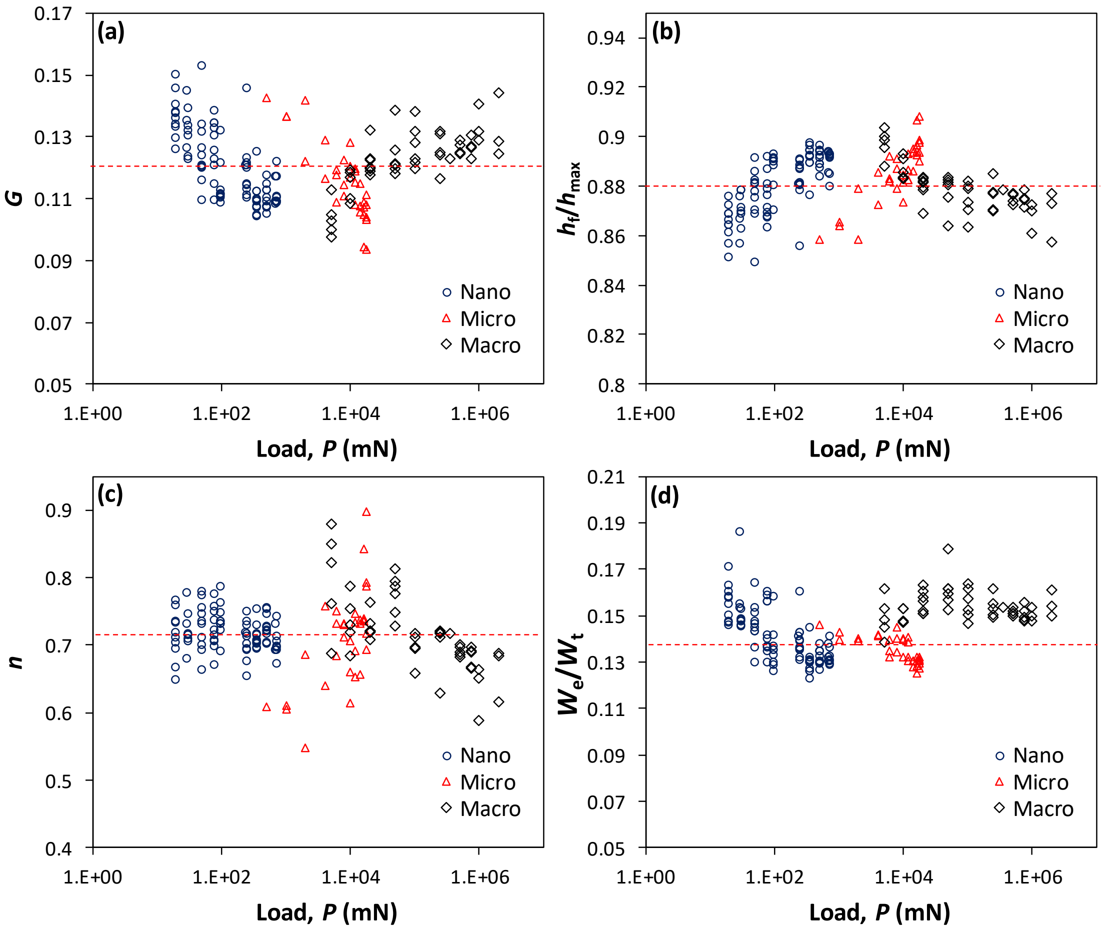

Fig. III.10. Fitting parameters of the unloading curves as a function of the applied load obtained by the inverted approach at nano, micro and macroindentation in the steel sample 39HRC.

The fitting parameters G, n and h_f/h_{max} are approximately constant with load and the scale of measurement, nevertheless slightly variations were obtained. The results at the nano scale shows less dispersion, they are more clustered. Similarly, the ratio W_e/W_t shows a constant variation at the three scales, but its average value increases at the macro scale. In Chapter IV we will discuss the effect of these variations on the calculation of the mechanical properties.

CHAPTER IV

Multiscale indentation in homogeneous metallic materials

Instrumented indentation testing is a widely used technique for material characterization across different lengths scales. From nanoindentation to macroindentation it is possible to obtain the local properties to the overall response of the material. Therefore, it is a very attractive method for the characterization of non-homogeneous materials, which heterogeneities change with the scale of measurement, *e.g.* a composite or polycrystalline metallic material.

The elastic-plastic contact under indentation is very complex, affecting the material response and consequently the estimation of the mechanical properties [5]. The study by multiscale indentation of this phenomenon has been a subject of interest for many researchers, developing theoretical models looking to understand the behavior from the atomic scale to the continuum [33,167].

This chapter address the mechanical characterization of industrial metallic materials by multiscale indentation. The main objective is to elucidate the similarities on the material response through different scales; despite the local heterogeneities and the functioning of the instruments. In order to stablish relations among them, validating the use of different methodologies for the analysis, which could be used in the study of more complex materials such as brake pads.

IV.1. Correction of the frame compliance

Frame compliance (C_f) correction is an extremely important procedure to accomplish in order to determine properly the elastic modulus and hardness through indentation tests; a wrong estimate can affect about 50% the computation of these properties [110]. The frame compliance characterizes a composite elastic stiffness of every element in the system that is deformed during the load application, such as the indenter column, mounting and fixation of the specimen and indenter, connection between the internal elements, translation mechanisms [115,168].

A misconception about the frame compliance correction is that it is a unique value no matter the material tested or the conditions of testing, which should be valid for all the tests performed with the instrument, since this value does not represent a unique response of the load frame and it is rather a composite response of many elements that is not independent of the material and its surface preparation. The term frame compliance literally means the compliance of the load frame, but the term includes several elements mentioned above, consequently in this work it will be called system compliance (C_s) instead of frame compliance to be more consistent with the meaning, nevertheless while presenting information of other studies both terms have the same connotation unless otherwise stated. Therefore, the total compliance (C_t) would be the sum of the system compliance and the contact compliance (C_c), which corresponds to the contact between the two bodies (indenter and sample). Typically, the estimates of the C_s have the same order of magnitude at least for tests performed with the same indenter in similar materials (*e.g.* metallic materials), but slightly changes can greatly affect the correction at high loads where the load frame becomes the dominating factor. This will be illustrated in the next sections presenting the correction of the system compliance for each instrument.

We selected two methods to compute C_s that are frequently used in indentation, there are mentioned in Chapter I and the calculation procedure is explained in Chapter II. Method 1 (Eq. IV.1) consists in the determination of C_s as the intercept with y- axis (by extrapolation) of the plot of the total compliance ($1/S$) being S the total stiffness measured using the unloading curve, as a function of the inverse square root of the contact area ($1/A_c{}^{0.5}$); in this method, the elastic modulus is supposed constant independently of the applied load. Method 2 (Eq. IV.2) determines C_s as the intercept with y-axis of the plot $1/S$ *vs* $1/P^{0.5}$ being P the load, this method assumes a constant ratio $HIT/E_R{}^2$ for all the range of loads. The results presented in the next sections consider the contact area assuming sink-in as the main deformation mode. The total stiffness measured from the unloading curve was computed using the inverted method described in Chapter III.

$$C_t = C_s + C_c = C_s + \frac{\sqrt{\pi}}{2E_R\sqrt{A_c}} \tag{IV.1}$$

$$C_t = C_s + C_c = C_s + \frac{\sqrt{\pi}\,\sqrt{HIT}}{2E_R\sqrt{P_{max}}} \tag{IV.2}$$

The computation of the system compliance may depend on the load or the range of loads [110,168,169]. Many studies advice [48,110,111] to compute the system compliance using only the high loads of the instrument because at this region the data are less sensitive to the tip blunting while increasing the load.

In the ISO14577-4 [127] the correction of the system compliance is based on the hypothesis of constant elastic modulus for all the range of loads, indistinctly of the method used for its computation. Nevertheless, some studies have shown that elastic modulus decrease while increasing the load may be explained by a continuum damage mechanic model, the damage in the material is created by the formation of micro defects due to surface roughness, machining marks, inclusions, etc. that decrease the material density. Likewise, the plastic deformation generated in the material due to the triaxial deformation by indentation tests increases the residual stresses and the number of dislocations, which lose mobility, leading to a diminution of the elastic modulus [170–173]. Chunyu *et al.* [174] presented that the diminution of the elastic properties may be related to the load frame of the instrument, but also to the anisotropic damage produced by shear deformation. To distinguish between both events the pattern decay of the elastic modulus against the indentation depth should be evaluated. Most of the studies explaining damaging due to indentation in ductile materials do not mention the load frame compliance correction, which is an important procedure to consider into the computation of the mechanical properties. To prove the existence of damage a previous suitable estimation of the system compliance is necessary, but also the use of systems conceived to reduce this effect [122]. Researches in instrumented indentation testing frequently assume a constant elastic modulus for all the range of testing loads, independently of the scale of measurement; accordingly in our work we considered this hypothesis, emphasizing that the data plotted for methods 1 and 2, were usually well approximated to a straight line, where the slope represents the elastic modulus E or the constant relation $HIT/{E_R}^2$; deviations from the straight line could be interpreted as a change in the material properties. Nevertheless, we do not discard the possibility that damaging mechanisms could be developed in metallic materials essentially in the micro and macro load ranges.

It is worth mentioning that system compliance determination is related to an important uncertainty, which can be higher than the requested to get reliable mechanical properties (1 nm/N) [113], therefore the obtained values are estimations of the system behavior involving many elements such as the load, the indenter, mounting materials, tip mounting materials, etc. [168].

IV.1.1. Correction of the frame compliance in nanoindentation

At the nanometric scale using the Nanoindenter XP the modification of the system compliance is not considered as an important factor, because it is calibrated at the factory and predefined in the software prior to testing ($C_{\mathrm{instrument}}$), Eq. IV.3. The calibration is performed using continuous stiffness measurement (CSM) tests in fused silica. The procedure consists in plotting P/S^2 versus the indenter displacement, discarding the initial data (a few hundreds of nanometers) where hardness and modulus of fused silica are not independent of the penetration and the tip imperfection affects the measurements, then the adequate frame compliance is found when the curve P/S^2 versus h is represented by a flat curve based in Eq. IV.4 [48]. We verified by methods 1 and 2 that C_s was different from zero giving small changes in the elastic modulus results, because the estimated system compliance differs a little from $C_{\mathrm{instrument}}$ determined prior to testing. Similar variations had been found in comparable instruments, specifically in metallic materials [168,175].

$$C_t = C_{instrument} \pm C_s + C_c \tag{IV.3}$$

$$\frac{P}{S^2} = \frac{\pi}{(2\beta)^2}\frac{H}{E^2} \tag{IV.4}$$

At the nanoindenter the samples are glued with Crystalbond (mounting glue) to an aluminum stub (Chapter II). Crawford *et al.* [115] found that the mounting resin modifies the variation of the elastic modulus with increasing load because it is not considered during the initial calibration of the system compliance, a more compliant resin would lead to a diminution of the elastic modulus, a similar effect would be obtained increasing the thickness of the resin. Generally, if the elastic modulus of the resin is less than 1% of the elastic modulus of the testing sample a significant error is added to the modulus while increasing the penetration depth. The Crystalbond glue has a Young's modulus of 4.0±0.2 GPa [115], that is greater than 1% of the elastic modulus of all the testing materials (70-210 GPa), indicating that the measurements should not be importantly modified by this effect. Moreover, we put especial attention to have a very thin layer of mounting resin to reduce its influence in the results.

Fig. IV.1 shows the graphical calculation of the frame compliance corresponding to classic tests in metallic materials. The minimum penetration depth considered for the calculation of C_s was 400 nm, nevertheless it depends on the variation of the data at low loads. For aluminum, we chose the results starting at ~1600 nm equivalent to an applied load of 50 mN, at smaller loads the dispersion of the data due to the microstructure and surface preparation was important.

Note that the values of C_s are not the same for the four materials, indicating the dependency of this parameter on other elements of the system more than just the load frame. Nevertheless, we must obtain similar order of magnitude in materials with similar behavior and the same mounting conditions.

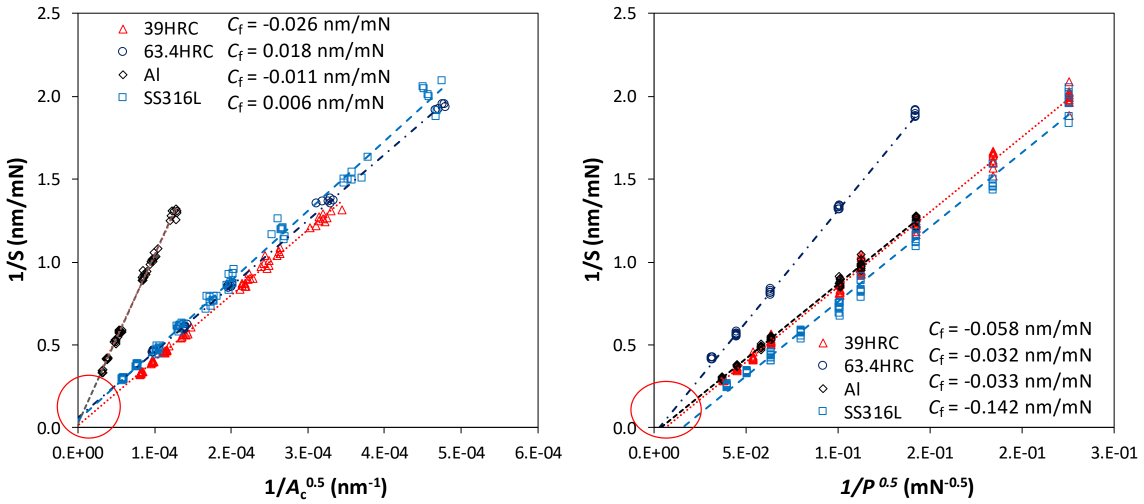

Fig. IV.1. Variation of $1/S$ vs $1/A_c^{\ 0.5}$ and $1/S$ vs $1/P^{\ 0.5}$, the interception of the curves with the y-axis in both plots represents the frame compliance for each tested material; A_c corresponds to the computation assuming sink-in as predominant deformation mode.

If C_s is zero, supposing that it is equal to $C_{instrument}$, the experimental data plotted in Fig. IV.1 must pass through zero; in this case the elastic modulus determined by Eq. IV.1 exhibits insignificant variations (less than 5%) for the four materials in comparison with the regression obtained for $C_s \neq 0$. The coefficient of correlation R^2 is close to one in the two cases ($C_s = 0$ and $C_s \neq 0$) for all the materials, but it is higher when C_s is different to zero. Fig. IV.2 presents an example of the elastic modulus variation for aluminum without and with correction of C_s ($C_s \neq 0$).

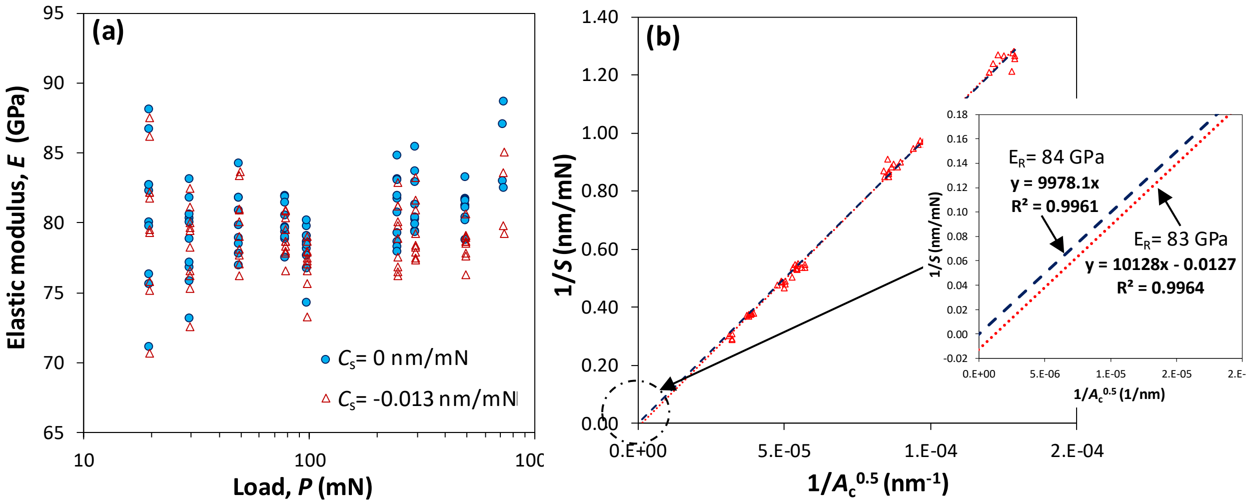

Fig. IV.2. a) Variation of the elastic modulus before and after correction of C_s, the small correction of C_s leads to a diminution of the modulus at larger loads (>100 mN). b) Calculation of the frame compliance by method 1 (dotted line) giving C_s = 0.013 nm/mN, the dashed line is forced to pass by zero for C_s = 0 nm/mN, both cases lead to a similar slope and the same elastic modulus.

Fig. IV.2a shows the elastic modulus computed for aluminum using the contact area determined by the method of Oliver and Pharr (sink-in) [48]. The correction of the data with the system compliance ($C_s = -0.013$ nm/mN) slightly impacts the calculation of the modulus only at higher loads (>100 mN) decreasing the dispersion. Fig. IV.2b shows a small change of the slope, emphasizing that a minor correction of C_s does not carry important modifications in the results, in both cases the reduced modulus takes almost the same value of 83 or 84 GPa, E_R is overestimated since we considered sink-in instead of pile-up, this will be discussed in section IV.2.2. Nevertheless, to decrease the dispersion of the results regarding the entire range of loads the correction of C_s was performed for all the samples.

Slightly variations of the frame compliance were obtained in CSM tests, the estimated values are usually much smaller (approximately two orders of magnitude less), and thus the calculation of the mechanical properties is not greatly affected.

Table IV.1 summarizes the values of C_s obtained by methods 1 and 2. Negative values indicate that the initial system compliance is overestimated and positive values the contrary regarding the tested system. C_s have similar orders of magnitude in the four materials, indicating a similar response among them. The difference of C_s calculated by method 1 using the contact area for sink-in or pile-up is not relevant. Method 2 leads to larger values in all the cases, this method was not used for further computations, since the assumption of a constant hardness at small loads is not correct, due to the phenomenon of indentation size effect observed at this scale, *i.e.* higher values of hardness at smaller loads.

It is worth mentioning that the values of the mechanical properties are coherent with the reference values presented in Chapter II as references, the corresponding estimates after the system compliance corrections are presented in section IV.2.2.

Table IV.1. System compliance values for the four metallic materials computed by methods 1 and 2.

Method	C_s 39HRC (nm/mN)	C_s 63.4HRC (nm/mN)	C_s Al (nm/mN)	C_s SS316L (nm/mN)
$1/S$ *vs* $1/A_c^{0.5}$ sink-in	-0.026	0.018	-0.013	0.006
$1/S$ *vs* $1/A_c^{0.5}$ pile-up	-0.023	0.027	-0.010	0.011
$1/S$ *vs* $1/P^{0.5}$	-0.058	-0.032	-0.033	-0.142

IV.1.2. Correction of the frame compliance in microindentation.

The system compliance was not initially calibrated in the microindenter, *i.e.* its value is zero ($C_{\text{instrument}} = 0$). Impressively C_s may take different values for the same sample tested in identical conditions giving in some cases important variations on the mechanical properties. For this reason, we performed all the tests with $C_{\text{instrument}} = 0$, in order to get the corresponding value of C_s to each set of data. The correction should be performed although the penetration depth is a differential measure between the indenter and the sample surface, indicating that this parameter is affected by diverse elements in the instrument-sample system.

Without correction of C_s the properties decrease with load (Fig. IV.3), Chunyu *et al.* [174] suggested that the decay pattern may help to distinguish if the material experienced damage due to indentation: an exponential decay indicates damage and a sublinear one the effect of the load frame. The experimental data can be roughly approximated by an exponential equation or a linear fit, nevertheless as the system compliance has not been corrected previously is senseless to suppose damage in first instance, consequently we preserved the hypothesis of constant elastic modulus for the further analysis.

C_s could take negative values, which is meaningless, because $C_{instrument}$ is zero and the definition of the total compliance as two springs in series ($C_s + C_c$) would not be valid; in this case the tests corresponding to negative values were removed from the results. The analysis of the data revealed that C_s values depend on the selected range of loads used for their computation. We chose different examples to exhibit these difficulties and the procedure to compute the system compliance in the microindenter.

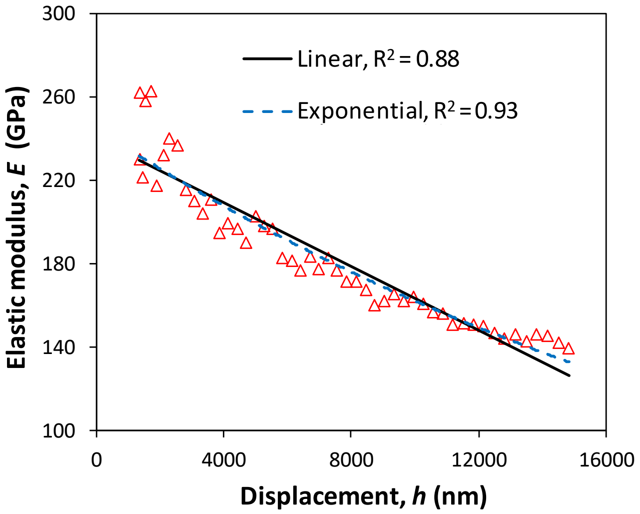

Fig. IV.3. Variation of elastic modulus without correction of the frame compliance in the microindenter.

Fig. IV.4 presents some examples of the system compliance determination for the specimen 63.4HRC studied by multicyclic and classic tests; multicyclic tests were done with identical conditions on the same day, and classic tests were performed another day; both set of tests were done with reference fork 1 (described in Chapter II). Each multicyclic test gives a different estimation of C_s (Fig. IV.4a-b), however most of them yield to similar values of the same order of magnitude using methods 1 and 2. If a multicyclic test gives a very different estimation of C_s comparing with the rest of the tests, probably the mechanical properties will show an anomalous variation with load, then this test should be discarded from the further analysis. In summary, the load frame represents an important parameter in the microindenter; in order to achieve more reliable results, it is necessary to perform several tests (minimum 5) and subsequently compute C_s with all the data (Fig. IV.4c), though the dispersion of results is typically elevated.

The system compliance values determined for classic and multicyclic tests for 63.4HRC have the same order of magnitude (Fig. IV.4d). The plot $1/S$ vs $1/A_c^{0.5}$ for classic tests shows a change in the slope at higher loads that modifies the elastic modulus results, which is linked to the functioning of the system. The possibility of damage is discarded because this variation does not appear in the steel sample 39HRC with a similar elastic modulus. In this case C_s was calculated for all the range of loads regardless the change in the slope, obtaining approximately constant properties with load. This variation in the slope might be related to the test position, arrangement of the sample relative to the fixturing system or surface/ indenter alignment [115,122,168].

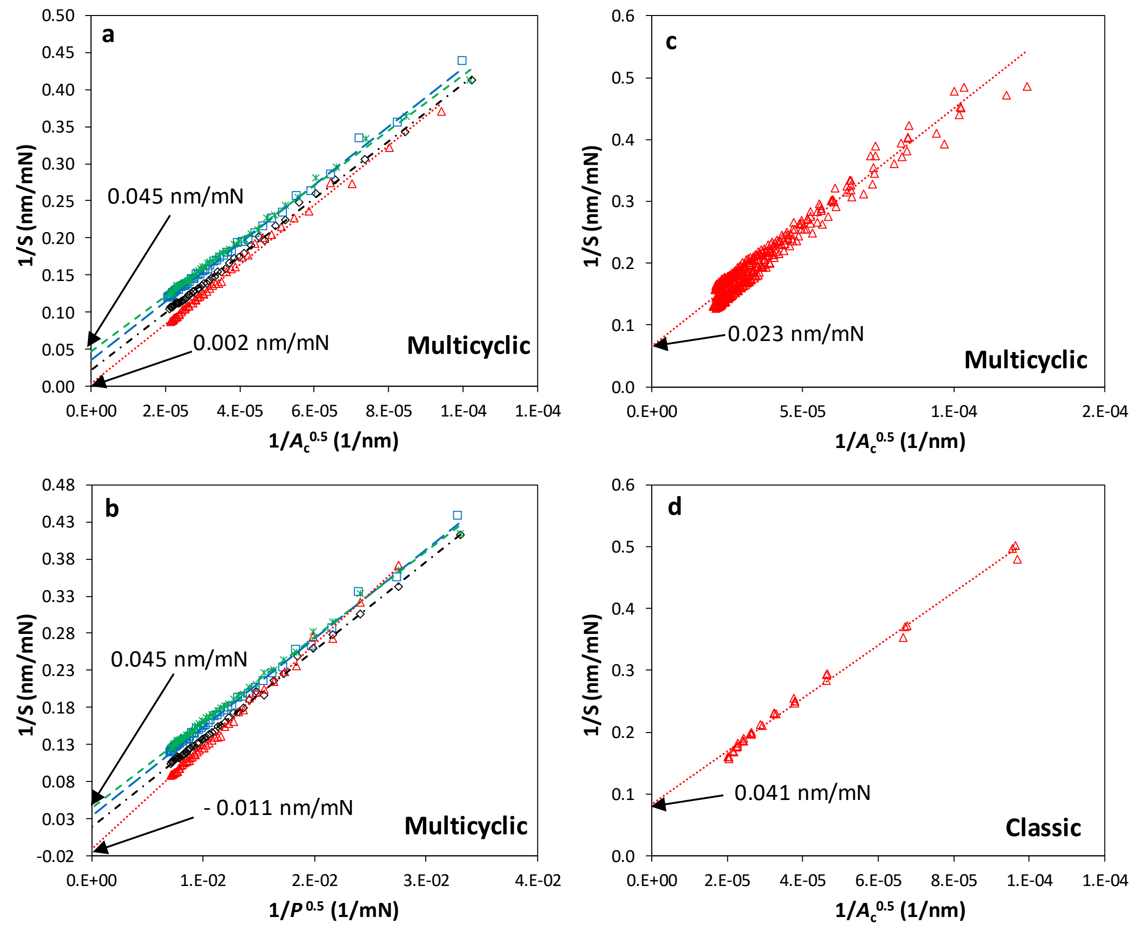

Fig. IV.4. System compliance calculation for the sample 63.4HRC tested with reference 1. a) individual multicyclic tests by method 1; b) individual multicyclic tests by method 2; c) all the data from multicyclic tests by method 1; d) classic tests by method 1.

Fig. IV.5 shows an example of multicyclic tests performed in aluminum using identical conditions and reference fork 2. We noted that using the reference fork 2 we always got positive values of C_s of the same order of magnitude, regardless the tested material (39HRC and Al). The tests were repeated different days finding comparable results, which is an improvement with respect to reference fork 1. The methods 1 and 2 lead to similar estimations of C_s. Nevertheless, in the graphical representation of both methods, we observed a loss in the linearity at loads greater than 6 N affecting the estimation of the mechanical properties. In the same way than in the previous example of classic tests in 63.4HRC, this variation is related to the instrument functioning rather than to the material behavior, since the response was comparable in the samples, 39HRC and Al, that have dissimilar properties. The calculation of C_s considering the portion of the data where the loss of linearity was identified, gives acceptable approximations of the mechanical properties like in the example of classic tests in 63.4HRC.

Nevertheless, the values of hardness and elastic modulus usually show an important dispersion.

The compilation of the frame compliance computed for all the samples is presented in Table IV.2.

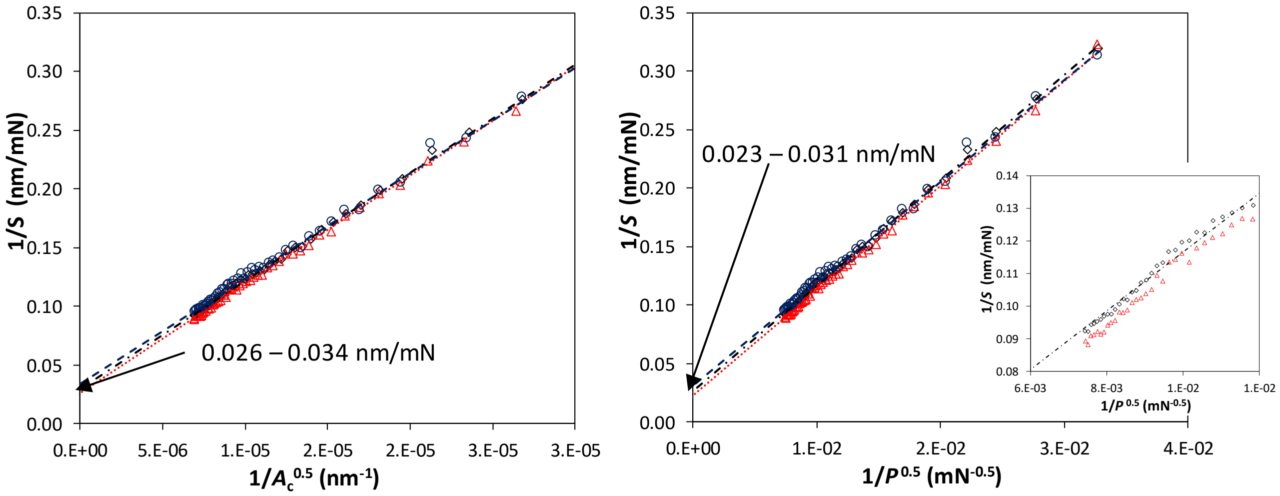

Fig. IV.5. System compliance calculation by methods 1 and 2 for aluminum sample tested using reference 2.

Table IV.2. System compliance values computed by methods 1 and 2 in multicyclic and classic tests for the four metallic samples.

Method	C_s 39HRC (nm/mN)/ Load range	C_s 63.4HRC (nm/mN)/ Load range	C_s Al (nm/mN)/ Load range	C_s SS316L (nm/mN)/ Load range
$1/S$ *vs* $1/A_c^{0.5}$ sink-in (multicyclic)	0.031/ 0.5-18 N*	0.023/ 1-20 N	0.022/ 0.5-18 N*	0.029/0.5-20 N
$1/S$ *vs* $1/A_c^{0.5}$ pile-up (multicyclic)	0.031/ 0.5-18 N*	0.020/ 1-20 N	0.022/ 0.5-18 N*	0.029/0.5-20 N
$1/S$ *vs* $1/P^{0.5}$ (multicyclic)	0.023/ 0.5-18 N*	0.016/ 1-20 N	0.015/ 0.5-18 N*	0.038/0.5-20 N
$1/S$ *vs* $1/A_c^{0.5}$ sink-in (multicyclic)	0.018/ 0.5-18 N*	0.041/ 1-20 N	0.020/ 0.5-18 N	-
$1/S$ *vs* $1/A_c^{0.5}$pile-up (classic)	0.018/ 0.5-18 N*	0.041/ 1-20 N	0.020/ 0.5-18 N	-
$1/S$ *vs* $1/P^{0.5}$ (classic)	0.015/ 0.5-18 N*	0.035/ 1-20 N	0.018/ 0.5-18 N*	-

* tests performed with reference fork 2

Summarizing, in microindentation the procedure to compute the system compliance affects directly the mechanical properties results, thus the corrections of C_s were done in order to satisfy the initial hypothesis of constant elastic modulus using method 1, making variable the data range to compute C_s. For multicyclic and classic tests C_s was calculated considering the data of all the performed tests using the entire range of loads (starting at 0.5 to 1 N), even if the data slightly deviate from the linearity at higher loads. For the further calculations of the mechanical properties, we considered the results corresponding to the tests performed with the reference fork 1 for samples 63.4HRC and SS316L, and with the reference fork 2 for samples 39HRC and Al. The corrections indicated here give coherent estimates of the mechanical properties that would be presented in sections IV.2.2-3.

IV.1.3. Correction of the frame compliance in macroindentation

The frame compliance at the macroindenter was initially calibrated at the factory; this calibration is performed on a steel hardness block using multicyclic tests with increasing load between 100 to 2000 N, then the value is obtained as the intercept with the y axis of the straight line from the plot $1/S$ vs $1/P^{0.5}$ (method 2). The setup value was 3.8 nm/N ($C_{\text{instrument}}$).

The macroindenter is conceived to make the displacements measurements directly between the specimen surface and a place above the indenter [113], thus the displacement should be independent of the load frame deformation, nevertheless the manual of the machine includes the correction described above. Ullner *et al.* [113] mentioned that the loaded element between the place of the displacement scale and the indenter tip gives a small contribution to the measured displacement. This corroborates the hypothesis that the term frame compliance includes other elements, *e.g.* deformation of the indenter tip, rather than only the load frame contribution to the deformation of the system, being more logic to call this term system compliance.

The system compliance is sensitive to different factors, one of them is the fixturing system. In this case the sample is deposited on the testing table and fixed with modeling clay around it to avoid its movement while testing, therefore this parameter should not greatly alter the stiffness of the system. In contrast, the flatness of the surface in contact with the table is a critical parameter, it should be of good quality, otherwise the estimation of the properties is incorrect because the sample moves during the tests, justifying the necessity of machining (rectify or mill) the samples.

Initially, the tests performed with the $C_{\text{instrument}}$ correction give a meaningless increase of the elastic modulus with load, for $P > 100$ N. Fig. IV.6a shows an example of this response for the specimen 39HRC, a similar behavior was found for the other materials. In this case the frame compliance was recalculated for different load ranges, obtaining negatives values for all the materials. Fig. IV.6.b shows examples for specimens 63.4HRC and SS316L, the negatives values (-0.8 nm/N) indicate that $C_{\text{instrument}}$ was too elevated for results obtained at high loads ($h > 30$ µm).

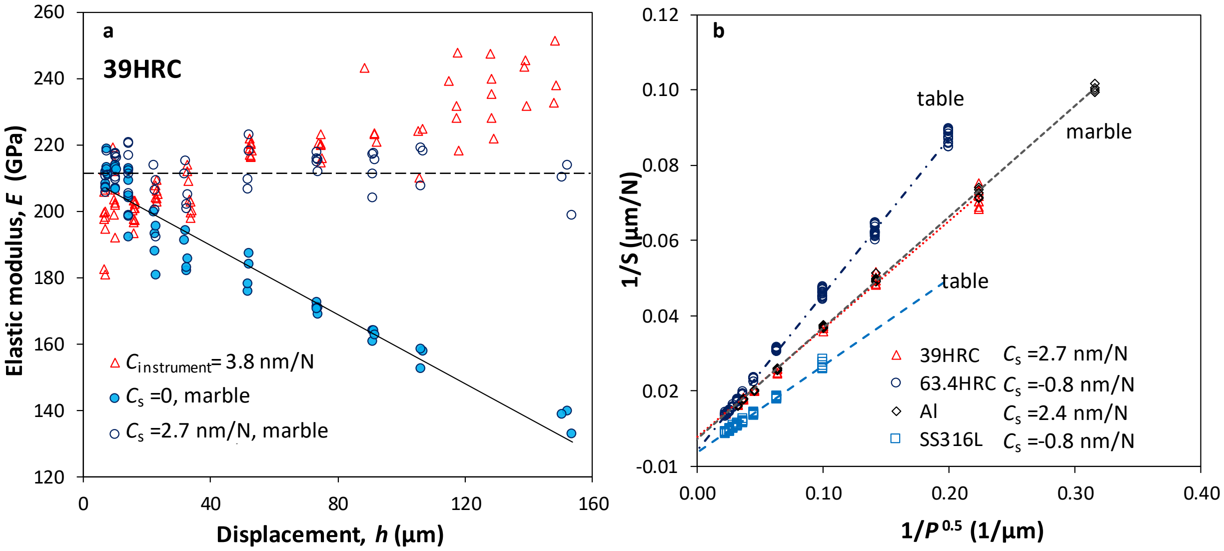

Fig. IV.6. a) Elastic modulus variation as a function of load with different values of compliance. b) Frame compliance calculation by methods 2 for 39HRC sample using the table or the metrology marble as support.

The increase of the elastic modulus when $C_{\text{instrument}}$ is used may be partially related to the stability of the motorized table at high loads. To verify this supposition, the table was disassembled, subsequently a measuring metrology marble (a perfectly flat and stiff surface) was used as the testing table for the sample and additionally the $C_{\text{instrument}}$ was reseated to zero. Subsequently, the samples 39HRC and Al were tested in these conditions. The corresponding results are presented in Fig. IV.6a.

Fig. IV.6a shows a decrease of the elastic modulus while the displacement increases using $C_s = 0$, then an approximately linear decay pattern is observed plotting E against displacement [174]. After correction of the data with C_s obtained by method 1 or 2, the mechanical properties are approximately constant for all the range of loads. C_s estimates are almost 1/3 smaller than the initial calibration value ($C_{\text{instrument}} = 3.8$ nm/N) for the two samples (39HRC and Al), signifying that the table is not stiff enough and increases the compliance of the system. Both samples lead to comparable estimations of C_s using the method $1/S$ vs $1/P^{0.5}$: 2.7 nm/N for 39HRC and 2.4 nm/N for Al (Fig. IV.6b), suggesting that for metallic materials the system compliance should not present great variations. Likewise, the same conclusion is obtained from the tests with the testing table where the second correction of C_s results in similar values for the four samples.

Table IV.3 presents the summary of the results using the table or the metrology marble.

Table IV.3. System compliance values obtained by methods 1 and 2 at the macroindenter.

Method	C_s 39HRC (nm/N)/Load range	C_s 63.4HRC (nm/N)/Load range	C_s Al (nm/N)/Load range	C_s SS316L (nm/N)/Load range
$1/S$ *vs* $1/A_c^{0.5}$ sink-in (table)	-1.1/ 100-2000 N	-0.5/ 25-2000 N	-1.1/ 100-2000 N	-0.9/ 750-2000 N
$1/S$ *vs* $1/A_c^{0.5}$pile-up (table)	-1.1/ 100-2000 N	-0.6/ 25-2000 N	-1.1/ 100-2000 N	-0.9/ 750-2000 N
$1/S$ *vs* $1/P^{0.5}$(table)	-1.1/ 100-2000 N	-0.8/ 25-2000 N	-0.4/ 100-2000 N	-0.8/ 750-2000 N
$1/S$ *vs* $1/A_c^{0.5}$sink-in (marble)	2.9/ 20-2000 N	---	3.0/ 10-2000 N	---
$1/S$ *vs* $1/A_c^{0.5}$pile-up (marble)	2.7/ 20-2000 N	---	3.0/ 10-2000 N	---
$1/S$ *vs* $1/P^{0.5}$(marble)	2.7/ 20-2000 N	---	2.4/ 10-2000 N	---

At high loads, independently of the support system used (motorized table or metrology marble), small changes of C_s affect the elastic modulus results because frame compliance becomes the dominating factor and the contact compliance decreases, both frame and contact compliances get a similar order of magnitude. Due to this reason, it is always advisable to effectuate the C_s correction; its uncertainty should be less than 1 nm/N in the load range up to 250 N [113]. It is worth mentioning that like in microindentation tests, the calculation of the system compliance depends on the chosen range of loads, frequently the fluctuations of the properties start to be problematic at loads about 250 N, consequently we selected the load range in order to obtain constant properties.

Ullner *et al.* [113] found in a similar instrument that frame compliance is load dependent for loads smaller than 200 N due to a component between the indenter holder and the diamond pyramid. Then for the force range between 100-2500 N the frame compliance decreases to an approximately constant value (5 nm/N). These differences were obtained by a sensitive method, plotting $h * P^{-0.5}$ against $P^{0.5}$, with the data corresponding to the loading curve. We applied the same method finding similar results as shown in Fig. IV.7, likewise to the results of Ullner *et al.* [113] the values are overestimated concerning the other methods to compute the system compliance. This method considers the loading curve to compute the frame compliance, the other methods use the total compliance obtained from the unloading curves; the discrepancies between the values at low loads and high loads, and the dissimilar results between methods could be related to a different response of the system while loading or unloading as was reported by Van Vliet *et al.* [112].

In the same study Ullner *et al.* [113] showed that the C_s obtained by extrapolation of the line in the plot $1/S$ vs $1/P^{0.5}$ for the complete load range leads to reliable estimations. Likewise, that in our results this method gives the best correction to obtain coherent mechanical properties.

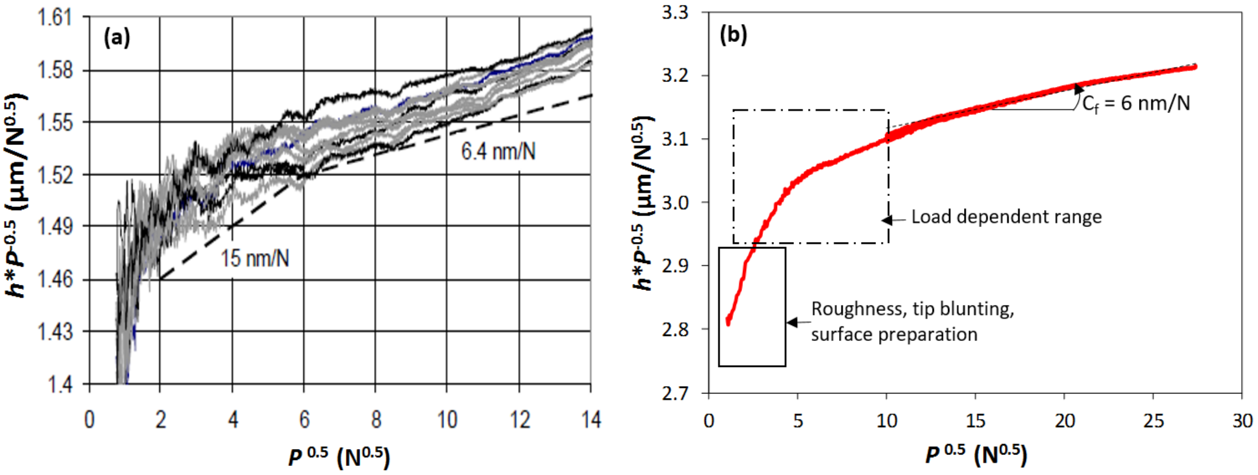

Fig. IV.7. Frame compliance computation by the method proposed by Ullner et al. [113] using the data from the loading curve, where the slope of the curve is the frame compliance, deviations from the straight line indicates load dependence of C_f. a) experimental results of Ullner et al. [113]. b) experimental results of this work.

As a conclusion, the computed properties would be valid up to a certain range of loads while the setup value of the instrument frame compliance is used; an additional correction at high loads leads to an acceptable estimation of the results. This procedure facilitates the calculation if the load is not higher than 250 N while testing metallic materials with Vickers indenter. Nevertheless, testing the samples using the metrology marble and calculating C_s directly from the measurements gives more precise results, but this procedure is time consuming because the sequence of tests cannot be automated. The method 2 used to compute C_s was preferred at this scale because hardness is supposed to be constant. The range of loads for the computation of C_s changes according to the material, and it is better to use the data starting at loads where the dispersion is reduced and do not lead to an increase of the properties at high loads. Generally, if the two methods 1 and 2, give comparable values for C_s, then the selected range of loads is appropriate.

IV.1.4. System compliance correction in the three instruments

Given the description of the system compliance correction in the three instruments, there are some common aspects to highlight.

First, the assumption of a constant elastic modulus with increasing penetration depth supposes: only elastic recovery upon unloading, a perfect rigid indenter, a homogenous material, and a perfect material surface [48,63]. Those elements are simplifications of the real material behavior that are usually appropriate to simulate the material properties, nevertheless they do not represent its real behavior, thus it is logic to obtain certain deviations in the experimental data.

Second, the frame compliance term is apparently erroneous, because in the model of two springs in series this factor represents all the other elements affecting the measurements with the exception of the contact between the two bodies, thus the term system compliance is more adequate. The effect of this parameter depends on the instrument, a better designed instrument shows less dependence on the factors different from the load frame, *e.g.* material, fixturing system, etc. Generally, we obtained C_s values for different materials with the same order of magnitude, but small differences lead to important changes in the data especially at high loads. For the three instruments, the selected range of loads to calculate C_s modifies its value, which should be determined empirically to get a constant elastic modulus. At the nanoindenter and macroindenter, $C_{\text{instrument}}$ gives good estimates of the hardness and elastic modulus up to certain load, due to this reason it is always advisable to perform the correction to get more reliable properties. The assumption of a constant system stiffness for all the range of loads is generally well adapted, nevertheless it depends directly on the instrument, the indenter, and the material.

Finally, we showed the effect of the system compliance in the calculation of the elastic modulus rather than in hardness even that both properties are modified by this parameter. The elastic modulus is proportional to the measured stiffness that is corrected directly by the system stiffness ($1/C_s$), but also depends on the correction of the contact depth only for sink-in (Eq. IV.5). In contrast, hardness only depends on the modification of the penetration depth by the factor $C_s.P$ (Eq. IV.12). An example of both properties computed before and after the system compliance correction at the macro scale is given in Table IV.4.

Table IV.4. Parameters and mechanical properties obtained at 2 kN for sample 39HRC, with the correction of the C_s 2.5 nm/N.

Parameter	Value
S (N/µm)	108
$S - 1/C_S$ (N/µm)	152
h_c (µm)	140.0
h_c corrected (µm)	138.6
HIT (GPa)	4.17
HIT corrected (GPa)	4.24
E (GPa)	133
E corrected (GPa)	199

The example presented in Table IV.4 clearly shows that the system compliance affects significantly the calculation of the elastic modulus and slightly the value of hardness.

IV.2. Mechanical properties obtained by multiscale indentation

This section displays the elastic modulus and hardness results obtained by multiscale indentation in order to establish the connection and comparisons between scales.

The procedure to calculate the mechanical properties is detailed in Chapter II and summary of the equations is presented in Table IV.5.

Table IV.5. Summary of equations used for the calculation of the elastic modulus and hardness.

$E_{\mathrm{R}} = \frac{S\sqrt{\pi}}{2\gamma\sqrt{A_c}}$	(IV.5)
$\frac{1}{E_{\mathrm{R}}} = \frac{(1-\nu^2)}{E} + \frac{(1-\nu_i^2)}{E_i}$	(IV.6)
$A_c\mathrm{nano} = 24.5{h_c}^2 + \sum_{n=1}^{8} C_n\,(h_c)^{1/2^{i-2}}$	(IV.7)
$A_c\mathrm{micro} = 24.5\left[h_c + h_b\left(1 - exp\left(-2\frac{h_c}{h_b}\right)^{3/2}\right)\right]^2$	(IV.8)
$A_c\mathrm{macro} = 24.5\,(h_c + h_b)^2$	(IV.9)
$h_{\mathrm{c\,sink\,in}} = h_{\max} - \varepsilon\frac{P_{\max}}{S}\ ;\ h_{\mathrm{c\,pile\,up}} = 1.2\left(h_{\max} - \frac{P_{\max}}{S}\right)$	(IV.10)
$\frac{h}{h_{\max}} = \frac{h_{\mathrm{f}}}{h_{\max}} + G\left(\frac{P}{P_{\max}}\right)^n$	(IV.11)
$S = \frac{1}{n\,G\,\frac{h_{max}}{P_{max}}}$	(IV.12)
$HIT_{sink\ in} = \frac{P}{A_{c\ sink\ in}};\ HIT_{pile\ up} = \frac{P}{A_{c\ pile\ up}}$	(IV.13)
$HM = \frac{P}{A_r};\ A_r = \frac{26.43}{24.5}\cdot A_c(h_{\max})$	(IV.14)
$\frac{W_e}{W_T} = 1 - \frac{W_P}{W_T} = \kappa\frac{4\gamma^2}{\pi}P_{\max}(C_{\mathrm{t}} - C_{\mathrm{f}})^2E_R$ $\frac{W_e}{W_T} < 0.15, \kappa = 7.30;\ \frac{W_e}{W_T} > 0.25, \kappa = 5.17;\ 0.15 < \frac{W_e}{W_T} < 0.25, \kappa = 6.6$	(IV.15)

The experimental curves were corrected with the system compliance performing the procedures described in the previous section. The unloading curves were fitted by the inverted method described in Chapter III using the data between 98 to 40% of the maximum load $P_{\max}$ (Eq. IV.11). Elastic modulus results were calculated by the work of indentation method (Eq. IV.15), and the contact stiffness relation (Eq. IV.5) considering sink-in and pile-up for the contact depth (Eq. IV.10). Hardness results are focused on Martens hardness (*HM*) and instrumented hardness (*HIT*) given by Eqs. IV.13-14. Additional calculations are indicated during the presentation of the results.

IV.2.1. Load-displacement curves in multiscale indentation

Load-displacement dimensionless curves were obtained dividing the load data by $P_{\max}$ and the displacement data by $h_{\max}$ in order to visualize the resemblance between scales (Fig. IV.8).

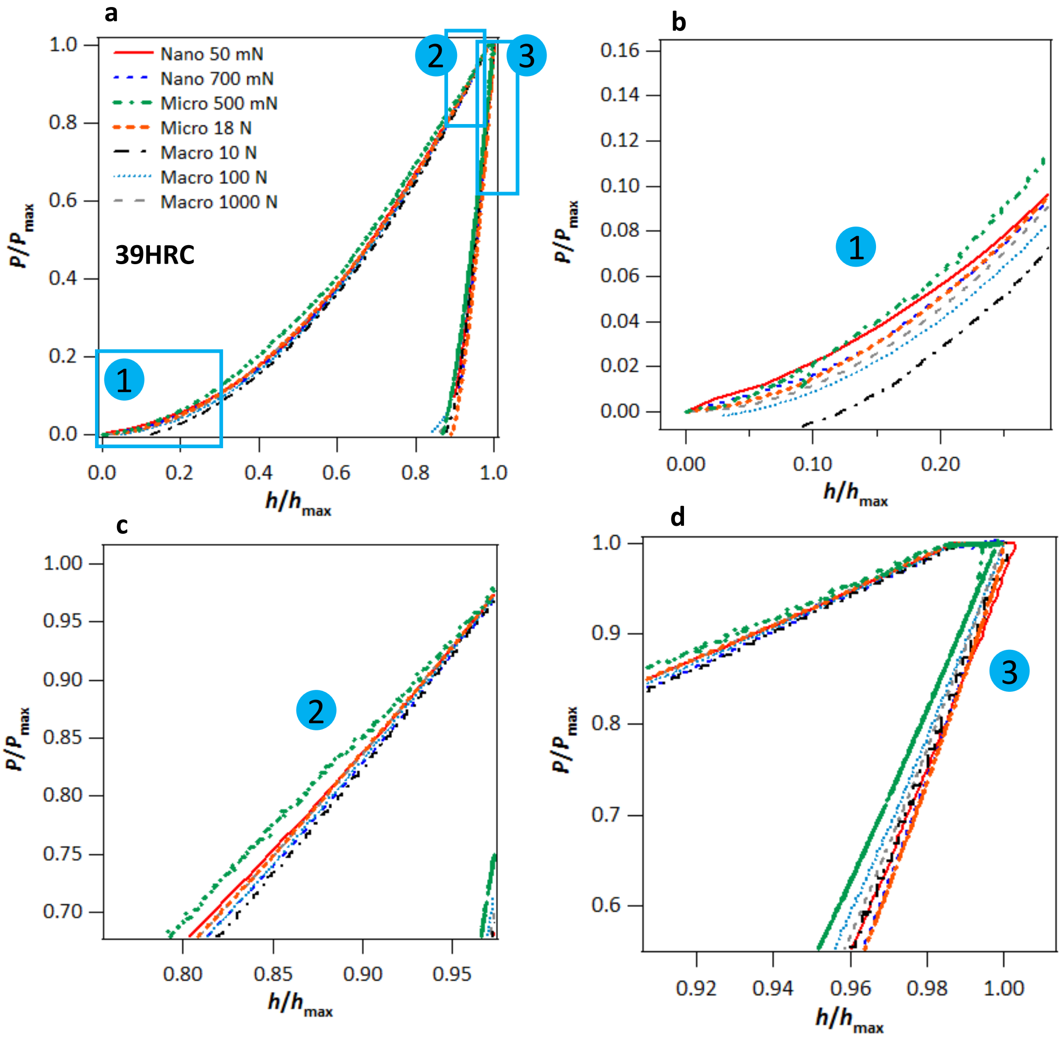

Fig. IV.8. a) Load-displacement dimensionless curves corresponding to classic tests performed with the three instruments on the sample 39HRC. b) Initial part of the loading curves, region 1 in a. c) Loading curves at the zone of maximum load, region 2 in a. d) Initial zone of the unloading curves, region 3 in a.

Fig. IV.8 shows the dimensionless curves corresponding to classic tests performed with the three instruments for the sample 39HRC, similar results were obtained for the other materials.

Fig. IV.9a-b show the comparison between the cycles of a multicyclic dimensionless load-displacement curve. The cycles were separated as individual curves, and then the data of each cycle are divided by $P_{\max}$ and $h_{\max}$ of the respective cycle. Fig. IV.9c-d present the same multicyclic test compared with nano and macroindentation tests. The tests correspond to the sample 39HRC.

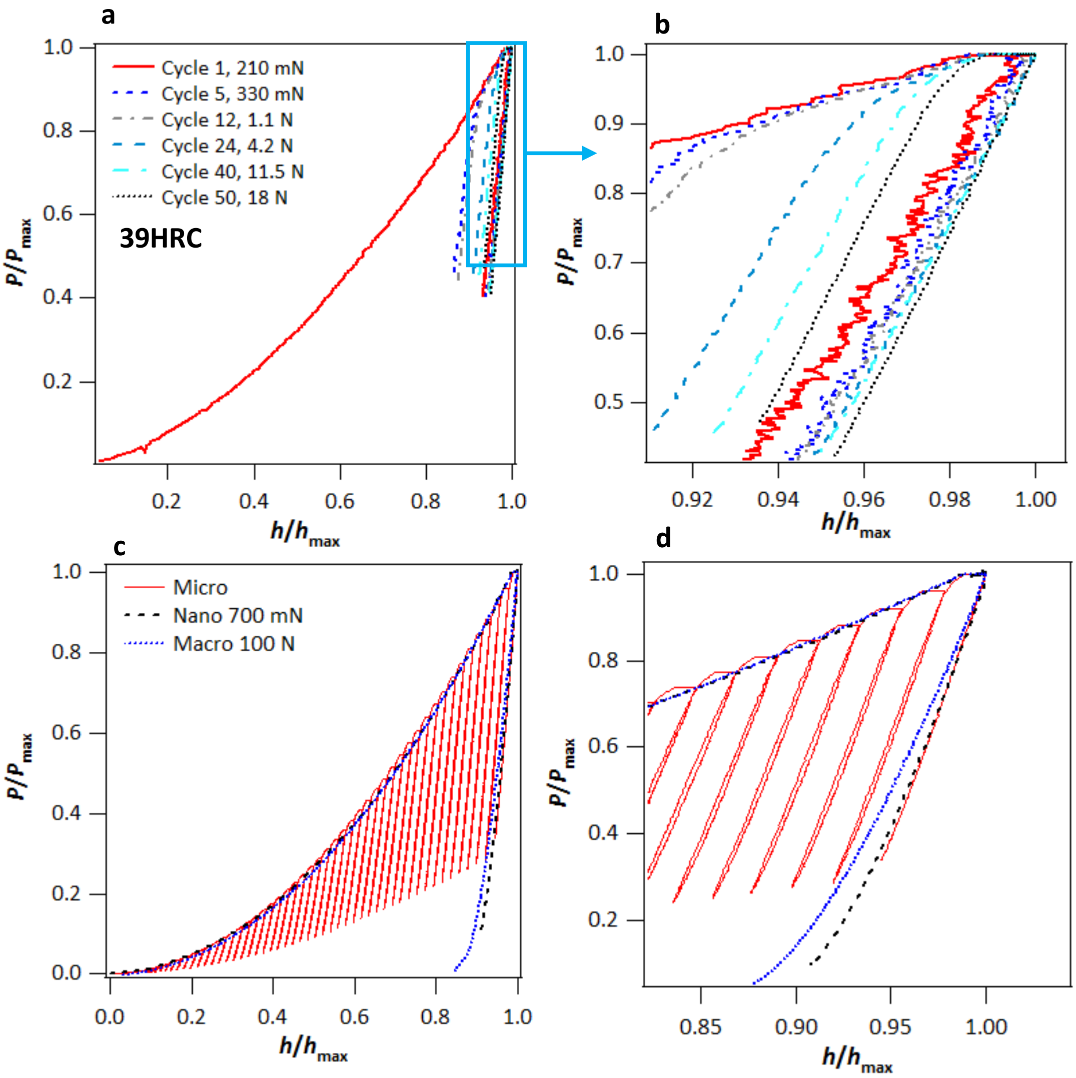

Fig. IV.9. a) Load-displacement dimensionless curves corresponding to multicyclic for the sample 39HRC, comparison between cycles. b) Detail of the unloading curves of various cycles. c) Load-displacement curve from multicyclic test in microindentation, and classic tests in nanoindentation and macroindentation. d) Zoom of the unloading part of (c).

In multicyclic tests the reloading curve of each cycle at the elastic stage (*i.e.* up to $P_{\max}$ of the previous cycle) is parallel to its unloading part (Fig. IV.9a-b). Then, the loading elastoplastic stage (*i.e.* at the point where load overpasses $P_{\max}$ of the previous cycle) shows a curvature distinct from the initial loading elastoplastic cycle (cycle 1) until a region of the curve close to $P_{\max}$ (n-cycle) where the patterns are similar; this part is reduced with the increasing load because the load step is not constant. At the point where a n-cycle reaches $P_{\max}$ of the previous one, apparently, elastic recovery continues further; subsequently the change in the curvature indicates a modification in the material response to an elastoplastic one.

Differences between the loading path of cycle 1 and the following cycles could be noticed in comparison with nano and macro load-displacement curves (Fig. IV.9c-d). We observe the same general trend of the loading curve at the three scales, but in multicyclic tests at the points where load increases for each cycle, the path differs with the nano and macroindentation curves. This behavior could be related to the material response due to the previous plastic deformation or also to the instrument functioning, however, we observed a resembling pattern in multicyclic tests with the macroindenter.

The unloading curve of cycle 1 (Fig. IV.9a-b) deviates slightly from those of the subsequent cycles, probably due to the noise in the data and the performance of the instrument at the limit of its working range (~100 mN). Regarding the comparison with nano and macroindentation tests (Fig. IV.9c-d), we noted that the loading path follows a comparable trend as mentioned above at the three scales; similarly, the unloading curves from nano and micro indentation are superposed, but at macroindentation the slope changes approximately by 20%.

On the other hand, it should be pointed out the existence of small hysteresis loops between the unloading curve and the subsequent reloading curve for each cycle (Fig. IV.9d), that could be explained by an effect of small reverse plasticity upon unloading as mentioned by Pharr and Bolshakov [64], nevertheless since unloading-reloading curves are almost superposed it should not modify the estimation of the elastic modulus and the assumption of elastic unloading is suitable, as found by Chicot *et al.* [176] in the study of dual phase crystal of magnetite and hematite. However, Shuman *et al.* [166] noticed important differences between the elastic modulus calculated from the reloading and unloading curves especially in metallic materials with pile-up. In our results, the estimation of the mechanical properties from multicyclic tests does not seem to be affected by this problem as will be presented in the following sections.

It is worth mentioning that the variation of the unloading slopes between scales seems to be unimportant since we obtained comparable differences in the unloading curves at the same scale of measurement or even at the same load. Therefore, further variations found in the elastic modulus values that depend directly on the contact stiffness are possibly related to other factors rather than to the stiffness calculations.

To illustrate the dissimilarities between the studied materials, Fig. IV.10 shows some examples of the load-displacement dimensionless curves corresponding to classic tests for the four studied materials at the nano and macro scale. A similar trend was obtained at the micro scale. The loading path of the curves is similar for the four materials at both scales; on the contrary the unloading path sets the differences among them, highlighting that for Al and SS316L they are almost superposed.

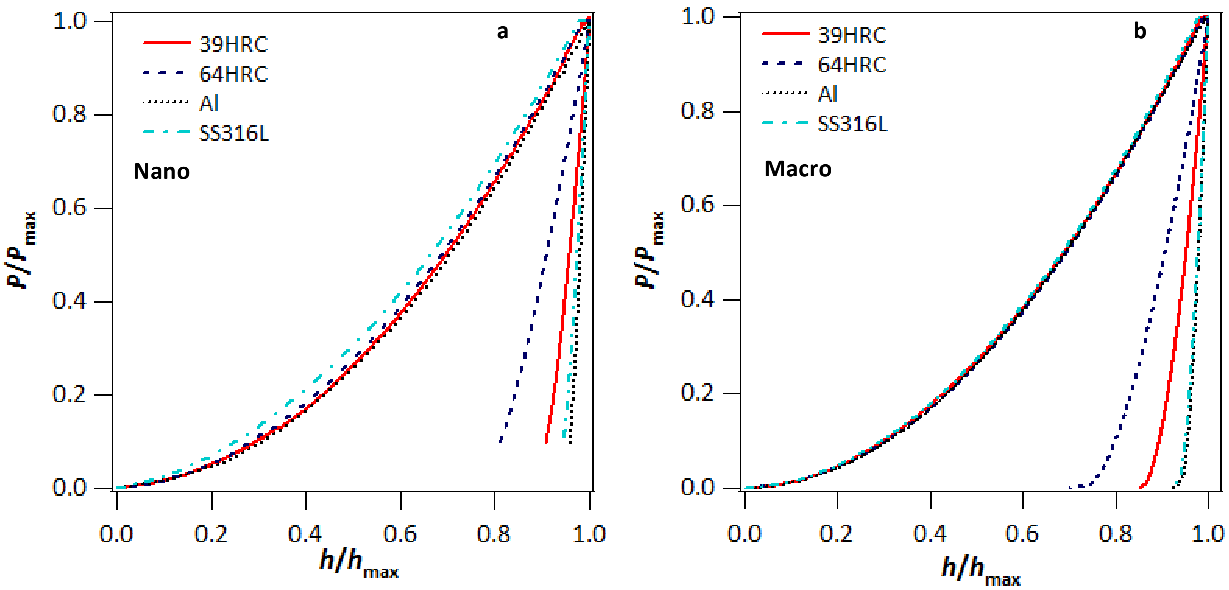

Fig. IV.10. Load-displacement curves obtained from nanoindentation and macroindentation in the samples 39HRC, 63.4HRC, SS316L and Al.

The loading parts of the dimensionless load-displacement curves of the four materials are comparable if they follow the relation $P = C.h^2$, since the given relation becomes independent of the constant C when the variables, P and h are divided by P_{max} and h_{max}.

The fitting parameters of the distinct materials were evaluated to understand the similarities and discrepancies between the unloading curves, in terms of n and G, which corresponds to the fitting parameters of the inverted approach (Eq. IV.11). The parameter n (power law exponent) takes values in the range of 0.62-0.80 for the four samples, which correspond to the range of coefficients found in the literature [48]. The parameter G is comparable for SS316L and Al, and it increases for the samples 39HRC and 63.4HRC, corresponding to differences in the obtained paths of the unloading curves (Fig. IV.10). An example of the fitting parameters at the micro scale for the four materials is presented in Fig. IV.11.

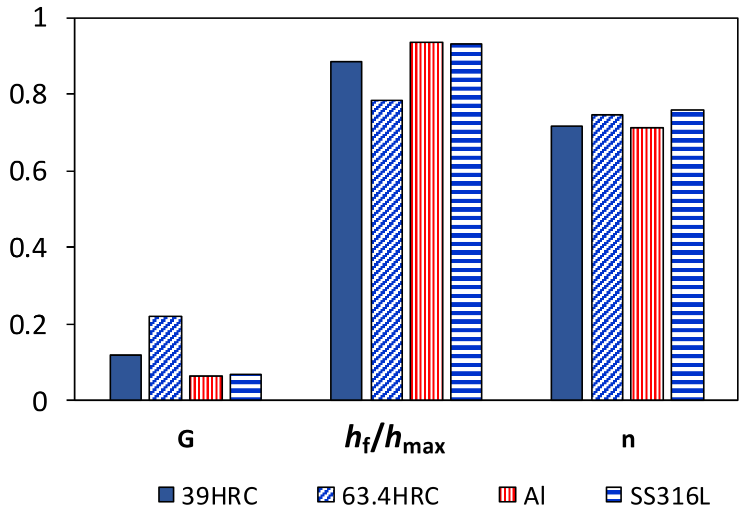

Fig. IV.11. Variation of fitting parameters of the unloading curve (Eq. VI.11) at microindentation, the represented values are the average for each material.

We observed that the unloading curves depend on the relation H/E_R, the values are similar for Al and SS316L (~0.009) leading to close unloading slopes; for samples 39HRC and 63.4HRC the relation change to ~0.02 and ~0.03, respectively, giving a different aspect of the curves. This indicates that from the direct observation of the dimensionless curves without previous analysis, we can quickly predict if the materials have the same ratio H/E_R. This ratio multiplied by a geometric factor is the plasticity index that describes the deformation between a rough and a smooth surface; the wear resistance of hard coatings is related to this ratio [35,177,178].

The contact stiffness is related to the ratio H/E_R^2 by Eq. IV.16, which allows its direct calculation knowing the stiffness [48,179].

$$\frac{H}{{E_R}^2} = \frac{4\gamma^2 P}{\pi S^2} \tag{IV.16}$$

If we can predict the ratio H/E_R or H/E_R^2 from the similarities of the unloading curve, we may think that the unloading curve does not represents only the elastic behavior of the material because it contents information about the hardness that is linked to the plastic deformation. Fischer-Cripps [6] pointed out that the elastic modulus calculation by Eq. IV.5 depends upon the stiffness and the area of contact at any load, indicating that the unloading curve does not only depend on E_R, but also on hardness and creep properties of the material, *e.g.* two materials having the same E_R and different hardnesses, tested at the same load will show different slopes (dP/dh stiffness). It will be greater for the material with smaller hardness to compensate the increase of h_c, noting that the slopes are evaluated at $h_{\max}$ and not at any subsequent point, this example is schematized in Fig. IV.12.

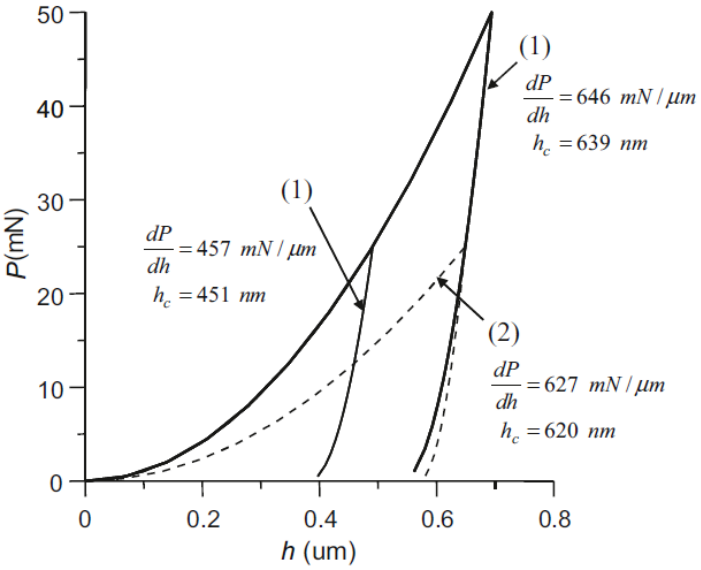

Fig. IV.12. Load-displacement curves for a conical indenter ($\theta = 70.3°$) for two specimens (1) and (2) with the same E = 210 GPa and hardness of 5 GPa and 2.65 GPa, respectively. The unloading curves are computed supposing a power law index, $m = 2$ [6].

IV.2.2. Elastic modulus obtained by multiscale indentation

Fig. IV.13 and Fig. IV.14 show the progress of the elastic modulus as a function of the applied load obtained for Al and SS316L samples; three different set of values are displayed, two of them calculated by the contact stiffness changing the contact depth according to the deformation mode (Eq. IV.5, Eq. IV.10), and the third one computed by the method of work of indentation (Eq. IV.15). Similar trends were found in the steels 63.4HRC and 39HRC.

Both figures exhibit that the elastic modulus is approximately constant at each range of loads, and the values are comparable between scales. The anomalous increase of E obtained for the multicyclic tests at the micro range in SS316L is attributed to systematic errors; we observed this behavior usually at loads higher than 5 N, and also at loads lower than 0.5 N (close to the inferior working load limit of the instrument).

The dispersion of the results given by its standard deviation is important at the three scales; typically, higher in microindentation than at the nano and macro scales that is approximately ±10% or less.

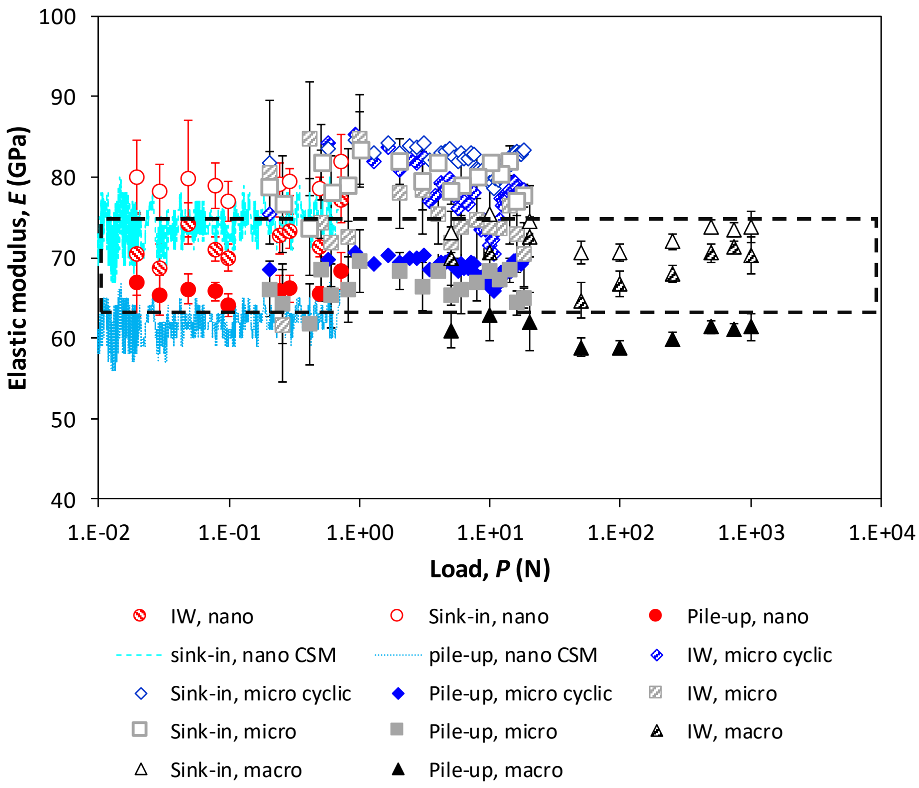

Fig. IV.13. Elastic modulus of aluminum sample obtained by multiscale indentation.

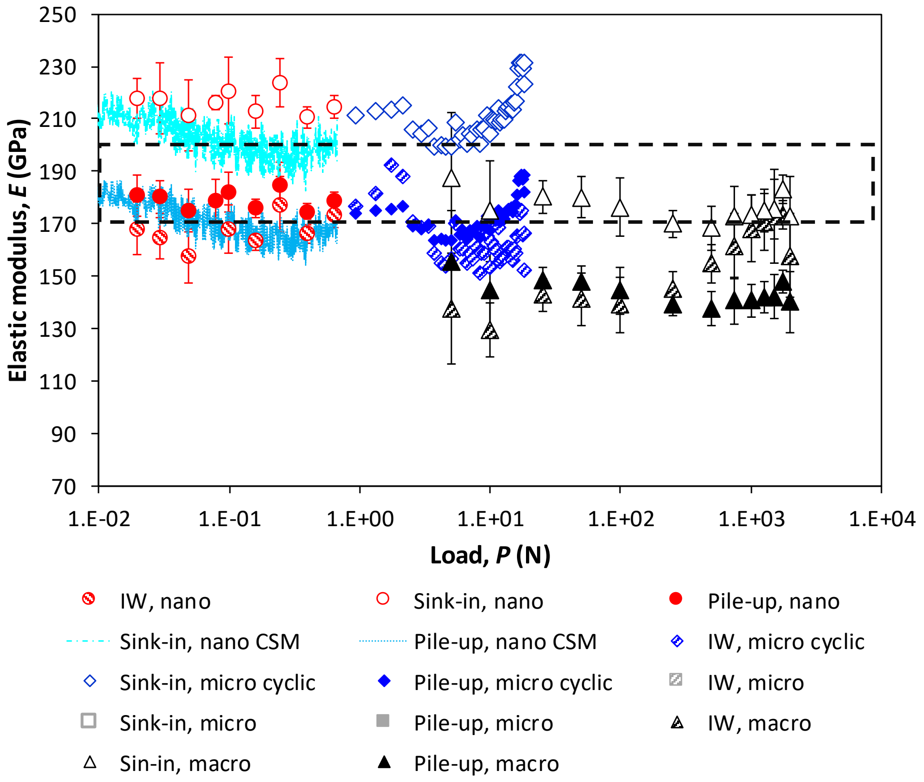

Fig. IV.14. Elastic modulus of stainless steel sample obtained by multiscale indentation.

Classical and CSM tests at the nano range lead to similar estimates of the elastic modulus. An analogous response is obtained between classic and multicyclic tests at the micro scale. These results indicate that the elastic response obtained by indentation is not modified by the cyclic effect, at least for the low frequency applied by the CSM method and for the number of cycles in multicyclic tests [180,181].

Since the elastic modulus is approximately constant with the increasing load, we averaged the obtained results at each scale of measurement for the three methods and all the studied materials. These results are summarized in a column chart (Fig. IV.15); the errors bars are given by the standard deviation of the values at the entire range of loads per scale.

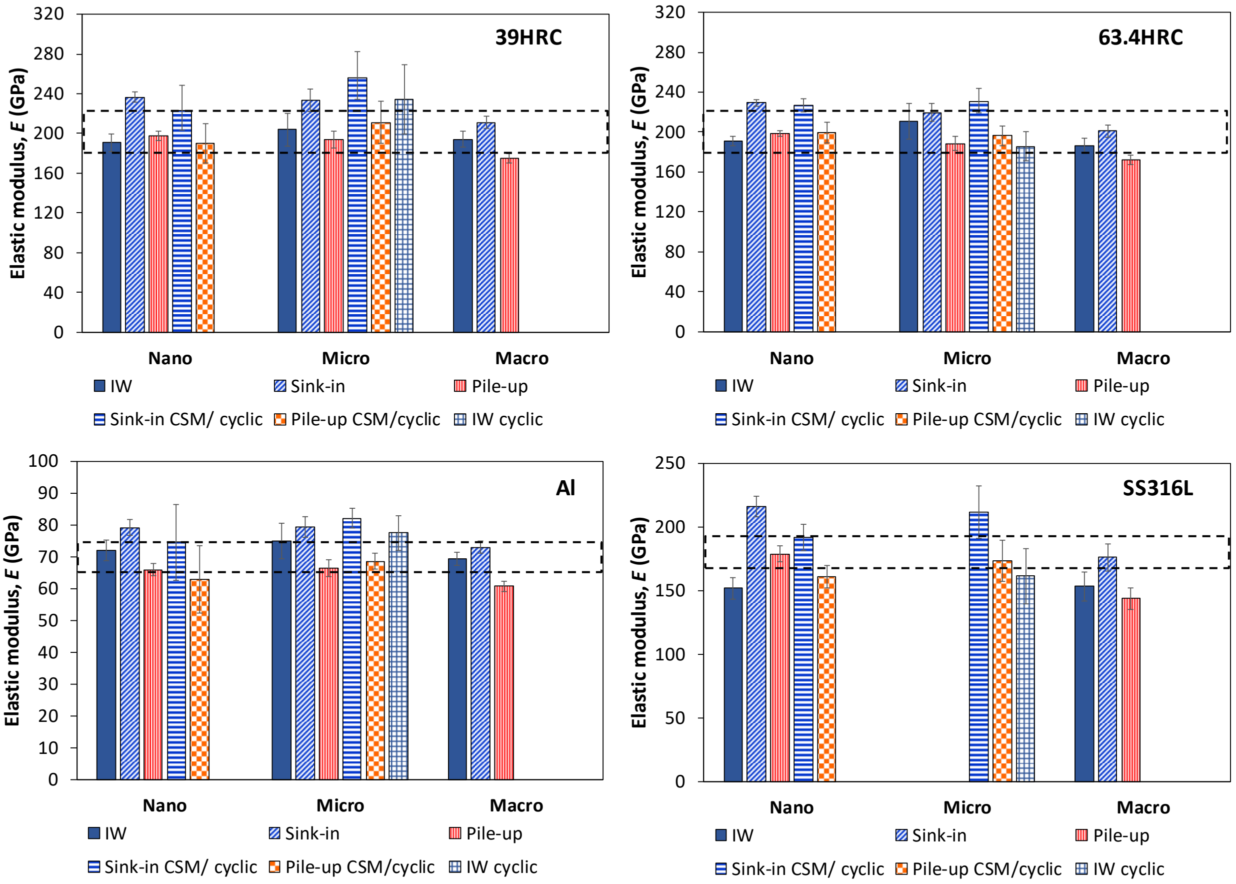

Fig. IV.15. Elastic modulus calculated by the stiffness method for sink-in and pile-up (Eq. IV.5) and by the work of indentation (Eq. IV.15). The reported values are the average for all the range of load at each scale of measurement. The dotted lines represent the regions of theoretical values for each sample.

In general, the estimated values of the elastic modulus are well approximated to their references values: 190-210 GPa for steels, 170-200 GPa for stainless steel and 68-74 GPa for aluminum. Fig. IV.15 shows the similarity between the results regardless the scale of measurement. Afterwards we should state which methodology gives a closer estimation of the reference values, the differences among the three methods is approximately 20%. According to these results, elastic modulus measured by indentation gives an intrinsic response of the material, the differences between scales are more likely to be related to the instruments performance and the uncertainties in the calculations. We should point out that at the macro scale exists a systematic variation among the values of elastic modulus, which are always inferior to those calculated at the nano and micro scales using the contact depth relation.

The methodology of Yetna *et al.* [103] was used to calculate the elastic modulus by the work of indentation since the relation does not depend on the contact area. The modulus obtained with this method are located in the range between the values calculated by the contact stiffness (Eq. IV.5) assuming sink-in (upper limit) and pile-up (inferior limit) for the samples 39HRC, 63.4HRC and Al. For SS316L the elastic modulus calculated by the work of indentation are inferior to the estimations by the contact stiffness assuming pile-up.

To calculate E by the work of indentation (Eq. IV.15) we used different values of the constant k according to the ratio W_e/W_t (Fig. IV.19), for samples 39HRC, Al and SS316L, $k = 7.3$ ($W_e/W_t < 0.15$). W_e/W_t is slightly higher than 0.25 for the sample 63.4HRC, leading to $k = 5.17$ along with Choi *et al.* [95], however this value overestimates the elastic modulus; $k = 6.6$ found by Yetna *et al.* [103] for the range $0.15 < W_e/W_t < 0.25$ is more suitable for this material, which is actually in the upper limit of the range.

The correction factor γ presented in the relations of the elastic modulus, frequently called β in the literature, has been a matter of discussion of many authors leading to different reported values. Generally, it is 1.034 for Berkovich indentation, and 1.05 or 1.012 for Vickers indentation [6,48,57,66,67]. King [67] was the first studying this correction, based in the effect of noncircular geometries in the elastic contact stiffness tested with rigid flat punches. In this work, we use the relation given by Hay *et al.* [66] that depends on the Poisson's ratio of the indented material and the half angle of the axisymmetric equivalent cone, in order to get a constant parameter at different scales. The factor takes the value 1.07 for steel samples and 1.05 for aluminum sample; this parameter takes into account the subtle curved surface after deformation. It is worth mentioning that the change in the correction factor gives modification of less than 5% in the elastic modulus.

As a first approach, we set that the main deformation mode in the four samples is pile-up at the nano and micro scales because the values are close to the theoretical ones. At the macro scale, the method of work of indentation leads to reliable values for samples 39HRC, 63.4HRC and Al; according to the deformation mode the method that considers the contact depth for sink-in gives better results than the contact depth considering pile-up, obtaining comparable values with the nano and micro scales.

Through observation of the indentations by optical profilometry in all the samples, we verified the formation of pile-up around the imprints, an example of the profiles at the macro scale with Vickers indenter is presented in Fig. IV.16. The behavior was similar at the nano and micro scales performed with Berkovich indenter. It is worth mentioning that the development of pile around the imprint does not discard that the sink-in phenomenon arises as well in the material surface.

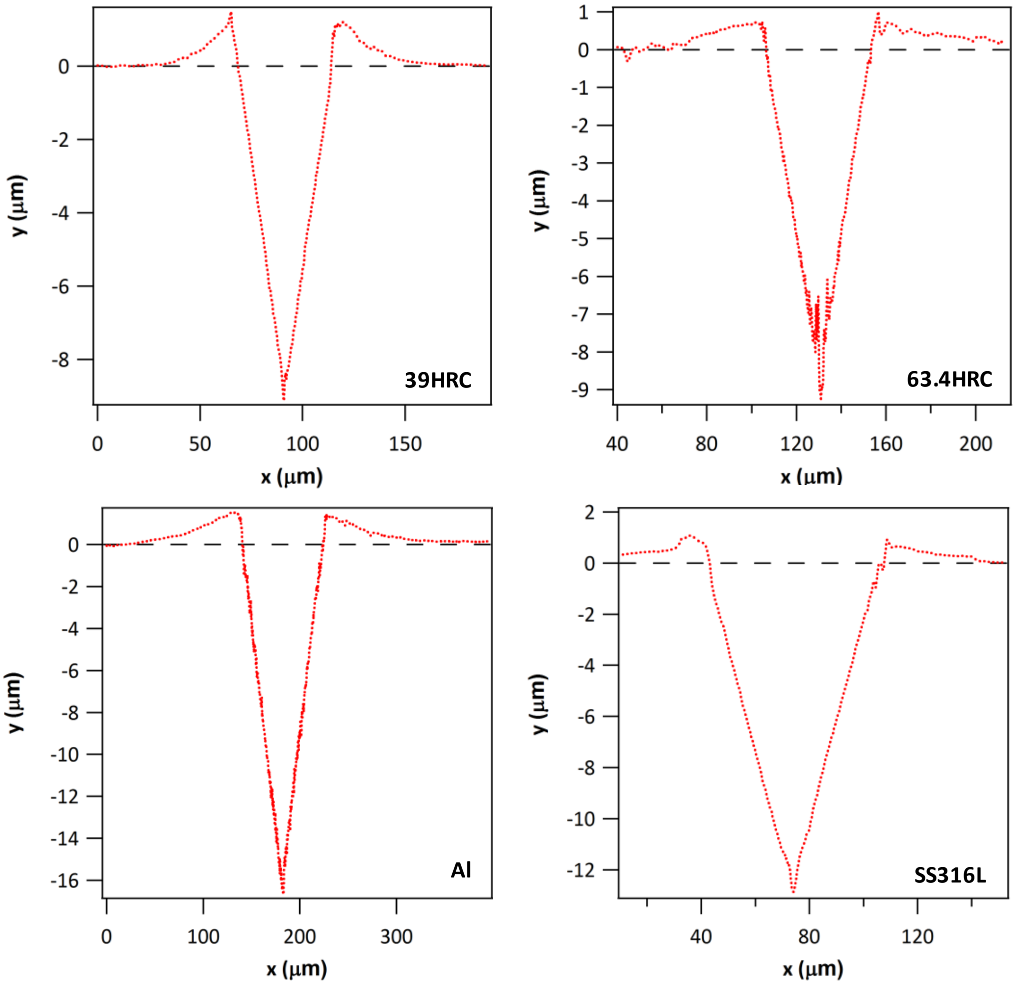

Fig. IV.16. Imprints profiles from macroindentation tests with Vickers indenter obained by optical profilometry.

Three-dimensional examples of the imprints in Al obtained at the three scales are presented in Fig. IV.17, emphasizing the formation of pile-up around of the indentations. It should be noted that at the nano scale roughness is apparently important but the sizes of the imprints are bigger, hence the elastic modulus was not affected by this parameter, emphasizing that the results are comparable with tests at higher loads in nanoindentation and with the results at the other instruments. It is worth mentioning that at the micro scale there is always one side of the imprint that shows a slightly increase on the pile-up height, this could suggest a small misalignment between the sample surface and the indenter, but accordingly to the obtained results in the four samples it is unimportant in the calculation of the elastic modulus, *i.e.* the angle between the surface and the indenter may be ~1° [122,132].

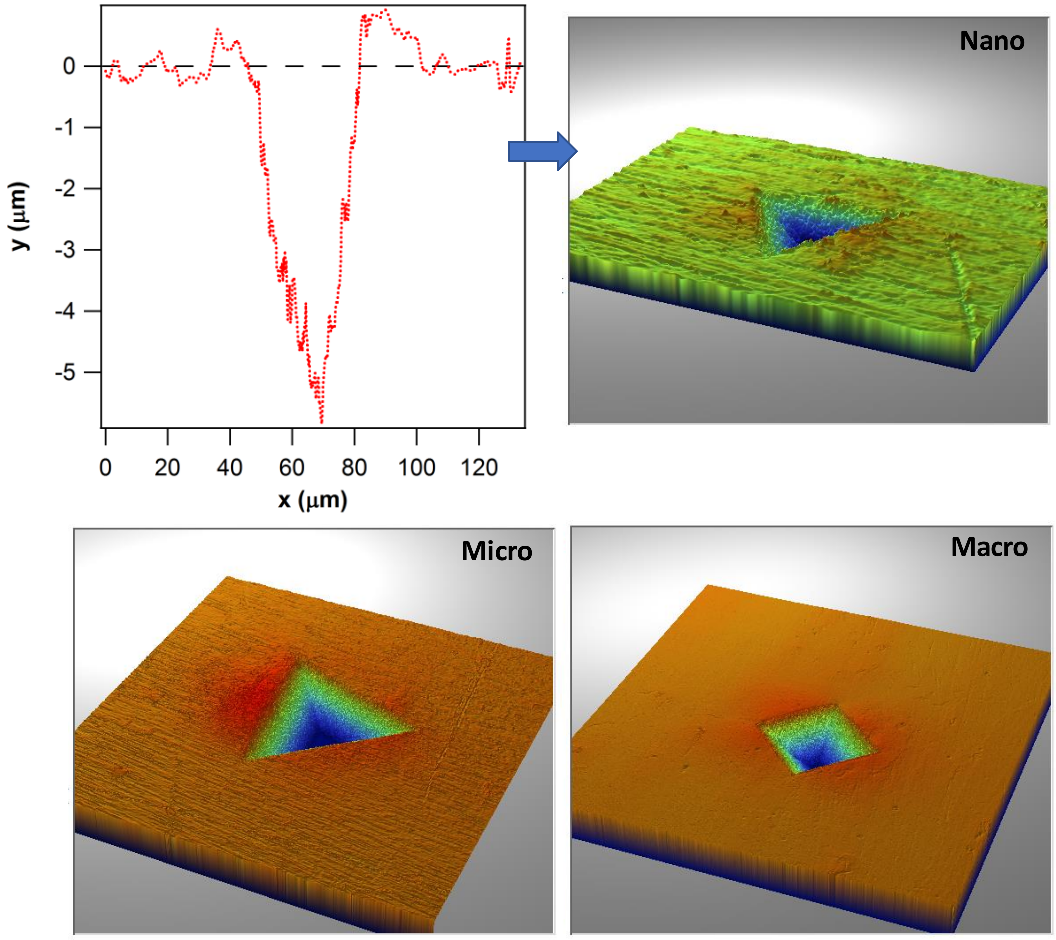

Fig. IV.17. Imprints in aluminum sample at the three scales. The observation of the imprints was done by optical profilometry.

The variations of the pile-up heights were evaluated for the sample 39HRC at the macro scale in order to determine if exists a significant change in the deformation mode with the increase of the applied load, the results are presented in Fig. IV.18. We measured the horizontal extension of the pile-up (h_{pile} x) and its height (h_{pile} y), then we calculate the ratio of both measurements to the residual depth estimated by the profilometry, which shows a very good correspondence with the values estimated by the fitting of the unloading curve indicating that the fitting of the unloading curve approximates well the material response.

The ratios $h_{\text{pile}}\, y/h_{\text{f}}$ and $h_{\text{pile}}\, x/h_{\text{f}}$ are approximately constant with the applied load, indicating that pile-up formation evolves proportionally with the load, respecting the self-similarity principle [6,35]. Nevertheless, this information should be verified through measurement of the pile volume to the volume of the residual imprint.

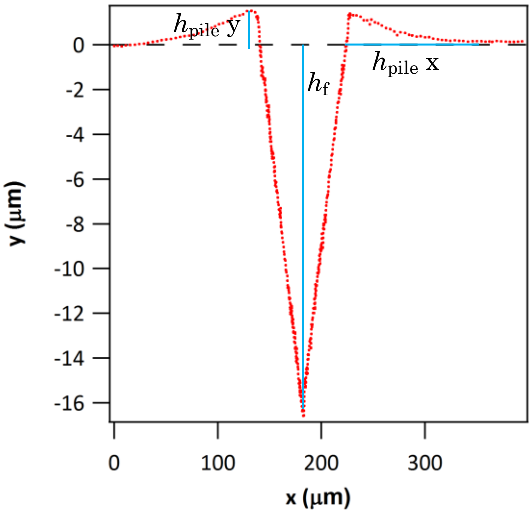

Load (N)	h_{pile} x /h_{f}	h_{pile} y/h_{f}
5	4.68 ± 0.81	0.15 ± 0.03
10	5.62 ± 1.09	0.14 ± 0.02
20	4.48 ± 0.62	0.13 ± 0.01
50	5.21 ± 0.46	0.12 ± 0.03
100	5.18 ± 0.44	0.13 ± 0.03

Fig. IV.18. Pile-up measures as function of the testing load in macroindentation for sample 39HRC.

On the other hand, we evaluate the ratios $h_{\text{f}}/h_{\text{max}}$ and W_e/W_t to confirm the predictions of the predominant deformation mode in the studied materials. Fig. IV.19 shows the average values per scale obtained by the load-displacement curves, the detailed procedure for the computation of the work of indentation (areas under the curves) was described in Chapter II.

Both ratios $h_{\text{f}}/h_{\text{max}}$ and W_e/W_t are approximately constant at the three scales indicating that the materials behavior is similar for all the range of loads. However, small variations in the ratio W_e/W_t give important changes for the elastic modulus (Eq. IV.15), the differences found for microindentation tests in samples 63.4HRC and SS316L are likely to be related to the precise computation of the areas and the correction of the curves with the frame compliance rather than to the material response.

The ratio $h_{\text{f}}/h_{\text{max}}$ is linked to the pile-up formation, which is affected by the ratio of the reduced modulus to the yield stress E_R/σ_y and the work hardening behavior. The pile-up deformation predominates when the material has a small capacity to work-hardening and large ratio E_R/σ_y [48,57]. The work hardening behavior restricts the formation of pile-up, because the material adjacent to the indenter becomes harder, constraining the upward flow of the material to the surface. Bolshakov *et al.* [92] found that pile-up predominates when $h_{\text{f}}/h_{\text{max}} > 0.7$ and does not work harden, if $h_{\text{f}}/h_{\text{max}} < 0.7$ the main deformation is sink-in and the relation given by Oliver and Pharr is suitable. Yetna *et al.* [100] found for a large range of materials that this limit ratio between sink-in and pile-up was 0.83 instead of 0.7.

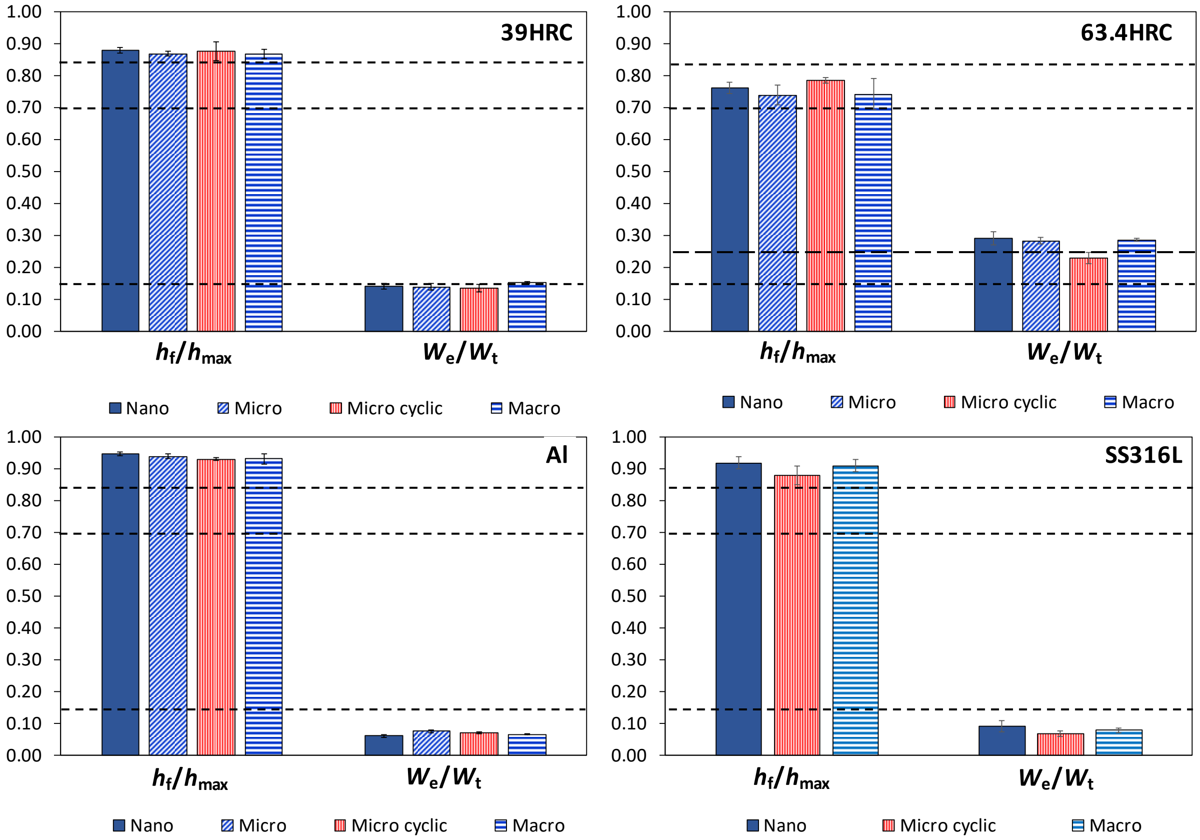

Fig. IV.19. Average values of the ratios h_f/h_{max} and W_e/W_t for all the range of loads at nano, micro and macro scales.

The ratio h_f/h_{max} is greater than 0.7 for the four materials, and greater than 0.83 for the samples 39HRC, Al and SS316L, suggesting that the limit 0.7 is more suitable because the steel sample 63.4HRC shows pile-up formation and the theoretical modulus is closer to the estimates by the relation $E_{R\ \text{pile-up}}$.

Samples 39HRC and 63.4HRC have the same elastic modulus and different hardnesses. The pile-up heights of the imprints obtained at 5 N in macroindentation were similar for both samples, but since the specimen 63.4HRC is harder, the maximum and residual depths at the same load are smaller than for the sample 39HRC, thus the relative importance of the pile-up is greater in 63.4HRC and also its elastic recovery (h_f/h_{max} 63.4HRC < h_f/h_{max} 39HRC). These results suggest that materials with the same elastic modulus in the range $h_f/h_{max} > 0.7$ would have a more important pile-up if the relation h_f/h_{max} is smaller.

Note that for materials showing pile-up having a ratio $h_f/h_{max} > 0.7$ Bolshakov *et al.* [92] found that the overestimation of the elastic modulus considering the methodology of Oliver and Pharr [63] ($E_{R\ \text{sink-in}}$) could be as much as 50% for non-work hardening materials. We obtain differences between $E_{R\ \text{pile-up}}$ [88,99] and $E_{R\ \text{sink-in}}$ of approximately 20% or less (Fig. IV.15), being the values estimated by the $E_{\mathrm{R\ pile\text{-}up}}$ at the nano and micro scales comparable with the reference values, suggesting that the studied materials work harden because the difference between the theoretical values and $E_{\mathrm{R\ sink\text{-}in}}$ are about 20%.

The ratio W_e/W_t is also a quantity reported in the literature to identify the deformation mode, Choi *et al.* [95] mentioned that for $W_e/W_t < 0.15$ pile-up is large compared to the elastic deflection, and for $W_e/W_t > 0.25$ sink-in predominates. For samples 39HRC, Al and SS316L $W_e/W_t < 0.15$, therefore the main deformation mode is pile-up as we mentioned. W_e/W_t is slightly greater than 0.25 for sample 63.4HRC but the material clearly piles-up. These results indicate that similarly than for the ratio $h_\mathrm{f}/h_\mathrm{max}$, the relation $W_\mathrm{e}/W_\mathrm{t}$ should be evaluated carefully to predict the deformation mode since it is also function of work hardening behavior, the ratio $E_\mathrm{R}/\sigma_\mathrm{y}$, the indenter angle and Poisson's ratio of the material [35,106].

The ratios $h_\mathrm{f}/h_\mathrm{max}$ and W_e/W_t could variate with the testing load (Fig. IV.20), they are influenced by the precise system compliance correction, because the maximum displacement is directly affected by it, and the areas measured under the curves are also significantly modified, especially in microindentation and macroindentation tests.

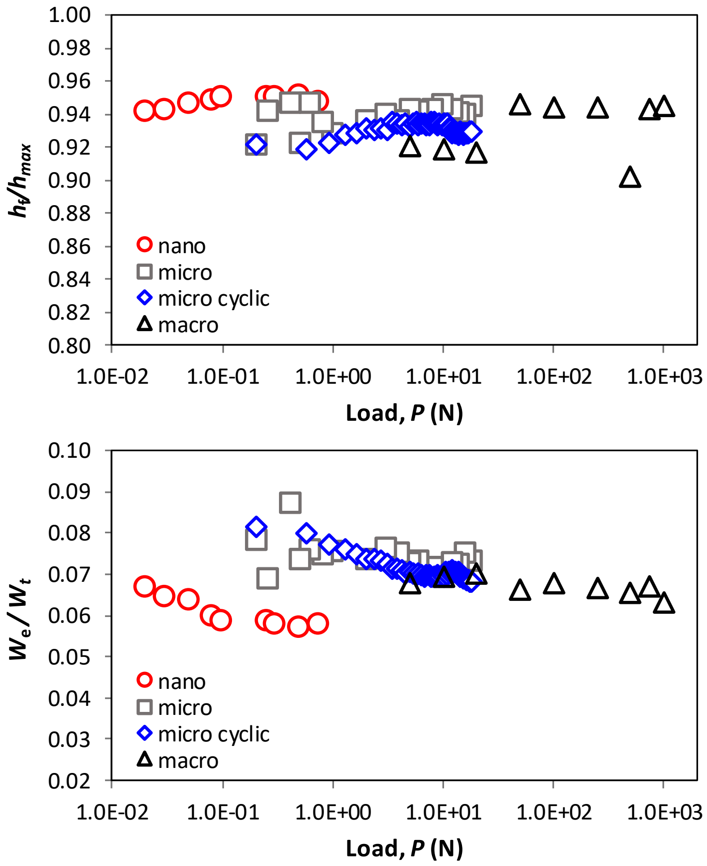

Fig. IV.20. Variation of ratios $h_\mathrm{f}/h_\mathrm{max}$ and $W_\mathrm{e}/W_\mathrm{t}$ with the indentation load for the three scales in the aluminum sample.

The evolution with the load of the ratios h_f/h_{max} and W_e/W_t is dissimilar in the studied materials, which could suggest that the differences are due to artifacts of the experimental data and not to the material response; in such a case, these variations would indicate the violation of the geometric similarity principle. The variation through the different scales could be given by the dissimilarities in the register of the experimental data, because the quality of the data affects the fitting of the unloading curve and the calculation of the areas by the numerical approach (explained in Chapter II). The study of the uncertainties in the three instruments should be performed exhaustively to estimate the real uncertainties in order to discard the evolution of the ratios h_f/h_{max} and W_e/W_t due to the material response.

Change on the contact area in macroindentation tests.

We determined previously that the predominant deformation mode is pile-up for the four samples, therefore the elastic modulus calculated by $E_{pile\text{-}up}$ (Eq. IV.5) considering the expression for the contact depth developed by Loubet *et al.* [88,99] is more suitable. Nevertheless, as we mentioned previously for the macro indenter the elastic modulus calculated using the same contact depth relation, $h_{c\_pile\text{-}up}$, is underestimated comparing with the results in nanoindentation and microindentation in the four materials; on the contrary, if the modulus is calculated using $h_{c\ sink\text{-}in}$ [63] we obtain equivalent results to $E_{pile\text{-}up}$ at the other scales.

If the hypothesis of constant modulus is true, the ratio $S/\sqrt{A_c}$ should be constant for the entire range of studied loads (Eq. IV.5). To elucidate the differences among the scales we present an example of the reduced modulus E_R as a function of $S/\sqrt{A_c}$ for SS316L in Fig. IV.21.

The values calculated at the macro scale using $h_{c\ pile\text{-}up}$ are shifted from the range of values obtained at the nano and micro scales and they are superposed for $h_{c\ sink\text{-}in}$. Apparently, this variation corresponds to a systematic response of the instrument because the same trend was obtained in the four materials (Fig. IV.15). The possibility of damaging is discarded because at the same load level (5-20 N) at microindentation, we obtained higher values using the same relations for the contact depth. The stiffness variations do not create these changes, because we demonstrated that the variations between the unloading curves were equivalent at each scale. Since we evaluate the reduced modulus, the difference between the values is not given by properties of the diamond tip. Therefore, the dissimilarities should be related to the instrument or to the indenter shape, because we used Vickers indenter with the macroindenter and Berkovich indenter at nano and micro indentation. However, both indenters are geometrically equivalent giving the same projected area to depth ratio, therefore the relations to calculate the mechanical properties must apply in the same way.

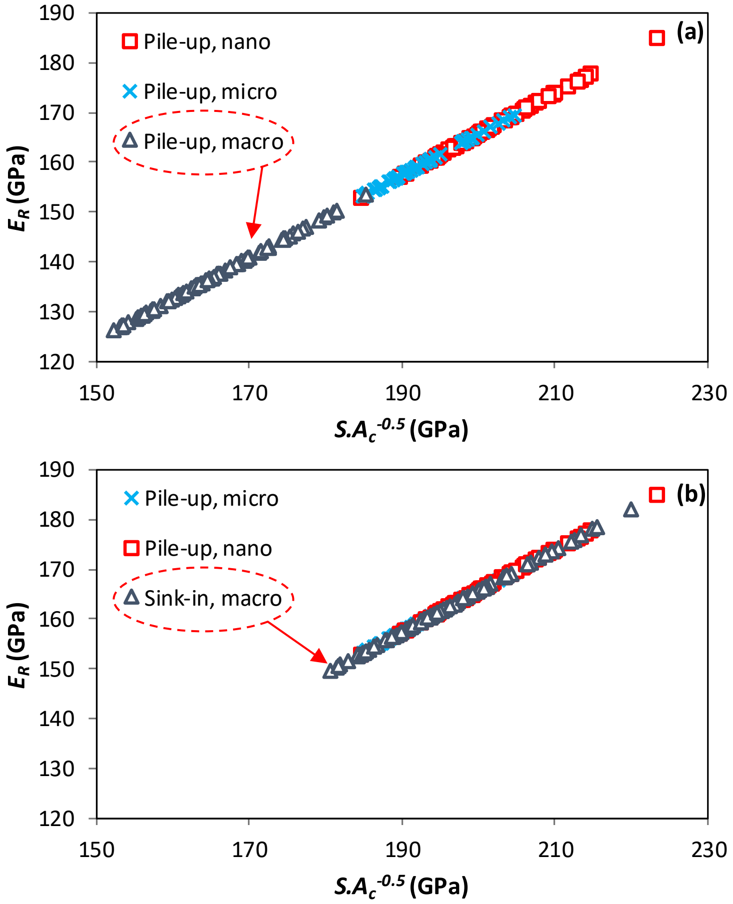

Fig. IV.21. Variation of the reduced elastic modulus at nano, micro and macro scales for SS316L as a function of the ratio $S/\sqrt{(A_c)}$. a) considering $h_{c\text{ pile-up}}$ at the macro scale, b) considering $h_{c\text{ sink-in}}$ at the macro scale.

It is worth mentioning that if we do not consider the correction factor γ (Eq. IV.5) in the calculation of the elastic modulus [182,183], the obtained results do not approximate more the values at the nano and micro scales.

We should point out that the elastic modulus values calculated using the method of the work of indentation at the macro scale are equivalent to the values calculated with the pile-up contact depth at the nano and micro scales for the materials 39HRC, 63.4HRC and Al.

As a conclusion, the elastic modulus estimations at the different scales corroborate the hypothesis that a constant modulus should be obtained by instrumented indentation tests without influence of the testing load, giving it an intrinsic character. The discrepancies among scales are principally related to the instruments and not to the material response. It is worth nothing that for the studied materials at the nano scale even if the microstructure is heterogeneous (precipitates, different phases, different grain orientations) the global response is comparable with the micro and macro scales.

IV.2.3. Hardness obtained by multiscale indentation: *HIT*, *HM*

Hardness is sensitive to the applied load and generally not considered as an intrinsic material property [51,72]. To evaluate the continuity of this property as a function of the scale of measurement we calculate the Martens hardness (HM) and the instrumented hardness (HIT) (Eqs. IV.13-14) at the three scales for the entire range of loads. Fig. IV.22 to Fig. IV.25 show the hardness evolution as a function of the load for the four samples; we presented the results for each material because they exhibit different trends.

Contrary to the elastic modulus results, hardness exhibits a dependency with the testing load, this phenomenon is called indentation size effect (ISE), and it shows a quasi-continuous progression from the nano to the macro scales for all the materials. The samples 39HRC and 63.4HRC also present this continuity at the micro scale; nevertheless, for multicyclic tests the standard deviation of the results is elevated (approximately ±10%); at the micro scale, the results corresponding to classic tests in these two samples lead to closer approximations with the nano and macro scales.

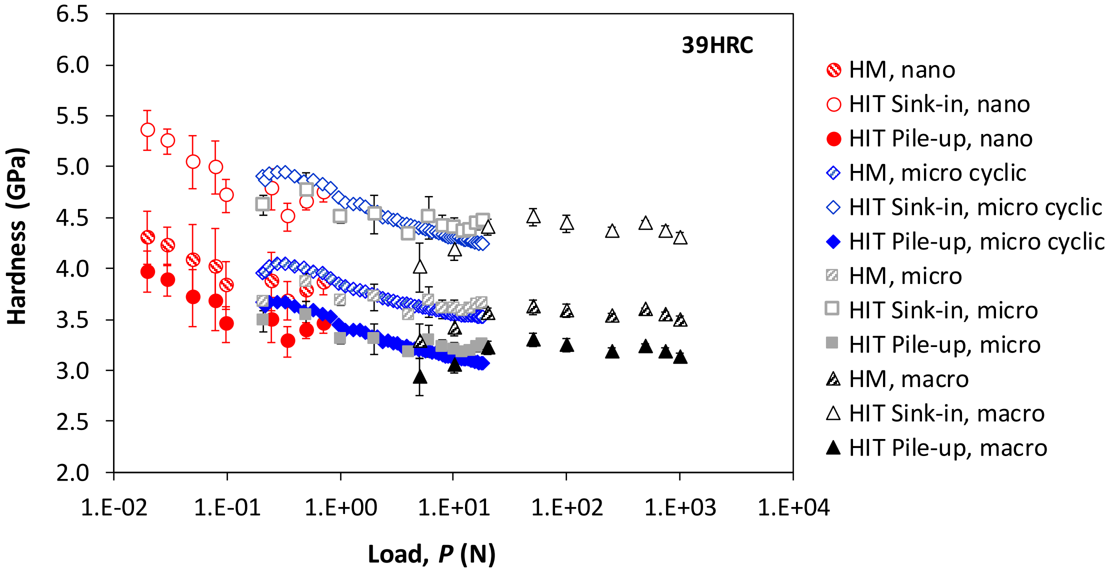

Fig. IV.22. Variation of hardness as a function of the testing load at the three scales of measurement for 39HRC sample. At the micro range the values corresponding to classical tests and multicyclic tests are presented.

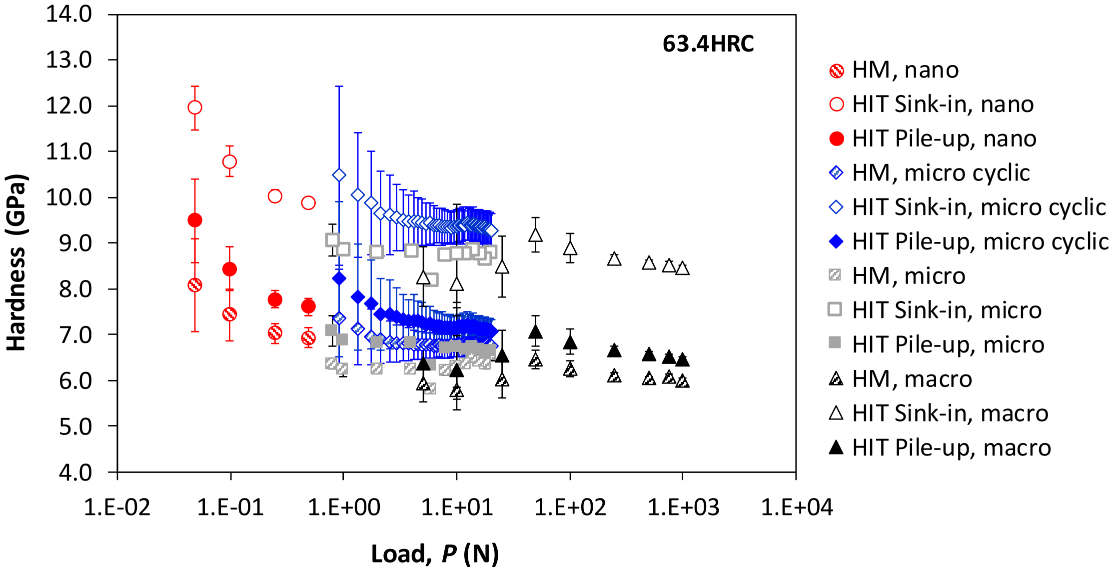

Fig. IV.23. Variation of hardness as a function of the testing load at the three scales of measurement for 63.4HRC sample. At the micro range the values corresponding to classical tests and multicyclic tests are presented.

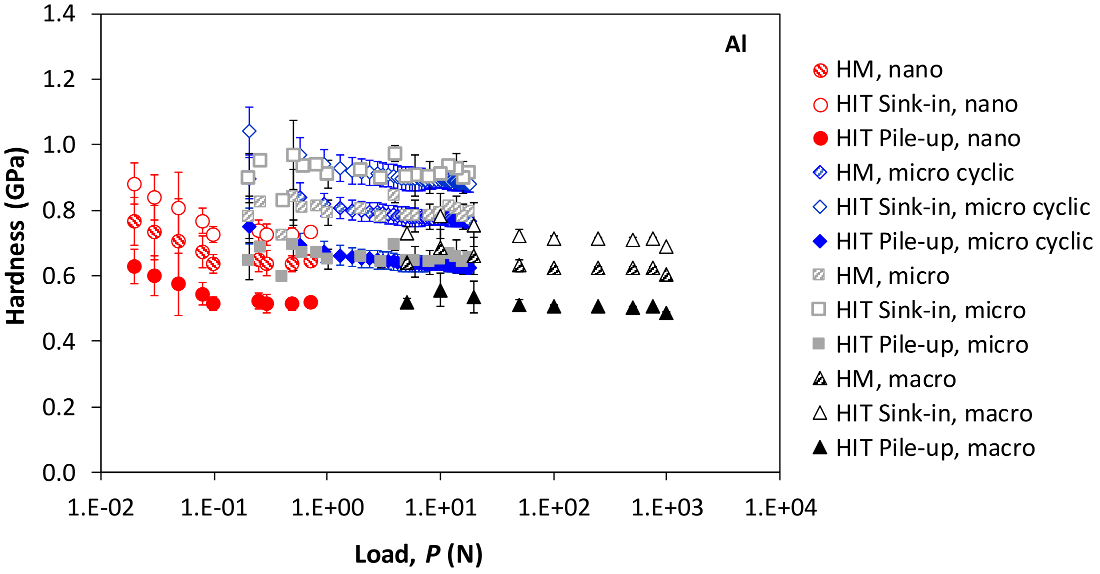

Fig. IV.24. Variation of hardness as a function of the testing load at the three scales of measurement for Al sample. At the micro range the values corresponding to classical tests and multicyclic tests are presented.

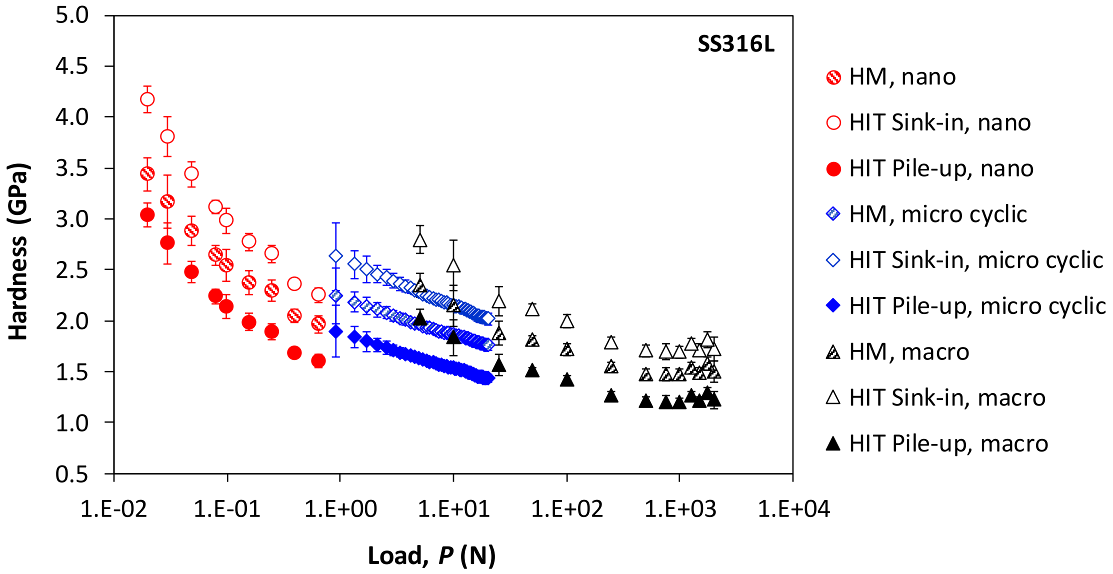

Fig. IV.25. Variation of hardness as a function of the testing load at the three scales of measurement for SS316L sample.

Martens hardness obtained for sample 39HRC at the macro scale agrees with the theoretical hardness of the standard block sample ~3.6 GPa. On the contrary, *HM* of sample 63.4HRC is underestimated regarding its theoretical number.

Microindentation tests in aluminum exhibit an increase of about 20% in hardness estimates in comparison with nano and macroindentation, which was unexpected because the elastic modulus values are comparable between scales (Fig. IV.13). Similarly, microindentation tests in SS316L also show higher hardness values. Multicyclic tests in microindentation in the four materials exhibit a continuous decrease of hardness with load that is less pronounced for classical tests.

It is worth nothing that possible errors in the displacement measurements due to the zero-contact point determination, tip defect, etc., affect more the calculation of hardness than elastic modulus, *e.g.* a 5% error over the displacement leads to a change of 10% in Martens hardness, instead elastic modulus is modified by only 5%. These estimations are just based in the relations to compute both properties without taking into account the uncertainties. Any defect in the alignment on the system (surface-indenter) gives greater errors in hardness than in modulus [132], which are more important for Berkovich indenter [122]. These statements could explain in part the differences in hardness measurements found for aluminum sample regarding the measurements of elastic modulus.

The uncertainties in hardness measurements are conditioned by diverse factors such as the apex angle precision, the zero-contact point, surface/indenter alignment, force and displacement errors [182,183]. The general uncertainty depends on the testing load and the scale of measurement, *e.g.* the effect of the geometrical factor related to the apex angle is greater at the nano and micro scales. The errors bars plotted in Fig. IV.22-Fig. IV.25 are given by the experimental dispersion of the hardness measurements. Nevertheless, we estimate the relative uncertainty assuming as main contributing factors the geometrical factor and the displacement dispersion; we obtained values inferior to 10% at the nano and macro scales, and up to 15% for the microindenter. Generally, the relative uncertainty given by these two factors decreases while increasing the test load.

The differences between classical and cyclic tests in microindentation could be associated to the material response, relative to the previous induced plastic deformation with the evolution of cycles [64,180]. These differences can also be related to systematic errors in the instrument, since a high dispersion is found even at the first cycles.

Another element to highlight from hardness results is that values of the instrumented hardness obtained at the macro scale considering the penetration depth corresponding to pile-up or sink-in, lead to comparable results with the analogous ones at the nano and micro scale, clearly observed in the sample 39HRC. These results differ from the systematic variation obtained for the elastic modulus, described in the previous section, where the penetration depth for sink-in at the macro scale lead to equivalent results of elastic modulus calculated considering pile-up at the nano and micro scales.

The indentation size effect has been explained by several authors and attributed to different factors such as sample preparation problems (surface hardened due to polishing, roughness), tip blunting, crystal anisotropy, surface energy, etc. In a more fundamental way this phenomenon is described by the dislocations and hardening mechanisms, modeling efforts in this field are focused on strain gradient plasticity models [46,184–190]. Another explanation is related to the formation of pile-up during the penetration of the indenter into the material [71].

The further analysis of the experimental results is performed with two approaches corresponding to Nix-Gao [46] and Iost-Bigot [71]. The Nix-Gao model is one of the most widely used to explain experimental variations of hardness with load, it is based on the concept of geometrically necessary dislocations (GNDs), *i.e.* the number of dislocations that must be near the indentation to accommodate the volume of the material displaced by the indenter at the surface. The model states that the GNDs exist in addition to the statistically stored dislocations produced during uniform straining, increasing an extra hardening component that is larger for smaller imprints, the hardness evolution is described by Eq. IV.17, where a straight line should be obtained.

$$H = H_0 \sqrt{1 + \frac{h^*}{h}} \qquad \text{(IV.17)}$$

where H vs $\sqrt{1/h}$ should be linear, H_0 is the macroscopic hardness given by the intercept and the slope is related to h^*, $h^* = (3tan^2\theta)/(2b\rho_s)$, θ is the indenter angle, b is the Burger's vector, ρ_s is the dislocation density of the statistically stored part.

The approach of Iost-Bigot is based on the underestimation of the contact surface due to the formation of pile-up during indentation tests, they found by Vickers indentation tests that the measured hardness increases with decreasing loads because the contact surface between the specimen is greater than the surface measured by the diagonal length, the hardness is given by Eq. IV.18.

$$H = H_0 + \frac{B}{h} \qquad \text{(IV.18)}$$

where B is the dependence of the hardness with the applied load.

To evaluate the indentation size effect, we used (Fig. IV.26 -Fig. IV.27) the Martens hardness as a function of the reciprocal square root of the maximum displacement (Eq. IV.17), and the Martens hardness as a function of the reciprocal of the maximum displacement (Eq. IV.18). The two studied models are approximated to the experimental data for both samples indicating that the ISE could be related to both hypotheses described above.

Fig. IV.26 presents the apparent ISE at the three scales for the sample SS316L. At the nano scale the hardness variation with the penetration depth is probably related to the theory of the dislocations geometrically necessary (Eq. IV.17) because the data is perfectly approached to the model. The parameter H_0 is almost constant for the three ranges, on the contrary the slopes (h^*, B) change with the scale of measurement. These variations could be associated to two possible hypotheses, first, a change in the mechanism at different range of loads; second, the inaccuracies of the experimental data due to systematic errors in the instruments or the analysis of the data (correction zero-point, correction tip defect). Chicot [184] found that the main difference between nanoindentation and microindentation size effect is related to the maximum allowed GND density and linked to the size of the plastic zone, which might explain the dissimilar slopes.

We suppose that hardness values between 5 to 100 N (macro scale) for SS316L are probably overestimated, because we found in the other materials a quasi-constant hardness for all the range of measurements. This issue could be related to an imprecise determination of the zero-contact point, that was usually problematic in the macroindenter as we mentioned previously, also found by Cagliero [182] in a similar instrument. However, a contribution of the material response due to a different deformation mechanism in comparison with the other samples is also possible, mentioning that the stainless steel could develop complex mechanism upon deformation such as martensitic transformation [191–193]. It is worth mentioning that the sliding bands are visible around the imprints. Additionally, regarding the microstructure at the nano range the tests are probably performed in different grains, on the contrary in macroindentation the imprints cover several grains (Chapter II).

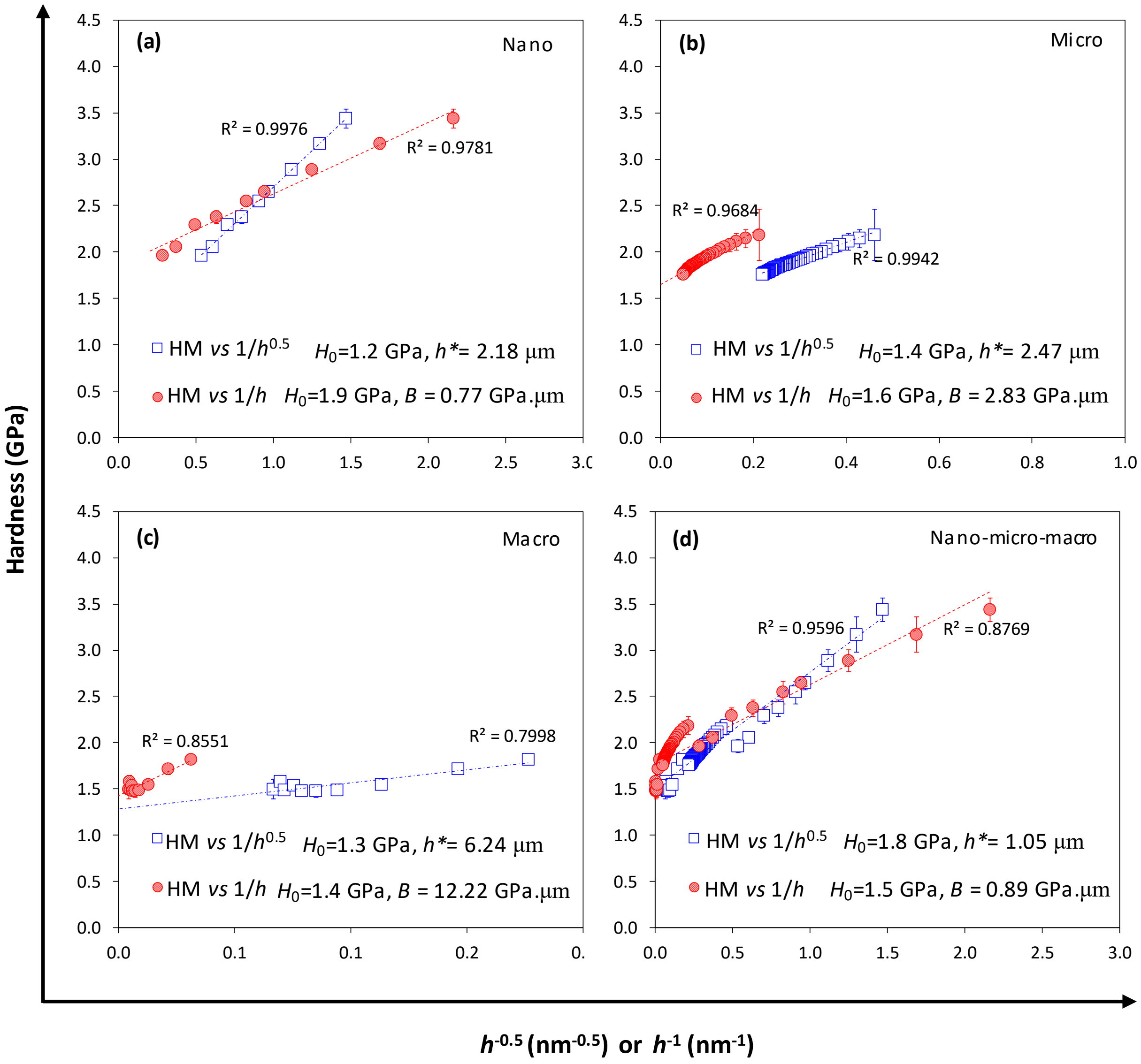

Fig. IV.26. Variation of hardness at the nano, micro and macro scales for sample SS316L as a function of the reciprocal penetration depth (circles) or the reciprocal square root of the displacement (squares), reveling the presence of indentation size effect phenomenom.

It should be noted that the superposition of the data at the three scales Fig. IV.26.d leads to close estimations of the hardness $H_0 = 1.5 - 1.8$ GPa.

Fig. IV.27 shows the ISE for the sample 39HRC, we used all the data because it presented an almost continuous progression with load. We took only the data corresponding to the classical tests at the micro range. Both models exhibit a good correspondence with the data. It should be pointed out that the values of the hardness are approximately constant starting at 5 N (micro and macro range) being comparable to the parameter H_0 = 3.6 GPa. The dispersion of the hardness values at smaller loads is important, being probably affected by the heterogeneities of the microstructure at this scale. On the other hand, this sample was carefully polished, nevertheless it is possible that a small layer in the surface was hardened because it was a manual process. In this case it is difficult to elucidate if the apparent increase of hardness with the diminution of the applied load would be uniquely related to the mentioned theories, nevertheless the results are apparently coherent with the geometrically necessary dislocations because of the continuity of hardness values that remains constant after ~5 N.

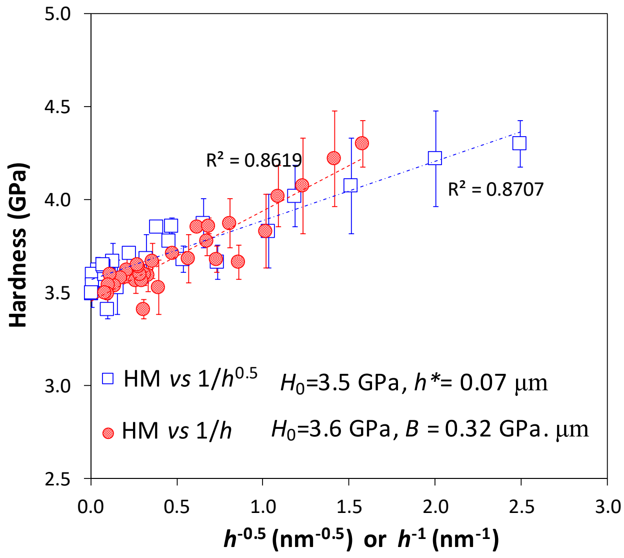

Fig. IV.27. Variation of hardness at the nano, micro and macro scales for sample 39HRC as a function of the reciprocal penetration depth (circles) or the reciprocal square root of the displacement (squares), reveling the presence of indentation size effect phenomenom.

The indentation size effect includes complex mechanisms and its comprehension is still a matter of concern in indentation, particularly meaningful measurements of hardness at the nanometric scale are difficult to achieve due to errors and misleading results. To elucidate with certainty if the hardness variations with load at the nano, micro and macro scales are related exclusively to the material behavior and not to the treatment of the experimental data or errors in the instruments a more detailed metrological study should be performed in order to correctly estimate the uncertainties related to the test.

IV.2.4. Hardness calculation by work of indentation

The work of indentation can be used to calculate the material hardness, there exists several approaches in the literature to calculate it [60,101,102,194,195], some of them were described in chapter I. Somehow in most of the cases the definitions state different types of hardness numbers to the usual ones reported in the literature. Here we present some examples of different hardness definitions calculated by the work of indentation, comparing with typical reported values such as Martens hardness, instrumented hardness and Meyer hardness (*HMeyer*). The next relations were used for the calculations

$$HP_c = \frac{W_P}{{V_P}^c} \tag{IV.19}$$

$$HT_c = \frac{W_T}{{V_T}^c} \tag{IV.20}$$

$$HT = \frac{W_T}{V_T} \tag{IV.21}$$

$${V_T}^c = \frac{\pi}{3} tan^2\theta\left[(h_{\max} + h_b)^3 - {h_b}^3\right] \tag{IV.22}$$

$$V_T = \frac{26.43}{3}\left[(h_{\max} + h_b)^3 - {h_b}^3\right] \tag{IV.23}$$

$${V_P}^c = {V_T}^c \frac{h_f}{h_{\max}} \tag{IV.24}$$

$$HP_{sink\ in} = \frac{W_P}{(A_{c\ \text{sink in}}\ h_f)/3} \tag{IV.25}$$

$$HP_{pile\ up} = \frac{3W_P}{(A_{c\ \text{pile up}}\ h_f)/3} \tag{IV.26}$$

We propose Eq. IV.25 and Eq. IV.26 to calculate the plastic hardness considering sink-in or pile-up to be comparable with the instrumented hardness, based in the explanations given by Tan [101]. We suppose that the plastic volume is given by the product of the contact area according to the deformation mode and the residual depth ($A_c . h_f/3$). Instead Tan [101] suggested the calculation considering the total contact volume by a polynomial expression, similar to the Oliver and Pharr function area, evaluated at the contact depth ($h_{c\ \text{sink-in}}$) (V_c); the same expression evaluated at h_f gives the plastic volume (V_P); he found that the values given by the relation W_T/Vc and W_P/V_P do not correspond with the HIT values computed by the relation of Oliver and Pharr ($HIT_{\text{sink-in}}$).

Eq. IV.19 and Eq. IV.20 are the relations described by Chicot *et al.* [195], they found that these values are both comparable to Meyer hardness, we propose to use the same definition given by them for the total volume changing the coefficient $\pi . tan^2\theta$ by 26.43 for the real surface area in order to establish a relation with the Martens hardness.

Fig. IV.28 shows the relation of the hardness numbers given by the previous relationships and the typical numbers (Table IV.5) for the samples 39HRC and Al, at the nano range the hardness values $HP_{sink\ in}$ and $HP_{pile\ up}$ are compared with the corresponding values of HIT; both samples show a similar trend that was also observed for sample 63.4HRC.

We establish different comparisons in order to elucidate the equivalence between the definitions. For the samples 39HRC and Al, $HIT_{\text{pile-up}}$ and $HIT_{\text{sink-in}}$ are comparable with the numbers $HP_{\text{pile-up}}$ and $HP_{\text{sink-in}}$ at the macro scale, however at the nano scale the values are slightly shifted from the identity line, this effect is more important at smaller loads, probably due to the inaccuracies in the calculation of the areas and volumes [102], indicating that hardness values calculated by the work of indentation are higher.

Martens hardness is apparently equivalent to the total hardness *HT* (Eq. IV.21), the correlation is better for the aluminum sample.

Meyer hardness was related to the plastic hardness *HP*c (Eq. IV.19) and to the total hardness *HT*c (Eq. IV.20), in this case both correlations are satisfied, hence the values are equivalent, which is in agreement with the results of Chicot *et al.* [195]. Slightly differences are observed between the *HP*c and *HT*c relations for the steel sample. The equality between *HP*c and *HT*c is true only if $W_P/W_T = h_f/h_{\text{max}}$, nevertheless many authors had suggested that it exist a relation between both ratios [35,106–109], in most of the cases they were obtained through finite element simulation; we select the relation of Cheng *et al.* [106] described by Eq. IV.27, who made an extensive research in different materials and found that the relationship was material independent.

$$\frac{W_P}{W_T} = (1 + ø)\left(\frac{h_f}{h_{max}}\right) - ø,\ ø = 0.27 \qquad \text{(IV.27)}$$

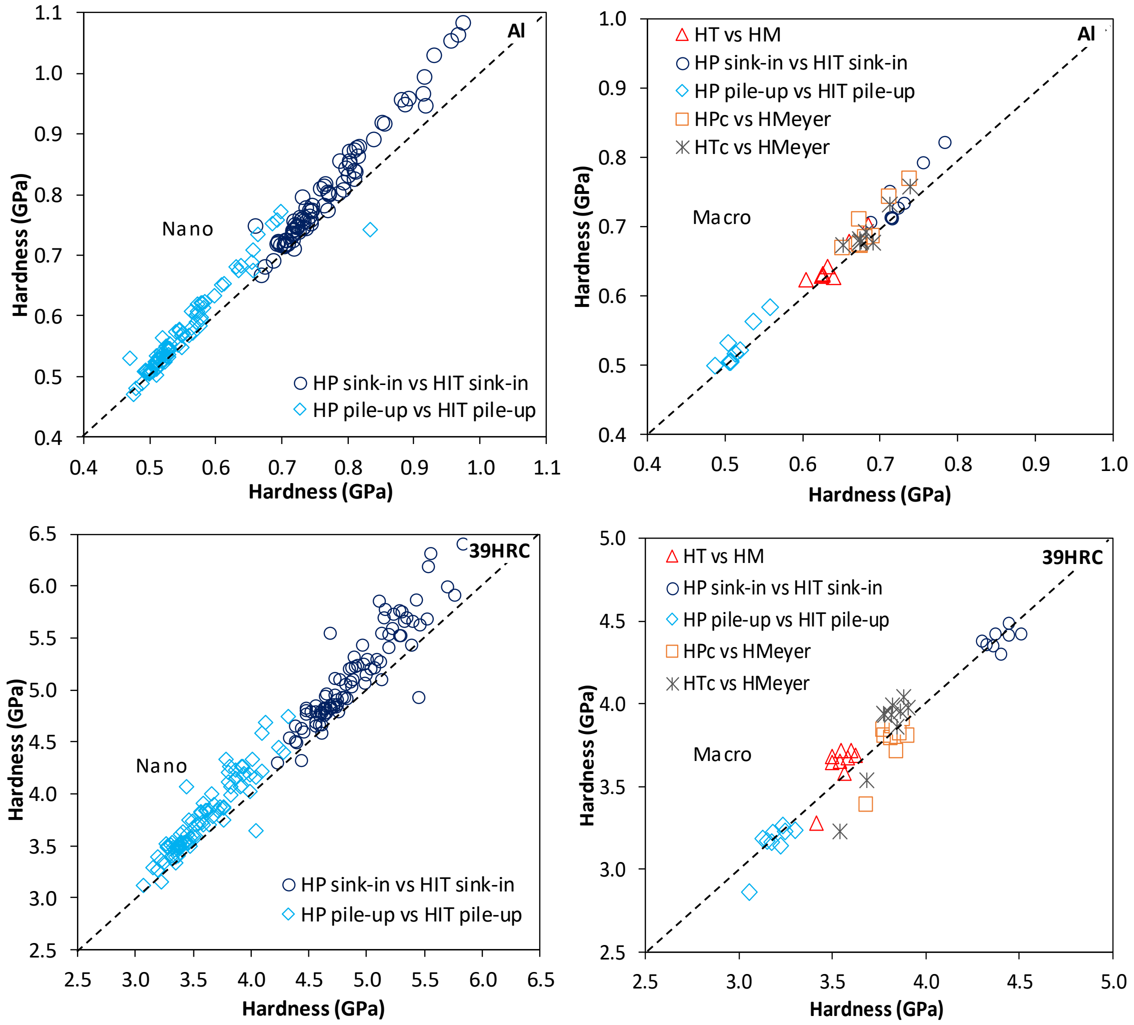

Fig. IV.28. Comparison between hardness numbers obtained by the work of indentation with *HM, HIT, HMeyer*, at the nano and macro scale for the samples Al and 39HRC. The values represented are the average obtained at each applied load at the macro scale.

According to the previous relation the approximation $W_{\mathrm{P}}/W_{\mathrm{T}} = h_{\mathrm{f}}/h_{\mathrm{max}}$ is not always valid because depends on the value that takes the ratio $h_{\mathrm{f}}/h_{\mathrm{max}}$, for higher ratios the value is close to one, then *HP*c and *HT*c are similar. As we mentioned Eq. IV.27 is obtained by finite element simulation that could differ from the actual experimental conditions. Our experimental results give a different relation, nevertheless it is approximated, which suggest that due to the important sources of errors related to the indentation tests dissimilar interpretations of the data could be found, the ratio W_P/W_T is close to the value $h_{\mathrm{f}}/h_{\mathrm{max}}$ in all the materials considering the average values for all the range of loads, consequently *HP*c and *HT*c are also similar. The example of the calculation is presented in Fig. IV.29.

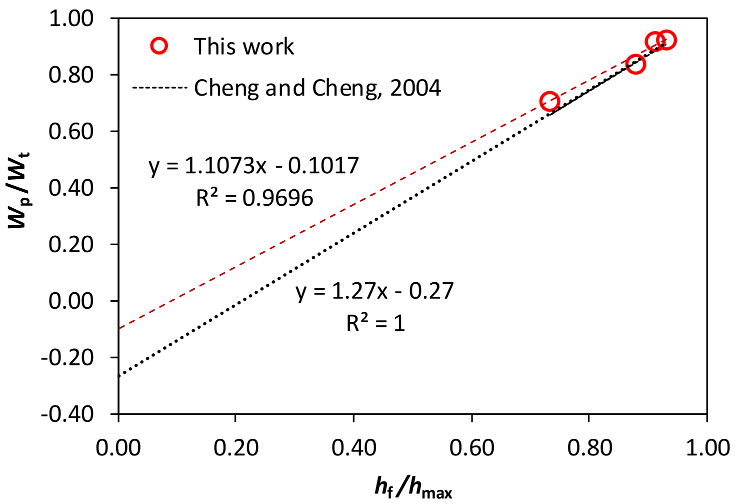

Fig. IV.29. Variation of the ratios W_p/Wt with h_f/h_{max} obtained from the average values of each ratio in the four studied materials.

Fig. IV.30 shows the relation of the hardness numbers for the sample SS316L, opposite to the results in the other samples any hardness number obtained by the work of indentation is equivalent to the typical reported values. Chicot et al. [195] found in a stainless-steel sample that the Meyer hardness was alike to HP_c and HT_c. Nevertheless, since the same trend was found at the nano and macro scales we do not think that the dissimilarities between the different values are mainly attributed to experimental and calculation errors, even that the results are always associated to an important degree of uncertainty. This behavior is unexpected because the material shows similar ratios W_p/W_t and h_f/h_{max} to the aluminum sample, however as we mentioned previously the deformation mechanisms in stainless steel are complex. The response of this material should be studied in detail to elucidate the possible explanations. It is worth mentioning that the elastic modulus results by work of indentation show differences as well from the other samples.

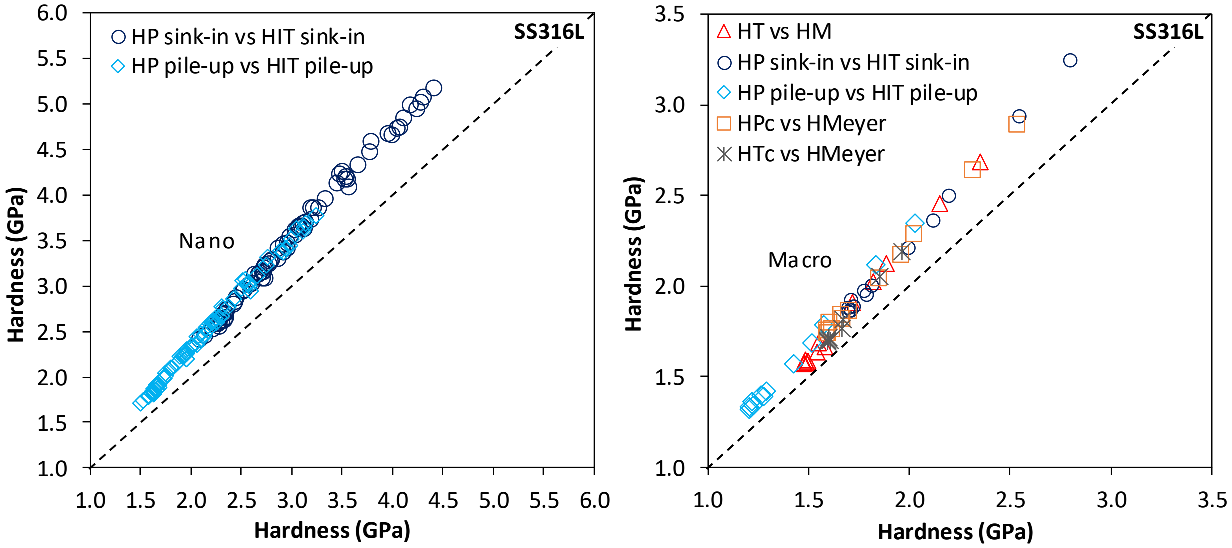

Fig. IV.30. Comparison between hardness numbers obtained by the work of indentation with *HM*, *HIT*, *HMeyer*, at the nano and macro scales for the sample SS316L. The values represented are the average obtained at each applied load.

In summary, hardness results exhibit dependency on the applied load and consequently with the scale of measurement. The interpretation of results is not obvious because this property represents a more complex material response that depends on different parameters as simple as the sample preparation and as complex as the implications of the geometrically necessary dislocations or deformation mechanisms. The dispersion of the data is important especially for the microindenter. Despite the inconvenient, it is possible to estimate the macro hardness at the different scales, that usually lead to similar values and allows to obtain a general material response, taking into consideration that errors will be about 10%.

IV.2.5. Round-robin comparison with previous studies in the literature

The round robin methodology is an interlaboratory test comparison performed independently several times. In instrumented indentation testing, this kind of study had been performed by several authors [34,169,182,196–198] in order to elucidate the discrepancies among the experimental data and analyze the tests performed with instruments of many commercial brands.

In this study, we compared the results of the three used instruments in order to obtain the similarities among them regarding the dispersion of the elastic modulus and hardness. We select some round robin studies found in the literature to be compared with our experimental results, first we compared with the elastic modulus results, they are summarized in Fig. IV.31.

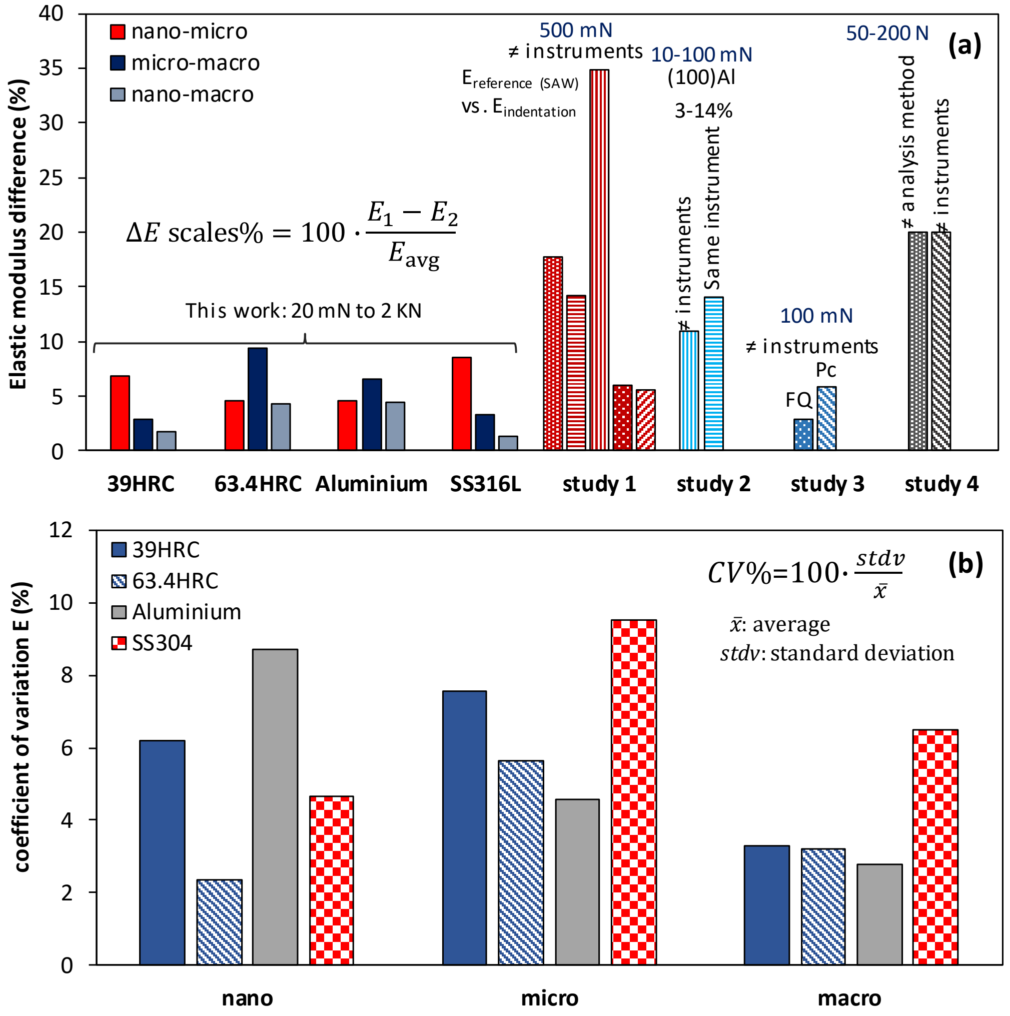

Fig. IV.31. a) Variation of elastic modulus between scales and comparison with previous Round-Robin studies [169,196,197]. b) Variation of elastic modulus for each material with the three instruments. The variation coefficient is computed considering the standard deviation and the average value of results.

We calculate the coefficients of variation between scales and for the same load range by the next relations (shown in Fig. IV.31):

$$\Delta E \text{ scales}\% = 100 \cdot \frac{E_1 - E_2}{E_{\text{avg}}} \tag{IV.28}$$

$$CV\% = 100 \cdot \frac{stdv}{\bar{x}} \tag{IV.29}$$

It is worth mentioning that the coefficient of variation is not equal to the uncertainties of the measurements, because it only represents the stochastic part of the uncertainty [197].

Chudoba and Griepentrog [196] (study 1) did the comparison between three instruments Fisherscope H100, Nanoindenter XP and UMIS-2000 of data performed in different German laboratories. The data were analyzed with the software of each instrument and an additional software (ASMEC Indent Analyser). All the tests were performed at the same load, 500 mN, over ten materials, ceramics, glasses and metals. The differences observed for the elastic modulus oscillate between 7% to 35% in comparison with the values measured by surface acoustic waves (SAW) or from the literature. The analysis using the software Indent Analyser decrease the gap with the data of the Nanoindenter XP, but it is increased for the data of the Fischerscope.

The study 2 [197] shows the results found by twelve international participants. They compare the measures of the elastic modulus between instruments, the maximum difference among them is called reproducibility coefficient, and it was 9% for a load range between 1 to 5 mN (where only six laboratories participated), and 11% for a load range of 10 to 100 mN. The dispersion obtained by each participant called repeatability coefficient, vary between 1 to 17% according to the testing load, the coefficients are higher at smaller loads.

The study 3 [169] compares the results obtained in six instruments, Hysitron UBI, Hysitron Triboscope, Micro Materials, Agilent G200, UNAT-ASMEC, and MTS XP. The procedures for the calibration of the frame compliance and indenter area function were the same. The data were analyzed with the software ASMEC Indent Analyser. The tests were performed in two materials, fused silica (FQ) and polycarbonate (Pc), that were tested in the load range from 2 to 100 mN with three indenters, cube corner, Berkovich and spherical. The average values of the elastic modulus for Berkovich indenter are presented in Fig. IV.31, the differences between the machines change according to the material, 3% for FQ and 6% for Pc, greater differences are found for the spherical indenter.

Dissimilarities in the estimation of the mechanical properties could be given only by the treatment of the data, Cagliero *et al.* [41] (study 4) found a variation of 20% over the elastic modulus according to the method used to obtain the contact stiffness from the unloading curve. They applied three methods, the power law of Oliver and Pharr, a method developed by them based in a sinus function and the linear extrapolation; the values were overestimated using the power law method. They also did a comparison between two instruments, Zwick ZHU2.5/Z2.5 and OMAG SR HU09 at the macro scale in stainless steel samples between 50-200 N; the results were not comparable between the two instruments, leading to differences greater than 20% over the elastic modulus, they were overestimated in the Zwick machine.

Concerning the hardness results, we show that the coefficient of variation at the macro scale for Martens and instrumented hardnesses are constants, it is meaningless to compare these values quantitatively with the average values at the nano and micro scales due to the variation of hardness with the indentation load (ISE). In addition, we present some studies that established comparisons under different conditions described below (Fig. IV.32).

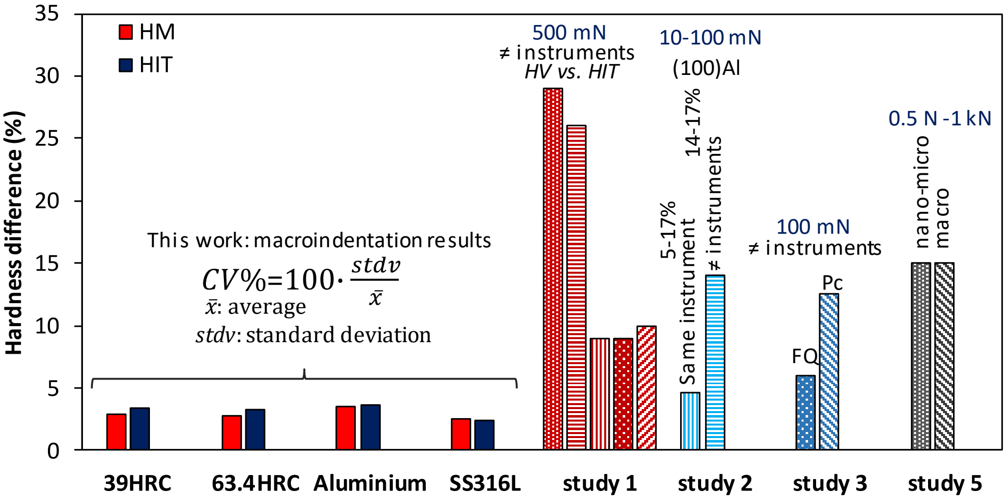

Fig. IV.32. Variation of hardness at the macro scale and comparison with previous Round-Robin studies [34,169,196,197]. The variation coefficient is computed considering the standard deviation and the average value of results.

Chudoba [196] (study 1) established differences between the Vickers hardness and the instrumented hardness they found differences between 10-30% according to the instrument.

Martens hardness was evaluated in study 2 [197], they found an increase of hardness at the low load range. The results at higher loads presented a better repeatability and reproducibility, the repeatability coefficient was 4.6% at this range and it increases to 17.4% for the low force range. The reproducibility coefficient was 13.7% for high load range and 16.9% for the low load range.

Griepentrog *et al.* [34] (study 5) established comparisons between Martens hardness measurements in a non-magnetic steel (X8 CrMnN18-18) at load ranging from 0.5 to 1000 N. They used four instruments Nano Indenter XP, Fischerscope H100, Zwick Z005 and a prototype instrument. At the same scale of measurement in the range nano-micro the maximum difference between the instruments is about 15%, then at the macro scale hardness decrease getting a constant and smaller value, at this scale the difference between the instruments is also ~15%.

We can consider that the results regarding the elastic modulus are reproducible at the different scales of measurement in comparison with the round robin studies found in the literature. The relative estimated differences between nano-micro, micro-macro and nano-macro are approximately 10% or inferior among the scales for loads from 10 mN up to 2 kN, a greater load range that the studied in the literature and using industrial metallic materials.

The variation coefficients were estimated for each material in the three instruments, the estimates are inferior to 10%. The most important variations were obtained with the microindenter, due to the functioning of the instrument. The standard ISO 14577 indicates that the error percentage should be inferior to 5% at the same testing load, whereas we considered the entire range of loads for each instrument. Consequently, the results are considered as good estimations of the material response because the indentation test is affected by numerous sources of uncertainties [41,125].

Hardness results at the macro scale for a range of loads between 5 N to 2 kN exhibit a good reproducibility comparing with the other studies, and the variations respect the 5% stated by the norm.

For both properties, we should always consider that the instrumented indentation testing is affected by an important number of uncertainties sources, as demonstrated by several studies. In order to get reliable results, it is needed to know the system functioning in order to estimate the correct uncertainties related to the measurements.

IV.3. Conclusions

This chapter treated the subject of multiscale indentation in industrial metallic materials to answer to an initial question: do the obtained mechanical properties change with the scale of measurement in indentation? After this study, we got the following general concluding remarks:

- The dimensionless load-displacement curves showed that the different instruments lead to similar responses of the unloading curves, the differences among the scales are similar to those at the same scale of load. In addition, this dimensionless representation allows to classify the materials according to its ratio E/H using the unloading curves, which suggests that this curve contents information about the elastic and plastic behavior of the material.
- Frame compliance is a determinant parameter for the correct calculation of the elastic modulus.
- The hypothesis of constant elastic modulus was corroborated at the three scales, without evidence of damaging in the studied materials. Discrepancies among scales are principally related to the instruments and not to the material response. The microstructure was not a critical parameter for the overall determination of the elastic modulus. Multicyclic and CSM tests give a similar response to the classic

tests. The work of indentation generally leads to suitable results and the method adopted for the calculation of the contact depth with pile-up lead to comparable results with the reference values.

- Hardness results exhibit dependency on the applied load and consequently with the scale of measurement. The dispersion of the data is important especially for multicyclic tests. Its interpretation is difficult due to the fact that the value is sensitive to several parameters.
- The instrumented indentation testing is affected by an important number of uncertainties sources. In order to get reliable results, it is needed to know the system functioning in order to estimate the correct uncertainties related to the measurements, and correlate it with the dispersion of the results.

The analysis through multiscale indentation obtained at three different instruments, resulted to be suitable for material characterization. Especial attention should be given to the calibration of the instruments to avoid such kind of errors. The procedure for the calculation of properties should be similar among the scales. We validated the methodologies in each instrument in order to reduce the errors during calculation. These general procedures will be applied in the study of heterogeneous materials.

CHAPTER V

Multiscale indentation in brake pads

V.1 Introduction and theoretical basis

Nowadays, composite or heterogeneous materials (two or more components) are desirable for many applications in the fields of construction, aeronautics, automotive, medicine, etc. Their main mechanical properties are improved for a specific application, and these are different from the properties of each constituent [199,200]. Some common heterogeneous materials are concrete, cement paste, slag, biomaterials, brake pads, carbon fiber, etc.

In heterogeneous materials, the mixed components can react or not chemically; when a chemical reaction is involved, it is difficult to define the volumes and microstructural distribution, their microstructure is complex resulting in an impossibility to separate the phases to be mechanically characterized. The formation of new phases in composite materials comprises porosity, partly reacted matrix, interfacial zones with different chemical and mechanical properties, and particles of the initial raw material [201–203].

Brake pads are typically heterogeneous materials with a complex microstructure. In the railway industry, the braking system has been evolved through the years, looking for the continuous requirements of high speed trains (320 to 360 km/h). The main purpose of an optimum braking system is to increase the dissipated energy and reduce the mass to guarantee the performance and safety at high loading levels [3]. Therefore, commercial materials for these applications could be composed of more than 20 different constituents. Until now, most of the time the manufacture of friction materials is obtained by empirical methods based on trial and error, due to the complexity of the system. Several studies have been done to characterize the mechanical properties of these materials that are essential for modeling their structural behavior in service [2,204,205]. A recent methodology has been developed to mechanically characterize brake pads for railway applications to improve the braking system, based in compression tests and digital image correlation, they found an evolution of the mechanical properties with thermomechanical loading by braking [3]. It is worth noting that the understanding of the system is difficult since many factors interfere in the performance of the braking system, such as the temperature, friction, microstructure, mechanical properties, loading levels, wear, squeal noise, etc.

The knowledge of mechanical properties of brake pads is needed in the estimation of the lifetime of any material, because they are involved in the contact pressure and temperature distribution, the tribological performance or fatigue behavior [1,204]. In the last ten years, instrumented indentation has become a useful technique to characterize the mechanical properties of heterogeneous materials [203,206–208]. Properties can be measured from the nanometric to the macrometric scales according to the material configuration and size of the phases.

The aim of this work is to provide a methodology to characterize a brake pad with a complex microstructure for railway applications in the original state (without wear) by means of instrumented indentation tests at different scales of measurement, from the nano scale by grid indentation technique to the macro scale by multicyclic tests.

In the following paragraphs, some methodologies and theoretical basis are described regarding the application of the instrumented indentation to the study of heterogeneous materials.

Continuum mechanics is based in the spatial homogeneous mechanical response of materials, independent of length scales factors, such as indentation depth, h. The representative volume element (RVE) of a homogeneous mechanical response and characteristic length size, L, must follow the length scale separation condition:

$$d << L << D \tag{V.1}$$

Where d is the size of the largest microstructural heterogeneity in the RVE, and D is the structural dimension of a macroscopically homogeneous material which can be continuously built from the RVE units [203,206].

From self-similarity principle, the indentation solutions are frequently applied to an infinite half-space model. Consequently, the use of the equations developed for instrumented indentation in the study of heterogeneous materials, do not fully apply because the self-similarity principle is violated [35,203,206].

V.1.1. Grid indentation

At the nanometric scale, grid indentation technique has become a very useful method to determine the properties of the phases and of the composite (bulk) material by homogenization methods. It was initially proposed by Constantinides *et al.* [206], then it has been studied by many authors who had achieved the determination of mechanical properties of complex materials as biological tissues, concrete, biphasic coatings, matrix-aggregates systems [5,203,207–211]. The technique provides, with some restrictions, qualitative and quantitative information about the morphology and properties of each phase.

The basis of the grid indentation technique is to perform a matrix of numerous (*N*) tests in a large area to detect the heterogeneity of the sample; then, a statistical analysis of a large data is performed by the evaluation of the histograms, followed by deconvolution techniques or mixture of Gaussian laws to provide the volumetric proportions and the space distribution of phases with their corresponding properties. The micromechanical analysis obtained at this small scale, holds the scaling-up of the properties to a higher scale by classical analytical micromechanics or numerical approaches [203,206,210].

To determine the mechanical properties of a biphasic composite material, two main cases are described below regarding the microstructural heterogeneities [206,207], the schematic representation is presented in Fig. V.1.

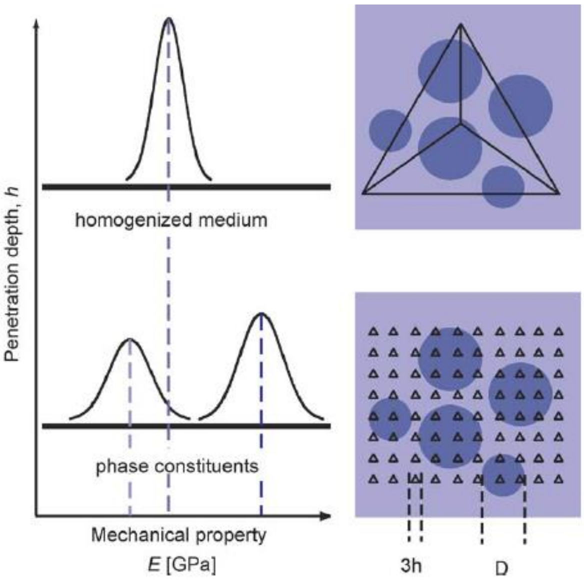

Fig. V.1. Schematic representation of grid indentation for heterogeneous materials. Top: large indentation depths $h >> D$, to obtain the properties of the homogenized medium. Bottom: low penetration depth $h << D$, to identify the intrinsic properties of each constituent by a multimodal distribution [206].

Case 1. Phase properties $h << D$, $h/D \rightarrow 0$

The penetration depth, *h*, is much smaller than the characteristic size of the phases, *D*, *e.g.* particle size. Thus, the microstructural length scales do not interfere significantly with the indentation response, providing the intrinsic properties of each phase. If $h/D \rightarrow 0$ the problem respects the self-similarity condition, being h the single length scale in the infinite half-space, then the behavior is representative of the elasticity and strength of the phase of size D [203,206,207].

For this case the grid spacing, l_{grid}, should be larger than the size of the indentation impression and much larger that the characteristic size of the two phases, to have the same probability of encountering the phase 1 or phase 2 on the indented area without statistical bias [206,207].

The selection of a critical depth, h_{crit}, below which the properties of a single phase can be identified without the influence of the other phase, is extremely important to obtain reliable results. Typically, the indentation depth for the case $h \ll D$ can be approximated to 1/10 ($h/D < 0.1$) of the characteristic length size D (rule of Bückle) [212] to obtain hardness values without influence of other phases [206,207]. Likewise, this rule is generally valid in coated systems where $h < 0.1t$, being t the coating thickness. Commonly, coated systems (thin films on a substrate) are compared with heterogeneous materials, which is useful to make some approximations about their behavior, *i.e.* in a coated system the effect of the substrate is negligible if the mismatch ratio between the elastic modulus of the coating (E_f) and substrate (E_s) is $E_f/E_s \in [0.5, 2]$ for $h < 0.1t$ [206,213]. Special attention should be taken when the phases present an important difference between their properties and the indentation response affected by the microstructure.

Durst *et al.* [209] studied three configurations of heterogeneous systems (particle-matrix, fiber-matrix and film-substrate) by finite element simulations. They concluded that thin film configuration is the most critical because it yields to severe restrictions on the indentation depth, consequently the solutions for coated system could be conservative regarding its application in composite materials [206]. For a particle-matrix system if the contact radius $a < 0.7D$ (soft/hard configuration), the hardness of a phase is properly measured [207]. Randall *et al.* [207] based on the results of Durst *et al.* [209] proposed that h_{crit} is almost independent of the shape phase, and rather depends on the characteristic size D. Nevertheless, for elastic modulus these approximations are not valid, since it is a measure of the elastic material response, thus, the volume elastically impacted by the indenter is much larger than the plastic volume. It had been suggested that the limit for penetration depth to compute the elastic modulus without influence of the underneath material could be 1% of the particle size or film thickness [132].

Although grid indentation technique presents some limitations and restrictions, such as: surface roughness, work hardening due to polishing, difficult identification of phases by optical microscopy, grains surrounded by a compliant matrix, etc. Generally, the method works properly in many composite systems such as Ti-TiB [206], naval brass [207], Ti64-10TiC [207], M3 high-speed steel [207], cement paste [203,210], glycosaminoglycan [211], aluminum foams [214].

Case 2. Composite properties, $h >> D$.

Indentation tests performed at a penetration depth much larger than the characteristic size of the individual phase, *D,* lead to the estimation of the average response and properties of the composite material. Therefore, the properties are statistically representative of the average properties of the heterogeneous material. The indentation depth that determine the composite properties could be approximated to $h > 2D\cot\theta$ (θ, equivalent cone semi-angle) [206]. Depending on the phase sizes on the composite materials, microindentation or macroindentation tests could be needed to reach penetration depths of the suggested order.

Analysis of the grid indentation results. Deconvolution technique.

The large data obtained by N indentation tests is statistically analyzed; the analysis starts with the generation of the probability density function (PDF) or a cumulative distribution function (CDF) of the obtained mechanical property. The PDF is physically intuitive, since the peaks representing the distinct mechanical properties of each phase can be identified in the histograms. PDF from experimental results is constructed using the total number of indentation test N^{exp}, for N_{bins} of size b, each bin is associated to a frequency of occurrence, f_i^{exp} that is normalized with the total number of measurements as $f_i^{\text{exp}}/N^{\text{exp}}$. Then, the experimental PDF can be described as a set of discrete values [203]:

$$p_i^{\text{exp}} = \frac{f_i^{\text{exp}}}{N^{\text{exp}}}\frac{1}{b}; i = 1, \ldots, N_{\text{bins}} \tag{V.2}$$

For a composite material with M phases, the deconvolution of the data allows the identification of $r = 1, \ldots, M$ individual distributions related to each phase. The distributions of the elastic modulus and hardness values for one phase are assumed as Gaussian distributions, identified respectively by the mean values $\mu_r{}^E, \mu_r{}^H$ and standard deviations $s_r{}^E, s_r{}^H$. Then, the PDF is given by the next relation:

$$p_r(x) = \frac{1}{\sqrt{2\pi s_r{}^2}} \exp\frac{-(x-\mu_r)^2}{2s_r{}^2} \tag{V.3}$$

The mean value and standard deviation, μ_r, s_r, of the r-th phase are computed from n_r values, by the following expressions:

$$\mu_r = \frac{1}{n_r}\sum_{k=1}^{n_r} x_k \; ; \; {s_r}^2 = \frac{1}{n_r - 1}\sum_{k=1}^{n_r}(x_k - \mu_r)^2 \tag{V.4}$$

where x is the mechanical property (E, H). The overall PDF for the M phases is described by:

$$C(x) = \sum_{r=1}^{M} f_r p_r(x) \tag{V.5}$$

where f_r is the volume fraction of a phase and the sum of the volume fractions of all the phases is equal to 1, defined as:

$$f_r = \frac{n_r}{N^{\text{exp}}} \tag{V.6}$$

Therefore, the individual distributions can be found by minimizing the next error function:

$$\min \sum_{i=1}^{N^{\text{bins}}} [({P_i}^{\text{exp}} - C(x_i)){P_i}^{\text{exp}}]^2 \tag{V.7}$$

The quadratic deviations among the experimental and theoretical PDF are computed in a set of discrete points. The function is weighted given emphasis to the measurements with higher occurrence. On the other hand, the Gaussian mixture model also provides a solution for the estimation of the phase properties and proportions, the principle is similar to the deconvolution algorithm; the mean, the variance and the amplitude of each Gaussian distribution is determined, then these parameters are optimized according to the maximum likelihood a criterion to the searched distribution. Frequently, the procedure is performed by the iterations of the expectation maximization (EM) algorithm [211,215].

V.2. Material and experimental procedure

V.2.1. Microstructural characterization of brake pad

Brake pads used in this study were obtained industrially, the volume fractions and particle sizes of the compounds are given in Table V.1, as well the references values of the hardness and elastic modulus from the literature of each phase. The material is constituted of an iron-copper matrix with embedded particles of graphite and ceramics. The composite material is obtained by mixing of the powders, followed by cold pressing and finally, sintering at 1100 °C during 8 hours. The schematic representation of the fabrication procedure is shown in Fig. V.2.

Table V.1. Composition of brake pad material *f* (volume fraction), particles sizes, elastic modulus (E_{ref}) and hardness (H_{ref}) of each phase.

Material	*f*	Particle size (µm)	E_{ref} (GPa)	H_{ref} (GPa)
Copper (Cu)	0.139	<100	95-120 [139]	0.3-1 [139]
Iron (Fe)	0.239	<220	190-210 [139]	0.5-6 [139]
Tin (Sn)	0.020	0-60	43[216]	---
MnS_2	0.028	0-20	---	---
Graphite 1	0.161	50-600	4-17 [217]	
Graphite 2	0.299	400-1100	4-17 [217]	
$ZrSiO_4$	0.084	80-320	160-399 [218–222]	10-20 [219,221–223]
SiC	0.030	50-260	300-430 [224–226]	12-35 [224,225]

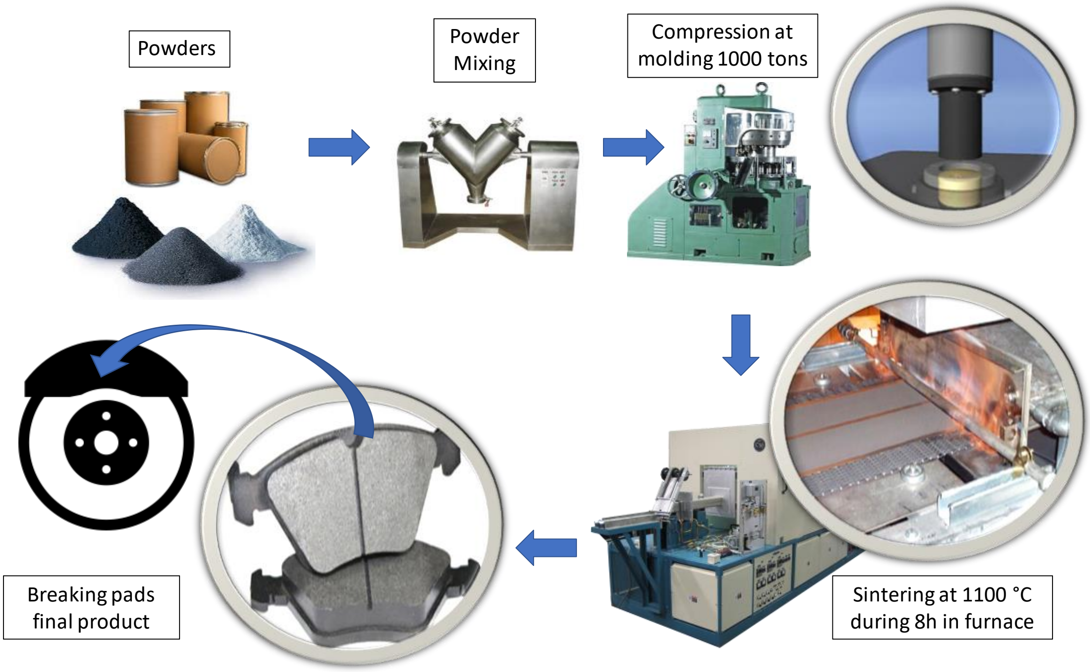

Fig. V.2. Manufacturing procedure of brake pads.

Fig. V.3 shows the scanning electron microscopy (SEM) micrographs of the material surface and the cross-section, exhibiting the heterogeneity of the brake pad, the different sizes of the embedding particles, and porosity mainly in graphite particles and between graphite and ceramics. A tomographic study in the material revealed the alignment of the graphite phase which decreases the thermal diffusivity and conductivity in the loading direction, indicating the anisotropy of the material [227].

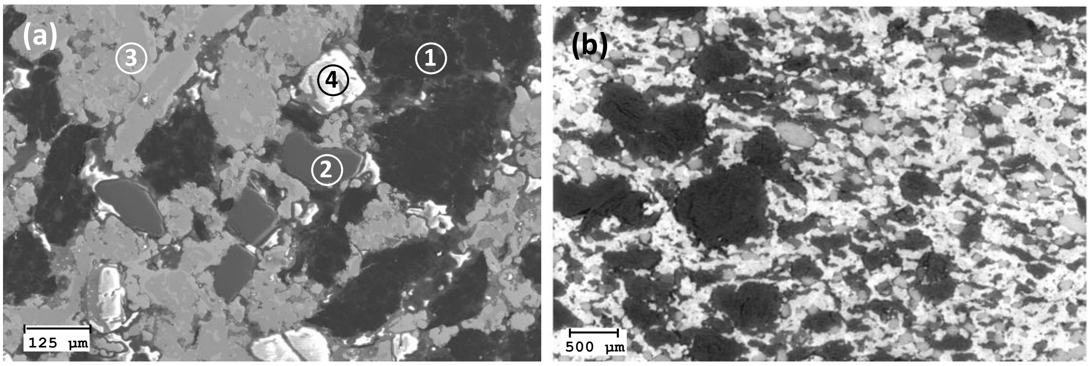

Fig. V.3. Microstructural characterization of brake pads by SEM, (a) top surface after polishing, identifying the main constituents, (b) cross-section of the material after polishing. Where: ① graphite, ② SiC, ③ metallic matrix, and ④ $ZrSiO_4$.

During the fabrication process at 1100 °C for 8 h, the diffusion of carbon in γ-Fe surrounded by graphite is possible. The diffusion profile theoretically computed by the second Fick's law, is presented in Fig. V.4. The concentration at the surface is assumed as the maximum solubility of C in γ-Fe at 1100 °C (1.9 wt.%) during the fabrication process. At small distances, less than 500 µm because the phases are smaller than this size, the diffusion procedure theoretically involves the formation of perlite and pro-eutectoid cementite in some regions of the material [228], an example of these phases in the material microstructure is presented in Fig. V.5. The detailed figure obtained by SEM (right), clearly shows the formation of perlite.

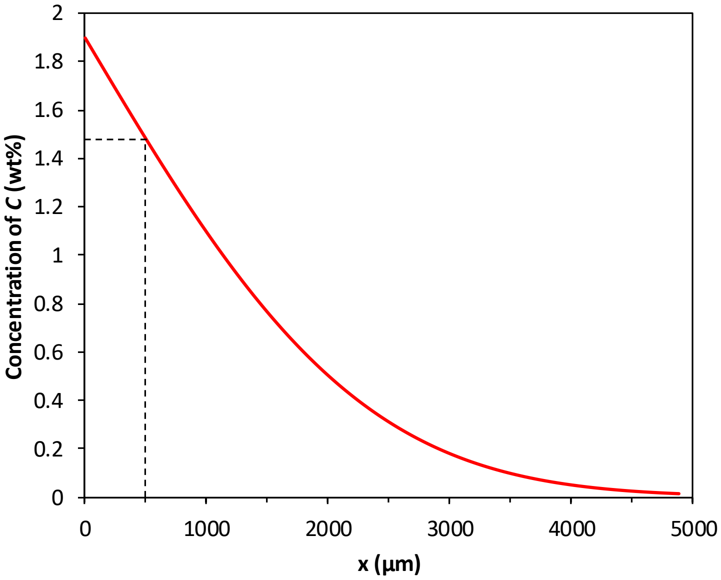

Fig. V.4. Theoretical diffusion profile for Carbon in γ-Fe, assuming the concentration in the surface as the maximum solubility of Carbon in γ-Fe at 1100 °C during 8 hours.

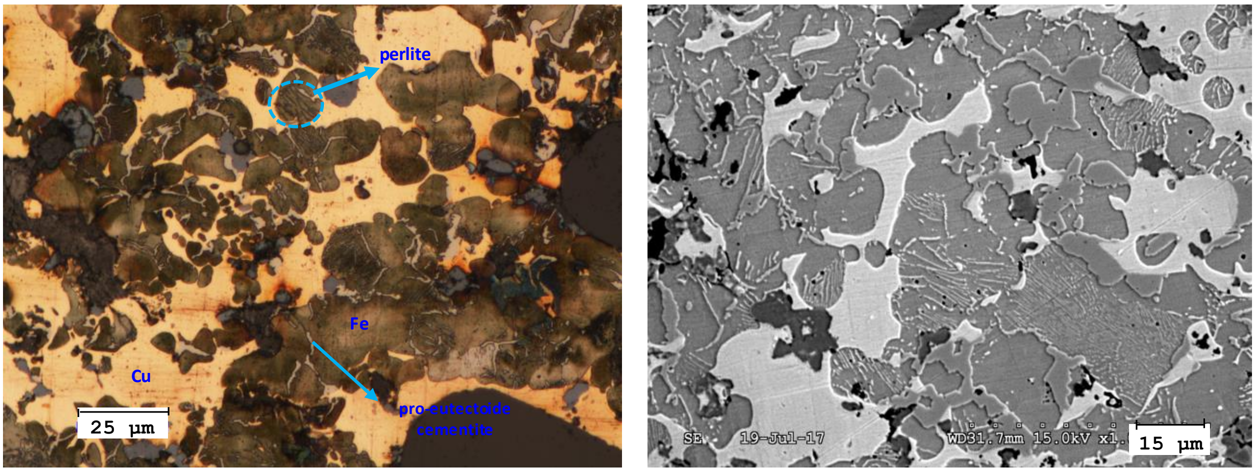

Fig. V.5. Microstructure of brake pad after chemical etching with nital 2%. Left: optical microscopy. Right: detail of the formation of perlite by SEM.

The interaction of the phases is complex during the fabrication process, different events may happen, such as melting of copper at 1084 °C, this temperature decreases with the addition of other elements like Sn (present in the formulation); the Sn can form an intermetallic compound with Cu (Cu_3Sn) [229,230]. The addition of copper to the system Fe-Cu-C could decrease the activity of carbon in the austenite phase, highlighting that solubility of carbon in the copper phase is negligible [231]. The microstructure of the Fe-Cu matrix in the brake pad would be varied regarding the interaction with the other phases, the binary system Fe-Cu does not show intermetallic compounds [231,232].

The energy dispersive X-ray spectroscopy (EDX) analysis in different regions revealed that Cu phase exhibits a clear color and Fe a darker one, letting distinguish between both phases. An example of the EDX analysis was performed in an imprint performed in nanoindentation, the image and the corresponding analysis is presented in Fig. V.6.

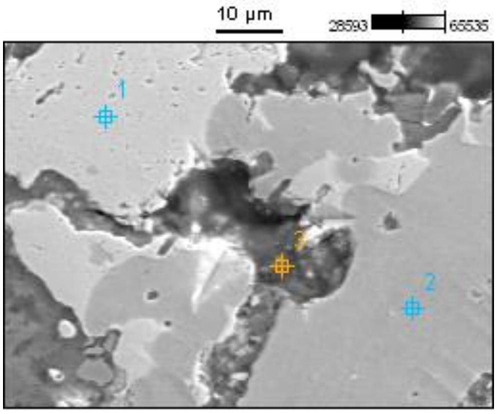

	Weight %							
spot	**C**	**O**	**Si**	**S**	**Mn**	**Fe**	**Cu**	**Sn**
1		2.9			0.3	1.8	85.0	10.0
2			0.3			99.3	0.4	
3	8.7	2.4	23.8	1.1	6.0	12.8	5.2	

Fig. V.6. Analysis EDX in an imprint obtained by nanoindentation, to reveal the differences between the phases of the matrix, accompanied of graphite (spot 3).

The Fe phase presented a small percentage of Cu (spot 2), and the Cu phase a slight concentration of Fe (spot 2). Sn was frequently found in the analysis of the Cu phase. Impurities such as Mn and Si were identified as well.

The spot 3 in Fig. V.6 corresponds to the graphite phase, it is difficult to correctly identify and quantify the C element through the EDX analysis due to its low photon energy [233], nevertheless we found higher content of C than in other spots. Fe and Cu elements are identified in the graphite phase, due to the manufacturing process, during the mechanical mixing and compression the smaller particles would be easily mixed getting trapped during compression; and through the polishing procedure where the harder materials being removed could remain embedded in the very soft graphite.

The ceramic phases SiC and $ZrSiO_4$ are not modified by the fabrication process that was verified by EDX analysis. The initial particles of these ceramics are visible in the microstructure of the material, because their melting point and sintering temperature are higher than 1100 °C [222,225,234,235]. On the contrary, the compound MnS_2 is decomposed in MnS and S upon heating about 400 °C [236,237], nevertheless the phase MnS would endure in the microstructure after the fabrication of the brake pad since its melting point is 1600 °C [31].

In conclusion, the brake pad material has a very heterogeneous microstructure, which impacts in its mechanical, tribological and thermal behavior, and certainly in the mechanical response by indentation tests.

V.2.2 Instrumented indentation tests

The brake pad was studied by multiscale indentation at the nano and macro scales. To perform the indentation tests the samples were cut by water jet to the dimensions of 20 x 20 x 22 mm. Subsequently, a chemical-mechanical polishing was performed, in a first stage with SiC papers (grades 80 to 4000), then a final step with suspension of colloidal silica OP-U, using a disc MD-Chem, both from Struers©.

At the nanometric scale, the grid nanoindentation technique was performed by the MTS Nanoindenter XP, using the continuous stiffness measurement mode up to a maximum penetration depth of 2500 nm. A Berkovich indenter was used for the tests, the calibration of its function area was performed on fused silica [48]. The test parameters were: strain rate 0.05 s^{-1}; frequency 45 Hz; harmonic displacement 2 nm; and surface approach sensitivity 20% for a more sensitive surface detection. The grid configuration was 10 x 10 indents, with 75 µm space between indents, which is equivalent to 30 times the indentation depth to avoid the effects of the side imprints and to reunite enough information to be representative of the material behavior considering the heterogeneity of this material (Fig. V.3). Fourteen grid indentation tests were done in the same conditions, leading to 1400 indentation tests on the sample covering an approximate total area of 7.3 mm^2 considering the interspaces between grids, that is approximately 10 times larger than the maximum particle size, emphasizing that just some particles of graphite have this size.

Macroindentation tests were performed on the universal hardness tester Zwick ZHU 2.5. Multicyclic tests were done in the material top surface (normal to the compression direction) and cross-section to evaluate the properties with the penetration depth using the following conditions: 6 cycles from 10 N to 260 N with an increasing step of 50 N; dwell time at maximum load ($P_{\max}$), 30 s; unload up to 2 N; distance between indents equivalent to 30 times the maximum penetration depth; and loading and unloading rates 520 N/min. Due to limitations in the instrument software the same load and unload rates are used for all the cycles. Vickers diamond and spherical indenters were used for these tests. The spherical indenter has a diameter of 10 mm and is made of WC (E_i = 600 GPa, ν_i = 0.24). In addition, multicycle tests up to 1450 N were performed with the spherical indenter with similar conditions of the previous tests: 8 cycles from 50 N to 1450 N with an increasing step of 200 N; loading and unloading rates 2900 N/min. The spherical indenter was only used for characterizing the top surface material.

Table V.2 summarizes the test conditions of multiscale indentation tests. The optimum dwell time for the tests in macroindentation was fixed at 30 s according to the results obtained by creep indentation tests at the macro scale. An example is presented in Fig. V.7. The high unloading rate also avoids displacement from being altered by creep effects.

Table V.2. Test conditions of multiscale indentation in brake pads.

Conditions	Type of indenter	Type of test	Range of load
Nano surface	Berkovich	CSM (grid indentation)	up to 2500 nm
Macro surface	Vickers	Multicyclic	10-260 N (6 cycles)
	spherical (d= 10 mm)	Multicyclic	10-260 N, 50-1450 N (8 cycles)
Macro cross section	Vickers	Multicyclic	10-260 N (6 cycles)

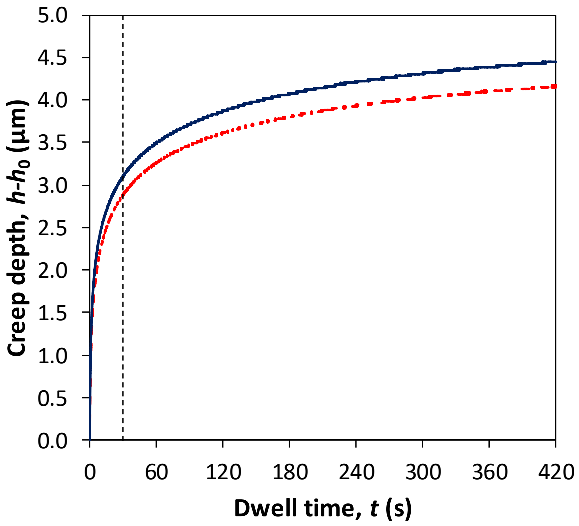

Fig. V.7. Example of creep tests: penetration depth as a function of time 150 N at maximum load, the curves represent two tests made with the same conditions at different places.

Elastic modulus and hardness for Vickers indentation were computed through the classical equations presented in Chapter II. The predominant deformation mode was considered as sink-in, due to the lubrication properties of the graphite phase. The Poisson's ratio for the computation of the elastic modulus of the brake pad material was 0.18, due to previous studies in a similar material [238], nevertheless a Poisson's ratio ranging between 0.05-0.4 would lead a maximum error of 10% over the elastic modulus [206].

For spherical indentation, we used the equations listed below, which are similar to the relations used for sharp indentation, with small differences regarding the contact area:

$$a = \sqrt{2R_i h_c - {h_c}^2} \tag{V.8}$$

$$h_c = h_{max} - \frac{3}{4} P \frac{dh}{dP} \tag{V.9}$$

$$E_R = \frac{dP}{dh}\frac{\sqrt{\pi}}{2\gamma\sqrt{A}} = S\frac{\sqrt{\pi}}{2\gamma\sqrt{A}};\ A = \pi a^2 \tag{V.10}$$

$$p_m = H_{Meyer} = \frac{4P}{\pi d^2} \tag{V.11}$$

$$P = \frac{4}{3} E_R R^{1/2} h^{3/2} \tag{V.12}$$

where a is the radius of the circle of contact, h_c the contact depth, R_i radius of the indenter, d the diameter of the circle at full load, P is the load, p_m the mean preassure and often called Meyer hardness, dP/dh stiffness. Eq. V.12 gives the relation between load and penetration depth for elastic contact (Hertz relation) by spherical indentation.

The stiffness S was computed for macroindentation results by fitting of the unloading curve using the inverted method described in Chapter III.

V.3 Results and discussion

V.3.1 Grid indentation by nanoindentation tests

The nanoindentation tests revealed the important heterogeneity of the material, even at small penetration depths because the properties change with the increasing loading. Some examples of the load-displacement curves obtained at different locations are presented in Fig. V.8.

The evolution of the properties with penetration depth is related to the diverse arrangements that encounters the indenter during the penetration in the material, *e.g.* a hard particle over a soft material and/or porosity, or conversely a soft material over a harder one. At the material surface, we can observe and identify the different types of constituents; we perceive a 2D representation of a three-dimensional complex microstructure as revealed by the cross-section image of the material (Fig. V.3). Consequently, the average properties up to 2500 nm are meaningless since they do not represent the actual properties of the material but rather a composite local response that is not characteristic of the global material behavior.

Despite the difficulty of analyzing the properties evolution with penetration depth, we performed a statistical analysis with the obtained data due to the large number of tests (1400 tests). For this analysis, the properties were extracted at a shallow penetration depth, 250 nm, to do an approximation of the intrinsic properties of each phase without the effect of the surrounding material. Nevertheless, the porosity and interfaces effects are unavoidable. This procedure was repeated for all the grids. The statistical analysis was performed considering all the data.

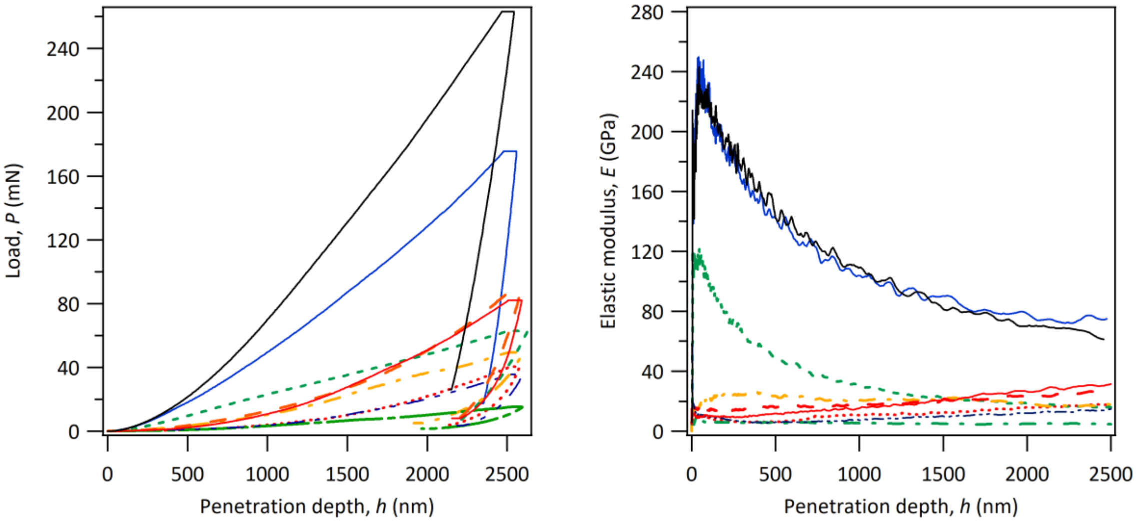

Fig. V.8. Examples of load-displacement curves and elastic modulus as a function of the penetration depth obtained by CSM nanoindentation tests performed on the brake pad**.**

The average surface roughness (Ra) was measured locally (on 10 µm length) for each phase by optical profilometry. Generally, the values of Ra should be no more than 5% of the penetration depth, otherwise the dispersion on the measured properties increases and the number of tests should increase as well [132]. The roughness measurements ranged between 10-20 nm for ceramic, 10-40 nm for metallic matrix, and 30-80 nm for graphite phases. The variation in roughness in these three phases is related to their important difference in hardness, and to the lubricating effect of the graphite phase during polishing. Graphite phase has higher roughness because the particles are crushed and compacted during the polishing process. Nevertheless, the values are acceptable to obtain reasonable results according to the study of Marteau and Bigerelle [239], where they found that indentation results are affected by roughness in the case of wavy surfaces when the wave length is in the same order of magnitude that the imprint size, either much smaller or significantly larger wave length of roughness lead to small scatter in the indentation curves. In general, the imprints at h = 250 nm are smaller than the wave length for the three phases, that would lead to a small scatter in the curves; in addition, the number of tests performed would lead to average values with their dispersion, that probably will be increased due to the porosity and interfaces. Consequently, we supposed that results at 250 nm of penetration are not mainly affected by roughness but rather by the complex microstructure.

To proceed to the analysis of the grid nanoindentation tests, we initially present the mapping of elastic modulus and hardness associated with their microstructure (Fig. V.9) for one grid (10 x 10 indents). The mapping of the mechanical properties is obtained using the raw data (elastic modulus and hardness at h = 250 nm) from the instrument software, each pixel represents a nanoindentation test; then, the data are interpolated (linear interpolation). The interpolation of data allows to numerically increase the mapping resolution by filling-in missing data, making predictions with the existing data, and avoiding pixelation and noise data effects leading to a better approximation of the actual properties of the material [224]. The code to accomplish the previous procedure was built in Matlab language, a detailed description is found in [240].

Fig. V.9 shows the microstructure of the tested surface obtained by optical microscopy *in situ* and the mapping of one grid, displaying the contrast among the hardness and elastic modulus of the phases. The mapping and micrograph were superposed to compare the similitude between them. Only one grid is presented for simplicity; however, the remarks were similar for the other grids. Clearly, one grid is not representative of the global microstructure but the total tested area (~7.3 mm^2) does it.

Fig. V.9 shows that higher values of hardness and modulus match with the metallic matrix and ceramic particles, and lower values are mostly related to the darkest phase corresponding to graphite (blue regions). Generally, the order of magnitude of the obtained properties agrees with their microstructure according to the values found in the literature (Table V.1); for example, for the orders of magnitude of the elastic modulus are 10^2 GPa for ceramics, 10^1-10^2 GPa for metals, and 10^0-10^1 GPa for graphite.

Hardness represents a better estimation of the material response because the plastic field is smaller than the elastic zone developed during the indentation test, which means that elastic modulus would lead quickly to a composite response. Typically, at penetration depths larger than 10% for hardness and 1% for modulus of a characteristic length (*e.g.* coating thickness, particle size) [26,241–245], the measured properties are considered as a composite material response; these conditions were fulfilled at the selected displacement (250 nm), but certainly it is a roughly estimation for a very complex system. However, in both examples hardness and modulus exhibit a similar response, the harder particles are associated with the higher modulus, which correspond to the metallic matrix and the ceramic particles. Likewise, the access to both mechanical properties allows to differentiate the phases with similar properties, *e.g.* the enclosed imprints pointed as I30 and I50 in Fig. V.9, presented a similar elastic modulus (200 GPa and 227 GPa), and different hardness (6 GPa and 18 GPa), which correspond to the microstructural observations of the metallic matrix (I30) and ceramic phase (I50); thus, the access to both properties lets distinguish between different phases. The elastic modulus in both tests, correspond to the range of theoretical values for iron and $ZrSiO_4$ [218] (Table V.1).

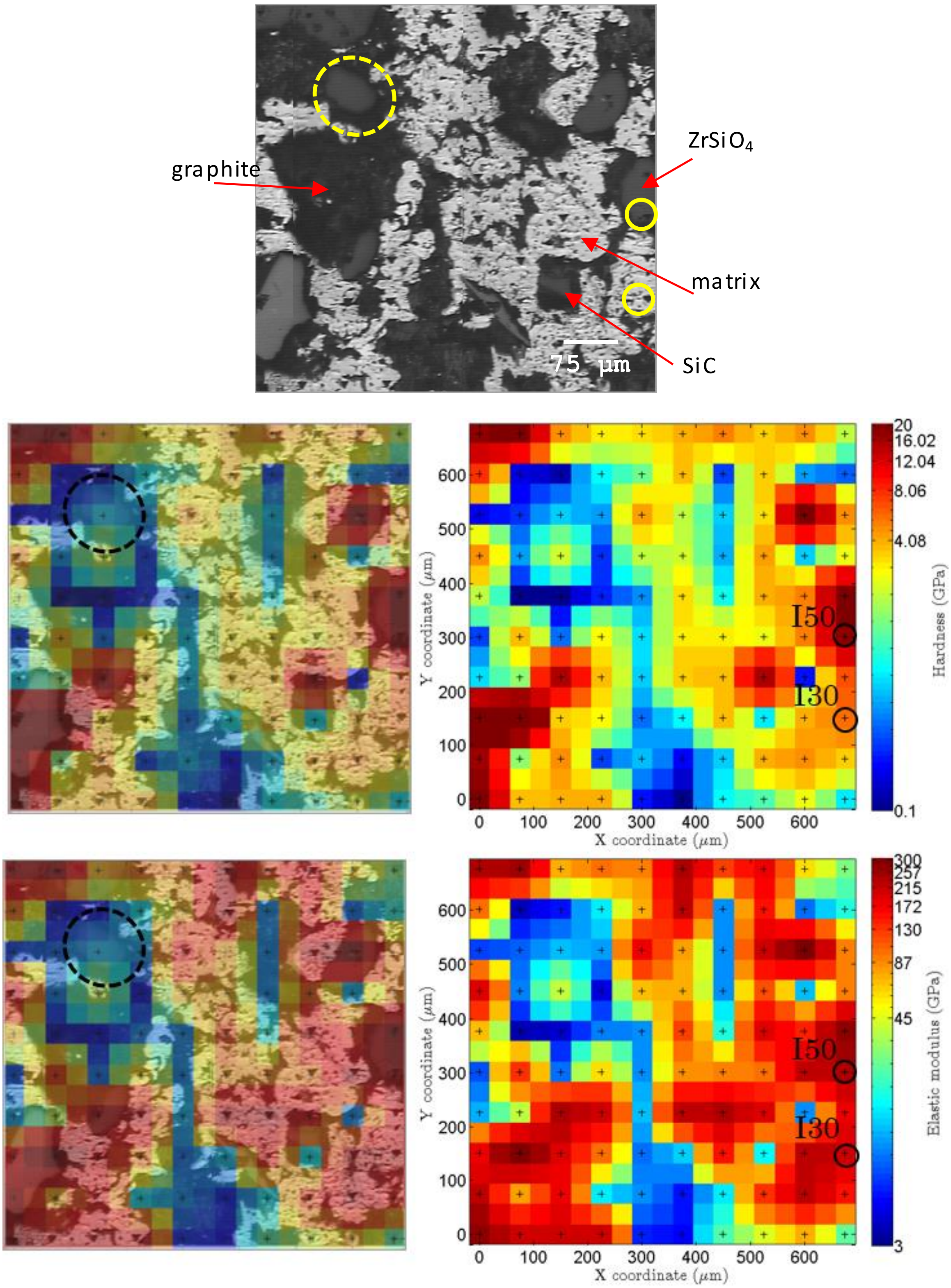

Fig. V.9. Microstructure and mapping of elastic modulus and hardness obtained by nanoindentation grid on brake pad material at 250 nm penetration depth.

Hence, the results obtained at 250 nm of penetration depth could be approximated to the intrinsic properties of each phase. Nevertheless, we shall know that porosity and interfaces effects could modify the estimated properties, typically elastic modulus of a porous material is smaller than its analogous dense [246], similarly the interface effect could lead to a decrease of the mechanical properties with the penetration depth [247].

The enclosed area by a dotted line in Fig. V.9 (microstructure and mapping) shows an erroneous representation of the mechanical properties regarding the microstructure; we can observe a ceramic phase at this place, nonetheless the irregularities of the sample such as the porosity and different of heights between phases conduct to failed tests, leading to missing values. Therefore, to plot the mapping we approximated the missing values to the properties of the surrounded pixels by interpolation, but due to the high heterogeneity of the material, the program cannot always conduct to a correct estimation of the properties, as in this case. For the statistical analysis, we only considered the effectively performed tests.

The distance between indents is strictly related to the characteristic lengths of the material, it should be larger than the size of the indentation imprint and much larger than the characteristic size of two phases to avoid statistical bias [206,207], generally grid indentation technique is performed in materials presenting a microstructure suited to the nanometric scale leading to a space between indents of hundreds of nanometers to some micrometers [203,206,248]. In the brake pad, the phases are in the micrometric and millimetric scales. The difference between the ceramics particles and graphite could reach few hundreds of micrometers, due to the larger size that could have the graphite phase. Consequently, we must have selected a length greater than 1 mm, nevertheless, a length in this order of magnitude would discard lots of information due to the significant size differences between graphite, ceramic and metallic matrix, and the volume occupied by the graphite in the material. Therefore, the selected distance of 75 µm (30 times the indentation depth) is apparently suitable for the grid indentation to store enough information to be representative of the material response.

Statistical analysis of the results obtained by grid indentation

The phases in the studied brake pad exhibit great differences between their mechanical properties, the data of hardness and elastic modulus of approximately 1400 indentation tests (due to the failed tests) were collected and processed together. The histograms of both properties at 250 nm are presented in Fig. V.10.

We used the probability density function to observe the differences between the peaks that theoretically represent each phase in the material. The bin sizes were 0.2 GPa and 3 GPa, for hardness and elastic modulus, respectively. The identification of the individual distributions related to each phase and the estimation of their volume fractions were performed by the deconvolution method [203,206], which allows the identification of the individual distributions related to each phase. The technique assumes that the properties of the phases have an important contrast to be separated; also, the surface distribution of particles is supposed to be representative of the volume distribution.

The deconvolution method described in Eqs. V.2-7 was applied to hardness results, because it should be more meaningful regarding the actual properties of each phase due to the smaller plastic deformation zone [249,250]. As a simplification previously mentioned the phases are separated by the material nature, evidentially this is an approximation, because each phase is composed by different phases, *e.g.* matrix iron-copper.

Heterogeneities, porosity, interfaces and manufacturing process of the brake pad material rise difficult to perform an accurate estimation of the mechanical properties by indentation. However, the histograms of hardness and modulus guide us to some hints to determine the mechanical properties of the individual phases.

In the hardness histogram (Fig. V.10) we can identify three Gaussian distributions that correspond to the principal constituents of the brake pad, graphite, metallic matrix and ceramics. The detailed region of the ceramic phases is presented on the right side of Fig. V.10. The volume fractions are computed assuming that surface and volume distributions are similar, which is a rough approximation due to the complex configuration of phases in the brake pad material. The order of magnitude of average hardness values is coherent with the nature of each phase, $\mu_1 = 0.3$ GPa, $\mu_2 = 2.7$ GPa, and $\mu_3 = 19.6$ GPa, for graphite, metallic matrix and ceramics, respectively. The elevated standard deviations associated to the graphite and metallic matrix distributions indicate that both are an average of different phases that agrees with the microstructural composition, *i.e.* graphite phase is composed by graphite 1 and 2, and metallic matrix is integrated by iron and copper.

The volume fractions computed by the deconvolution method of the hardness data lead to a close approximation of the volume fractions estimated theoretically summarized in Table V.3: 0.48 for graphite phases, 0.49 for metallic matrix and 0.03 for ceramic phase; nevertheless, the obtained differences could be related to diverse issues such as the theoretical density of the metallic matrix and graphite without considering the porosity, the difference between the surface and volume distributions of the phases, the interfaces effects, a non-random distribution of the particles in the material, or a decrease in the hardness values of the ceramic due to porosity.

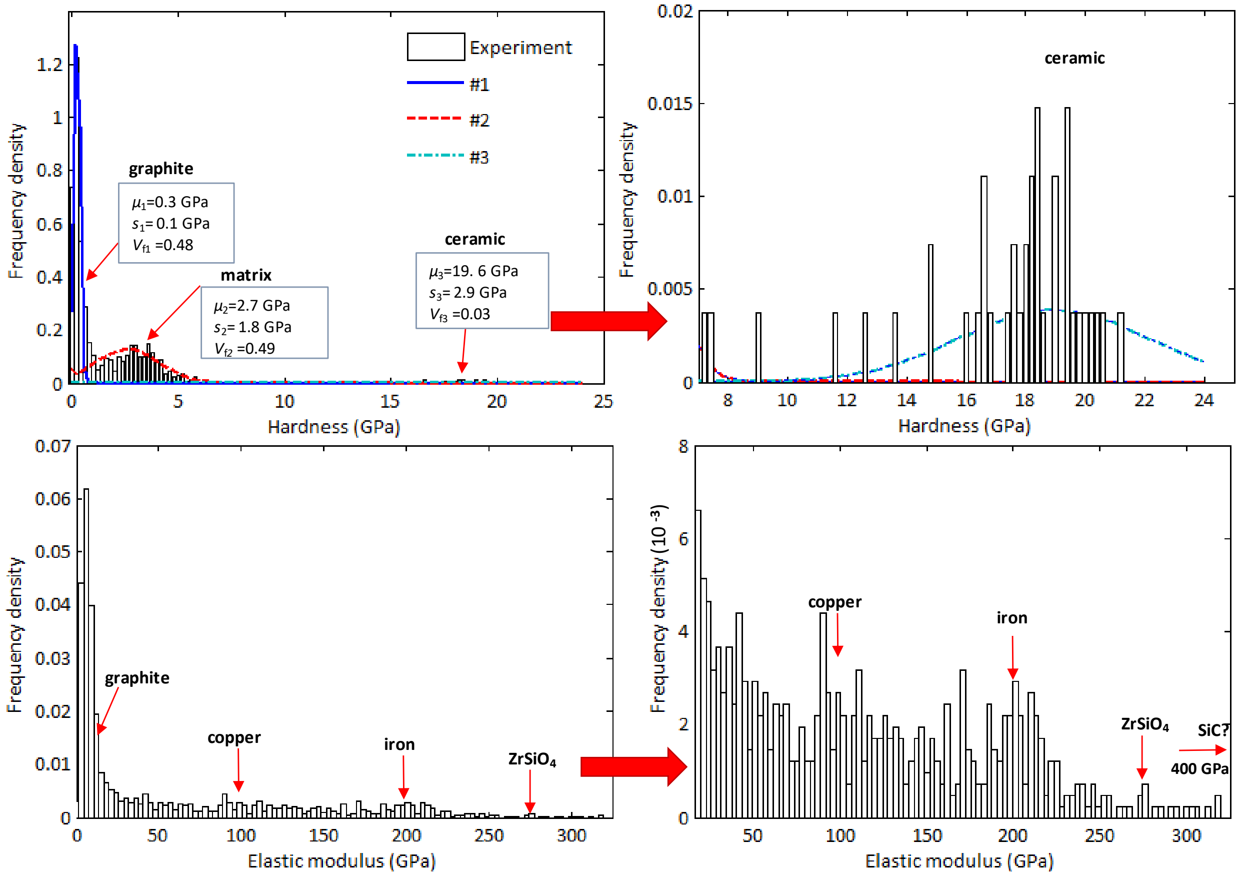

Fig. V.10. Histogram of instrumented hardness with deconvolution results, and histogram of elastic modulus obtained at 250 nm of penetration depth from 1400 grid indentation tests. The bin size to plot the histograms was 0.2 GPa for hardness, and 3 GPa for elastic modulus. The right-side figures show the detailed regions of ceramic and matrix phases. μ_i represents the mean value, s_i is the standard deviation and V_i the volume fraction.

Table V.3. Comparison theoretical volume fractions of the phases and experimental volume fraction obtained from the deconvolution of hardness at 250 nm.

Material		f_{th}	f_{exp}	$\Delta f = \lvert f_{th} - f_{exp} \rvert$
Copper (Cu)	0.139	$\sum_{matrix}$= 0.43	0.49	0.064
Iron (Fe)	0.239			
Tin (Sn)	0.020			
MnS_2	0.030			
Graphite 1	0.161	$\sum_{graphite}$= 0.46	0.48	0.02
Graphite 2	0.299			
$ZrSiO_4$	0.084	$\sum_{ceramic}$= 0.11	0.03	0.084
SiC	0.03			

On the contrary, in the elastic modulus histogram (Fig. V.10) it is difficult to distinguish the properties associated to each phase into Gaussian distributions, except for the graphite that is clearly identified by the first distribution, because its elastic modulus is much smaller comparing to the metallic matrix and ceramics. The theoretical values are indicated in the histogram. Typically grid indentation studies contemplate that the mechanical properties of the phases should be distinguishable to perform an accurate estimation of the intrinsic properties of each phase [206]. The brake pad under study does not totally fulfill this condition regarding the elastic modulus, emphasized in Fig. V.9, *e.g.* the elastic modulus of the $ZrSiO_4$ and iron matrix could lead to similar estimates (~210 GPa). Thus, the elastic response of different phases can be superposed on the histogram, hindering their distinction. Besides, both measurements could be affected by the surrounded phases, being these values not representative of the real properties of the individual phases. Nevertheless, we can predict that values higher than 210 GPa correspond to the ceramic phases, because the matrix is composed principally by iron and copper base alloys, which theoretical elastic modulus vary between 190-210 GPa for iron, and between 95-120 GPa for copper and their alloys, therefore, the elastic modulus should vary between these ranges. Additionally, the mechanical properties decrease with the porosity [246], therefore the elastic modulus of the matrix may be inferior to the mentioned ranges.

Due to the difficulty to differentiate the phases, the deconvolution method was applied separately for each phase distribution for a detailed comprehension of the material and to elucidate the differences between the constituents of the three main phases. The conditions to perform this analysis and the summary of the results are presented in Table V.4.

Table V.4. Results of the analysis of the hardness and elastic modulus by the deconvolution method of the separated phases distributions from data measured at 250 nm of penetration depth.

	HIT graphite (GPa)	*E* graphite (GPa)	*HIT* matrix (GPa)	*E* matrix (GPa)	*HIT* ceramic (GPa)	*E* ceramic (GPa)
Range of values (GPa)	0-1	0-25	0.8-30	20 - 400	0.8-30	20 - 400
Bin size (GPa)	0.05	1	0.05	5	0.5	10
Number of phases	2	2	2	3	1	1
Constituent #1	0.2 ± 0.1 (graphite 2)	7 ± 2 (graphite 2)	1.4 ± 0.4	42 ± 17 (interface)	19.3 ± 3.6	289 ± 27 ($ZrSiO_4$, SiC+matrix/graphite)
Constituent #2	0.5 ± 0.1 (graphite 1)	14 ± 4 (graphite 1)	3.6 ± 0.9	118 ± 24 (copper)		
Constituent #3				202 ± 20 (iron)		

The formulation of the brake pad includes two varieties of graphite, the distinction of graphite 1 and 2 was possible reducing the bin size to 0.05 GPa for hardness, and to 1 GPa for elastic modulus; this distinction was difficult to achieve when the ceramic phases were considered, since their properties have different orders of magnitude and the bin size was bigger; both mechanical properties were approximated to a bimodal distribution in Fig. V.11.

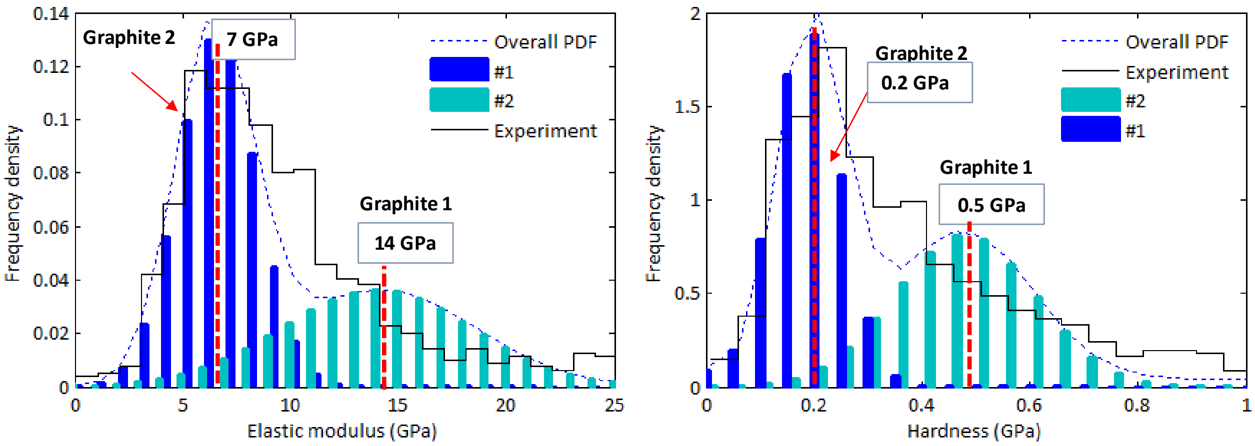

Fig. V.11. Deconvolution of the results of elastic modulus and hardness for graphite phases obtained at 250 nm. Two types of graphite were found, corresponding to an approximated bimodal distribution. The bin sizes to plot the histograms were 1 GPa for the elastic modulus, and 0.05 GPa for hardness.

In metallic and ceramics phases the bin size was increased to identify better each phase. We distinguished for ceramic constituents one phase by the analysis of the elastic modulus at 289 GPa, which probably corresponds to the contribution of $ZrSiO_4$ and SiC, both might be affected by the matrix or graphite because they could have higher elastic modulus (Table V.1). However, for $ZrSiO_4$ different studies reported elastic modulus close to 300 GPa [218,221,222], thus, the obtained result 289 GPa corresponds well to the intrinsic property of this ceramic. The elastic modulus of SiC changes as function of the fabrication conditions, but the values are usually superior to 300 GPa [226], therefore the estimated value is probably affected by surrounding phases.

The analysis of the hardness data of ceramic phase, exhibits one phase (19.3 GPa), which is linked to a mixture of SiC and $ZrSiO_4$, the value is approximated to some hardness results reported in the literature for the SiC [225] and $ZrSiO_4$ [219,221].

In the metallic matrix two phases can be roughly identified from the hardness results, nevertheless it is difficult to link each value to one material due to the complex microstructure of the matrix associated to the fabrication procedure. Hence probably we always measure a composite property, principally connected to one of the base materials (copper or iron), or to the interfaces between them. The higher values are related to the copper and iron phases, which reach similar values according to the identification by the indentation curves; hereafter, the lower values are probably linked to the interfaces and adjacent materials affected by the graphite.

For the elastic modulus, the response is difficult to interpret due to the large dispersion and the complex microstructure; the deconvolution analysis leads to a rough estimation of three phases. Two of the obtained values approximate well the theoretical elastic modulus of copper and iron, 118 GPa and 202 GPa, respectively. The third phase could be related to the interfaces between the different materials (graphite-matrix, ceramic-matrix, and ceramic-graphite), also to the effect of the very soft graphite phases under the measured surface, the porosity, and the presence of oxides in the surface.

It is worth mentioning that hardness and elastic modulus results are not going to be necessarily related, for example we performed separately the analysis of the elastic modulus for the copper and iron phase (range of values according to theoretical properties), identifying the intrinsic values of each phase; nevertheless, the corresponding values of hardness are represented by overlapping distributions, emphasizing the importance of the study of both properties simultaneously. Typically, the studies in heterogeneous materials are focused in one of these mechanical properties; our work highlights the importance of studying both mechanical properties, in order to obtain more reliable results.

Regarding the previous analysis and the difficulty to identify the intrinsic properties of the metallic matrix and ceramics, particularly the elastic modulus, we extracted the properties at a smaller penetration depth (100 nm) to evaluate if the response approaches better the individual properties of the phases. The results are summarized in Table V.5, and the deconvolution analysis for metallic matrix and ceramics are presented in Fig. V.12.

Table V.5. Deconvolution results of elastic modulus and hardness for ceramic, graphite and metallic phases in the brake pad from data measured at 100 nm of penetration depth.

	HIT graphite (GPa)	*E* graphite (GPa)	*HIT* matrix (GPa)	*E* matrix (GPa)	*HIT* ceramic (GPa)	*E* ceramic (GPa)
Range of values (GPa)	0-8	0-25	0.8-30	24 - 425	0.8-30	24 - 425
Bin size (GPa)	0.1	1	0.3	5	0.3	5
Number of phases	2	2	2	3	1	2
Constituent #1	0.2 ± 0.1 (graphite 2)	7 ± 3 (graphite 2)	1.5 ± 0.6 (interface?)	37 ± 13 (interface?)	20.5 ± 7.0	292 ± 27 ($ZrSiO_4$)
Constituent #2	0.5 ± 0.1 (graphite 1)	15 ± 4 (graphite 1)	4.1± 0.9 (copper, iron)	121 ± 28 (copper)		419 ± 44 (SiC)
Constituent #3				218 ± 26 (iron)		

The properties obtained at 100 nm are very similar to the properties found at 250 nm, indicating that the effect of the roughness is not significant, since the results are comparable at both penetration depths. A slightly increase of the elastic modulus was observed for copper and iron phases, 121 GPa and 218 GPa respectively. The average elastic modulus for the iron phase is higher than the reference range (Table V.1), which is probably related to the hypothesis of Oliver and Pharr [48] assumed for the calculations of the contact area that suppose sink-in as a main deformation mode; nonetheless, typically metallic materials exhibit an upward flow of the material (pile-up), this supposition might lead to a small overestimation of the properties (approximated to 10%) leading in this case to a better estimation of the elastic modulus (~196 GPa) of these phases.

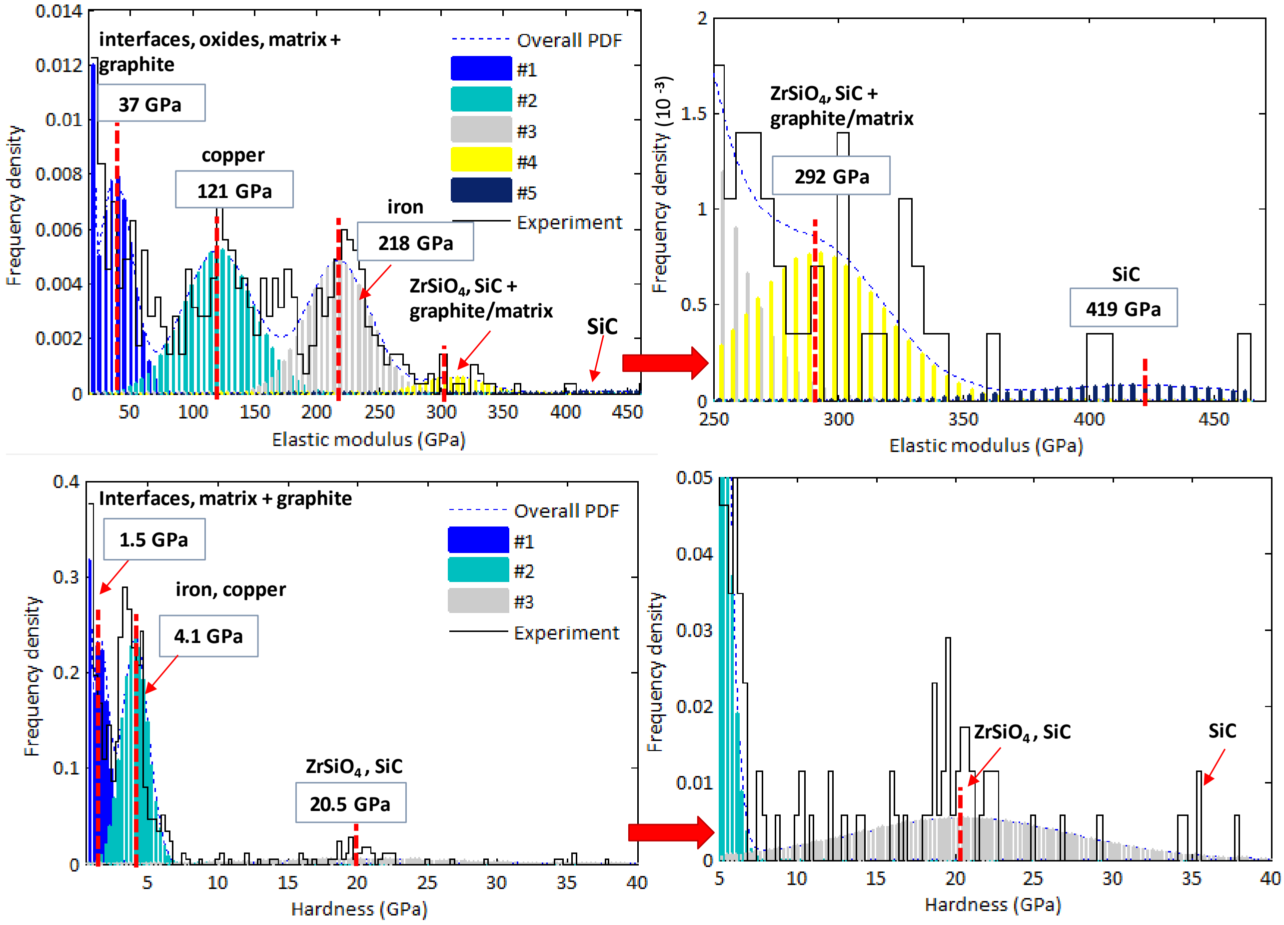

Fig. V.12. Deconvolution results of elastic modulus and hardness of ceramic phases and metallic matrix (left) and zoom for the ceramic distributions (right) obtained at 100 nm of penetration depth.

At 100 nm of penetration depth we identified few values corresponding to the elastic modulus of SiC ~419 GPa, corresponding with the reference value [225,226]. The elastic modulus of $ZrSiO_4$ similarly that at 250 nm is associated to the value of 292 GPa in agreement with its reference values [222]. Nevertheless, it is possible that this distribution of values considers some tests performed in the SiC with softer phases around, already affected at this penetration. On the other hand, hardness for ceramics phases exhibits a similar value than the results performed at 250 nm depth (20.5 GPa) however we detected some values higher than 30 GPa linked to SiC phase. Consequently, hardness and elastic modulus obtained at 100 nm penetration depth are a better estimate of the intrinsic properties of each phase in the brake pad.

The analysis of the mechanical properties of the individual phases by the deconvolution of the histograms approaches the properties values and response of each phase, however hardness values could be slightly overestimated due to the possible indentation size effect at shallow penetration depths, nevertheless this effect is difficult to quantify due to the material heterogeneity. The volume fraction estimation should be considered cautiously, since there are many factors affecting these measurements such as interfaces, complex microstructure, porosity, volume distribution different from surface distribution, etc.

Grid indentation technique typically leads to a good estimation of the mechanical properties of heterogeneous materials [203,206,207,210], nonetheless it is rarely performed in such a complex material as the brake pad under study, although most of the estimated properties of each material in the initial formulation of the brake pad agree with their reference values (Table V.1). Nevertheless, it is difficult to confirm that the number of identified phases is the correct one, we recognized the peaks related to the components in the formulation of the brake pad, and an additional distribution in the range of values of the matrix, which is probably related to the interfaces and composite response of different materials that is unavoidable

In addition, the statistical analysis allowed the characterization of graphite, which properties were initially unknown. We shall mention that we performed some tests on samples of phenolic resin with different concentrations of powders of graphite 2, fabricated in a mounting machine. The analysis of results was rendered difficult by the fact that the resin was not homogeneous and its mechanical properties had the same order of magnitude than the graphite phase, however the addition of graphite to the mixture decreased the values of the properties. Therefore, by the application of a mixture law relation we did an approximation obtaining that the elastic modulus ranges from 1.5 to 3 GPa, which are inferior to the estimated values by grid indentation, these differences were connected to the manufacturing process that probably densifies the graphite due to the high pressure applied, increasing its elastic modulus.

It is important to envision that the dispersion of the properties is significant due to the material morphology and its complex microstructure, *i.e.* a ceramic indented in the middle of the particle (Fig. V.13a) can lead to different values than an indentation close to the border of the particle (Fig. V.13b) [251]. Consequently, the measured response differs according to the specific place where the test is performed on the phase, we shall remember as well that the samples were previously polished, thus the thickness of the phases is reduced in the surface arising to a quicker composite response (Fig. V.13c-d).

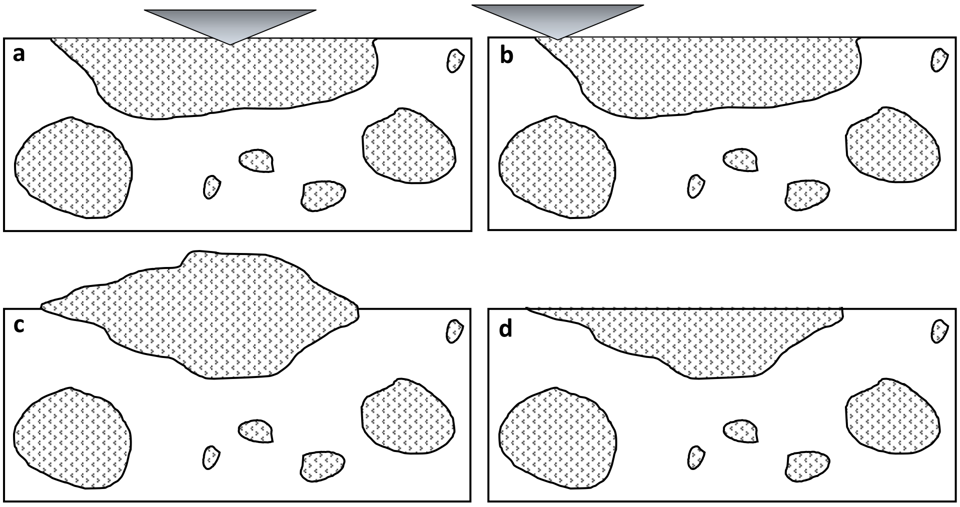

Fig. V.13. Schematic representation of testing positions in brake pad a) test performed in the middle of a particle implicating a larger thickness. b) test performed at the edge of the particle obtaining a quick influence of the underneath material. c) unpolished material with an initial particle thickness d) polished material reducing the particle thickness.

As mentioned previously, the properties of each phase are affected by the surrounded materials in the brake pad at a certain penetration depth, leading to a composite response instead of the intrinsic properties of each material; for example, the elastic modulus of SiC was identified at 100 nm but not at 250 nm. For heterogeneous materials, the analogy with multilayers systems allows to understand the variation of the mechanical properties with penetration depth (Fig. V.8), the multiple staked phases are considered as multiple layers, then the contribution of each phase to the composite response is evaluated. For this analysis we used the multilayer model proposed by Rahmoun *et al.* [243] described by Eq. V.13-14, initially performed for the analysis of hardness, but it could be generalized for elastic modulus as well [252].

$$H_c = \frac{A_f}{A} H_f + \sum_{i=1}^{n} \frac{A_i}{A} H_i + \frac{A_s}{A} H_s \tag{V.13}$$

$$\frac{A_i}{A} = 2\frac{C_i t_i}{h} - \frac{2{C_i}^2 {t_i}^2}{h^2} - 2\frac{C_i t_i C_f t_f}{h^2} \tag{V.14}$$

where H_c is the composite hardness given by: the film hardness H_f, the i-intermediate layer hardness H_i, and the substrate hardness H_s. A_f, A_i and A_s are the areas of the top film, i-intermediate layers and substrate transmitting the mean contact pressure to the respective hardness, $A = A_f + A_i + A_s$, then the ratios A_f/A, A_i/A, A_s/A must lie between 0 and 1. t_i and t_f are the thickness of the i-layer and film. C is a geometrical factor depending on the deformation of the material. For hardness C (C_i, C_f), may have the values $cos^2\varphi$ (plastically deformed) or

$(1 - sin\varphi)$ (brittle facture), where φ is the indenter semi angle (65.3° for Berkovich indenter). For elastic modulus, C is a constant dependent on the indented materials.

Two theoretical examples are presented in Fig. V.14 to illustrate the basis of the methodology, different configurations of the staked particles or layers could lead to the same composite response at a certain penetration depth. The high contrast between the hardness of the phases, as in the case of the graphite and ceramic conducts to a marked rise or drop of hardness according to the configuration soft/hard or hard/soft, respectively, which is observed rapidly for the hard/soft systems in the diagram of the volume fraction of each phase contributing to the composite hardness as a function of penetration depth.

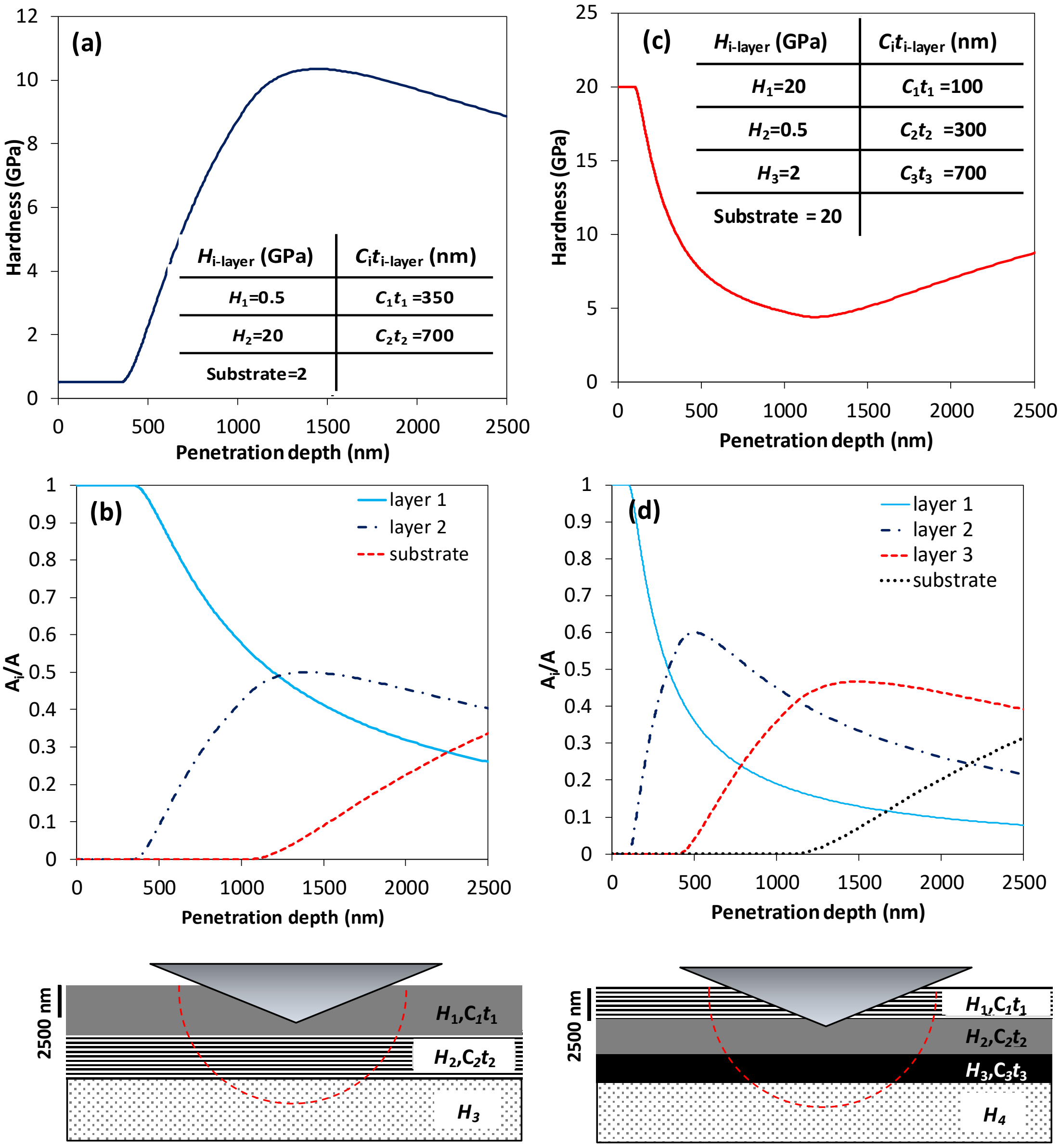

Fig. V.14. Possible configurations analyzed by a model used in multilayer coatings due to the analogy between both systems, composite and coated materials. A_i/A represents the contribution of each layer $\boldsymbol{i}$ to the measured hardness at a certain penetration depth.

Comparable results were obtained for the experimental data, we analyzed some aleatory curves, two examples of the variation of elastic modulus and hardness as a function of penetration depth are presented in Fig. V.15 and Fig. V.16 to show different phase configurations in the brake pad material.

Fig. V.15 shows the fitting by the multilayer model of an experimental curve of the elastic modulus variation against penetration depth obtained in the brake pad. In this example, the first phase is related to the matrix (copper), the value decreases immediately at 250 nm of penetration depth due to the influence of graphite phase, followed by the increase given by the subsequent matrix (copper), ceramic (SiC) and matrix (copper) phases, all of them contributing to the composite response of the material progressively starting at a particular penetration depth, as presented in Fig. V.15b. The elastic modulus values correspond with the predicted values by statistical analysis and the theoretical ones.

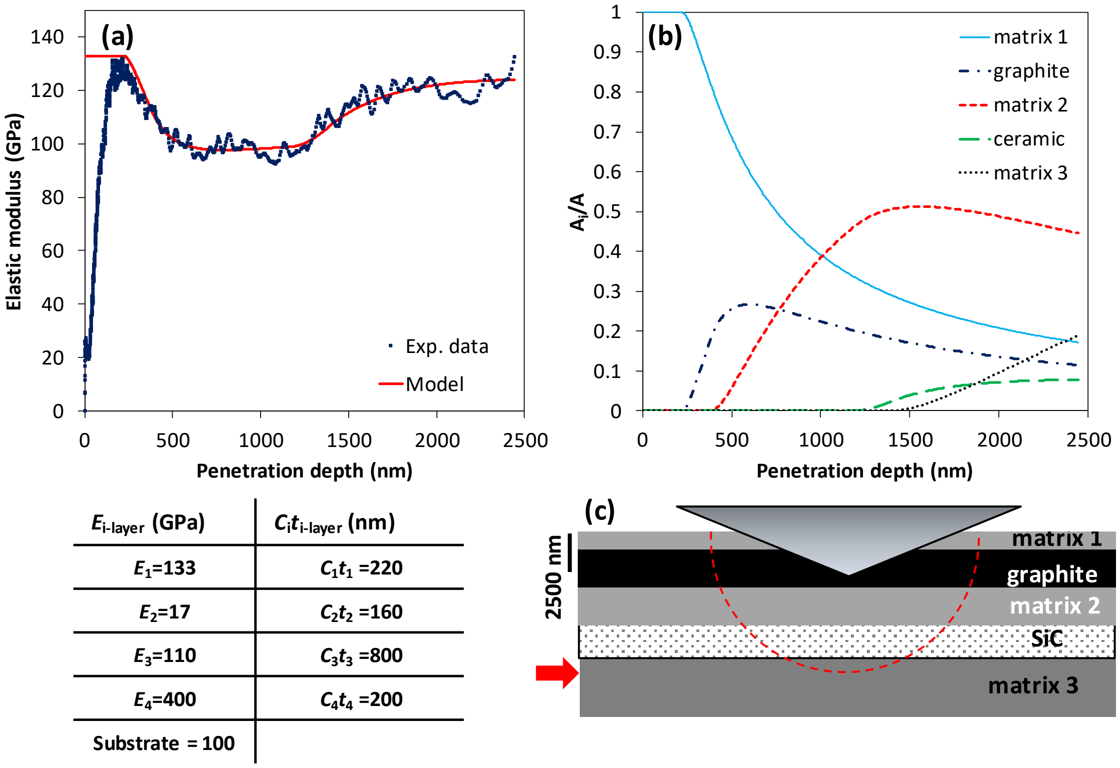

$E_{i\text{-layer}}$ (GPa)	$C_it_{i\text{-layer}}$ (nm)
E_1=133	C_1t_1 =220
E_2=17	C_2t_2 =160
E_3=110	C_3t_3 =800
E_4=400	C_4t_4 =200
Substrate = 100	

Fig. V.15. Analysis of an nanoindentation CSM curve with a multilayer model [243]. (a) Fit of the model to the experimental curve, the table shows the different staked phases that lead to the behavior of the curve, where $Ct_{\text{i-layer}}$, is given by the product of thickness of the phase (*t*) by a constant related to the deformation process (*C*). (b) Contribution of each phase to the composite response vs. the penetration depth. (c) Schematic representation of a multilayer system with the staked particles showing the plastic deformation zone.

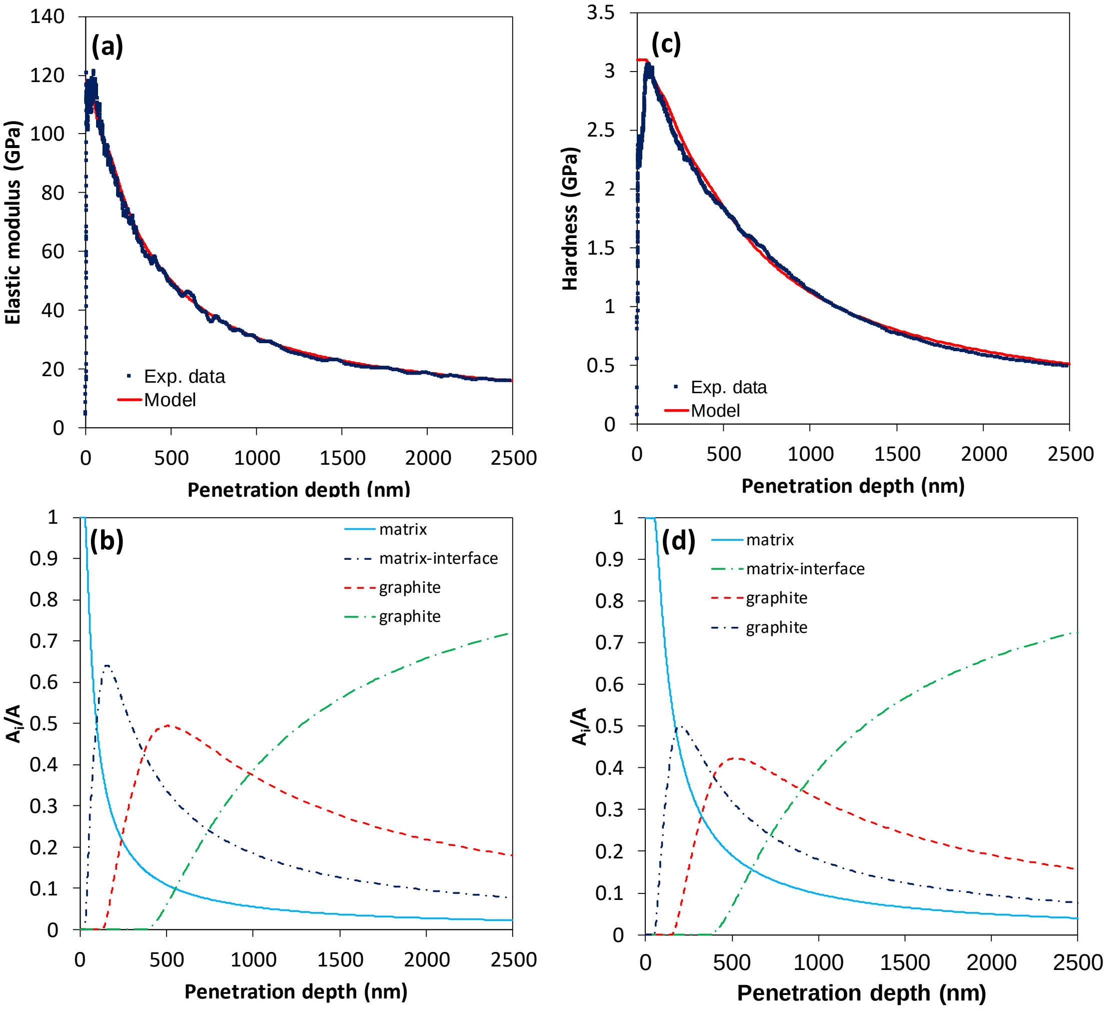

$E_{\text{i-layer}}$ (GPa)	$C_it_{\text{i-layer}}$ (nm)
E_1= 118	C_1t_1 = 28
E_2= 80	C_2t_2 = 100
E_3= 20	C_3t_3 = 250
Substrate = 5	

$H_{\text{i-layer}}$ (GPa)	$C_it_{\text{i-layer}}$ (nm)
H_1= 3.1	C_1t_1 = 50
H_2= 2.4	C_2t_2 = 100
H_3= 1.2	C_3t_3 = 220
Substrate = 0.03	

Fig. V.16. (a) Fit of the multilayer model to the elastic modulus variation, (b) Contribution of each phases to the composite elastic modulus vs. the penetration depth, the table shows the different staked phases that lead to the behavior of the curve, (c) Fit of the multilayer model to the hardness variation, (d) Contribution of each phases to the composite hardness vs. the penetration depth, the table shows the different staked phases that lead to the behavior of the curve.

Fig. V.16 exhibits an experimental example of the variation of elastic modulus and hardness analyzed by the multilayer model. Both properties showed a similar evolution with the penetration depth. Fig. V.16b-d shows the contribution of each phase to the composite response. We identified three stacked phases and the substrate by the multilayer model analysis, the first one corresponds to the copper matrix, the elastic modulus and hardness agree with the properties obtained by the deconvolution method; the second phase or layer is probably related to an interface in the matrix; the third phase corresponds to graphite 1 due to the small elastic modulus, nevertheless the hardness is elevated in comparison with the values obtained by the statistical analysis, highlighting the heterogeneity of this phase; the last phase matches with graphite 2, both E and H agree with the predicted properties.

In instrumented indentation testing, the elastic modulus physically represents a more sensitive property than hardness due to the dimension of the deformation field, the elastic deformation zone could be extended to 100 times the penetration depth [244,245], and the ratio of the plastic zone about 7 times the penetration depth [243]. Therefore, if penetration depth reaches 1% of the characteristic length size of the particle, the elastic modulus is affected by the subsequent phases staked under it. Noticeably, the approximation to the multilayer model is a simplification of the real response of the brake pad due to the disordered microstructure and morphology, where the edge effects, interfaces and porosity, would modify the measurements by indentation. The 1% of penetration depth means that we should have a particle of at least 10 µm of length in the indentation direction for the measurements at 100 nm, which is largely in conformity with the size of the phases, where the medium size is approximately 100 µm (Fig. V.3), similarly at 250 nm, or even at larger penetration depths as 500 nm we should obtain the intrinsic properties. Nevertheless, due to the complexity of the microstructure of the material and the important difference between the mechanical properties of graphite and the metallic and ceramic phases, at very shallow penetration depths this rule could be violated, especially when the upper phase is followed by the graphite phase. The effect of a very compliant material under the tested surface directly impacts the measurement of the mechanical properties demonstrated by Crawford *et al.* [115], even if the material thickness is 100 times larger than the penetration depth.

For hardness, the rule of thumb of 10% should be respected, therefore at 250 nm of penetration depth we could have a particle length of 2.5 µm that is two orders of magnitude smaller than the minimum particle size. Hence, theoretically according to the medium size of the phases (100 µm) to obtain a hardness variation the penetration depth should be larger than 10 µm. This rule was not fulfilled for the tested material, generally hardness variations with penetration depth start at slightly deeper displacements than modulus, when the graphite phase is close, probably related to the porosity, the high contrast between their properties, the shape of the particles, etc. We can suppose that an embedded hard particle surrounded by very soft matrix would lead to a strain field more complex that in a coating configuration soft/hard where generally the rule of 10% is satisfied, because of the confinement of the plastic deformed volume by spreading within the soft film [241]. Gouldstone *et al.* [5] showed through finite element simulations that hard particles embedded in a soft matrix conduct to particle agglomeration underneath the indenter. The particle agglomeration effect is partially explained by the very high hydrostatic pressure that implies greater volumetric compression for the soft matrix than for the stiffer particles. As the indenter penetrates, it encounters resistance from the material with agglomeration of hard particles, which locally work-hardens the matrix even more constrained, and a greater load is needed to achieve a penetration depth [253]. Consequently, given the complex microstructure of the brake pad system especially due to the large volume of graphite is reasonable that it behaves differently than a multilayer material.

In contrast, a constant hardness was found in some tests up to 2500 nm (limit indentation depth) when the graphite is firstly indented, that correspond with previous results in coated systems where the configuration soft-coating/hard-substrate leads to the coating hardness at depths greater than 10% of the coating thickness [94,209,254]. In this case the elastic modulus could show a composite response due to the other phases.

To conclude, the multilayer model predictions agree with the theoretical properties of the different phases in the material, indicating that through this analysis it is possible to obtain a good approximation of the intrinsic properties of each phase, and identify the properties of the interfaces. Regarding the constant C in the model (Eq. V.14), it could be modified according to the differences between the materials properties, the porosity, and the phases arrangement. Nevertheless, special attention should be taken regarding the rules of thumbs usually considered in this analysis because due to the very complex microstructure of the material, the elastic and plastic deformation fields are different than in a multilayer system affecting directly the measurements, thus, these rules would not be applicable in many tests. However, the multilayer analysis revealed that properties at 100 nm represent a close approximation of the mechanical properties of the system corresponding with the results obtained by grid indentation.

V.3.2 Macroindentation tests

Due to the heterogeneity and the micrometric dimensions of the phases in the brake pad it is necessary to reach deeper penetration depths in order to obtain the overall material behavior. Macroindentation tests give a closer approximation of the global material response, because the affected volume is larger. The brake pad was characterized by Vickers (top surface and cross-section) and spherical (top surface) indentation by multicyclic tests to obtain the properties evolution with load. The results would be presented in the mentioned order, followed by a common discussion.

Macroindentation with Vickers indenter in the top surface of the brake pad

The tests were performed up to 250 µm of penetration depth, settled limit relative to the Vickers indenter shape (height of the diamond pyramid) that is equivalent to 260 N in the brake pad material. Some examples of the loading-displacement curves are presented in Fig. V.17.

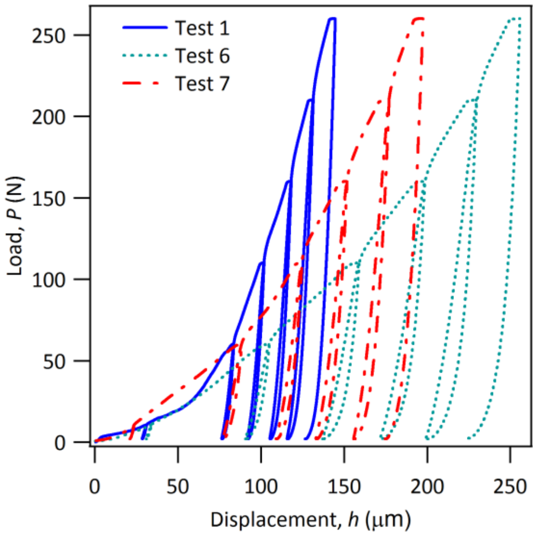

Fig. V.17. Load-displacement curves in brake pad by macroindentation multicyclic tests with Vickers indenter.

Fig. V.17 shows the important difference between the curves due to the heterogeneous behavior of the material during indentation. Hysteresis loops between unloading and the reloading curves were observed in the multicyclic load-displacement curves, these are more pronounced in some tests due to the test position, *e.g.* test 6 in Fig. V.17.

Fig. V.18 shows some examples of the variation of the elastic modulus and hardness as a function of the applied load. The properties could decrease or increase according to the configurations of the staked phases found during penetration of the indenter into the material.

Fig. V.17 and Fig. V.18 show that macroindentation tests do not lead to a unique material response at this range of loads. Because during multicyclic tests the heterogeneities modify the composite response of the material, therefore hardness and modulus experiment a large dispersion. One reason could be related to the large size of some graphite particles that hinders to reach the global material properties, the maximum penetration depth to obtain an actual global response should be approximately $h > 2D\cot\theta$ (θ, equivalent cone semi-angle) [206], where D is the larger characteristic length size in the material linked to the graphite phase, which has some particles bigger than 1 mm, leading to $h > 716$ µm, that overpass the limit indentation depth given by the Vickers indenter (~250 µm). Nevertheless, the response would be mainly conditioned by the arrangement of phases in the surface and across the depth, which is heterogeneous even at this scale.

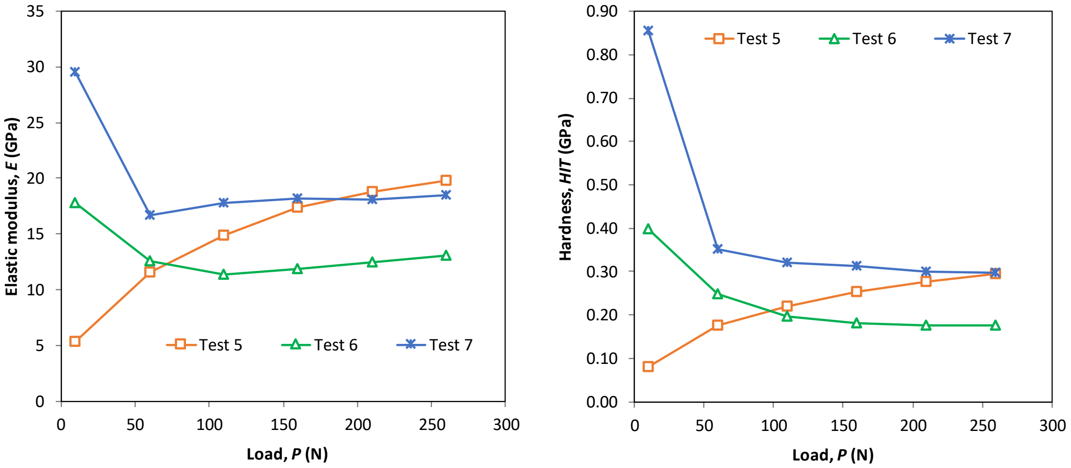

Fig. V.18. Elastic modulus and hardness variation vs the applied load in multicyclic macroindentation tests.

Fig. V.19 presents the histograms of the elastic modulus obtained at each load for all the performed tests. The elastic modulus distributions are comparable at different loads starting at 60 N, hence to study the material response the results at different loads could be equally considered and regrouped, on condition that at least 10 tests randomly distributed are performed. For the first cycle at 10 N, the dispersion increases because the contact area is smaller, then a more localized response is obtained. Nevertheless, the average E regardless the load was 17 ± 6 GPa, where 6 GPa represents one standard deviation in the normal distribution obtained for all the range of loads. The hardness and modulus responses were comparable, the histogram including all the range of loads (10-260 N) is presented in Fig. V.20, the average value is $HIT = 0.23 \pm 0.10$ GPa. It is worth mentioning that some load-displacement curves presented a similar behavior despite the great dispersion obtained in the results.

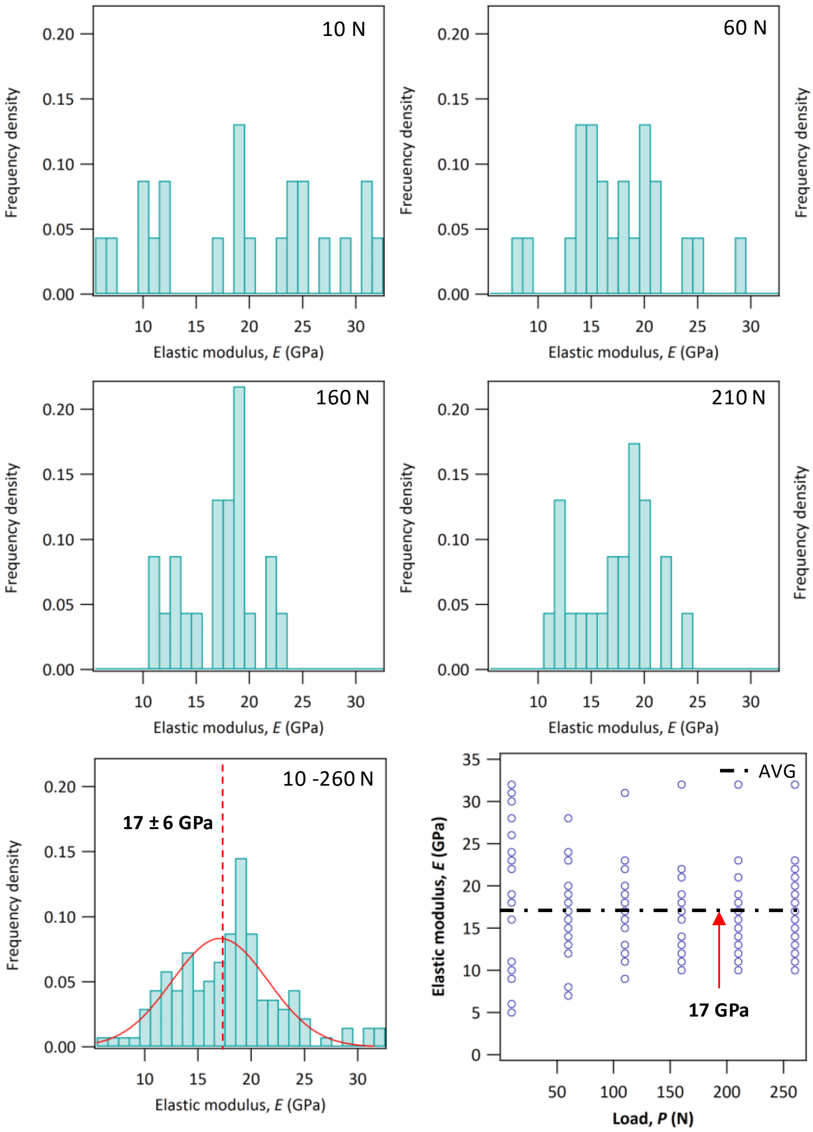

Fig. V.19. Histograms of the elastic modulus at each cycle load from 10 to 260 N, corresponding to the tests performed with Vickers indenter in the top surface of the brake pad.

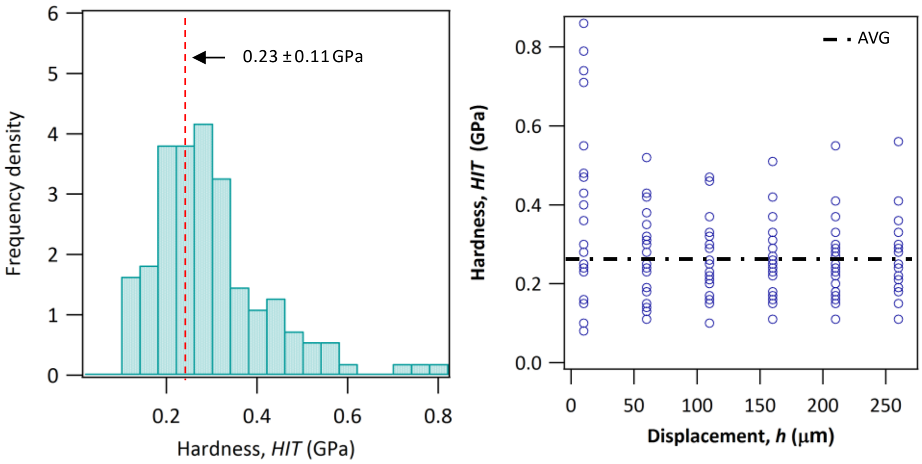

Fig. V.20. Histograms of the hardness at each cycle load from 10 to 260 N (left), and hardness variation with load (right) corresponding to the tests performed with Vickers indenter in the top surface of the brake pad.

Macroindentation with Vickers indenter in the cross section of the brake pad

The cross-section of the brake pad was tested by multicyclic macroindentation tests with Vickers indenter. The examples of the load-displacement curves are presented in Fig. V.21. Similarly than in the top surface, the curves illustrate the high heterogeneity of the material and the hysteresis loops between the unloading and reloading curves.

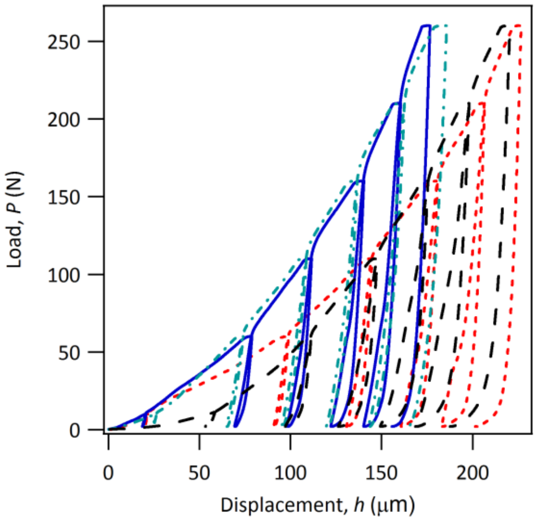

Fig. V.21. Load-displacement curves obtained by multicyclic macroindentation tests with Vickers indenter performed in the cross-section of the brake pad.

Fig. V.22 shows the histograms of the elastic modulus per load. The scattering of the values is slightly reduced starting at 160 N, nevertheless the results are comparable for all the range of loads between 60 to 260 N, but at 10 N the values are more widespread due to the smaller indented area. Considering all the results the histogram is approximated to a normal distribution centered at 22 GPa, with an elevated standard deviation of 10 GPa related to the material heterogeneity.

Fig. V.23 exhibits the instrumented hardness histogram for all the load range and the variation of its variation with displacement. The results are not load dependent since the scatter of the data is similar regardless the load, the average value is 0.29 ± 0.15 GPa.

In general, the material response in the cross section is more rigid in comparison with the obtained behavior in the top surface, even that some elastic modulus values correspond to same domain, likewise for hardness. These results corroborate the previous analysis performed by Serrano *et al.* [227] in the same material that demonstrated the alignment of the graphite particles with the x-y plane leading to a change in the thermal conductivity and diffusivity according to the direction of measurement revealing the material anisotropy.

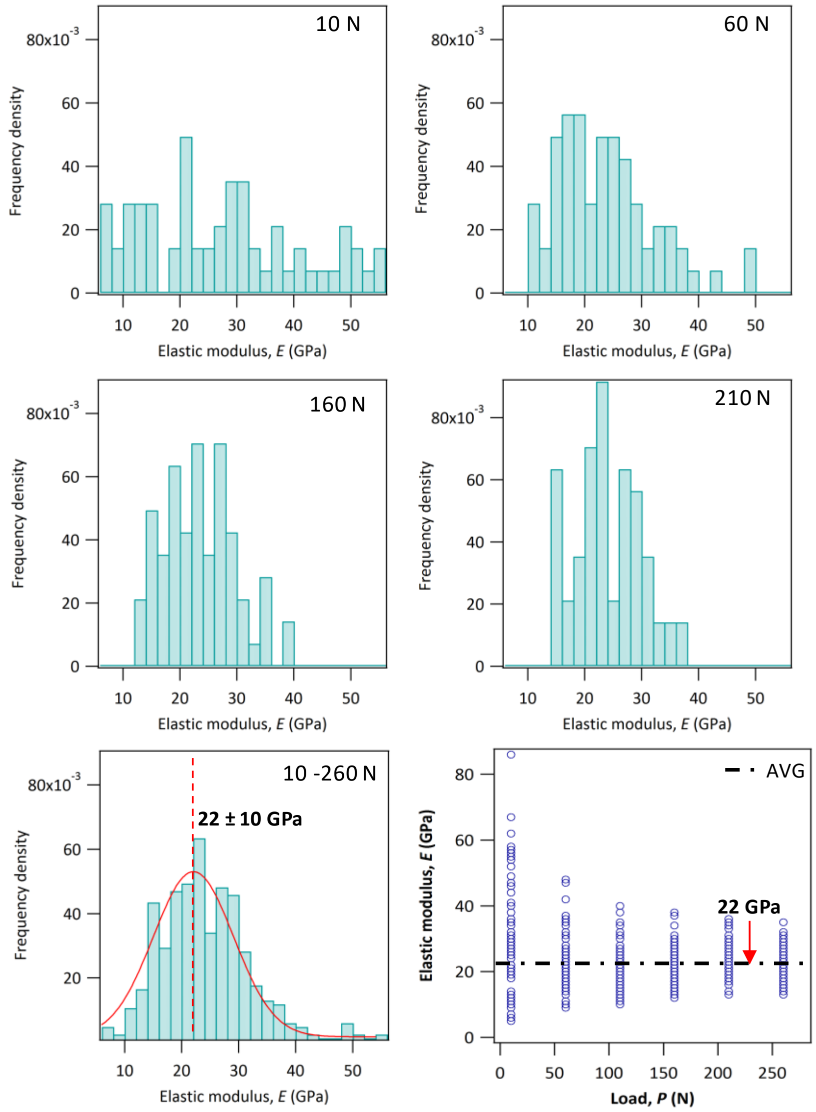

Fig. V.22. Histograms of the elastic modulus for different applied loads obtained by multicyclic tests with Vickers indenter, and its variation as function of the load corresponding to the tests performed in the cross section of the brake pad.

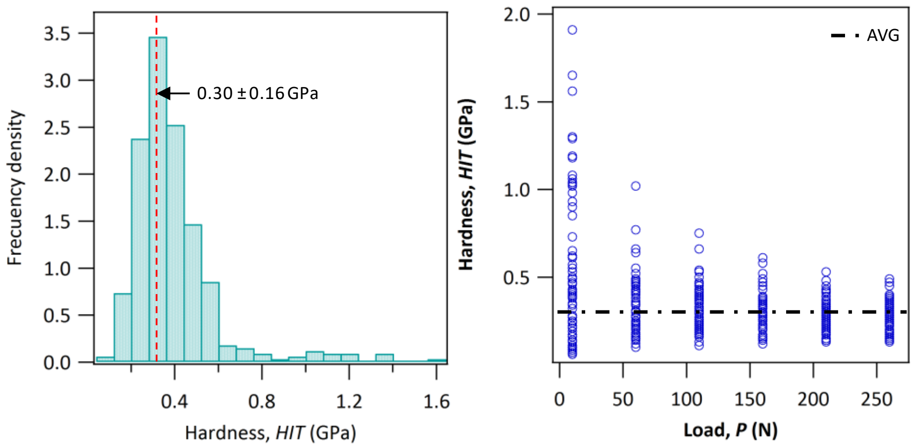

Fig. V.23. Histogram of the instrumented hardness (left) and hardness variation with load (right) obtained from macroindentation tests with Vickers indenter in the cross section of the brake pad.

On the other hand, Mann *et al.* [238] found in a similar brake pad material (with more components in the formulation) that the mechanical behavior changes according to the direction of the load application in uniaxial compression tests, presenting an increase of the elastic modulus in the cross section of almost 4 times bigger than the results in the normal direction. Although that the properties of both materials are dissimilar, the resembling microstructure will conduct to a similar behavior, corroborating the anisotropy of the brake pad under study.

Macroindentation with spherical indenter in the top surface of the brake pad

The multicyclic macroindentation tests with spherical indenter were performed in two ranges of loads, 10-260 N and 50-1450 N. Due to the dimension of the sphere there are not restrictions in the penetration depth because at the selected range of load the displacement is smaller than the ball radius.

The results are presented similarly than for the Vickers indenter. First, Fig. V.24 shows examples of the load-displacement curves for the two ranges of loads. Multicyclic tests between 10-260 N reveal the material heterogeneity at this scale, nevertheless the tests between 50-1450 N show a more homogeneous response with the rising load as the indented volume increases.

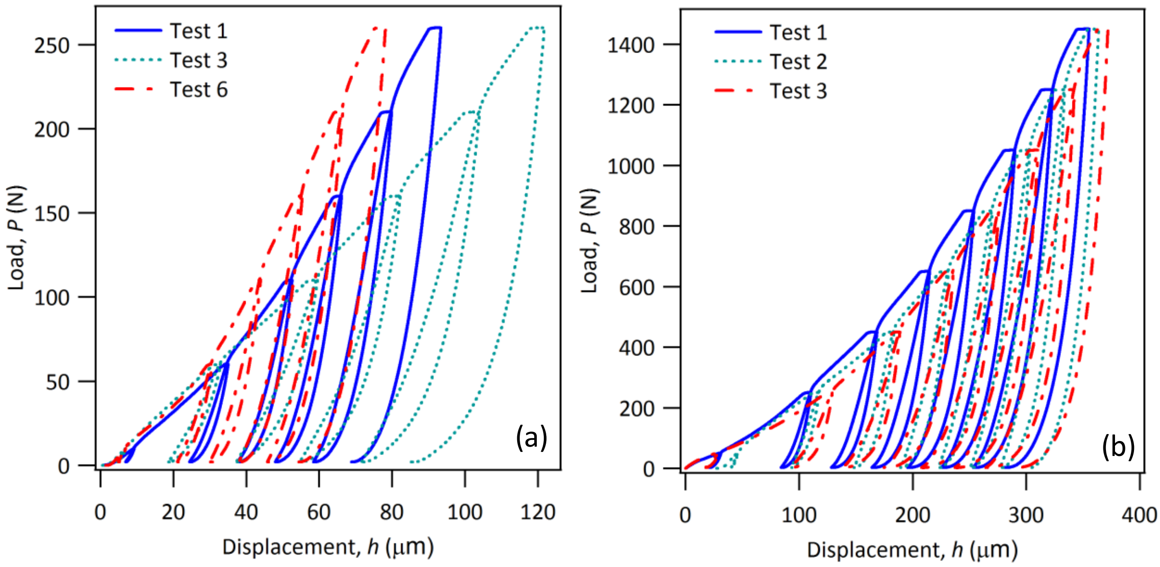

Fig. V.24. Load-displacement curves in brake pad by macroindentation multicyclic tests with spherical indenter. (a) load range 10-260 N, $\Delta P = 50$ N the difference of the curves because of the sample heterogeneities. (b) load range 50-1450 N, $\Delta P = 200$ N higher loads reduce the difference between curves due to a bigger indented volume.

The hysteresis loops between the unloading and reloading stages are visible, similarly that for Vickers indenter in the top surface and cross section, indicating that there are connected to the brake pad response rather than to the testing conditions.

The histograms of the elastic modulus for the two load ranges of multicycle tests revealed that this property does not change significantly with load (Fig. V.25 and Fig. V.26), however the dispersion is reduced with the increasing load, which is more noticeable for multicyclic tests between 50 to 1450 N. Hence, the results were regrouped in a single histogram for each range of loads leading to a comparable average value with a representative dispersion corresponding to the material heterogeneity at this scale.

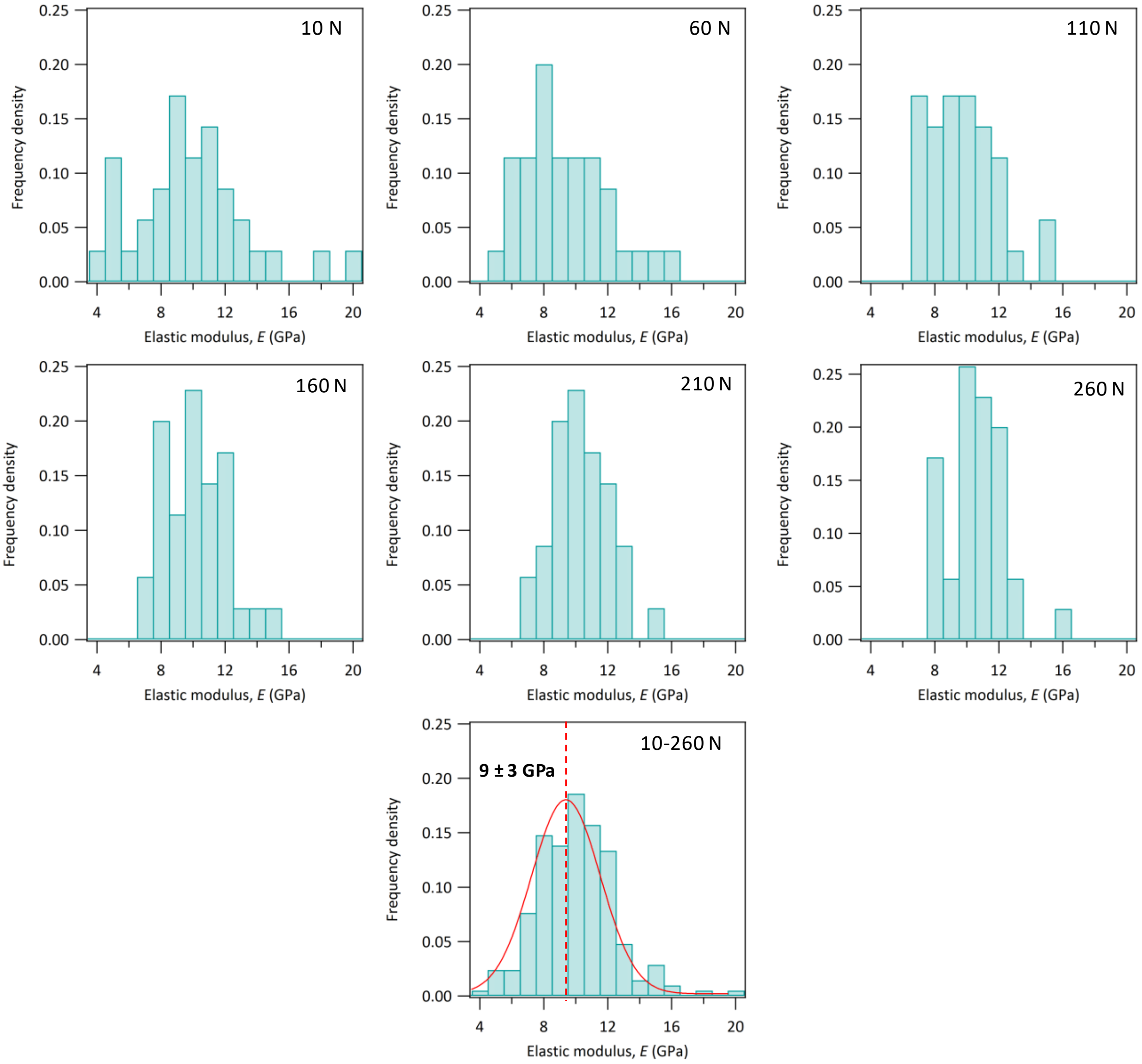

Fig. V.25. Histograms of the elastic modulus at each cycle load from 10 to 260 N, corresponding to the tests performed with spherical indenter.

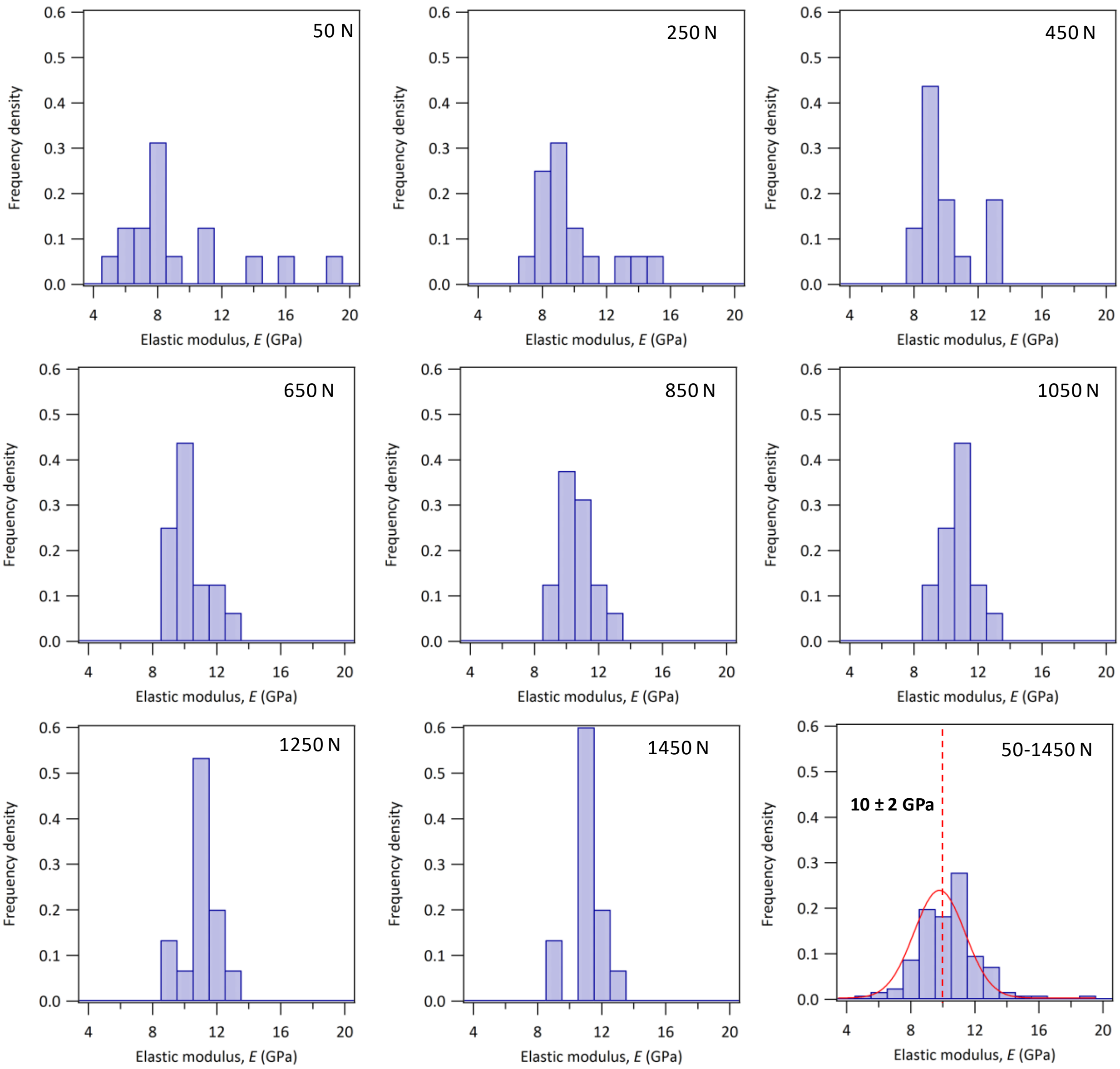

Fig. V.26. Histograms of the elastic modulus at each cycle load from 50 to 1450 N, corresponding to the tests performed with spherical indenter.

As the dispersion of the elastic modulus is considerably reduced with increasing load, the obtained property could be representative of the bulk material response. In the same way than with the Vickers indenter, the 1% rule to avoid the influence of the substrate in the elastic modulus is too conservative, since the measurements are not modified at deeper penetrations than 220 µm. It is important to notice that the standard deviation for the range 50-1450 N is only 20% of the average value (10 ± 2 GPa), which is a good approximation in instrumented indentation testing, nevertheless in the Gaussian distribution this represents just 68% of the values, if we considered 2 times the standard deviation the 95% of the results would be in the range of 10 ± 4 GPa. The tails of the distribution are given by the results at lower loads.

Hardness results obtained by spherical indentation should be treated differently that for Vickers indenter since the indenter is not geometrically similar, spherical indenters of different radii are needed to obtain geometrically similar indentations, therefore, the ratio between the circle of contact and the indenter radii (a/R) should be constant [6,255]. Hardness by indentation is usually computed at the condition of fully developed plastic zone since the mean contact pressure becomes independent of load and depends only on the material response. The assumption of a fully developed plastic zone with a spherical indenter occurs when the mean contact pressure becomes equal to the hardness, *i.e.* the ratio a/R is greater than 0.4 (usually in metals), this value was not achieved in the performed tests. At 1450 N the ratio is greater than 0.3, thus we can assume that hardness at this point corresponds with the fully developed plastic zone, though it is difficult to predict whether or not the obtained results belongs to this region due to the heterogeneities in the material. Meyer hardness defined by Eq. V.11 is recognized as a more meaningful concept than Brinell hardness [6], consequently we computed the average Meyers hardness at 1450 N, obtaining 0.16 ± 0.02 GPa.

Discussion macroindentation tests

For elastoplastic materials, the loading path in pyramidal/conical indentation is generally described by a quadratic relation $P = kh^2$, related to the geometric similarity principle. The loading curves in the brake pad exhibit irregularities due to the inhomogeneous microstructure; hence, due to local damage or heterogeneity beneath the indenter, the curves do not follow the quadratic relation (Fig. V.17 and Fig. V.21) [256,257]. During the test the indenter starts to penetrate a single phase which is rapidly affected by other phases given a composite elastoplastic response. Therefore, the mechanical properties measured at the unloading curve could represent an average response of the material, mainly dominated by the graphite phases.

In spherical indentation, the loading curve may be approximated at low loads to the Hertz equation for elastic contact, where P is proportional to $h^{3/2}$ [6]. Due to the material heterogeneity, this relation is only observed in some curves, few micrometers at the beginning of the loading curve (Fig. V.27). The elastic modulus can be computed by this approximation, we performed the calculation in some curves only for the first cycle for penetration depths inferior to 4 µm obtaining an elastic modulus lower than 10 GPa, indicating a composite response even at small penetration depths in this scale of measurement.

The large hysteresis observed for Vickers and spherical indentation could be principally related to the graphite phase. Sakai *et al.* [258] studied non-brittle polycrystalline graphite, in this material the load-displacement curves presented a large domain of elastic-plastic deformation, but without residual impression after indentation tests. They suggested that the amount of plastic deformation is partially or fully recovered during the unloading process; this procedure is connected to the dislocation-related plastic slips in graphite basal planes in a hexagonal lattice. The driving force for reverse the slip of dislocations is given to the local dislocations from the surrounding elastic field, therefore, if this process happens indicate that Peierls-Navarro force is extremely small [258]. This hysteresis can be also related to a viscoelastic behavior of the material, but graphite is more alike to be a quasi-brittle or brittle material than a viscoelastic material. Another explanation is found in the work of Nohava *et al.* [181] who found in alumina coatings that the compaction of the material at higher loads results in load-displacement hysteresis loops.

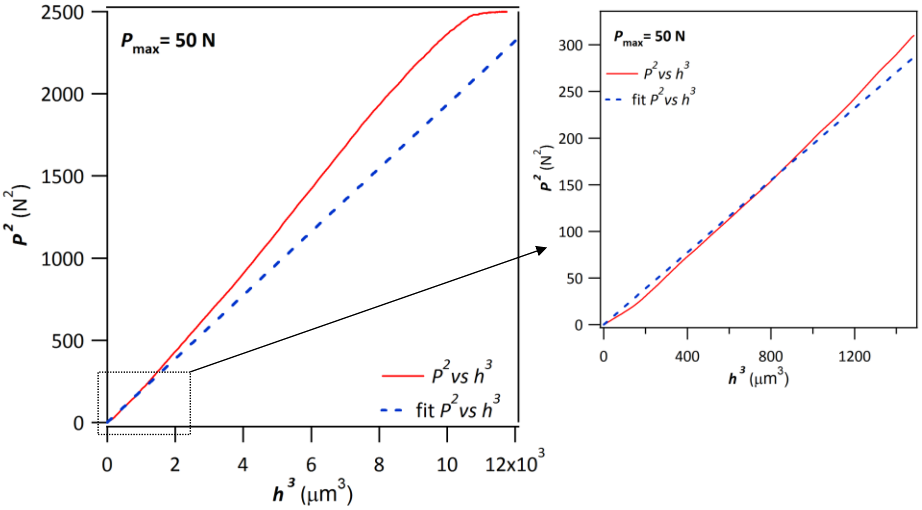

Fig. V.27. Example of load displacement curve obtained by spherical indentation at 50 N, plotting P^2 versus h^3 to obtain a straight line, which slope is directly related to the elastic modulus by the Hertz equation. Note that the curve is well fitted for the first micrometers of penetration. The computed elastic modulus for this case was ~5 GPa.

In order to understand the apparition of the hysteresis loops, a sample containing only the metallic matrix without the graphite and ceramic phases was fabricated using the same manufacturing process described in Fig. V.2. A few macroindentation tests were performed on this sample up to 30 N, some examples of the load-displacement curves are presented in Fig. V.28. In contrast with the brake pad sample, the hysteresis loops did not appear, indicating that this behavior is probably associated to the graphite phases, the properties mismatch between the iron-copper matrix, graphite and ceramics, and the cohesion between phases that changes the material response under indentation. The cohesion between metallic matrix and graphite could be affected by the wettability of copper to graphite, which is usually inert but the addition of alloying elements may improve the wetting behavior [259].

The small values of the elastic modulus and hardness indicate that the graphite phases dominate the global behavior of the material, these phases will probably undergo brittle fracture, presenting regions of crushed debris beneath the indentation [260]. Field and Swain [261] found for glassy carbon and pyrolytic graphite that the deformation in these materials is produced by elastic compression of the interplanar bonds, combined with an elastic component of interplanar slip along the basal plane, where the localized hydrostatic compressive stress would be critical, otherwise these materials would fail by fracture. Consequently, as the graphite phase controls the material response, it is expected that at larger indentation depths, required to have the global response, the brake pad material could present a decrease in its mechanical properties due to mechanisms of damage in the material, because of coalescence of porosity, multiple creation and propagation of cracks, loss of cohesion between phases, exalted by the complex state of stress-strain developed on the material due to the heterogeneity and anisotropy [257].

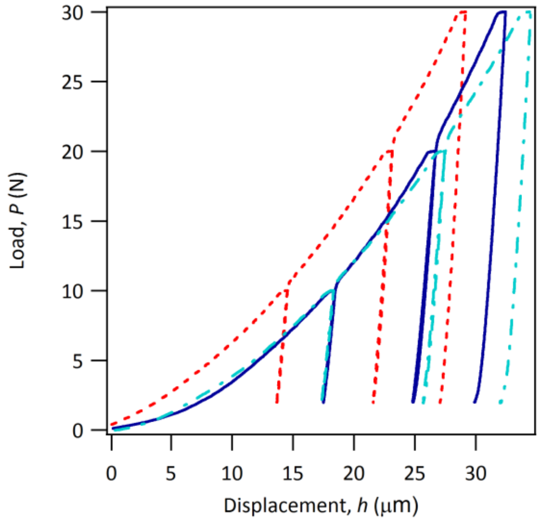

Fig. V.28. Load-displacement curves obtained by macroindentation with Vickers indenter in a sample of the equivalent metallic matrix of the brake pad.

Besides, the elastic modulus computed in the metallic matrix sample varies between 70 to 110 GPa (Fig. V.28), corroborating that the overall material response is dominated by the graphite phases, as was obtained in nanoindentation tests, where the graphite phase produced a quickly composite response even at shallow penetration depths.

Macroindentation results give some hints about the global behavior of the brake pad, especially spherical indentation arises to a good estimation of the average material response. The high dispersion in Vickers indentation is unavoidable due to the material microstructure;

nevertheless, at this scale a local composite response gives the properties distribution in the material that is helpful to understand its behavior in service.

V.3.3. Multiscale indentation: mixture law (nanoindentation) and macroindentation

To determine the global behavior of the material we used the equations of mixture laws from Reuss, Voigt, and Voigt-Reuss-Hill (VRH) models. The Reuss and Voigt models based in iso-stress and iso-strain, respectively [262] are considered as the lower and upper bounds. The Voigt-Reuss-Hill model is usually a good approximation for polycrystalline materials [222].

To compute the composite properties by the mixture law we treated different cases summarize in Table V.6. The next relations describe the Reuss, Voigt and Voigt-Reuss-Hill models for X, being X the elastic modulus or hardness:

$$X_{\text{Reuss}} = \left(\sum_{r=1}^{M} f_r/X_r\right)^{-1};\ X_{\text{Voigt}} = \sum_{r=1}^{M} f_r X_r;\ X_{\text{VRH}} = (X_{\text{Reuss}} + X_{\text{Voigt}})/2 \qquad \text{(V.15)}$$

Table V.6. Results obtained from the computation of the elastic modulus and hardness by the mixture law models Reuss, Voigt and Voigt-Reuss-Hill (Eq. V.15)

	Voigt	**Reuss**	**Voigt-Reuss-Hill**
$E_{\text{th}}$with f_{th} (GPa)	109	24	67
$E_{\text{exp}}$with f_{th} (GPa)	108	17	63
E_{exp1} with f_{exp} (GPa)	91	17	54
E_{exp2} with f_{exp} (GPa)	76	17	47
$HIT_{\text{exp}}$with f_{th} (GPa)	4.1	0.5	2.3
$HIT_{\text{exp1}}$with f_{exp} (GPa)	2.5	0.5	1.5

th. derived from theoretical properties, *exp.* obtained by the deconvolution method

Table V.6 presents the values of the global elastic modulus computed from the theoretical modulus (Table V.1), E_{th}, and the global modulus computed with the estimations obtained by the deconvolution method for each phase (Table V.5), $E_{\text{exp1-2}}$. For the computation of these values, volume fractions were obtained from the material formulation, f_{th}, and from the experimental data, f_{exp}, by deconvolution of hardness in three phases (Fig. V.10). In E_{exp1} we only considered the values related to the phases present in the formulation of the material, in E_{exp2} we considered the three phases found for the matrix (copper, iron, interface), volume fractions were taken from the analysis of the individual phases and recalculated to the fraction obtained for each type of phase. These results should be taken cautiously since the volume fraction is not an accurate estimation from deconvolution method due to the different factors affecting this analysis. Nevertheless, the estimated values of the elastic modulus whichever the volume fractions are taken have the same order of magnitude; the biggest differences between each condition are given by the Voigt model which is more sensitive since it is a direct summation of the volume fractions per the property value. Instead, Reuss model leads to similar values for all the evaluated conditions.

Hardness was calculated with the experimental values obtained from the deconvolution. Similarly, the Reuss model leads to comparable estimations regardless the volume fractions.

It is worth mentioning that the conditions of iso-strain and iso-stress for both models are not satisfied in the brake pad material, being these models just an approximation of the mechanical properties. According to the results, the response of both properties computed by the Reuss model is dominated by the graphite phases, and in Voigt model by the iron-copper matrix. Since Reuss and Voigt models represent the lower and upper bounds, the estimation by the Voigt-Reuss-Hill generally represents a close approximation of the overall material behavior. To validate the obtained results by the mixture laws, they were compared with the results obtained by macroindentation tests.

Fig. V.29 shows the comparison of the elastic modulus as a function of the penetrated volume obtained by macroindentation with Vickers and spherical indenters. The comparison of the indented volumes as a function of the penetration depth is presented as well to highlight the difference between both indenters.

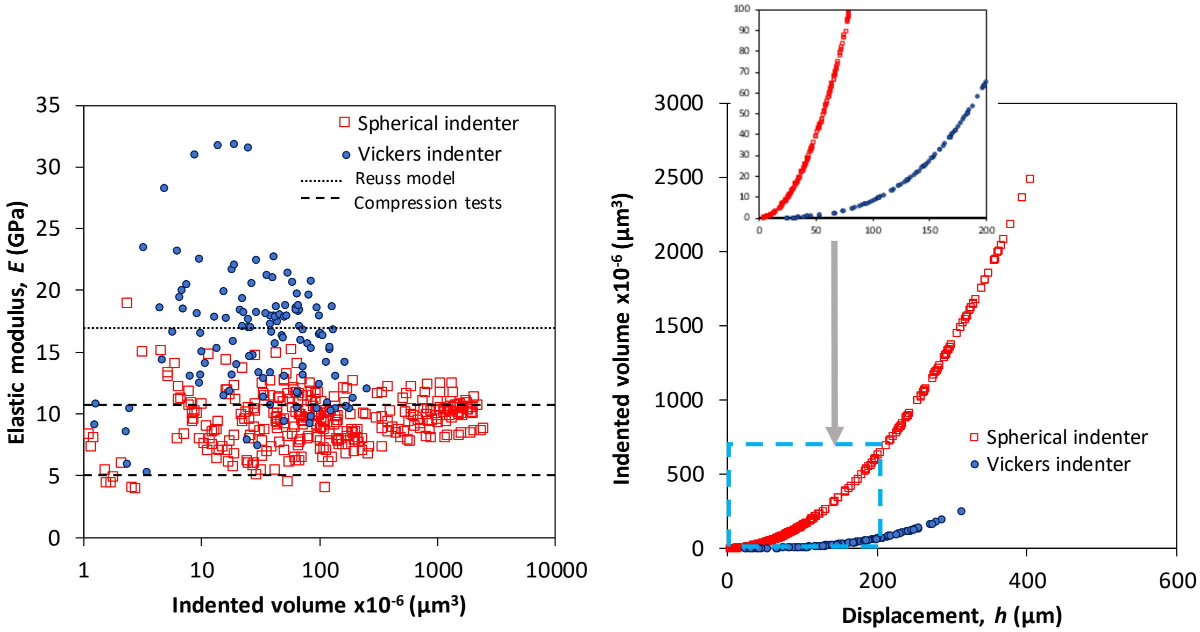

Fig. V.29. Left: comparison between elastic modulus as a function of the indented volume obtained by multicyclic Vickers and spherical indentation; the Reuss model estimation and the results obtained by compression tests are pointed out as reference values. Right: comparison between the indented volumes as a function of the displacement into surface for Vickers and spherical indentation (*d* = 10 mm).

The indented volume is larger in spherical indentation than with conical or pyramidal indenters. The radius of the circle of contact with a spherical indenter increases faster than the indentation depth as the load increases [6], thus the indented area growths quickly in the surface, measuring the average properties in surface. It is worth mentioning that some results obtained by Vickers indentation belong to the same range of values obtained by spherical indentation which is more alike to the overall material response. Thus, the results obtained with Vickers indenter are conditioned by the configuration of the stacked phases indented during test.

The instrumented hardness computed from Vickers indentation (0.23 ± 0.11 GPa) is of the same order of magnitude that hardness computed with Reuss model (0.50 GPa), nevertheless the results by macroindentation tests are almost the half regarding the average value, this difference could be related to the relation of mixture laws with the material elastic properties instead of plastic properties; on the other hand, to possibility that at the nanoscale the measurements could be affected by the indentation size effect, increasing the hardness values. Correspondingly, the average elastic modulus obtained by macroindentation with Vickers indenter (17 ± 6 GPa) is approximated to the results found by Reuss iso-stress model (~17 GPa) displayed in Fig. V.29. Reuss model is more suitable to be applicable for systems with porosity and reinforcements [263]. Nevertheless, as the brake pad does not fulfill the condition of iso-stress due to the material microstructure, regarding the particles shape and distribution, and the properties mismatch of the phases, Reuss model is just a rough approximation of the brake pad properties, that is probably overestimated since spherical indentation is likely to lead to a better estimation of the global material response ($E = 10 \pm 2$ GPa).

In contrast, Serrano *et al.* [3,227] found by compression tests with successive increasing load in the same of brake pad material a decreasing elastic modulus (from 11 to 5 GPa) presented in Fig. V.30.

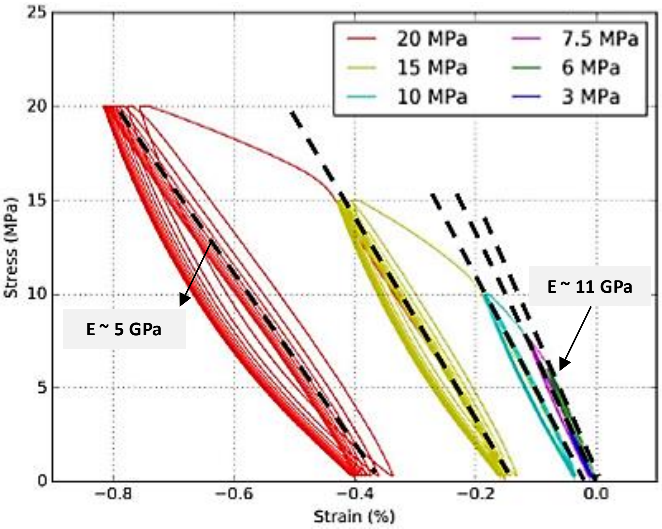

Fig. V.30. Stress-strain curves from uniaxial compression tests performed in the brake pad [227].

The elastic modulus obtained by macroindentation tests with spherical indenter is comparable to the estimated values by uniaxial compression tests, indicating that the response in the studied range of loads is representative of the global material behavior. Nevertheless, we did not obtain a remarkable decrease of the elastic modulus with load whichever the indenter used, the dispersion is almost constant for all the load ranges; the scattering at low load increases because the penetrated volumes are smaller giving a local composite response.

The response of a material by classic mechanical tests such as traction or uniaxial compression could differ to the material response by indentation. For example, in indentation tests the mean contact pressure required to initiated yield is higher than in uniaxial compression, due to the shear component responsible for plastic flow; in an indentation stress field, the stress material is constrained by the surrounding matrix, with an important hydrostatic component [6]. Obviously, the differences between classical tests and indentation tests depends on the type of material, for a material with a complex microstructure, probably the gap between the response given by both kinds of tests would be higher. During the penetration of the indenter in the brake pad, complex stress-strain fields are developed due to its microstructure.

Besides, the higher values obtained by indentation testing comparing with the homogenized response by compression tests obtained by Serrano *et al.* [227], could be related in part to some statements given by Gouldstone *et al.* [5] for composite systems regarding the hardness of hard particles embedded in soft matrix, there exist particle agglomeration that leads to a harder response than in the case of the homogenized composite response. The opposite occurs in porous materials, since a local pore crushing would lead to the underestimation of the properties comparing with the composite response. The brake pad material under study would experiment particles agglomeration and pores crushing, linked with complex mechanisms of deformation of the graphite phases accompanied by brittle fracture, work hardening of the matrix, crack formation in ceramic phases, and loss of cohesion between phases due to their different mechanical response, in addition to the material anisotropy. These phenomena are probably intensified during compression tests, especially the loss of cohesion between phases, leading to a decrease of the elastic modulus with the rising load.

To conclude, the estimated properties by macroindentation tests could differ from the overall response by uniaxial compression tests; nevertheless, the indentation tests allow to characterize the material relatively quickly obtaining a local composite response at different depths and locations (Vickers indenter), and a global response close to the bulk material behavior (spherical indenter). Both results would be helpful in further analysis regarding the squeal noise in service, that represents a determinant issue in the study of braking systems [2,205].

V.4. Conclusions

The mechanical characterization of highly heterogeneous brake pad with complex microstructure performed by means of grid indentation in the nanoindentation scale allowed to identify and estimate the intrinsic properties of the components despite the heterogeneity of this material. However, the results are approximations of the actual values, because many factors intervene in the measurements, principally the presence of interfaces, porosity, and high difference between materials properties. The contrast between properties of the phases facilitates its identification by statistical treatment of the results using deconvolution method, nevertheless when the properties are in different orders of magnitude the deconvolution technique by PDF is not very suitable, thus, the phases could be separated by range of values to obtain a better approximation. The volume fractions are rough estimations, because the method does not take into an account the disordered microstructure.

It is valuable to study the elastic modulus and hardness simultaneously, the access to both properties allows the identification of the different phases with similar elastic or plastic properties, approaching the intrinsic properties of each phase.

The analysis of CSM nanoindentation tests requires special attention to the selection of the maximum penetration depth to obtain the intrinsic properties of the phases in a composite material. If the difference between the mechanical properties is elevated like in the brake pad between graphite, metallic matrix and ceramics, the mechanical response is quickly affected at shallow penetrations even if the characteristic length scale of the material is supposed to be larger. Therefore, the average result of the entire loading part is meaningless because a local composite response is being measured upon loading. It is better to extract the values at shallow penetration depths putting attention in the material roughness. For this study, we chose the penetration depths of 100 nm and 250 nm to measure the mechanical properties. The resulting properties were similar for both penetration depths.

The multilayer analysis of nanoindentation tests arises in suitable estimates of the intrinsic properties of each phase. The rules of thumb of 10 % of penetration depth for hardness and 1% for elastic modulus are not fulfilled in the brake pad regarding the characteristic length scales in the material, due to the very compliant effect of the graphite phase. Both properties behave similarly, they lead to a composite response at small displacements, due to the complex stress-strain fields developed in the material. The results obtained through the analysis of each indentation curve by the multilayer model may lead to more precise results, helping to identify the properties related to the interfaces, porosity and stacked phases that helps to simulate a model material with a distribution of elastic modulus in the surface and in thickness, necessary in the analysis of the squeal noise in the braking system.

The Reuss model leads to a close approximation of the material properties that are comparable to the results obtained by macroindentation tests with Vickers indenter. Multicyclic macroindentation tests exhibit an almost constant variation of the mechanical properties with load presenting high dispersion, because the indentation depth is smaller than the required theoretical depth to achieve the global properties of the material, the response depends on the phases configuration. Spherical macroindentation tests lead to a good approximation of the elastic modulus of the brake pad. Nevertheless, the response given by these tests with both indenters is overestimated comparing with compression tests due to the differences in the material response under indentation, nevertheless macroindentation tests would give a quickly response associated to an important dispersion that is representative of the material.

Similarly, that through the analysis of the nanoindentation curves through the multilayer model, the local composite response obtained by each macroindentation test allows to know the distribution of mechanical properties in the material, which is helpful in the analysis of the squeal noise during service.

General conclusions

This work addressed the study of multiscale indentation applied to the study of heterogeneous materials. Within this objective, the research was divided in two parts, firstly the study of industrial metallic materials in order to establish relations across scales of measurement using three different instruments (10 mN up to 2 kN), looking for the validation of relations used to obtain the mechanical properties (elastic modulus and hardness) understanding the important uncertainties related to the test.

The second stage of the work consisted in the study of brake pad materials, after comprehension of the instruments functioning and material response in the "homogeneous" metallic materials. The purpose in this stage was to obtain the mechanical properties of the individual phases at the nano scale and the global properties at the macro scale.

Both stages lead to the following concluding remarks:

- Through the study of the unloading curves by multiscale indention we realized that we needed a more robust approach to fit the curve, especially for materials with small elastic recovery. Therefore, we proposed a new approach of the model of Oliver and Pharr that states the reciprocal function of the power law model, making the displacement the dependent variable, the expression was additional set to be dimensionless in order to allow the comparison of the fitting coefficients for different forces and scales. By Monte Carlo simulations introducing a random Gaussian noise to the displacement data, we verify that the robustness of the method is improved in comparison with the Oliver and Pharr model leading to a more accurate calculation of the mechanical properties. Consequently, we used this methodology to fit all the experimental curves for the further results.
- Multiscale indentation on metallic specimens leads to interesting conclusions based on an important question: do the obtained mechanical properties change with the scale of measurement in indentation?
    - The dimensionless load-displacement curves showed that the different instruments lead to similar responses for the unloading curves, the differences among the scales are similar to those at the same scale of load. In addition, this dimensionless representation allows to classify the materials according to its E/H ratio using the unloading curves, which suggests that this curve contents information about the elastic and plastic behavior of the material and that the

curves apparently do not correspond to a uniqueness response for a particular material.

- In the analysis of the load-displacement curve regardless the scale of measurement the frame compliance affects significantly the determination of the elastic modulus and it is rather a response of diverse elements on the indentation system such as mounting and fixation of the specimen and indenter, indenter column, connection between internal elements, translation mechanisms. Thus, is not just linked to the load frame.
- The area function of the indenter tip is critical in the determination of elastic modulus and hardness at the nanoindenter; similarly, at the microindenter in the range of loads under 1 N the consideration of the tip defect is important for the determination of the mechanical properties. At the macro scale, the correction of the tip defect in the contact area function does not modify the determination of the properties.
- The elastic modulus measured by indentation are comparable to the values reported in the literature if pile-up is considered (validating the relation used for the contact depth), it is representative of the intrinsic material response and the hypothesis of being constant at any load is respected, regardless the local nano scale heterogeneities of the steel and aluminum samples. Nevertheless, the error related to the instruments and to the tests themselves could lead to important modifications of this property (~20%). The work of indentation methodology gives good estimations of the elastic modulus, however the applicability in the stainless steel 316L (where complex mechanisms are apparently developed underneath the indenter) is questionable since elastic modulus and hardness are different from the values calculated directly from the parameters of the load-displacement curve. The determination of the work of indentation is as well strongly affected by the correction of the system compliance.
- Multicyclic and CSM tests give a similar response to the classic tests, with respect to the evaluation of the elastic modulus. For hardness determination, the response by multicyclic tests at microindentation differs slightly from the classic tests. Nevertheless, the materials do not present the same trend, rendering difficult to elucidate if this difference corresponds to the material response, dissimilar mechanisms, or to the instrument.
- Hardness results exhibit dependency on the applied load and consequently with the scale of measurement. For steel samples, there exist a continuity of the

  hardness values through the scales. For the microindenter the response is usually slightly shifted from the results found by the nano and macro indenters. The dispersion of the data is important especially for multicyclic tests, rather linked to the instrument functioning.
  - The instrumented indentation testing is affected by an important number of uncertainties sources. In order to get reliable results, it is needed to know the system functioning to estimate the correct uncertainties related to the measurements, and correlate it with the dispersion of the results.
- Multiscale indentation on brake pads allowed to obtain elastic modulus and hardness of this complex material, the achieved response was comparable to the macro characterization performed by compression tests, the principal concluding remarks are:
  - Characterization by grid indentation at the nanoindentation scale allowed to identify and estimate the intrinsic properties of the components despite the heterogeneity of this material. The results are approximations of the actual values due to the presence of interfaces and porosity. The significant difference (2 orders of magnitude) between the materials properties affects the applicability of the deconvolution method (separation of Gaussian distributions), hereafter, we separated by type of material (metals, ceramics and graphite) to obtain a better approximation.
  - Elastic modulus and hardness must be studied simultaneously; the access to both properties allows to distinguish phases with similar elastic and different plastic properties (or the opposite), approaching the intrinsic properties of each phase.
  - Selection of a maximum penetration depth to obtain the intrinsic properties of each phase with CSM tests is critical. If the difference between the mechanical properties is elevated like in the brake pad between graphite and ceramics, the mechanical response is modified at shallow penetrations even for larger length scales. The properties should be taken at small penetration depths. For this study, we chose the penetration depths of 100 nm and 250 nm to measure the mechanical properties. The resulting properties were similar for both penetration depths, indicating that the roughness effect on the measurements is not significant.
  - The multilayer analysis of nanoindentation tests gives suitable estimates of the intrinsic properties of each phase. The rules of thumb 10 % of penetration depth for hardness and 1% for elastic modulus are not fulfilled in the brake pad regarding the characteristic length scales in the material, related to the very

compliant effect of the graphite phase. The application of a multilayer model helps to identify the properties related to the interfaces, porosity and stacked phases for simulate a model material with a distribution of elastic modulus in the surface and in thickness, necessary in the analysis of the squeal noise in the braking system.

- Multicyclic macroindentation tests exhibit high dispersion of the mechanical properties that is kept almost constant with load. The mechanical response depends on the phases configuration. Spherical macroindentation tests lead to a good approximation of the elastic modulus of the brake pad. Nevertheless, the response given by these tests with both indenters are slightly overestimated comparing with compression tests due to the differences in the material response under indentation. The local composite response obtained by each macroindentation test allows to know the distribution of mechanical properties in the material, which is helpful in the analysis of the squeal noise during service. All these results indicate that, irrespective of the material complexity, it is possible to characterize it by means of instrumented indentation; nevertheless, the dispersion of results is significant and the interpretation should be evaluated carefully, especially if the composite materials contain viscoelastic or viscoelastic-plastic components.

This study enables us to highlight different points that deserve to be deepened:

- A rigorous study of the uncertainties is necessary. Typically, in the literature and in this work, the uncertainties are only representative of the stochastic part, that means the dispersion of the experimental results. However, we know that the indentation test is affected by several sources of uncertainties. Consequently, we wish to perform an exhaustively study using some concepts commonly applied in the 3D coordinate measuring machines, this concept concern to the ideas of virtual machines or numerical twin. To accomplish this study, we are going to use firstly an Ishikawa diagram (5M), where the main sources of uncertainty are identified. Therefore, taking the specific information of each instrument, schematizing and simulating the testing process using Monte Carlo method, we will be able to estimate the correct order of magnitude for the uncertainties.
- Study of other materials (polymers, ceramics, other metals) by indentation at various scales to verify whether the relationships used in this research are valid. Identification, of the effect of the loading rate.

- Analysis of the dimensionless load-displacement curves looking to elucidate what is the actual information contained on them, and the uniqueness for each material that it is still a matter of concern in instrumented indentation. Besides, it is necessary to corroborate the material dependence on the fitting parameters of the unloading curve, particularly G.
- Study of the mechanical properties of the brake pad after use, to evaluate the properties evolution after severe conditions of wear and temperature.

References

[1] P. Dufrenoy, V. Magnier, R. Mann, A.-L. Cristol, and I. Serrano, “Methodology Linking Formulation, Microstructure and Mechanical Properties of Friction Materials,” SAE Technical Paper, *SAE Inter.*, Sep. 2016.

[2] V. Magnier, D. Naidoo Ramasami, J. F. Brunel, P. Dufrénoy, and T. Chancelier, “History effect on squeal with a mesoscopic approach to friction materials,” *Tribol. Int.*, vol. 115, pp. 600–607, Nov. 2017.

[3] R. Mann, V. Magnier, J.-F. Brunel, F. Brunel, P. Dufrénoy, and M. Henrion, “Relation between mechanical behavior and microstructure of a sintered material for braking application,” *Wear*, vol. 386–387, pp. 1–16, Sep. 2017.

[4] S. Panier, P. Dufrénoy, and D. Weichert, “An experimental investigation of hot spots in railway disc brakes,” *Wear*, vol. 256, pp. 764–773, Apr. 2004.

[5] A. Gouldstone, N. Chollacoop, M. Dao, J. Li, A. Minor, and Y. Shen, “Indentation across size scales and disciplines: Recent developments in experimentation and modeling,” *Acta Mater.*, vol. 55, pp. 4015–4039, Jul. 2007.

[6] A. C. Fischer-Cripps, Nanoindentation, 3rd ed. New York, NY: Springer New York, 2011.

[7] I. M. Hutchings, “The contributions of David Tabor to the science of indentation hardness,” *J. Mater. Res.*, vol. 24, pp. 581–589, Mar. 2009.

[8] K. Herrmann, *Hardness Testing: Principles and Applications*. ASM International, 2011.

[9] S. M. Walley, “Historical origins of indentation hardness testing,” *Mater. Sci. Technol.*, vol. 28, pp. 1028–1044, Oct. 2012.

[10] M. R. VanLandingham, “Review of instrumented indentation,” *J. Res. Natl. Inst. Stand. Technol.*, vol. 108, pp. 249–265, Aug. 2003.

[11] J. B. Pethicai, R. Hutchings, and W. C. Oliver, “Hardness measurement at penetration depths as small as 20 nm,” *Philos. Mag. A*, vol. 48, pp. 593–606, Apr. 1983.

[12] J. R. Pratt, J. A. Kramar, D. B. Newell, and D. T. Smith, “Review of SI traceable force metrology for instrumented indentation and atomic force microscopy,” *Meas. Sci. Technol.*, vol. 16, pp. 2129–2137, Nov. 2005.

[13] B. Moser, J. Kuebler, H. Meinhard, W. Muster, and J. Michler, “Observation of Instabilities during Plastic Deformation by in-situ SEM Indentation Experiments,” *Adv. Eng. Mater.*, vol. 7, pp. 388–392, May 2005.

[14] M. A. Monclus, T. J. Young, and D. Di Maio, “AFM indentation method used for elastic modulus characterization of interfaces and thin layers,” *J. Mater. Sci.*, vol. 45, pp. 3190–3197, Jun. 2010.

[15] H.-J. Albrecht, A. Juritza, K. Muller, W. H. Muller, J. Sterthaus, J. Villain, and A. Vogliano, “Interface reactions in microelectronic solder joints and associated intermetallic compounds: an investigation of their mechanical properties using nanoindentation,” in *Electronics Packaging Technology*, Singapore, 2003, pp. 726–731.

[16] C. Z. Liu and J. Chen, “Nanoindentation of lead-free solders in microelectronic packaging,” *Mater. Sci. Eng. A*, vol. 448, pp. 340–344, Mar. 2007.

[17] V. Rizov, A. Shipsha, and D. Zenkert, “Indentation study of foam core sandwich composite panels,” *Compos. Struct.*, vol. 69, pp. 95–102, Jun. 2005.

[18] E. A. Abdallah, C. Bouvet, S. Rivallant, B. Broll, and J.-J. Barrau, “Experimental analysis of damage creation and permanent indentation on highly oriented plates,” *Compos. Sci. Technol.*, vol. 69, pp. 1238–1245, Jun. 2009.

[19] H. Fischer, “Fracture toughness of dental ceramics: comparison of bending and indentation method,” *Dent. Mater.*, vol. 18, pp. 12–19, Jan. 2002.

[20] B. Van Meerbeek, G. Willems, J. P. Celis, J. R. Roos, M. Braem, P. Lambrechts, and G. Vanherle, “Assessment by Nano-indentation of the Hardness and Elasticity of the Resin-Dentin Bonding Area,” *J. Dent. Res.*, vol. 72, pp. 1434–1442, Oct. 1993.

[21] M. V. Swain and B. R. Lawn, “Indentation fracture in brittle rocks and glasses,” *Int. J. Rock Mech. Min. Sci. Geomech. Abstr.*, vol. 13, pp. 311–319, Nov. 1976.

[22] Y. Sun, M. Aman, and D. N. Espinoza, “Assessment of mechanical rock alteration caused by CO_2 water mixtures using indentation and scratch experiments,” *Int. J. Greenh. Gas Control*, vol. 45, pp. 9–17, Feb. 2016.

[23] M. Lima, C. Godoy, P. Modenesi, J. Avelar-Batista, A. Davison, and A. Matthews, “Coating fracture toughness determined by Vickers indentation: an important parameter in cavitation erosion resistance of WC–Co thermally sprayed coatings,” *Surf. Coat. Technol.*, vol. 177–178, pp. 489–496, Jan. 2004.

[24] R. S. Lima, S. E. Kruger, G. Lamouche, and B. R. Marple, “Elastic Modulus Measurements via Laser-Ultrasonic and Knoop Indentation Techniques in Thermally Sprayed Coatings,” *J. Therm. Spray Technol.*, vol. 14, pp. 52–60, Mar. 2005.

[25] J. L. He and S. Veprek, “Finite element modeling of indentation into superhard coatings,” *Surf. Coat. Technol.*, vol. 163–164, pp. 374–379, Jan. 2003.

[26] D. Chicot, E. S. Puchi-Cabrera, R. Aumaitre, G. Bouscarrat, C. Dublanche-Tixier, F. Roudet, and M. H. Staia, “Elastic modulus of TiHfCN thin films by instrumented indentation,” *Thin Solid Films*, vol. 522, pp. 304–313, Nov. 2012.

[27] J. Zhang, M. M. Michalenko, E. Kuhl, and T. C. Ovaert, “Characterization of indentation response and stiffness reduction of bone using a continuum damage model,” *J. Mech. Behav. Biomed. Mater.*, vol. 3, pp. 189–202, Feb. 2010.

[28] M. Zhang, Y. P. Zheng, and A. F. T. Mak, “Estimating the effective Young’s modulus of soft tissues from indentation tests—nonlinear finite element analysis of effects of friction and large deformation,” *Med. Eng. Phys.*, vol. 19, pp. 512–517, Sep. 1997.

[29] C. T. McKee, J. A. Last, P. Russell, and C. J. Murphy, “Indentation Versus Tensile Measurements of Young’s Modulus for Soft Biological Tissues,” *Tissue Eng. Part B Rev.*, vol. 17, pp. 155–164, Jun. 2011.

[30] S. M. Goh, M. N. Charalambides, and J. G. Williams, “Characterization of the nonlinear viscoelastic constitutive properties of mild cheddar cheese from indentation tests,” *J. Texture Stud.*, vol. 36, pp. 459–477, Dec. 2005.

[31] N. Ozkan, H. Xin, and X. D. Chen, “Application of a Depth Sensing Indentation Hardness Test to Evaluate the Mechanical Properties of Food Materials,” *J. Food Sci.*, vol. 67, pp. 1814–1820, Jun. 2002.

[32] W. A. Curtin and R. E. Miller, “Atomistic/continuum coupling in computational materials science,” *Model. Simul. Mater. Sci. Eng.*, vol. 11, pp. R33–R68, May 2003.

[33] J. Knap and M. Ortiz, “Effect of Indenter-Radius Size on Au(001) Nanoindentation,” *Phys. Rev. Lett.*, vol. 90, Jun. 2003.

[34] M. Griepentrog, C. Ullner, and A. Duck, “Instrumented indentation test for hardness and materials parameter from millinewtons to kilonewtons,” in Proceedings of the International Conference on Force, Mass, Torque, Hardness and Civil Engineering Metrology in the Age Globalization, Celle, Germany, 2002, vol. 1685, pp. 105–112.

[35] Y.-T. Cheng and C.-M. Cheng, “Scaling, dimensional analysis, and indentation measurements,” *Mater. Sci. Eng. R Rep.*, vol. 44, pp. 91–149, Aug. 2004.

[36] L. Riester, P. J. Blau, E. Lara-Curzio, and K. Breder, “Nanoindentation with a Knoop indenter,” *Thin Solid Films*, vol. 377, pp. 635–639, Dec. 2000.

[37] T. Chudoba, P. Schwaller, R. Rabe, J.-M. Breguet, and J. Michler, “Comparison of nanoindentation results obtained with Berkovich and cube-corner indenters,” *Philos. Mag.*, vol. 86, pp. 5265–5283, Feb. 2006.

[38] E. Herbert, G. Pharr, W. Oliver, B. Lucas, and J. Hay, “On the measurement of stress–strain curves by spherical indentation,” *Proc. 28th Int. Conf. Metall. Coat. Thin Films*, vol. 398–399, pp. 331–335, Nov. 2001.

[39] M. Beghini, L. Bertini, and V. Fontanari, “Evaluation of the stress–strain curve of metallic materials by spherical indentation,” *Int. J. Solids Struct.*, vol. 43, pp. 2441–2459, Apr. 2006.

[40] Y. Cao, D. Ma, and D. Raabe, “The use of flat punch indentation to determine the viscoelastic properties in the time and frequency domains of a soft layer bonded to a rigid substrate,” *Acta Biomater.*, vol. 5, pp. 240–248, Jan. 2009.

[41] R. Cagliero, G. Barbato, G. Maizza, and G. Genta, “Measurement of elastic modulus by instrumented indentation in the macro-range: Uncertainty evaluation,” *Int. J. Mech. Sci.*, vol. 101–102, pp. 161–169, Oct. 2015.

[42] G. E. Dieter, *Mechanical metallurgy*. McGraw-Hill, 1976.

[43] L. Riester, T. J. Bell, and A. C. Fischer-Cripps, “Analysis of depth-sensing indentation tests with a Knoop indenter,” *J. Mater. Res.*, vol. 16, pp. 1660–1667, Jun. 2001.

[44] D. Ferro, S. M. Barinov, J. V. Rau, A. Latini, R. Scandurra, and B. Brunetti, "Vickers and Knoop hardness of electron beam deposited ZrC and HfC thin films on titanium," *Surf. Coat. Technol.*, vol. 200, pp. 4701–4707, Apr. 2006.

[45] T. Zhang, Y. Feng, R. Yang, and P. Jiang, "A method to determine fracture toughness using cube-corner indentation," *Scr. Mater.*, vol. 62, pp. 199–201, Feb. 2010.

[46] W. D. Nix and H. Gao, "Indentation size effects in crystalline materials: A law for strain gradient plasticity," *J. Mech. Phys. Solids*, vol. 46, pp. 411–425, Mar. 1998.

[47] Z. Shi, X. Feng, Y. Huang, J. Xiao, and K. C. Hwang, "The equivalent axisymmetric model for Berkovich indenters in power-law hardening materials," *Int. J. Plast.*, vol. 26, pp. 141–148, Jan. 2010.

[48] W. C. Oliver and G. M. Pharr, "Measurement of hardness and elastic modulus by instrumented indentation: Advances in understanding and refinements to methodology," *J. Mater. Res.*, vol. 19, pp. 3–20, 2004.

[49] L. Min, C. Wei-min, L. Nai-gang, and W. Ling-Dong, "A numerical study of indentation using indenters of different geometry," *J. Mater. Res.*, vol. 19, pp. 73–78, Jan. 2004.

[50] J. Qin, Y. Huang, J. Xiao, and K. C. Hwang, "The equivalence of axisymmetric indentation model for three-dimensional indentation hardness," *J. Mater. Res.*, vol. 24, pp. 776–783, Mar. 2009.

[51] A. G. Atkins and D. Tabor, "Plastic indentation in metals with cones," *J. Mech. Phys. Solids*, vol. 13, pp. 149–164, Jun. 1965.

[52] R. Hill, B. Storakers, and A. B. Zdunek, "A theoretical study of the Brinell hardness test," *Proc. R. Soc. Lond. Ser. Math. Phys. Sci.*, pp. 301–330, 1989.

[53] S. D. Mesarovic and N. A. Fleck, "Spherical indentation of elastic–plastic solids," in *Proceedings of the Royal Society of London A: Mathematical, Physical and Engineering Sciences*, 1999, vol. 455, pp. 2707–2728.

[54] A. E. H. Love, "Boussinesq's problem for a rigid cone," *Q. J. Math.*, vol. 10, pp. 161–175, Jan.1939.

[55] I. N. Sneddon, "The relation between load and penetration in the axisymmetric Boussinesq problem for a punch of arbitrary profile," *Int. J. Eng. Sci.*, vol. 3, pp. 47–57, May 1965.

[56] D. Tabor, "The hardness of solids," *Rev. Phys. Technol.*, vol. 1, pp. 145–179, Jan. 1970.

[57] P.-L. Larsson, A. E. Giannakopoulos, E. SÖderlund, D. J. Rowcliffe, and R. Vestergaard, "Analysis of Berkovich indentation," *Int. J. Solids Struct.*, vol. 33, pp. 221–248, Jan. 1996.

[58] K. Zeng and C.h. Chiu, "An analysis of load–penetration curves from instrumented indentation," *Acta Mater.*, vol. 49, pp. 3539–3551, Oct. 2001.

[59] J. Gubicza, A. Juhász, P. Tasnádi, P. Arató, and G. Vörös, "Determination of the hardness and elastic modulus from continuous vickers indentation testing," *J. Mater. Sci.*, vol. 31, pp. 3109–3114, Jan. 1996.

[60] M. Sakai, "Energy principle of the indentation-induced inelastic surface deformation and hardness of brittle materials," *Acta Metall. Mater.*, vol. 41, pp. 1751–1758, Jun. 1993.

[61] J. Malzbender, G. de With, and J. den Toonder, "The P–h2 relationship in indentation," *J. Mater. Res.*, vol. 15, pp. 1209–1212, May 2000.

[62] M. F. Doerner and W. D. Nix, "A method for interpreting the data from depth-sensing indentation instruments," *J. Mater. Res.*, vol. 1, pp. 601–609, Aug. 1986.

[63] W. C. Oliver and G. M. Pharr, "An improved technique for determining hardness and elastic modulus using load and displacement sensing indentation experiments," *J. Mater. Res.*, vol. 7, pp. 1564–1583, Jun. 1992.

[64] G. M. Pharr and A. Bolshakov, "Understanding nanoindentation unloading curves," *J. Mater. Res.*, vol. 17, pp. 2660–2671, Oct. 2002.

[65] T. Chudoba and N. M. Jennett, "Higher accuracy analysis of instrumented indentation data obtained with pointed indenters," *J. Phys. Appl. Phys.*, vol. 41, pp. 215407, Nov. 2008.

[66] J. C. Hay, A. Bolshakov, and G. M. Pharr, "A critical examination of the fundamental relations used in the analysis of nanoindentation data," *J. Mater. Res.*, vol. 14, pp. 2296–2305, Jun. 1999.

[67] R. B. King, "Elastic analysis of some punch problems for a layered medium," *Int. J. Solids Struct.*, vol. 23, pp. 1657–1664, Apr.1987.

[68] J. Gong, H. Miao, and Z. Peng, "Analysis of the nanoindentation data measured with a Berkovich indenter for brittle materials: effect of the residual contact stress," *Acta Mater.*, vol. 52, pp. 785–793, Feb. 2004.

[69] M. Dao, N. Chollacoop, K. J. Van Vliet, T. A. Venkatesh, and S. Suresh, "Computational modeling of the forward and reverse problems in instrumented sharp indentation," *Acta Mater.*, vol. 49, pp. 3899–3918, Nov. 2001.

[70] D. Chicot and A. Tricoteaux, *Mechanical Properties of Ceramic by Indentation: Principle and Applications*. INTECH Open Access Publisher, 2010.

[71] A. Iost and R. Bigot, "Indentation size effect: reality or artefact?" *J. Mater. Sci.*, vol. 31, pp. 3573–3577, Jan. 1996.

[72] J. L. Bucaille, S. Stauss, E. Felder, and J. Michler, "Determination of plastic properties of metals by instrumented indentation using different sharp indenters," *Acta Mater.*, vol. 51, pp. 1663–1678, Apr. 2003.

[73] Y.-T. Cheng and Z. Li, "Hardness obtained from conical indentations with various cone angles," *J. Mater. Res.*, vol. 15, pp. 2830–2835, Dec. 2000.

[74] D. Tabor, "A Simple Theory of Static and Dynamic Hardness," *Proc. R. Soc. Math. Phys. Eng. Sci.*, vol. 192, pp. 247–274, Feb. 1948.

[75] M. R. VanLandingham, "Review of instrumented indentation," *J. Res. Natl. Inst. Stand. Technol.*, vol. 108, pp. 249–265, Aug. 2003.

[76] W. W. Gerberich, W. Yu, D. Kramer, A. Strojny, D. Bahr, E. Lilleodden, and J. Nelson, "Elastic loading and elastoplastic unloading from nanometer level indentations for modulus determinations," *J. Mater. Res.*, vol. 13, pp. 421–439, Feb. 1998.

[77] M. Troyon and L. Huang, "Critical Examination of the Two-slope Method in Nanoindentation," *J. Mater. Res.*, vol. 20, pp. 2194–2198, Aug. 2005.

[78] W. C. Oliver, "Alternative technique for analyzing instrumented indentation data," *J. Mater. Res.*, vol. 16, pp. 3202–3206, Nov. 2001.

[79] T. F. Page, G. M. Pharr, J. C. Hay, W. C. Oliver, B. N. Lucas, E. Herbert, and L. Riester, "Nanoindentation Characterization of Coated Systems: P/S^2 - A New Approach Using the Continuous Stiffness Technique," *MRS Proc.*, vol. 522, Jan. 1998.

[80] J. Malzbender and G. de With, "Indentation load–displacement curve, plastic deformation, and energy," *J. Mater. Res.*, vol. 17, pp. 502–511, Feb. 2002.

[81] K. Herrmann, N. Jennett, W. Wegener, J. Meneve, K. Hasche, and R. Seemann, "Progress in determination of the area function of indenters used for nanoindentation," *Thin Solid Films*, vol. 377–378, pp. 394–400, Dec. 2000.

[82] J. Thurn and R. F. Cook, "Simplified Area Function for Sharp Indenter Tips in Depth-sensing Indentation," *J. Mater. Res.*, vol. 17, pp. 1143–1146, May 2002.

[83] H. Bei, E. P. George, J. L. Hay, and G. M. Pharr, "Influence of Indenter Tip Geometry on Elastic Deformation during Nanoindentation," *Phys. Rev. Lett.*, vol. 95, Jul. 2005.

[84] M. Troyon and L. Huang, "Correction factor for contact area in nanoindentation measurements," *J. Mater. Res.*, vol. 20, pp. 610–617, Mar. 2005.

[85] A. R. Franco Jr., G. Pintaúde, A. Sinatora, C. E. Pinedo, and A. P. Tschiptschin, "The use of a vickers indenter in depth sensing indentation for measuring elastic modulus and vickers hardness," *Mater. Res.*, vol. 7, pp. 483–491, Sep. 2004.

[86] J. Antunes, A. Cavaleiro, L. Menezes, M. Simões, and J. Fernandes, "Ultra-microhardness testing procedure with Vickers indenter," *Surf. Coat. Technol.*, vol. 149, pp. 27–35, Jan. 2002.

[87] L. A. Berla, A. M. Allen, S. M. Han, and W. D. Nix, "A physically based model for indenter tip shape calibration for nanoindentation," *J. Mater. Res.*, vol. 25, pp. 735–745, Apr. 2010.

[88] J. L. Loubet, M. Bauer, A. Tonck, S. Bec, and B. Gauthier-Manuel, "Nanoindentation with a surface force apparatus," in *Mechanical Properties and Deformation Behavior of Materials Having Ultra-Fine Microstructures*, Dordrecht: Springer, 1993, pp. 429–447.

[89] K. Herrmann, K. Hasche, F. Pohlenz, and R. Seemann, "Characterisation of the geometry of indenters used for the micro- and nanoindentation method," *Measurement*, vol. 29, pp. 201–207, Apr. 2001.

[90] D. Chicot, M. Yetna N'Jock, E. S. Puchi-Cabrera, A. Iost, M. H. Staia, G. Louis, G. Bouscarrat, and R. Aumaitre, "A contact area function for Berkovich nanoindentation: Application to hardness determination of a TiHfCN thin film," *Thin Solid Films*, vol. 558, pp. 259–266, May 2014.

[91] J. Woirgard and J. C. Dargenton, "An alternative method for penetration depth determination in nanoindentation measurements," *J. Mater. Res.*, vol. 12, pp. 2455–2458, Sep. 1997.

[92] A. Bolshakov and G. M. Pharr, “Influences of pileup on the measurement of mechanical properties by load and depth sensing indentation techniques,” *J. Mater. Res.*, vol. 13, pp. 1049–1058, Apr. 1998.

[93] K. L. Johnson, “The correlation of indentation experiments,” *J. Mech. Phys. Solids*, vol. 18, pp. 115–126, Apr. 1970.

[94] X. Zhou, Z. Jiang, H. Wang, and R. Yu, “Investigation on methods for dealing with pile-up errors in evaluating the mechanical properties of thin metal films at sub-micron scale on hard substrates by nanoindentation technique,” *Mater. Sci. Eng. A*, vol. 488, pp. 318–332, Aug. 2008.

[95] Y. Choi, H.-S. Lee, and D. Kwon, “Analysis of sharp-tip-indentation load–depth curve for contact area determination taking into account pile-up and sink-in effects,” *J. Mater. Res.*, vol. 19, pp. 3307–3315, Nov. 2004.

[96] J. L. Hay, W. C. Oliver, A. Bolshakov, and G. M. Pharr, “Using the Ratio of Loading Slope and Elastic Stiffness to Predict Pile-Up and Constraint Factor During Indentation,” *MRS Proc.*, vol. 522, Jan. 1998.

[97] Y. H. Lee, J. H. Hahn, S. H. Nahm, J. I. Jang, and D. Kwon, “Investigations on indentation size effects using a pile-up corrected hardness,” *J. Phys. Appl. Phys.*, vol. 41, pp. 074027, Apr. 2008.

[98] M. Bigerelle, P. E. Mazeran, and M. Rachik, “The first indenter-sample contact and the indentation size effect in nano-hardness measurement,” *Mater. Sci. Eng. C*, vol. 27, pp. 1448–1451, Sep. 2007.

[99] G. Hochstetter, A. Jimenez, and J. L. Loubet, “Strain-rate effects on hardness of glassy polymers in the nanoscale range. Comparison between quasi-static and continuous stiffness measurements,” *J. Macromol. Sci. Part B*, vol. 38, pp. 681–692, Sep. 1999.

[100] M. Yetna N’jock, D. Chicot, J. M. Ndjaka, J. Lesage, X. Decoopman, F. Roudet, and A. Mejias, “A criterion to identify sinking-in and piling-up in indentation of materials,” *Int. J. Mech. Sci.*, vol. 90, pp. 145–150, Jan. 2015.

[101] M. Tan, “A study of indentation work in homogeneous materials,” *J. Mater. Res.*, vol. 21, pp. 1363–1374, Jun. 2006.

[102] J. R. Tuck, A. M. Korsunsky, S. J. Bull, and R. I. Davidson, “On the application of the work-of-indentation approach to depth-sensing indentation experiments in coated systems,” *Surf. Coat. Technol.*, vol. 137, pp. 217–224, Mar. 2001.

[103] M. Yetna N’Jock, F. Roudet, M. Idriss, O. Bartier, and D. Chicot, “Work-of-indentation coupled to contact stiffness for calculating elastic modulus by instrumented indentation,” *Mech. Mater.*, vol. 94, pp. 170–179, Mar. 2016.

[104] D. Chicot, M. Y. N’Jock, F. Roudet, X. Decoopman, M. H. Staia, and E. S. Puchi-Cabrera, “Some improvements for determining the hardness of homogeneous materials from the work-of-indentation,” *Int. J. Mech. Sci.*, vol. 105, pp. 279–290, Jan. 2016.

[105] M. Lei, B. Xu, Y. Pei, H. Lu, and Y. Q. Fu, “Micro-mechanics of nanostructured carbon/shape memory polymer hybrid thin film,” *Soft Matter*, vol. 12, pp. 106–114, Oct. 2015.

[106] Y.-T. Cheng, Z. Li, and C.-M. Cheng, “Scaling relationships for indentation measurements,” *Philos. Mag. A*, vol. 82, pp. 1821–1829, Jul. 2002.

[107] J. L. Loubet, J. M. Georges, O. Marchesini, and G. Meille, “Vickers indentation curves of magnesium oxide (MgO),” *J. Tribol.*, vol. 106, pp. 43–48, Jan. 1984.

[108] B. R. Lawn and V. R. Howes, “Elastic recovery at hardness indentations,” *J. Mater. Sci.*, vol. 16, pp. 2745–2752, Oct. 1981.

[109] J. Menčík and M. Swain, “Micro-indentation Test with Pointed Indenters,” *Met. Forum*, vol. 18, pp. 277–288, Jan. 1994.

[110] A. C. Fischer-Cripps, “Critical review of analysis and interpretation of nanoindentation test data,” *Surf. Coat. Technol.*, vol. 200, pp. 4153–4165, Apr. 2006.

[111] J. Hay, “Introduction to Instrumented Indentation Testing,” *Exp. Tech.*, vol. 33, pp. 66–72, Nov. 2009.

[112] K. J. Van Vliet, L. Prchlik, and J. F. Smith, “Direct measurement of indentation frame compliance,” *J. Mater. Res.*, vol. 19, pp. 325–331, Jan. 2004.

[113] C. Ullner, E. Reimann, H. Kohlhoff, and A. Subaric-Leitis, “Effect and measurement of the machine compliance in the macro range of instrumented indentation test,” *Measurement*, vol. 43, pp. 216–222, Feb. 2010.

[114] G. Barbato, G. Genta, R. Cagliero, M. Galetto, M. J. Klopfstein, D. A. Lucca, and R. Levi, “Uncertainty evaluation of indentation modulus in the nano-range: Contact stiffness contribution,” *CIRP Ann. - Manuf. Technol.*, vol. 66, pp. 495–498, Apr. 2017.

[115] G. A. Crawford, N. Chawla, M. Koopman, K. Carlisle, and K. K. Chawla, "Effect of Mounting Material Compliance on Nanoindentation Response of Metallic Materials," *Adv. Eng. Mater.*, vol. 11, pp. 45–51, Jan. 2009.

[116] "Nano Indenter XP: Operating instructions V.1.1". Nano Instruments Innovation Center, Oak Ride, Tennessee.

[117] T. Chudoba, N. Schwarzer, and F. Richter, "Determination of elastic properties of thin films by indentation measurements with a spherical indenter," *Surf. Coat. Technol.*, vol. 127, pp. 9–17, May 2000.

[118] C. Ullner, "Requirement of a robust method for the precise determination of the contact point in the depth sensing hardness test," *Measurement*, vol. 27, pp. 43–51, Jan. 2000.

[119] S. R. Kalidindi and S. Pathak, "Determination of the effective zero-point and the extraction of spherical nanoindentation stress–strain curves," *Acta Mater.*, vol. 56, pp. 3523–3532, Aug. 2008.

[120] J. Marteau, P.-E. Mazeran, S. Bouvier, and M. Bigerelle, "Zero-Point Correction Method for Nanoindentation Tests to Accurately Quantify Hardness and Indentation Size Effect," *Strain*, vol. 48, pp. 491–497, Dec. 2012.

[121] J. R. Pratt, D. T. Smith, D. B. Newell, J. A. Kramar, and E. Whitenton, "Progress toward Système International d'Unités traceable force metrology for nanomechanics," *J. Mater. Res.*, vol. 19, pp. 366–379, Jan. 2004.

[122] J. D. Ellis, S. T. Smith, and R. J. Hocken, "Alignment uncertainties in ideal indentation styli," *Precis. Eng.*, vol. 32, pp. 207–214, Jul. 2008.

[123] "The Nano Indenter XP", version 16, no. D1418XPA-10629. MTS System Corporation, 2002.

[124] A. C. Fischer-Cripps, "A review of analysis methods for sub-micron indentation testing," *Vacuum*, vol. 58, pp. 569–585, Sep. 2000.

[125] J. Menčík and M. Swain, "Errors associated with depth-sensing microindentation tests," *J. Mater. Res.*, vol. 10, pp. 1491–1501, Jun. 1995.

[126] M. R. VanLandingham, T. F. Juliano, and M. J. Hagon, "Measuring tip shape for instrumented indentation using atomic force microscopy," *Meas. Sci. Technol.*, vol. 16, pp. 2173–2185, Nov. 2005.

[127] ISO 14577-4:2007, Metallic materials- Instrumented indentation test for hardness and materials parameters - Part 4: Test method for metallic and non-metallic coatings.

[128] A. M. Daniel, S. T. Smith, and M. H. Lewis, "A scanning electron microscope based microindentation system," *Rev. Sci. Instrum.*, vol. 65, pp. 632–638, Mar. 1994.

[129] M. R. VanLandingham, J. S. Villarrubia, W. F. Guthrie, and G. F. Meyers, "Nanoindentation of polymers: an overview," *Macromolecular symposia*, vol. 167, pp. 15–44, Mar. 2001.

[130] J. M. Meza, M. C. Farias, R. Souza, and L. J. Riaño, "Using the Ratio: Maximum Load over Unload Stiffness Squared P_m/S_u^2, on the Evaluation of Machine Stiffness and Area Function of Blunt Indenters on Depth-sensing Indentation Equipment." *Mater. Res.*, vol. 10, pp. 437-447, Oct. 2007.

[131] C. G. N. Pelletier, E. C. A. Dekkers, L. E. Govaert, J. M. J. den Toonder, and H. E. H. Meijer, "The influence of indenter-surface misalignment on the results of instrumented indentation tests," *Polym. Test.*, vol. 26, pp. 949–959, Oct. 2007.

[132] Application note: "Indentation Rules of Thumb", Agilent Technologies.

[133] J. Menčík, "Uncertainties and Errors in Nanoindentation," in *Nanoindentation in Materials Science*, J. Nemecek, Ed. InTech, 2012.

[134] Y. Xia, M. Bigerelle, J. Marteau, P.-E. Mazeran, S. Bouvier, and A. Iost, "Effect of surface roughness in the determination of the mechanical properties of material using nanoindentation test: Effect of surface roughness," *Scanning*, vol. 36, pp. 134–149, Jan. 2014.

[135] "ISO 14577-1:2002 - Metallic materials-Instrumented indentation test for hardness and materials parameters-Part 1: Test method.

[136] J. Marteau, M. Bigerelle, Y. Xia, P.-E. Mazeran, and S. Bouvier, "Quantification of first contact detection errors on hardness and indentation size effect measurements," *Tribol. Int.*, vol. 59, pp. 154–162, Mar. 2013.

[137] "Indentation software", version 3, CSM Instruments, 2006.

[138] "Instruction manual for testing machines BTC-FRR.5NT.DP14", Zwick GmbH & Co., 2013.

[139] M. F. Ashby, *Materials selection in mechanical design*, 2nd ed. Oxford; Boston, MA: Butterworth-Heinemann, 1999.

[140] M. Ketabchi, M. A. Shafaat, I. Shafaat, and M. Abbasi, “Effect of cooling rate on mechanical properties of 7075 aluminum rods extruded in semisolid state,” *J. Eng. Mater. Technol.*, vol. 136, pp. 021002, 2014.

[141] “ASM Material Data Sheet.” [Online]. Available: http://asm.matweb.com/search/SpecificMaterial.asp?bassnum=MQ316Q. [Accessed: 09-Aug-2017].

[142] “Data Sheet 316L AK Steel.” [Online]. Available: https://www.google.fr/url?sa=t&rct=j&q=&esrc=s&source=web&cd=1&cad=rja&uact=8&ved=0ahUKEwiByfS_ivrWAhVFfRoKHQd-CrAQFgguMAA&url=http%3A%2F%2Fwww.aksteel.com%2Fpdf%2Fmarkets_products%2Fstainless%2Faustenitic%2F316_316l_data_sheet.pdf&usg=AOvVaw2tKZm0yVyXd67UIIHy9af1

[143] M. Jurczyk, *Bionanomaterials for Dental Applications*. CRC Press, 2012.

[144] M. Troyon and L. Huang, “Comparison of different analysis methods in nanoindentation and influence on the correction factor for contact area,” *Surf. Coat. Technol.*, vol. 201, pp. 1613–1619, Oct. 2006.

[145] Y. P. Cao and J. Lu, “A new method to extract the plastic properties of metal materials from an instrumented spherical indentation loading curve,” *Acta Mater.*, vol. 52, pp. 4023–4032, Aug. 2004.

[146] M. T. Attaf, “Connection between the loading curve models in elastoplastic indentation,” *Mater. Lett.*, vol. 58, pp. 3491–3498, Nov. 2004.

[147] K. K. Jha, N. Suksawang, and A. Agarwal, “Analytical method for the determination of indenter constants used in the analysis of nanoindentation loading curves,” *Scr. Mater.*, vol. 63, pp. 281–284, Aug. 2010.

[148] D. Chicot and D. Mercier, “Improvement in depth-sensing indentation to calculate the universal hardness on the entire loading curve,” *Mech. Mater.*, vol. 40, pp. 171–182, Apr. 2008.

[149] D. Chicot, L. Gil, K. Silva, F. Roudet, E. S. Puchi-Cabrera, M. H. Staia, and D. G. Teer, “Thin film hardness determination using indentation loading curve modelling,” *Thin Solid Films*, vol. 518, pp. 5565–5571, Jul. 2010.

[150] J. Gong, H. Miao, and Z. Peng, “A new function for the description of the nanoindentation unloading data,” *Scr. Mater.*, vol. 49, pp. 93–97, Jul. 2003.

[151] K. K. Jha, N. Suksawang, and A. Agarwal, “A new insight into the work-of-indentation approach used in the evaluation of material’s hardness from nanoindentation measurement with Berkovich indenter,” *Comput. Mater. Sci.*, vol. 85, pp. 32–37, Apr. 2014.

[152] P. R. Bevington and D. K. Robinson, *Data reduction and error analysis for the physical sciences*. McGraw-Hill, 2003.

[153] L. C. Brown and P. Mac Berthouex, *Statistics for environmental engineers*. CRC press, 2002.

[154] K. Smyth, “Nonlinear regression,” in *Encyclopedia of environmetrics*, A. H. El-Shaarawi and W. W. Piegorsch, Eds. New York: Wiley, 2002, pp. 1405–1411.

[155] “4.1.4.2. Nonlinear Least Squares Regression.” [Online]. Available: http://www.itl.nist.gov/div898/handbook/pmd/section1/pmd142.htm. [Accessed: 13-Aug-2016].

[156] K. Madsen, H. B. Nielsen, and O. Tingleff, *Methods for non-linear least squares problems*, 2nd ed. Denmark: Informatics and Mathematical Modeling, Technical University of Denmark, 2004.

[157] S. Gratton, A. S. Lawless, and N. K. Nichols, “Approximate Gauss-Newton methods for nonlinear least squares problems,” *SIAM J. Optim.*, vol. 18, pp. 106–132, Feb. 2007.

[158] D. J. Whitehouse, *Handbook of Surface and Nanometrology*, 2nd ed. Coventry, UK: CRC Press, 2010.

[159] C. A. Peters, “Statistics for analysis of experimental data,” in *Environmental Engineering Processes Laboratory Manual*, S. E. Powers, Ed. Champaign: Department of Civil and Environmental Engineering Princeton University, 2001, pp. 1–25.

[160] L. N. Trefethen and D. Bau, *Numerical Linear Algebra*. SIAM, 1997.

[161] J. Erhel, N. Nassif, and P. Bernard, “Calcul matriciel et systèmes linéaires.” INSA Rennes, 2012.

[162] M. Sofroniou and G. Spaletta, “Precise numerical computation,” *J. Log. Algebr. Program.*, vol. 64, pp. 113–134, Jul. 2005.

[163] “JCGM 101:2008-Suplement 1 to the ‘Guide to the Expression of Uncertainty in Measurement’-Propagation of distributions using a Monte Carlo method.” [Online]. Available: http://www.bipm.org/en/publications/guides/gum.html. [Accessed: 27-Feb-2017].

[164] A. Iost, G. Guillemot, Y. Rudermann, and M. Bigerelle, “A comparison of models for predicting the true hardness of thin films,” *Thin Solid Films*, vol. 524, pp. 229–237, Dec. 2012.

[165] J. Isselin, A. Iost, J. Golek, D. Najjar, and M. Bigerelle, “Assessment of the constitutive law by inverse methodology: Small punch test and hardness,” *J. Nucl. Mater.*, vol. 352, pp. 97–106, Jun. 2006.

[166] D. J. Shuman, A. L. M. Costa, and M. S. Andrade, “Calculating the elastic modulus from nanoindentation and microindentation reload curves,” *Mater. Charact.*, vol. 58, pp. 380–389, Apr. 2007.

[167] H.-J. Chang, M. Fivel, D. Rodney, and M. Verdier, “Multiscale modelling of indentation in FCC metals: From atomic to continuum,” *Comptes Rendus Phys.*, vol. 11, pp. 285–292, Apr. 2010.

[168] W. Li, H. Bei, J. Qu, and Y. Gao, “Effects of machine stiffness on the loading–displacement curve during spherical nano-indentation,” *J. Mater. Res.*, vol. 28, pp. 1903–1911, Jul. 2013.

[169] M. Cabibbo, P. Ricci, R. Cecchini, Z. Rymuza, J. Sullivan, S. Dub, and S. Cohen, “An international round-robin calibration protocol for nanoindentation measurements,” *Micron*, vol. 43, pp. 215–222, Feb. 2012.

[170] J.-S. Lee, J. Jang, B.-W. Lee, Y. Choi, S. G. Lee, and D. Kwon, “An instrumented indentation technique for estimating fracture toughness of ductile materials: A critical indentation energy model based on continuum damage mechanics,” *Acta Mater.*, vol. 54, pp. 1101–1109, Feb. 2006.

[171] A. Iost, “Détermination de la ténacité de matériaux fragiles ou ductiles à partir de l’essai d’indentation,” *Rev. Métallurgie*, vol. 110, pp. 215–233, 2013.

[172] J. Cai, F. Li, T. Liu, and B. Chen, “Investigation of mechanical behavior of quenched Ti–6Al–4V alloy by microindentation,” *Mater. Charact.*, vol. 62, pp. 287–293, Mar. 2011.

[173] C. C. Tasan, J. P. M. Hoefnagels, and M. G. D. Geers, “Indentation-based damage quantification revisited,” *Scr. Mater.*, vol. 63, pp. 316–319, Aug. 2010.

[174] Z. Chunyu, Z. Yulong, C. Youbin, C. Nanfeng, and C. Lei, “Understanding indentation-induced elastic modulus degradation of ductile metallic materials,” *Mater. Sci. Eng. A*, vol. 696, pp. 445–452, Jun. 2017.

[175] J. Hay, Webinar: “Frame Stiffness and Area Function,” Nanomechanics Inc. Nov-2016.

[176] D. Chicot, F. Roudet, A. Zaoui, G. Louis, and V. Lepingle, “Influence of visco-elasto-plastic properties of magnetite on the elastic modulus: Multicyclic indentation and theoretical studies,” *Mater. Chem. Phys.*, vol. 119, pp. 75–81, Jan. 2010.

[177] J. A. Williams, *Engineering Tribology*. Oxford University Press, 1994.

[178] A. Leyland and A. Matthews, “On the significance of the H/E ratio in wear control: a nanocomposite coating approach to optimised tribological behaviour,” *Wear*, vol. 246, pp. 1–11, Nov. 2000.

[179] J. Chen and S. J. Bull, “Relation between the ratio of elastic work to the total work of indentation and the ratio of hardness to Young’s modulus for a perfect conical tip,” *J. Mater. Res.*, vol. 24, pp. 590–598, Mar. 2009.

[180] Y. Jia, F. Xuan, X. Chen, and F. Yang, “Finite element analysis of the cyclic indentation of bilayer enamel,” *J. Phys. Appl. Phys.*, vol. 47, pp. 175401, Apr. 2014.

[181] J. Nohava, R. Mušálek, J. Matějíček, and M. Vilémová, “A contribution to understanding the results of instrumented indentation on thermal spray coatings — Case study on Al2O3 and stainless steel,” *Surf. Coat. Technol.*, vol. 240, pp. 243–249, Feb. 2014.

[182] R. Cagliero, “Macro instrumented indentation test for structural materials: experimental and numerical methods,” Doctoral thesis, *Politecnico di Torino*, 2016.

[183] C. Ullner, “Critical points in ISO 14577 part 2 and 3 considering the uncertainty in measurement,” *Proc HARDMEKO*, pp. 11–12, Nov. 2004.

[184] D. Chicot, “Hardness length-scale factor to model nano- and micro-indentation size effects,” *Mater. Sci. Eng. A*, vol. 499, pp. 454–461, Jan. 2009.

[185] D. Chicot, E. S. Puchi-Cabrera, A. Iost, M. H. Staia, X. Decoopman, F. Roudet, and G. Louis, “Analysis of indentation size effect in copper and its alloys,” *Mater. Sci. Technol.*, vol. 29, pp. 868–876, Jul. 2013.

[186] S. J. Bull, “On the origins and mechanisms of the indentation size effect,” *Z. Für Met.*, vol. 94, pp. 787–792, Jul. 2003.

[187] J. G. Swadener, E. P. George, and G. M. Pharr, “The correlation of the indentation size effect measured with indenters of various shapes,” *J. Mech. Phys. Solids*, vol. 50, pp. 681–694, Apr. 2002.

[188] Y. Huang, F. Zhang, K. Hwang, W. Nix, G. Pharr, and G. Feng, “A model of size effects in nano-indentation,” *J. Mech. Phys. Solids*, vol. 54, pp. 1668–1686, Aug. 2006.

[189] H. Gao, “Mechanism-based strain gradient plasticity? I. Theory,” *J. Mech. Phys. Solids*, vol. 47, pp. 1239–1263, Apr. 1999.

[190] H. Li and R. C. Bradt, “The microhardness indentation load/size effect in rutile and cassiterite single crystals,” *J. Mater. Sci.*, vol. 28, pp. 917–926, Jan. 1993.

[191] M. F. McGuire, *Stainless Steels for Design Engineers*. ASM International, 2008.

[192] V. Mertinger, E. Nagy, F. Tranta, and J. Sólyom, “Strain-induced martensitic transformation in textured austenitic stainless steels,” *Mater. Sci. Eng. A*, vol. 481–482, pp. 718–722, May 2008.

[193] T.-H. Ahn, S. B. Lee, K.-T. Park, K. H. Oh, and H. N. Han, “Strain-induced ε-martensite transformation during nanoindentation of high-nitrogen steel,” *Mater. Sci. Eng. A*, vol. 598, pp. 56–61, Mar. 2014.

[194] D. Beegan, S. Chowdhury, and M. T. Laugier, “Work of indentation methods for determining copper film hardness,” *Surf. Coat. Technol.*, vol. 192, pp. 57–63, Mar. 2005.

[195] D. Chicot, M. Y. N’Jock, F. Roudet, X. Decoopman, M. H. Staia, and E. S. Puchi-Cabrera, “Some improvements for determining the hardness of homogeneous materials from the work-of-indentation,” *Int. J. Mech. Sci.*, vol. 105, pp. 279–290, Jan. 2016.

[196] T. Chudoba and M. Griepentrog, “Comparison between conventional Vickers hardness and indentation hardness obtained with different instruments,” *Z. Für Met.*, vol. 96, pp. 1242–1246, Nov. 2005.

[197] K. Herrmann, D. A. Lucca, M. J. Klopfstein, and F. Menelao, “CIRP sponsored international comparison on nanoindentation,” *Metrologia*, vol. 47, pp. S50–S58, Apr. 2010.

[198] L. Qian, M. Li, Z. Zhou, H. Yang, and X. Shi, “Comparison of nano-indentation hardness to microhardness,” *Surf. Coat. Technol.*, vol. 195, pp. 264–271, May 2005.

[199] V. Buryachenko, *Micromechanics of Heterogeneous Materials*. Springer Science & Business Media, 2007.

[200] *Astm D3878-07: Standard Terminology for Composite Materials. Doi*. Astm.

[201] H. F. W. Taylor, *Cement Chemistry*. Thomas Telford, 1997.

[202] D. Bentz, E. Garboczi, and P. E. Stutzman, “Computer Modelling of the Interfacial Transition Zone in Concret,” in *Interfaces in Cementitious Composites*, London: E. and F.N. Spon, 1993.

[203] J. Nemecek, “Nanoindentation Based Analysis of Heterogeneous Structural Materials,” in *Nanoindentation in Materials Science*, J. Nemecek, Ed. InTech, 2012.

[204] A. Heussaff, L. Dubar, T. Tison, M. Watremez, and R. F. Nunes, “A methodology for the modelling of the variability of brake lining surfaces,” *Wear*, vol. 289, pp. 145–159, Jun. 2012.

[205] F. Bergman, M. Eriksson, and S. Jacobson, “The effect of reduced contact area on the occurrence of disc brake squeals for an automotive brake pad,” *Proc. Inst. Mech. Eng. Part J. Automob. Eng.*, vol. 214, pp. 561–568, May 2000.

[206] G. Constantinides, K. S. Ravi Chandran, F.-J. Ulm, and K. J. Van Vliet, “Grid indentation analysis of composite microstructure and mechanics: Principles and validation,” *Mater. Sci. Eng. A*, vol. 430, pp. 189–202, Aug. 2006.

[207] N. X. Randall, M. Vandamme, and F.-J. Ulm, “Nanoindentation analysis as a two-dimensional tool for mapping the mechanical properties of complex surfaces,” *J. Mater. Res.*, vol. 24, pp. 679–690, Mar. 2009.

[208] M. Vandamme, F.J. Ulm, and P. Fonollosa, “Nanogranular packing of C–S–H at substochiometric conditions,” *Cem. Concr. Res.*, vol. 40, pp. 14–26, Jan. 2010.

[209] K. Durst, M. Göken, and G. M. Pharr, “Indentation size effect in spherical and pyramidal indentations,” *J. Phys. Appl. Phys.*, vol. 41, pp. 1-5, Apr. 2008.

[210] F.-J. Ulm, M. Vandamme, C. Bobko, J. Alberto Ortega, K. Tai, and C. Ortiz, “Statistical Indentation Techniques for Hydrated Nanocomposites: Concrete, Bone, and Shale,” *J. Am. Ceram. Soc.*, vol. 90, pp. 2677–2692, Sep. 2007.

[211] A. A. Zadpoor, “Nanomechanical characterization of heterogeneous and hierarchical biomaterials and tissues using nanoindentation: The role of finite mixture models,” *Mater. Sci. Eng. C*, vol. 48, pp. 150–157, Mar. 2015.

[212] J. H. Westbrook, H. Conrad, and A. S. for Metals, *The Science of hardness testing and its research applications*. Metals Park, Ohio: American Society for Metals, 1973.

[213] H. Gao, C. Cheng-Hsin, and J. Lee, “Elastic contact versus indentation modeling of multi-layered materials,” *Int. J. Solids Struct.*, vol. 29, pp. 2471–2492, Feb. 1992.

[214] V. Králík and J. Němeček, “Comparison of nanoindentation techniques for local mechanical quantification of aluminum alloy,” *Mater. Sci. Eng. A*, vol. 618, pp. 118–128, Nov. 2014.

[215] R. Sridharan, “Gaussian mixture models and the EM algorithm,” *Available in: http://people.csail.mit.edu/rameshvs/content/gmm-em.pdf.*

[216] J. R. Davis, *Concise Metals Engineering Data Book*. ASM International, 1997.

[217] Application note: “Properties and characteristics of graphite for industrial applications,” Entegris, Inc, Massachusetts, USA, 2015.

[218] V. V. Bannikov, I. R. Shein, and A. L. Ivanovskii, “Mechanical properties and electronic structure of zircon: Ab inito FLAPW-GGA calculations,” *Inorg. Mater. Appl. Res.*, vol. 3, pp. 7–10, Jan. 2012.

[219] B. C. Chakoumakos, W. C. Oliver, G. R. Lumpkin, and R. C. Ewing, “Hardness and elastic modulus of zircon as a function of heavy-particle irradiation dose: I. *In situ*-decay event damage,” *Radiat. Eff. Defects Solids*, vol. 118, pp. 393–403, Nov. 1991.

[220] D. B. Sirdeshmukh and K. G. Subhadra, “Note on the elastic properties of zircon,” *J. Appl. Phys.*, vol. 46, pp. 3681–3682, Aug. 1975.

[221] W. C. Oliver, J. C. McCallum, B. C. Chakoumakos, and L. A. Boatner, “Hardness and elastic modulus of zircon as a function of heavy-particle irradiation dose: II. Pb-ion implantation damage,” *Radiat. Eff. Defects Solids*, vol. 132, pp. 131–141, Oct. 1994.

[222] H. Xiang, Z. Feng, Z. Li, and Y. Zhou, “Theoretical investigations on mechanical and thermal properties of MSiO4 (M = Zr, Hf),” *J. Mater. Res.*, vol. 30, pp. 2030–2039, Jul. 2015.

[223] N. M. Rendtorff, S. Grasso, C. Hu, G. Suarez, E. F. Aglietti, and Y. Sakka, “Dense zircon (ZrSiO4) ceramics by high energy ball milling and spark plasma sintering,” *Ceram. Int.*, vol. 38, pp. 1793–1799, Apr. 2012.

[224] D. Mercier, J.-F. Vanhumbeeck, M. Caruso, and X. V. Eyndes, “Caractérisation mécanique par nanoindentation d'un revêtement composite ? matrice nickel électrodéposé ?” *Matériaux Tech.*, vol. 105, , pp. 106, Feb. 2017.

[225] R. G. Munro, “Materials properties of a sintered α-SiC,” *J. Phys. Chem. Ref. Data*, vol. 26, pp. 1195–1203, May 1997.

[226] “CRC Materials Science and Engineering Handbook, Third Edition,” *CRC Press*, 26-Dec-2000. [Online]. Available: https://www.crcpress.com/CRC-Materials-Science-and-Engineering-Handbook-Third-Edition/Shackelford-Alexander/p/book/9780849326967. [Accessed: 30-Jun-2017].

[227] I. Serrano, "Microsctructural and mechanical characterization of G36S". Internal communication, 2017, PolytechLille.

[228] W. D. Callister and D. G. Rethwisch, *Materials Science and Engineering: An Introduction, 9th Edition: Ninth Edition*. John Wiley and Sons, Incorporated, 2013.

[229] R. R. Chromik and E. J. Cotts, “Thermodynamic and kinetic study of phase transformations in solder/metal systems,” *MRS Online Proc. Libr. Arch.*, vol. 445, 1996.

[230] N. Esakkiraja, “Diffusion in Cu-Sn System.”, 2015. Available on: http://rgdoi.net/10.13140/RG.2.1.3378.0321

[231] K. Parameswaran, “Phase equilibrium and thermodynamic study of the iron-copper-carbon system,” Master thesis *University of Missuri-Rolla*, 1971.

[232] M. Hasebe and T. Nishizawa, “Calculation of phase diagrams of the iron-copper and cobalt-copper systems,” *Calphad*, vol. 4, pp. 83–100, Jan. 1980.

[233] L. Ingemarsson and M. Halvarsson, “SEM/EDX Analysis of Boron,” *High Temp. Corros. Cent. HTC Chalmers Univ. Technol.*, p. 115, 2011.

[234] R. Finch and J. Hanchar, “Structure and chemestry of Zircon and Zircon-Group minerals.” Mineralogical Society of America, vol. 53, pp. 1-25, Jan. 2003

[235] C. C. Berndt, K. A. Khor, and L. F Erich, *Thermal Spray 2001: New Surfaces for a New Millenium; Proceedings of the 2nd International Thermal Spray Conference, 28-30 May 2001, Singapore*. ASM International, 2001.

[236] S. P. Clark, *Handbook of Physical Constants*. Geological Society of America, 1966.

[237] R. D. W. Kemmitt and R. D. Peacock, *The Chemistry of Manganese, Technetium and Rhenium: Pergamon Texts in Inorganic Chemistry*. Elsevier, 2016.

[238] R. Mann, "Thermomechanical characterization of brake pads", Internal communication, 2016, PolytechLille.

[239] J. Marteau and M. Bigerelle, “Toward an understanding of the effect of surface roughness on instrumented indentation results,” *J. Mater. Sci.*, vol. 52, pp. 7239–7255, Jun. 2017.

[240] “DavidMercier/TriDiMap,” *GitHub*. [Online]. Available: https://github.com/DavidMercier/TriDiMap. [Accessed: 26-Jun-2017].

[241] X. Cai and H. Bangert, “Hardness measurements of thin films-determining the critical ratio of depth to thickness using FEM,” *Thin Solid Films*, vol. 264, pp. 59–71, Aug.1995.

[242] T. Chudoba, N. Schwarzer, and F. Richter, “Steps towards a mechanical modeling of layered systems,” *Surf. Coat. Technol.*, vol. 154, pp. 140–151, May 2002.

[243] K. Rahmoun, A. Iost, V. Keryvin, G. Guillemot, and N. E. C. Sari, “A multilayer model for describing hardness variations of aged porous silicon low-dielectric-constant thin films,” *Thin Solid Films*, vol. 518, pp. 213–221, Nov. 2009.

[244] E. S. Puchi-Cabrera, M. H. Staia, and A. Iost, “A description of the composite elastic modulus of multilayer coated systems,” *Thin Solid Films*, vol. 583, pp. 177–193, May 2015.

[245] F. Cleymand, O. Ferry, R. Kouitat, A. Billard, and J. von Stebut, “Influence of indentation depth on the determination of the apparent Young’s modulus of bi-layer material: Experiments and numerical simulation,” *Surf. Coat. Technol.*, vol. 200, pp. 890–893, Oct. 2005.

[246] J. Luo and R. Stevens, “Porosity-dependence of elastic moduli and hardness of 3Y-TZP ceramics,” *Ceram. Int.*, vol. 25, pp. 281–286, Apr. 1999.

[247] J. Čech, P. Haušild, A. Materna, and J. Matějíček, “Approche statistique pour identifier les propriétés mécaniques des phases individuelles à partir de données d’indentation,” *Matér. Tech.*, vol. 105, p. 105, Jan. 2017.

[248] L. S. de Vasconcelos, R. Xu, J. Li, and K. Zhao, “Grid indentation analysis of mechanical properties of composite electrodes in Li-ion batteries,” *Extreme Mech. Lett.*, vol. 9, pp. 495–502, Dec. 2016.

[249] M. Mata, M. Anglada, and J. Alcalá, “Contact Deformation Regimes Around Sharp Indentations and the Concept of the Characteristic Strain,” *J. Mater. Res.*, vol. 17, pp. 964–976, May 2002.

[250] M. Mata, O. Casals, and J. Alcala, “The plastic zone size in indentation experiments: The analogy with the expansion of a spherical cavity,” *Int. J. Solids Struct.*, vol. 43, pp. 5994–6013, Oct. 2006.

[251] K. Durst, M. Göken, and H. Vehoff, “Finite element study for nanoindentation measurements on two-phase materials,” *J. Mater. Res.*, vol. 19, pp. 85–93, Jan. 2004.

[252] H. Y. Abib, A. Iost, A. Montagne, K. Rahmoun, B. Ayachi, and J.-P. Vilcot, “Investigations on the mechanical properties of the elementary thin films composing a CuIn 1-x Ga x Se 2 solar cell using the nanoindentation technique,” *Thin Solid Films*, vol. 633, pp. 71–75, Jul. 2017.

[253] R. Pereyra, “Characterization of Indentation-induced ‘Particle Crowding’ in Metal Matrix Composites,” *Int. J. Damage Mech.*, vol. 14, pp. 197–213, Jul. 2005.

[254] R. Saha and W. D. Nix, “Effects of the substrate on the determination of thin film mechanical properties by nanoindentation,” *Acta Mater.*, vol. 50, pp. 23–38, Jan. 2002.

[255] A. C. Fischer-Cripps, *Introduction to contact mechanics*, 2nd ed. New York: Springer, 2007.

[256] Y.-T. Cheng and C.-M. Cheng, “Scaling, dimensional analysis, and indentation measurements,” *Mater. Sci. Eng. R Rep.*, vol. 44, pp. 91–149, Aug. 2004.

[257] T. Futami, M. Ohira, H. Muto, and M. Sakai, “Indentation contact behavior of copper-graphite particulate composites: Correlation between the contact parameters and the electrical resistivity,” *Carbon*, vol. 46, pp. 671–678, Apr. 2008.

[258] M. Sakai and Y. Nakano, “Instrumented pyramidal and spherical indentation of polycrystalline graphite,” *J. Mater. Res.*, vol. 19, pp. 228–236, Jan. 2004.

[259] D. A. Mortimer and M. Nicholas, “The wetting of carbon by copper and copper alloys,” *J. Mater. Sci.*, vol. 5, pp. 149–155, Feb. 1970.

[260] M. Hartley and B. McEnaney, “Blunt indentation of core graphite,” *Graph. Moderator Lifecycle Behav. Int. At. Energy Agency Vienna IAEATECDOC-901*, pp. 263–274, 1996.

[261] J. S. Field and M. V. Swain, “The indentation characterisation of the mechanical properties of various carbon materials: Glassy carbon, coke and pyrolytic graphite,” *Carbon*, vol. 34, pp. 1357–1366, 1996.

[262] K. Z. Markov, “Elementary Micromechanics of Heterogeneous Media,” in *Heterogeneous Media*, 1st ed., Birkhäuser Basel, 2000.

[263] P. Alam, “A mixtures model for porous particle polymer composites,” *Mech. Res. Commun.*, vol. 37, pp. 389–393, Jun. 2010.

DOCTORAT DE L'UNIVERSITE DE LILLE 1 SCIENCES ET TECHNOLOGIES

Ecole doctorale : SPI Sciences Pour l'Ingénieur

Laboratoire : Laboratoire de Mécanique de Lille – FRE 3723

Discipline : Mécanique des solides, des matériaux, des structures et des surfaces

TITRE DE LA THÈSE :

Indentation instrumentée multi-échelles de matériaux homogènes et multi-matériaux

RÉSUMÉ ÉTENDU

Les matériaux composites sont largement utilisés ces dernières décennies du fait de leurs propriétés remarquables qui combinent celles de chaque élément constitutif. Du fait de ces propriétés améliorées, ils peuvent être soumis à des conditions en service extrêmes de température, frottement et de corrosion comme le sont en particulier les patins de frein utilisés dans l'industrie ferroviaire. Les patins de frein sont des multi matériaux qui présentent la particularité d'être fortement hétérogènes. Pour prévoir leur durée de vie et leur comportement pendant le freinage, une des clés repose sur la connaissance des propriétés mécaniques à différentes échelles de contrainte et de déformation, ce qui est rendu très difficile du fait de leur complexité structurale. C'est sans doute pourquoi, pendant plusieurs années, les patins de frein ont été fabriqués par tâtonnement ou par erreur. Mais aujourd'hui, comme les exigences d'utilisation sont beaucoup plus sévères, une meilleure connaissance du comportement réel du matériau est fortement souhaitée et sa caractérisation mécanique est un véritable défi pour optimiser sa conception.

L'objectif de mon travail consiste à déterminer les propriétés mécaniques de dureté et de module d'élasticité, de patins de frein fortement hétérogènes utilisés dans l'industrie ferroviaire. À l'échelle macrométrique, ceux-ci sont classiquement caractérisés par des essais de compression uniaxiale et une méthodologie souvent très complexe pour obtenir les propriétés globales. En suivant le même objectif, nous proposons de déterminer les propriétés mécaniques intrinsèques de chaque composant du matériau et les propriétés globales en utilisant l'indentation instrumentée multi-échelles.

L'indentation instrumentée est utilisée depuis les années soixante-dix. Elle est devenue une technique indispensable pour le contrôle qualité des matériaux de toutes natures (céramiques, métaux, polymère, composites, etc.) pour obtenir relativement rapidement les propriétés mécaniques comme le module d'élasticité et la dureté. La technique consiste à faire pénétrer une pointe rigide (indenteur), de géométrie et de propriétés connues, dans un matériau aux propriétés recherchées tout en enregistrant de manière continue et le plus précisément possible la force (*P*) nécessaire en fonction son déplacement ou de son enfoncement (*h*) comme le montre la figure 1.

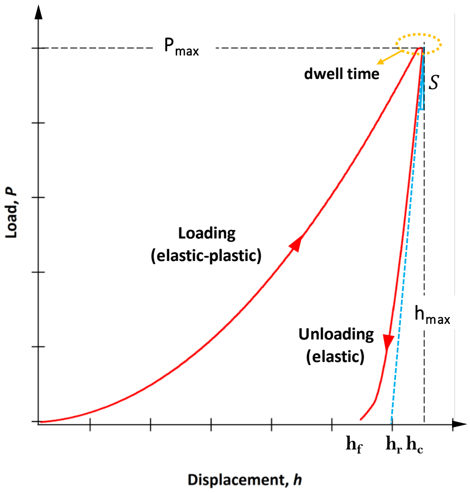

Fig. 1. Courbe force déplacement d'un essai d'indentation instrumentée classique.

Dans ce travail, nous étudions les comportements aux échelles nano, micro et macroscopiques, grâce à une gamme d'appareils expérimentaux en indentation instrumentée qui permettent d'appliquer des forces allant de 10 mN à 2 kN et de provoquer des enfoncements mesurables de 50 nm à 250 µm. Nous disposons de trois instruments dont les caractéristiques principales sont rassemblées dans le tableau 1.

Tableau 1. Caractéristiques principales des instruments utilisés.

Instrument	Domaine de charge	Résolution
Nanoindenteur XP, MTS	1 mN – 10 N	Force : 50 nN Déplacement 0,01 nm
Microindenteur CSM2-107, Anton Paar	100 mN – 20 N	Force : 100 µN Déplacement : 0,3 nm
Macroindenteur ZHU 2,5, Zwick	5 N – 2,5 kN	Force : grade 1, DIN EN ISO 7500-1 Déplacement : 20 nm

Compte tenu de la microstructure complexe du patin de frein et des difficultés possibles dans l'analyse des résultats par indentation des trois instruments, nous avons décidé de séparer ce travail en deux parties. D'abord, la caractérisation par indentation multi-échelles de matériaux usuels suffisamment homogènes (aciers et alliage d'aluminium) afin de préciser les contours de la méthodologie et de mettre en avant les précautions d'emploi (changement d'échelles, déformation autour de l'empreinte, défaut de pointe de l'indenteur, rigidité de l'instrument, etc.) puis une deuxième étape de caractérisation proprement dite du patin de frein.

Caractérisation par indentation instrumentée multi-échelles de matériaux métalliques homogènes

La première partie consiste à optimiser les conditions expérimentales sur deux cales étalons en acier de dureté (39HRC et 63.4HRC), un acier inoxydable (SS316L) et un alliage d'aluminium (Al, série 7000), puis de dépouiller et d'interpréter les données en suivant une démarche métrologique rigoureuse dans le but d'effectuer le raccordement entre les résultats obtenus aux trois échelles de mesure. Les conditions expérimentales sont résumées dans le Tableau 2.

Tableau 2. Résumé des types d'essais d'indentation faits avec les trois instruments.

Paramètres	**Nano classique**	**Nano CSM**	**Micro classique**	**Micro multicyclique**	**Macro classique**
Domaine de charge	20 - 700 mN	Jusqu'à $h_{\max}$	0.1 – 20 N	0.1 – 20 N	5 – 2000 N
Vitesse charge/décharge	30 s	---	$2P_{\max}$ (N/min)	30 s	$2P_{\max}$ (N/min)
Temps d'attente à $P_{\max}$	15 s	15 s	15 s	15 s	15 s
Indenteur	Berkovich		Berkovich		Vickers
Fonction d'aire	Oliver and Pharr [1]		Chicot *et al.* [2]		Troyon and Huang [3]
Fixation	Collage sur support et fixation sur le porte-échantillons.		Etau		Pâte à modeler autour de l'échantillon
Autres paramètres d'essai		Fréquence 45 Hz, vitesse de déformation 0.05 s^{-1}		50 cycles, décharge jusqu'à 20-30% $iP_{\max}$. Incrément linéaire de la force.	

Préalablement à l'analyse des essais sur les matériaux homogènes, nous avons développé une méthodologie alternative à celle d'Oliver et Pharr [1,4] (Eq. 1) pour approximer la courbe de décharge utilisée aussi bien pour le calcul de la dureté que celui du module d'élasticité. La méthode consiste principalement à utiliser une fonction réciproque (dite méthode inverse), c'est-à-dire que pour ajuster la courbe de décharge nous considérons le déplacement comme variable dépendante et la force comme variable indépendante ($h = f(P)$). Cette approche permet également de comparer les paramètres d'ajustement aux différentes charges, donc à différentes échelles de mesure, en proposant une écriture adimensionnelle pour notre méthode (Eq. 2) et pour celle d'Oliver et Pharr (Eq. 3).

$$P = B'(h - h_f)^m \tag{1}$$

$$\frac{h}{h_{\max}} = \frac{h_f}{h_{\max}} + G\left(\frac{P}{P_{\max}}\right)^n \tag{2}$$

$$\frac{P}{P_{\max}} = B\left(\frac{h}{h_{\max}} - \frac{h_f}{h_{\max}}\right)^m \tag{3}$$

où m, h_f et B', B, $h_f/h_{\max}$, G, et n sont des paramètres d'ajustement.

Pour tester la convergence et la stabilité des deux méthodologies proposées, nous avons utilisé la méthode de Monte Carlo. La figure 2 présente schématiquement la procédure utilisée. Cette procédure a été testée en particulier pour les essais en nanoindentation sur les échantillons en aluminium et en silice fondue qui présentent un comportement mécanique très différent.

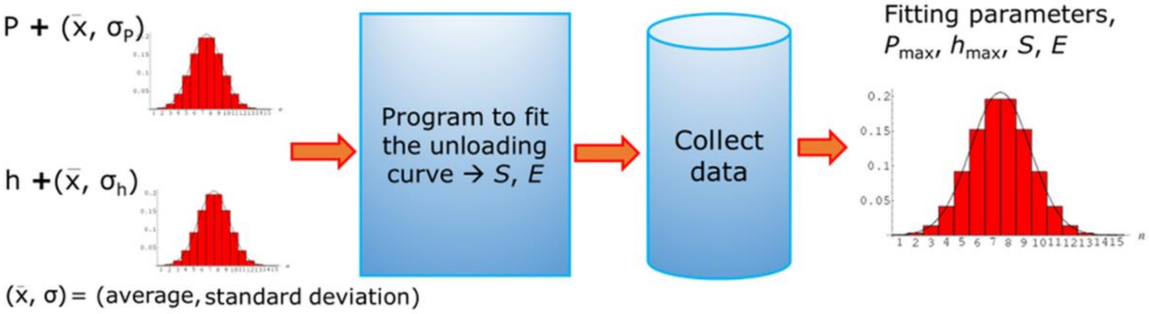

Fig. 2 Représentation schématique de la simulation de Monte Carlo, où P et h, sont la force et le déplacement, auxquels est ajouté un bruit Gaussien centré à zéro ($\bar{x}$) et d'écart-type (σ).

Les conclusions parmi les plus pertinentes sont :

- La convergence de l'ajustement de la courbe par moindres carrés est améliorée avec la méthode inverse. Le problème est mieux conditionné, c'est-à-dire que de petites variations sur les données d'entrée entrainent des petites variations sur les données de sortie.
- La méthode inverse améliore la stabilité des résultats relatifs au calcul de la pente à la décharge et par conséquent du module d'élasticité. La figure 3 montre l'écart entre les deux méthodes pour le calcul de la raideur avec différentes valeurs de bruit Gaussien.

- L’approche adimensionnelle permet de comparer différentes charges d’indentation et peut donner ainsi des informations supplémentaires sur le comportement des matériaux.

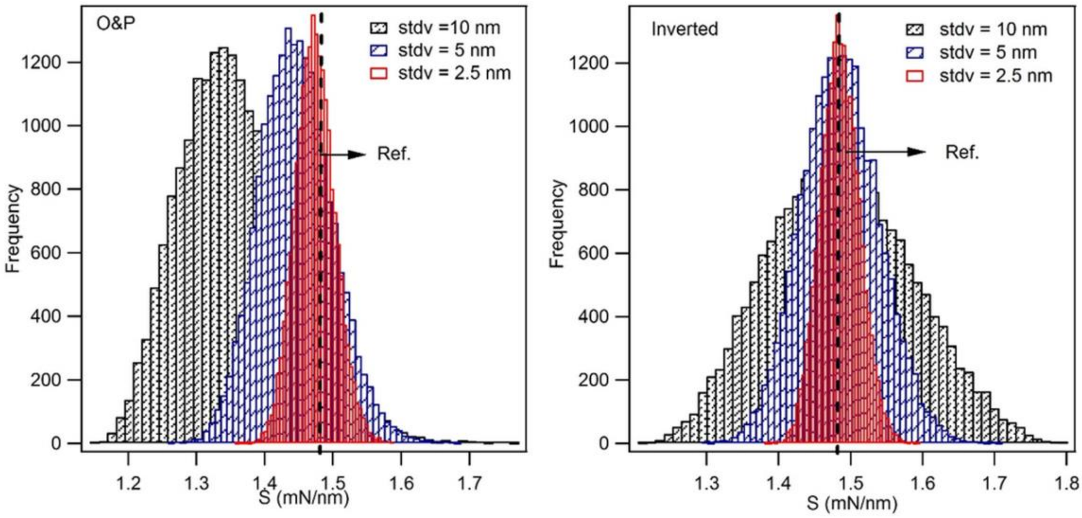

Fig. 3 Histogrammes de la raideur, *S*, calculée avec les paramètres d’ajustement des modèles inverse (inverted) et d’Oliver et Pharr (O&P), obtenus par simulation Monte Carlo avec différents bruits Gaussiens (Ref.) sans perturbation.

Après avoir validé l’amélioration de la stabilité du modèle inverse pour ajuster la courbe de décharge, nous avons appliqué cette méthode (Eq. 2) à différents essais effectués avec les conditions rassemblées dans le Tableau 2. Cette analyse basée sur des matériaux homogènes nous a permis de mettre en évidence les influences combinées des appareils expérimentaux utilisés, de la gamme de force et de profondeur de pénétration, du matériau et des méthodes de traitement de données sur la précision des mesures.

De manière générale, pour les quatre matériaux étudiés, les mesures sont affectées par différents paramètres qui doivent être corrigés sont : le point de contact, la fonction d’aire de la pointe et la complaisance du bâti. Pour les matériaux homogènes, l’instrument de nanoindentation permet d’obtenir des résultats plus précis et moins affectés par ces paramètres. Le microindenteur et le macroindenteur peuvent être très sensibles à la calibration de la complaisance, des petites variations peuvent entrainer des modifications importantes sur l’estimation du module d’élasticité dans le domaine des charges élevées, mais l’hypothèse du module constant en fonction de la charge reste en général valable. Cependant, il faut bien préciser que la complaisance dite du bâti, prend en compte plusieurs éléments dans le système comme la fixation de l’échantillon, l’échantillon en lui-même… et pas seulement la déformation du bâti. Dans la détermination du point de contact, le macroindenteur est l’instrument le plus sensible, en tous cas pour les matériaux étudiés, car la précision n’est pas bonne dans le domaine des faibles charges (5-50 N). Nous pouvons trouver des écarts importants sur le déplacement selon la méthode de détermination (~ 1 µm). En nanoindentation, la fonction d'aire estimée par étalonnage sur de la silice fondue (Eq. 5) est pertinente. Par contre, en microindentation et en macroindentation, nous considérons que la prise en compte de la longueur du défaut de la pointe est suffisante pour estimer correctement les aires de contact (Eqs. 6-7). Le Tableau 3 présente les principales équations utilisées pour le calcul des propriétés mécaniques.

Tableau 3. Résumé des équations utilisées pour le calcul du module d'élasticité et de la dureté.

$E_R = \frac{S\sqrt{\pi}}{2\gamma\sqrt{A_c}}, \frac{1}{E_R} = \frac{(1-\nu^2)}{E} + \frac{(1-\nu_i^2)}{E_i}$	(4)
$A_c\text{nano} = 24{,}5{h_c}^2 + \sum_{n=1}^{8} C_n\,(h_c)^{1/2^{i-2}}$	(5)
$A_c\text{micro} = 24{,}5 \cdot \left[h_c + h_b \cdot \left(1 - exp\left(-2\frac{h_c}{h_b}\right)^{3/2}\right)\right]^2$	(6)
$A_c\text{macro} = 24{,}5\,(h_c + h_b)^2$	(7)
$h_{c\,sink\,in} = h_{max} - \varepsilon\frac{P_{max}}{S}$; $h_{c\,pile\,up} = 1{,}2\left(h_{max} - \frac{P_{max}}{S}\right)$	(8)
$HIT = \frac{P}{A_c}$; $HM = \frac{P}{A_r}$; $A_r = \frac{26{,}43}{24{,}5} \cdot A_c(h_{\text{max}})$	(9)

E_R, E_i, E modules d'élasticité respectivement réduit, de l'indenteur et du matériau ; S la raideur ; γ une constante géométrique ; ν et ν_i les coefficients de Poisson du matériau et de l'indenteur ; A_c la fonction d'aire du contact ; h_c la profondeur de contact ; h_b le défaut de pointe ; HM et HIT, les duretés Martens et instrumentée.

Dans cette étude, nous avons choisi d'analyser les courbes force/déplacement obtenues avec les trois instruments de façon adimensionnelle, des exemples sont montrés figures 4 et 5.

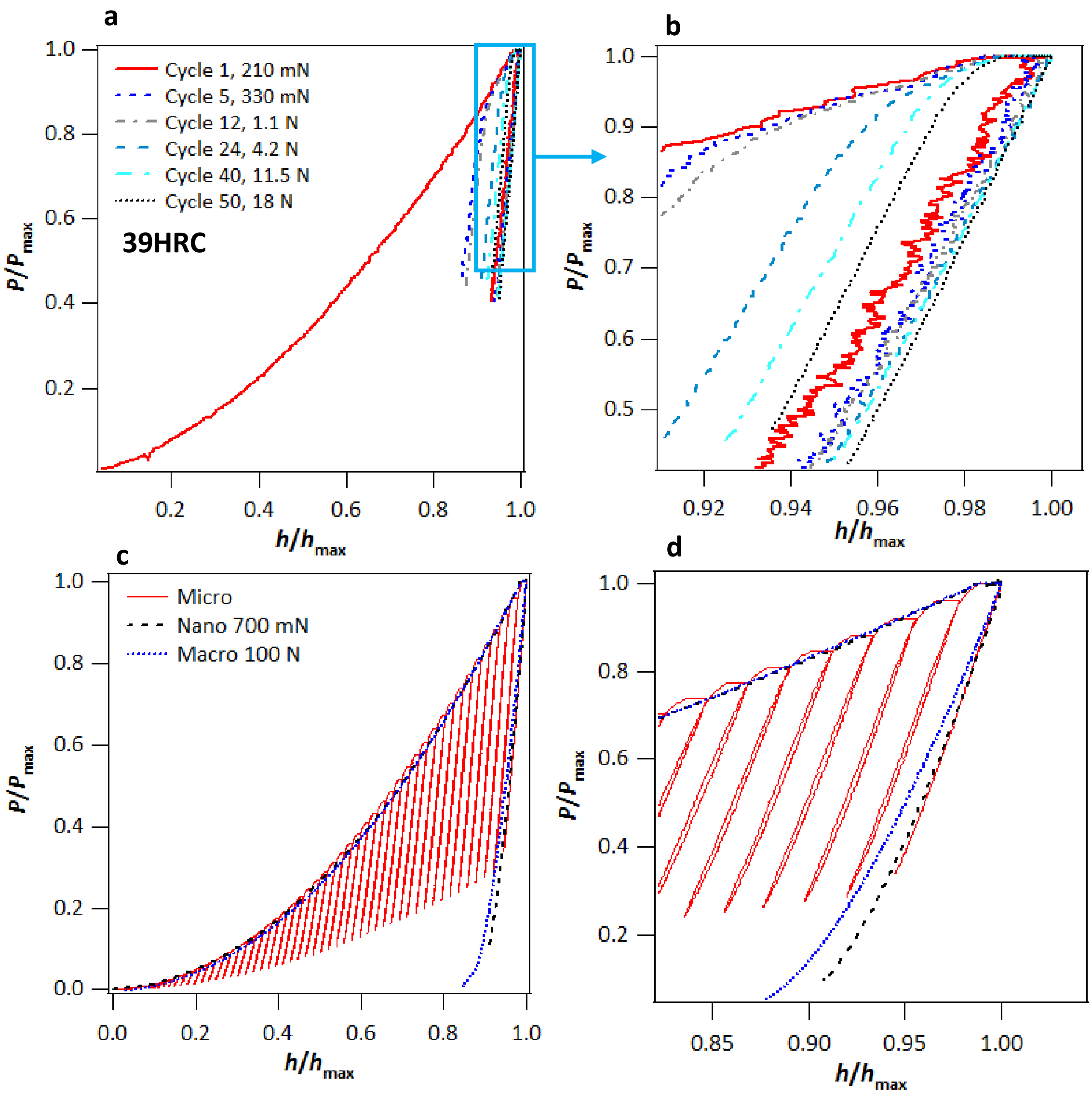

Fig. 4 a) Courbe force-déplacement adimensionnelle correspondant aux essais multicycliques obtenus sur l'acier 39HRC ; b) détail des courbes de décharge de plusieurs cycles ; c) comparaison des courbes force-déplacement micro multicyclique, nano classique et macro classique ; d) zoom sur les courbes de décharge de la figure (c).

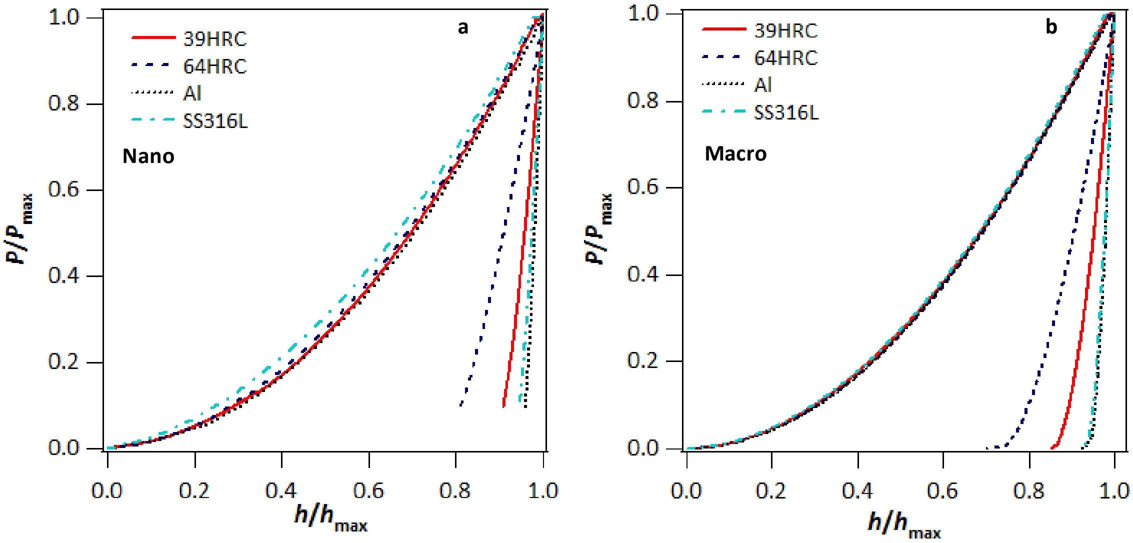

Fig. 5 Courbes force-déplacement adimensionnelles obtenues en nanoindentation et macroindentation sur les échantillons : 39HRC, 63.4HRC, SS316L et Al.

Cette analyse aboutit à quatre conclusions importantes :

- Les essais effectués avec les trois instruments donnent des courbes comparables, les différences de pente *S* entre les différentes échelles sont du même ordre de grandeur que les dispersions observées pour une même échelle (même instrument).
- Les essais multicycliques en microindentation donnent des résultats comparables à ceux obtenus par les essais classiques en micro, nano et macro indentation.
- Pour les quatre matériaux étudiés, les courbes de chargement décrites par une équation du type $P = Ch^2$ sont quasiment superposées, ce qui indique qu'elles deviennent indépendantes de la constante *C* lors d'une représentation adimensionnelle telle que celle présentée figure 5.
- Les courbes de décharge dépendent du rapport H/E_R, et sont voisines pour l'acier inoxydable et l'alliage d'aluminium qui possèdent des valeurs différentes de module et de dureté mais sensiblement le même rapport H/E_R. Ce type d'information peut apporter une meilleure compréhension de l'unicité des courbes d'indentation.

Pour poursuivre l'analyse des essais d'indentation multi-échelles, nous avons calculé le module d'élasticité et la dureté pour les quatre matériaux en considérant le mode de déformation prédominant sink-in (effondrement) ou pile-up (bourrelet) ainsi que le calcul du travail d'indentation en mesurant les aires sous la courbe force-déplacement.

La dispersion sur le module d'élasticité est supérieure à 10% en microindentation, et inférieure à 10 % en nano et en macroindentation. Un exemple est montré sur la figure 6 pour l'échantillon d'aluminium. Indépendamment de l'échelle de mesure, les valeurs estimées sont proches des valeurs de référence trouvées dans la littérature : 190-210 GPa pour les aciers, 170-

200 GPa pour un acier inoxydable et 68-74 GPa pour l'aluminium. Les différences entre les méthodologies liées au mode de déformation et celle du travail d'indentation sont voisines de 20%. Comme le module d'élasticité est une propriété intrinsèque aux matériaux, les différences constatées entre les échelles sont plutôt liées aux instruments et aux incertitudes sur les calculs.

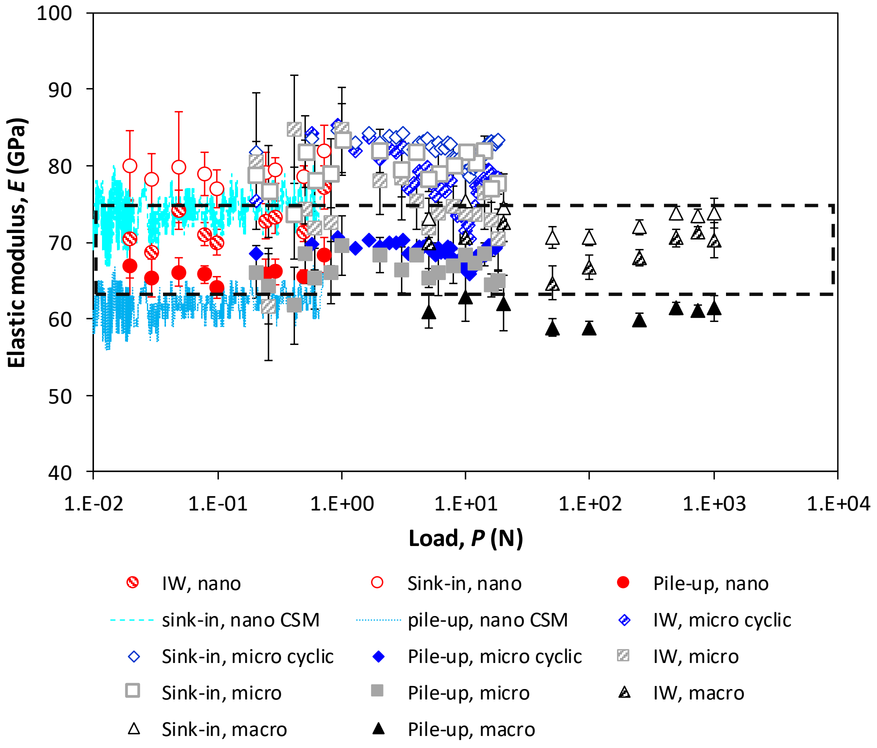

Fig. 6 Module d'élasticité obtenu par indentation multi-échelles : influence du domaine de charge (appareil utilisé) et du mode de dépouillement des résultats.

Les valeurs de dureté montrent également une forte dépendance avec la force appliquée, cet effet est connu sous le nom d'effet de taille n ou en anglais *Indentation Size Effect (ISE).* Cependant, et de manière similaire, elles montrent une variation quasi-progressive avec la charge et ce quel que soit l'instrument. De la même manière que pour le module, il n'y a pas de variation significative entre les propriétés obtenues par les essais multicycliques et les essais classiques. Les incertitudes dans la mesure de la dureté sont principalement affectées par la détermination du point de contact, l'alignement de la surface, la géométrie de l'indenteur, les erreurs de mesure en force et déplacement.

Comparaison avec des études de type Round-Robin précédentes

La méthodologie Round-Robin consiste en une comparaison inter laboratoires d'essais effectués indépendamment les uns des autres. En indentation instrumentée, ce type d'étude a été réalisée par de nombreux auteurs pour comprendre les différences entre les données expérimentales et leurs analyses effectuées avec des instruments de marques différentes [5–10]. Dans notre étude, nous avons comparé les résultats obtenus avec nos trois instruments dans le but de déterminer les similitudes entre eux par rapport à la dispersion dans l'estimation du module d'élasticité et de la dureté. Dans la figure 7, nous présentons la comparaison entre nos résultats expérimentaux et ceux de la littérature.

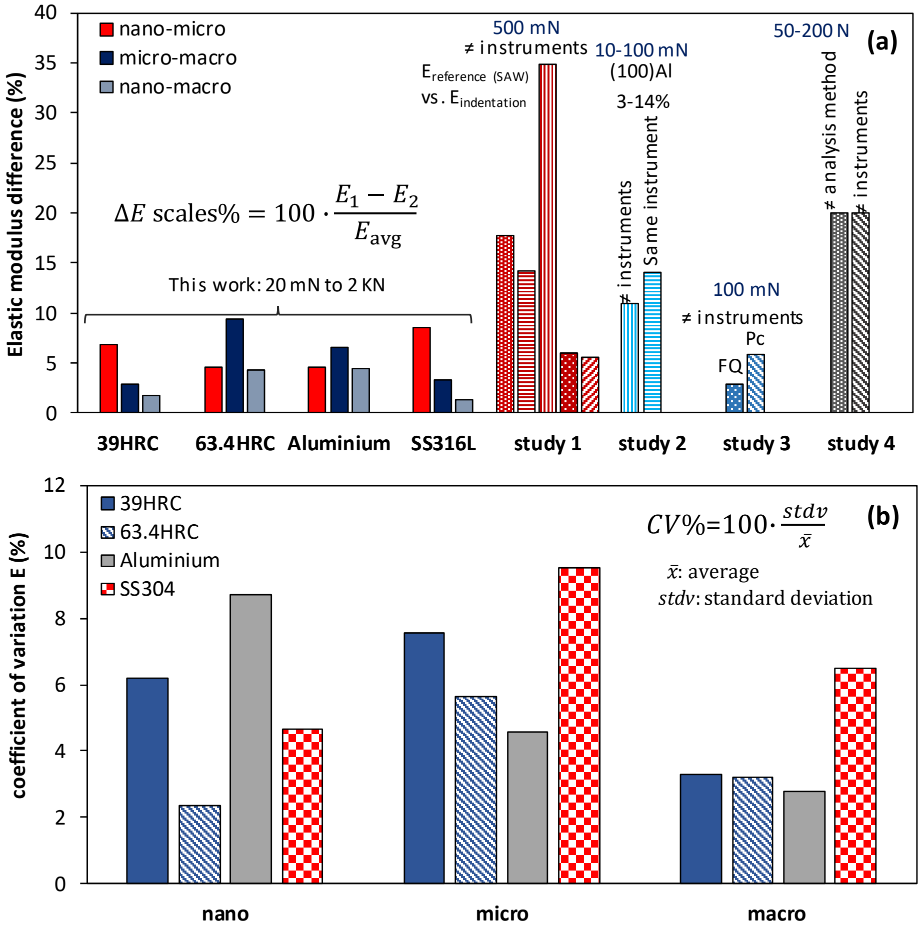

Fig. 7 a) Variation du module d'élasticité entre échelles et comparaison avec des études Round-Robin de la bibliographie [6–9]; b) Variation du module d'élasticité pour chaque matériau avec les trois instruments. Le coefficient de variation est calculé avec l'écart-type et la moyenne des résultats.

Pour le module d'élasticité, cette comparaison met en avant la reproductibilité de nos résultats, aux différentes échelles de mesure, par rapport aux études Round Robin de la littérature. Les différences relatives entre nano-micro, micro-macro et nano-macro sont environ de 10% ou inférieures dans le domaine de charges comprises entre 10 mN et 2 kN, et les coefficients de variation *CV* (Fig. 7b) sont inférieurs à 10%. Par contre, les résultats de la littérature [6-9] montrent que les différences relatives peuvent atteindre 35% selon les variables utilisées : matériaux, instruments ou méthode d'analyse. Pour nos essais, les variations les plus importantes sont obtenues pour le microindenteur. Selon la norme ISO

14577, ce coefficient *CV* doit être inférieur à 5% pour une même charge alors que nous avons considéré toutes les charges, et par conséquent nous considérons que nos résultats sont valables. Pour la dureté évaluée dans le domaine macro, nous obtenons aussi une bonne reproductibilité.

Caractérisation par indentation instrumentée multi-échelles du patin de frein.

Dans le but de caractériser le patin de frein par indentation instrumentée, nous avons utilisé les instruments de nanoindentation et de macroindentation, car les incertitudes avec le microindenteur sont supérieures d'après notre étude sur les matériaux homogènes. La première étape consiste à déterminer les propriétés intrinsèques de chaque composant du patin de frein. Pour cela, nous proposons de réaliser des cartographies de propriétés par nanoindentation en mode CSM, puis d'effectuer une analyse statistique des résultats en termes de module d'élasticité et de dureté. L'étape suivante consiste en la caractérisation par essais d'indentation multicyclique en macroindentation, avec les indenteurs Vickers et sphérique, suivie également par une analyse statistique des résultats. L'objectif est de comparer les propriétés globales mesurées et celles estimées à partir des données individuelles grâce à des lois de mélanges. Les résultats obtenus par macroindentation et par compression sont ensuite comparés. Les conditions expérimentales sont résumées dans le Tableau 4.

Tableau 4. Conditions expérimentales pour les essais d'indentation multi-échelles sur le patin de frein

Conditions	Type d'indenteur	Type d'essai	Domaine de charge
Nano surface	Berkovich	CSM (cartographies)	Jusqu'à 2500 nm
Macro surface	Vickers Sphérique (*d*= 10 mm)	Multi-cyclique Multi-cyclique	10-260 N (6 cycles) 10-260 N, 50-1450 N (8 cycles)
Macro section transversal	Vickers	Multi-cyclique	10-260 N (6 cycles)

La microstructure du patin de frein est présentée figure 8. Elle se caractérise principalement par une matrice métallique Cu-Fe avec des agrégats de 2 types de graphite et des phases céramiques (SiC, $ZrSiO_4$). Les différents composants de ce matériau sont indiqués Tableau 5 avec les propriétés de référence de la littérature.

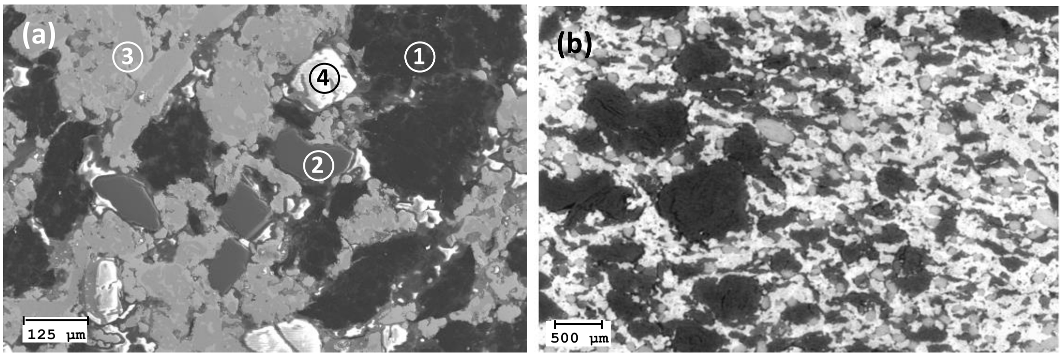

Fig. 8 Caractérisation microstructurale du patin de frein par microscopie à balayage, a) surface après polissage ; b) section transversale après polissage. Où : (1) graphite, (2) SiC, (3) matrice métallique, et (4) $ZrSiO_4$.

Tableau 5. Composition du patin de frein (*f*), taille de particules, module d'élasticité (E_{ref}) et dureté de référence (H_{ref}) pour chaque phase.

Material	***f***	**Taille (µm)**	**E_{ref} (GPa)**	**$H_{ref.}$ (GPa)**
Cuivre (Cu)	0,139	<100	95-120 [11]	0.3-1 [11]
Fer (Fe)	0,239	<220	190-210 [11]	0.5-6 [11]
Etain (Sn)	0,020	0-60	43[12]	---
MnS_2	0,028	0-20	---	---
Graphite 1	0,161	50-600	4-17 [13]	
Graphite 2	0,299	400-1100	4-17 [13]	
$ZrSiO_4$	0,084	80-320	160-399[14–18]	10-20 [15,17–19]
SiC	0,03	50-260	300-430 [20–22]	12-35 [20,21]

Cartographies et analyse statistique en nanoindentation

La méthodologie qui consiste à réaliser des cartographies de propriétés a été utilisée par de nombreux auteurs pour l'étude de matériaux hétérogènes. Toutefois, nous n'avons trouvé aucune étude portant sur des matériaux avec une microstructure aussi complexe que celle du patin de frein (Fig. 8). Nous avons effectué des cartes d'empreintes 10x10, en respectant un espacement entre empreintes de 75 µm, la même procédure a été répétée 14 fois (soit 1400 essais) pour donner une aire totale d'essai de 7,3 mm². Selon l'observation de la microstructure, la dimension caractéristique du matériau est approximativement de 250 µm. Nous avons donc choisi de réaliser nos essais en mode CSM avec une profondeur maximale de 2500 nm, c'est-à-dire 1% de la taille caractéristique prise comme hypothèse. Toutefois, cette profondeur n'est pas parfaitement adaptée car la plupart des courbes montrent une variation significative des propriétés qui correspond au fait que plusieurs phases sont simultanément indentées ou influencent les propriétés mesurées. Pour limiter ces effets, et pour ce type d'analyse, nous avons extrait les données de toutes les courbes à 100 nm et 250 nm de profondeur. La figure 9 montre un exemple d'une cartographie (10x10) en module d'élasticité et en dureté obtenue à 100 nm d'enfoncement de l'indenteur, avec la microstructure de la zone correspondante.

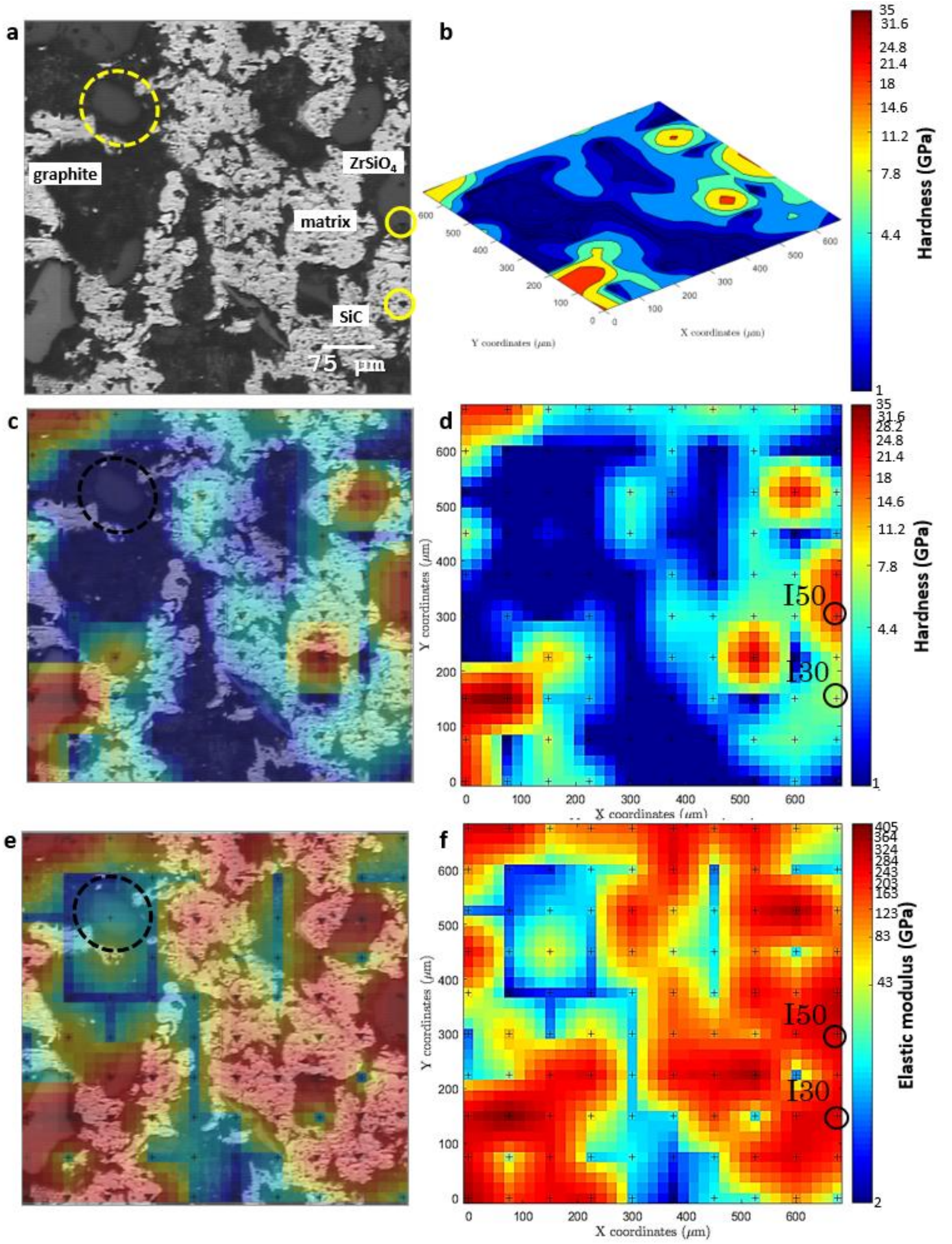

Fig. 9 Cartographie à 100 nm (a) microstructure du patin de frein sur le nanoindenteur ; (b) graphique de contours pour la dureté ; (c) cartographie de la dureté superposée avec la microstructure ; (d) cartographie de la dureté ; (e) cartographie du module superposée avec la microstructure ; (f) cartographie du module.

Sur la figure 9, nous observons une bonne corrélation entre la microstructure et les valeurs des propriétés mécaniques. En général, les ordres de grandeur sont cohérents : les valeurs les plus élevées sont liées aux céramiques (10^2 GPa) et à la matrice métallique (10^1-10^2 GPa), et les valeurs plus faibles au graphite (10^0-10^1 GPa). Avoir accès à la dureté et au module d'élasticité simultanément nous permet de distinguer les phases, au moins en termes de propriétés.

La distance choisie entre les empreintes est adaptée à notre matériau. Mais en pratique cette distance devrait être supérieure à la taille de deux phases pour éviter un biais statistique.

Comme les phases de graphite peuvent avoir une taille assez grande de l'ordre de 1 mm, il faudrait un espacement beaucoup plus grand, mais ce qui ne permettrait pas d'avoir une information suffisamment pertinente pour caractériser correctement le patin de frein.

L'analyse statistique des propriétés mécaniques dans le patin de frein prend en compte la totalité des essais (1400 essais). L'écart significatif entre les propriétés mécaniques des différentes phases, spécialement entre les modules d'élasticité, rend difficile la séparation entre les distributions Gaussiennes de chaque composant. Si le nombre de phases à déterminer est grand, le nombre de paramètres à trouver aussi. Indifféremment de la méthode utilisée l'analyse est assez compliquée, soit avec la densité de probabilité (PDF) soit avec la probabilité cumulée, pour déconvoluer des pics qui correspondent à chaque composant. Le patin de frein étant très complexe, nous avons utilisé la densité de probabilité qui intuitivement permet d'identifier de manière plus simple la distribution de chaque phase. De même, nous avons séparé les données selon la nature du matériau en prenant les valeurs les plus faibles comme étant liées aux graphites et les valeurs les plus élevées pour la matrice et les céramiques. Les figures 10 et 11 montrent des exemples de ces analyses effectuées à 100 nm et 250 nm d'enfoncement.

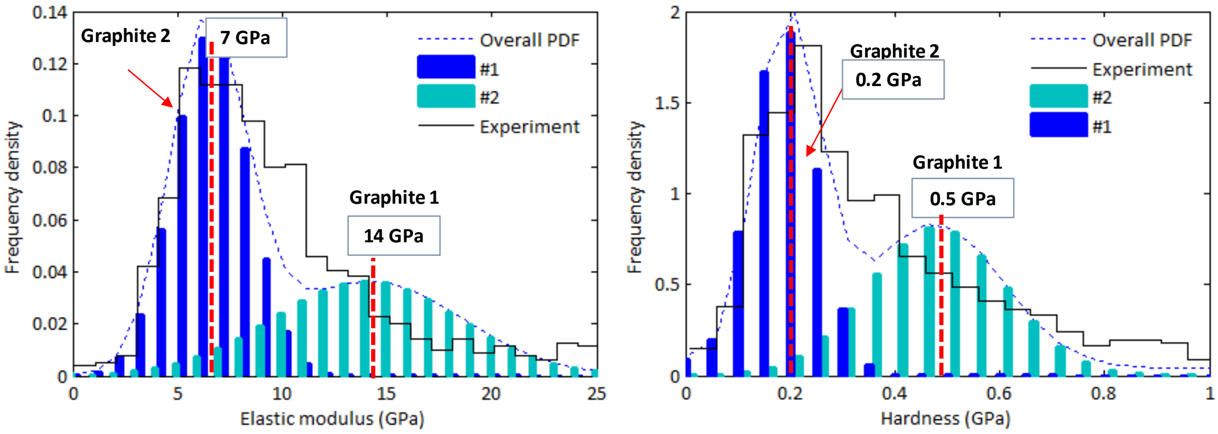

Fig. 10 Résultats de l'analyse statistique avec déconvolution de la PDF pour les graphites à 250 nm. Deux types de graphite ont été trouvés, correspondant à une distribution bimodale.

Les résultats de l'analyse statistique montrent qu'il n'existe pas de différence significative aux deux profondeurs étudiées. Ceci signifie aussi que l'effet de la rugosité n'est pas déterminant dans notre étude, même si les valeurs de rugosité sont élevées, ce que nous pouvons expliquer par le fait que les ondulations de la surface sont en général plus grandes que les tailles des empreintes, l'effet de la rugosité est ainsi limité. Finalement, les valeurs sont moyennées statistiquement autour de la valeur moyenne réelle.

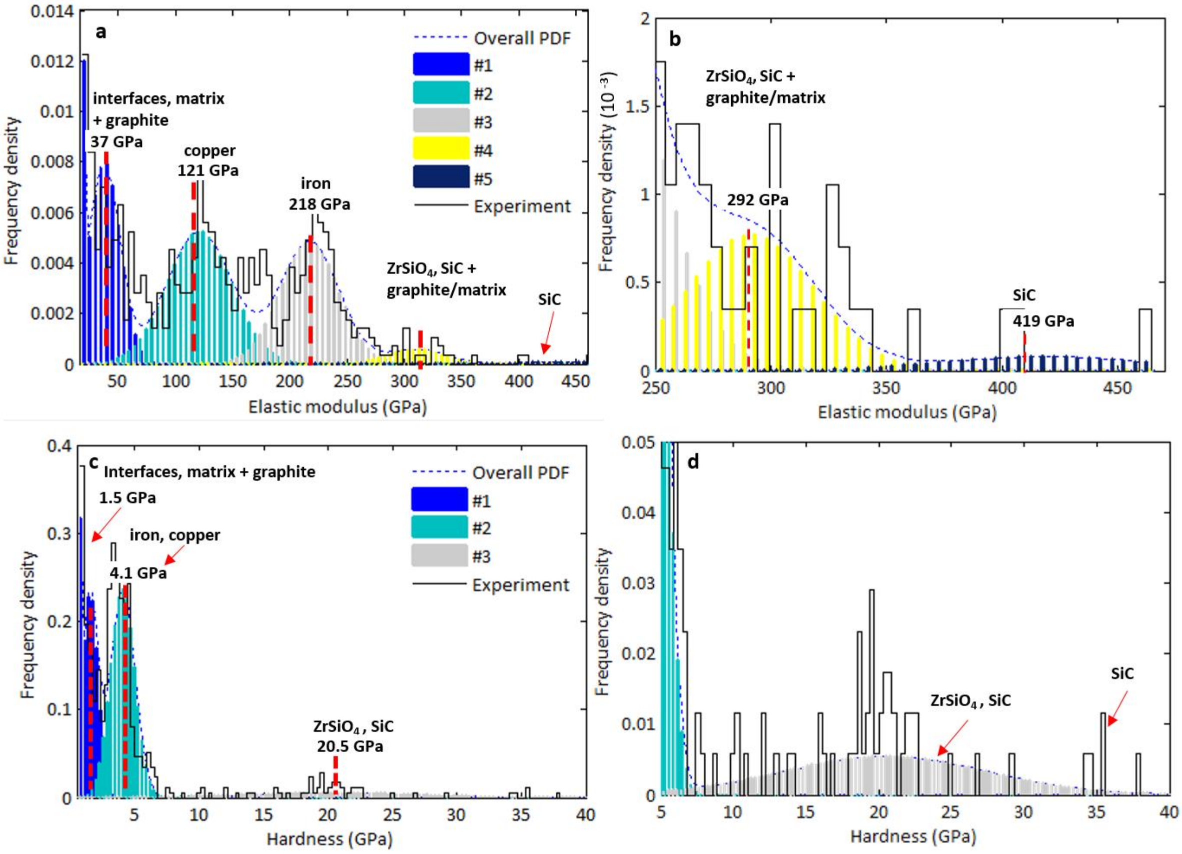

Fig. 11 Résultats de l'analyse statistique avec déconvolution de la PDF pour la matrice métallique et les céramiques à 100 nm.

Les valeurs des propriétés mécaniques estimées correspondent aux valeurs de référence du Tableau 5. Les principaux composants ont été identifiés, une distribution bimodale pour le graphite, puis des distributions qui identifient le cuivre, le fer et les céramiques (Fig. 11). Dans cette analyse, l'influence des interfaces n'est pas négligeable comme permettent de le constater les histogrammes. Nous pouvons obtenir également une réponse composite à faibles profondeurs indentées, liée à l'effet des graphites et au contraste très grand entre toutes les propriétés. Malgré ces effets, l'estimation des propriétés mécaniques est très satisfaisante.

Pour mieux comprendre notre matériau, nous avons utilisé l'analogie avec un système multi-couches, en appliquant le modèle proposé par Rahmoun *et al.* [23] qui permet de séparer chaque contribution des phases dans l'analyse de la variation du module d'élasticité et de la dureté en fonction de la profondeur de pénétration. Un exemple est montré dans la figure 12.

Le modèle permet d'ajuster correctement la courbe expérimentale. Les valeurs trouvées par cette analyse sont comparables à celles obtenues par l'analyse statistique, ce qui nous permet d'avoir une distribution des propriétés. Par l'approche multi-couches, nous pouvons imaginer la possibilité de concevoir un matériau théorique avec les distributions de propriétés pour répondre aux propriétés physiques et mécaniques souhaitées du matériau.

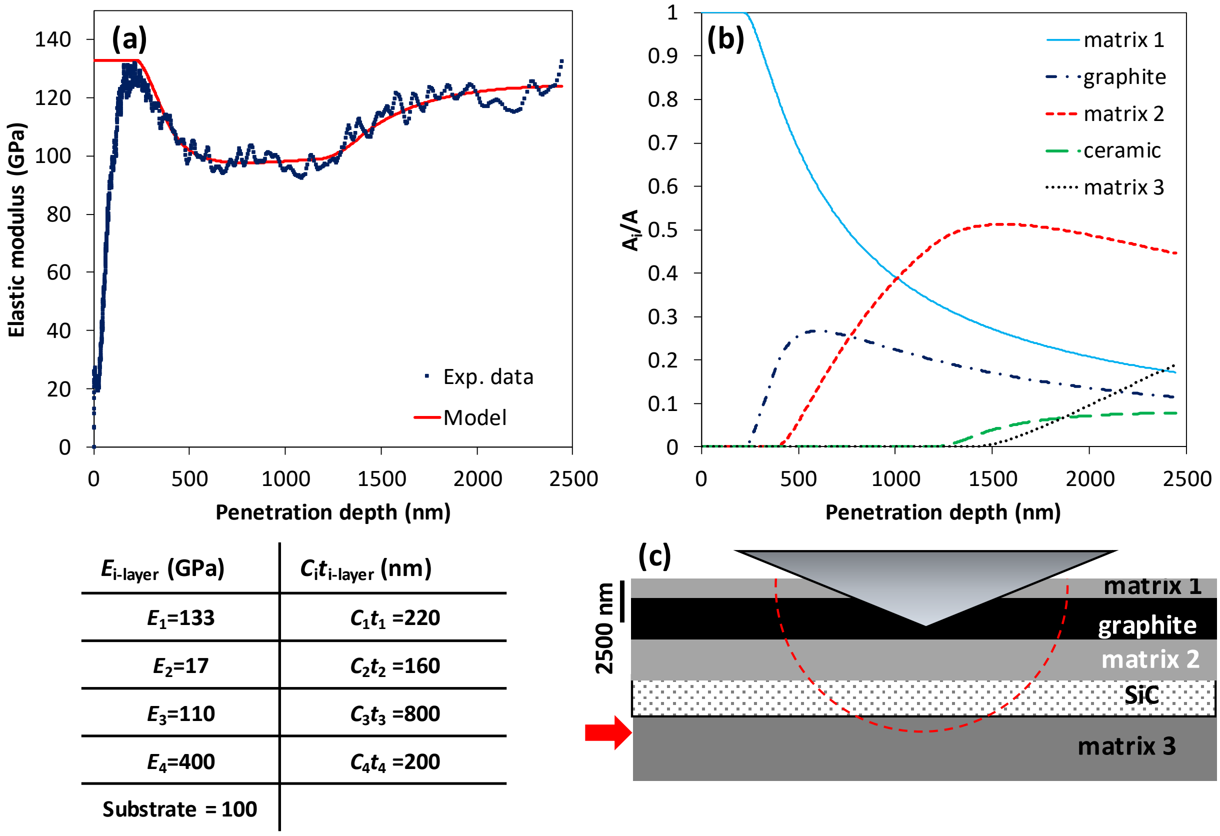

$E_{\text{i-layer}}$ (GPa)	$C_i t_{\text{i-layer}}$ (nm)
E_1=133	$C_1 t_1$ =220
E_2=17	$C_2 t_2$ =160
E_3=110	$C_3 t_3$ =800
E_4=400	$C_4 t_4$ =200
Substrate = 100	

Fig. 12 Analyse d'une courbe obtenue par nanoindentation CSM avec un modèle multicouches [23] ; (a) Ajustement du modèle à la courbe expérimentale, le tableau montre les différentes phases superposées qui donnent l'allure de la courbe, où $C_i t_{\text{i-layer}}$, c'est le produit de l'épaisseur de la phase (*t*) par une constante liée à la déformation du matériau (*C*) ; (b) contribution de chaque phase à la réponse composite en fonction de la profondeur de pénétration ; (c) représentation schématique du système multicouches.

Essais de macroindentation

À cette échelle de mesure, nous cherchons à obtenir des propriétés plus ou moins homogènes selon l'échelle de l'hétérogénéité du patin de frein. L'obtention des propriétés globales n'est pas si simple, même à cette échelle, car les variations entre les courbes d'indentation et les résultats sont significatives (Fig. 13). Pour évaluer de manière effective les propriétés du patin de frein, nous avons fait une analyse statistique en tenant compte des propriétés calculées à chaque cycle.

Avec l'indenteur Vickers et des charges comprises entre 60 et 260 N, nous avons obtenu des propriétés quasiment constantes avec la charge : 17 ± 5 GPa pour le module d'élasticité et

0.3 ± 0.1 GPa pour la dureté, par contre, pour les plus faibles charges (10 N) les valeurs augmentent.

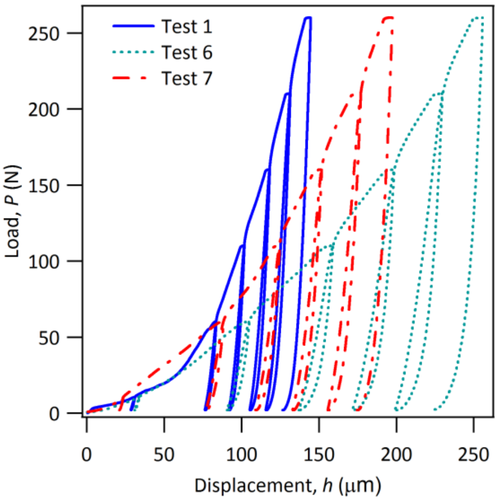

Fig. 13 Courbes force-déplacement dans le patin de frein obtenues par des essais de macroindentation multicyclique.

Avec l'indenteur sphérique et dans les deux domaines de charges étudiées, c'est-à-dire 10-260 N et 50-1450 N, les résultats sont moins dispersés car la surface affectée pendant l'essai est plus grande et, par conséquent, les propriétés mesurées sont plus homogènes. Le module d'élasticité obtenu est de 10 ± 2 GPa.

Indentation multi-échelles

À partir des résultats de nanoindentation et à l'aide de lois de mélange (Eq. 10), nous avons estimé les propriétés globales. Les résultats sont montrés dans le

Tableau 6.

$$X_{\text{Reuss}} = \left(\sum_{r=1}^{M} f_r / X_r\right)^{-1};\; X_{\text{Voigt}} = \sum_{r=1}^{M} f_r X_r;\; X_{\text{VRH}} = (X_{\text{Reuss}} + X_{\text{Voigt}})/2 \tag{10}$$

où Reuss, Voigt et Voigt-Reuss-Hill sont les modèles de lois de mélange et où X représente le module d'élasticité ou la dureté, sachant toutefois que ces relations sont habituellement utilisées pour le calcul des propriétés élastiques.

Tableau 6. Valeurs du module d'élasticité et de la dureté obtenues à partir des lois de mélange de Reuss, Voigt et Voigt-Reuss-Hill (Eq. 10)

	Voigt	**Reuss**	**Voigt-Reuss-Hill**
E_{ref} avec f_{th} (GPa)	109	24	67
E_{exp} avec f_{th} (GPa)	108	17	63
HIT_{exp} avec f_{th} (GPa)	4,1	0,5	2,3

th. Calculé avec les valeurs de référence du Tableau 5 et *exp.* avec les valeurs estimées par l'analyse statistique en nanoindentation.

La comparaison entre les lois de mélange et les essais en macroindentation montre que la réponse globale du matériau est dominée par les propriétés du graphite. C'est pourquoi la loi de mélange de Reuss est la mieux adaptée. La réponse comparable entre les deux échelles de mesure valide l'utilisation de la méthode d'indentation multi-échelles pour la détermination des propriétés mécaniques des matériaux fortement hétérogènes.

D'autre part, une étude précédente sur le même type de matériau a montré par essais de compression uniaxiale que le module d'élasticité diminuait en fonction de la charge appliquée [24]. Les auteurs ont trouvé une variation de 11 à 5 GPa, pour respectivement une variation de la contrainte appliquée de 3 à 20 MPa. Cette variation n'est pas encore bien expliquée mais il est possible qu'elle soit liée à un phénomène d'endommagement.

L'ensemble de ces résultats montre la validité de l'analyse de matériaux hétérogènes par indentation instrumentée qui donne des valeurs pour les propriétés mécaniques du même ordre de grandeur. Cependant la petite variation que nous constatons entre les valeurs peut être due à plusieurs raisons, par exemple des mécanismes de déformation complexes dans les patins de frein, comme la fracture du graphite, l'écrouissage de la matrice, la propagation de fissures, la décohésion entre phases, les différents états de contraintes entre phases (plus critique en indentation), etc. Néanmoins, la technique d'indentation est intéressante car elle est relativement simple à appliquer et parce qu'elle permet d'obtenir une distribution des propriétés qui permet de mieux comprendre et de prévoir le comportement du patin de frein en service.

Conclusions

Ce travail de thèse basé sur la technique d'indentation multi-échelles a été divisé en deux étapes, d'abord l'étude des matériaux homogènes dans le but de déterminer le raccordement entre les instruments pour étudier le changement d'échelles. Ensuite, la caractérisation d'un patin de frein, matériau fortement hétérogène, en estimant les propriétés mécaniques globales et propres à chaque composant. Les deux étapes mènent à plusieurs conclusions présentées ci-dessous :

- L'ajustement de la courbe de décharge nécessite une méthodologie plus rigoureuse que celle couramment utilisée (méthode d'Oliver et Pharr). C'est pourquoi nous proposons une méthodologie alternative qui améliore la convergence et la stabilité. Cette méthode consiste d'une part à utiliser la fonction réciproque, c'est-à-dire de prendre la variable du déplacement comme la variable dépendante où les incertitudes sont supérieures au lieu de la charge, et d'autre part d'écrire l'expression de manière adimensionnelle. Ceci nous permet également de plus facilement comparer les différentes charges et les différents appareils.

- Dans l'étude des matériaux métalliques homogènes, nous constatons que les courbes adimensionnelles sont similaires quel que soient l'instrument utilisé et l'échelle de mesure : la réponse mécanique est comparable entre les instruments bien que les incertitudes changent avec chaque instrument. Par ailleurs, les courbes adimensionnelles de décharge permettent de classifier les matériaux selon le rapport *E*/*H* qui contient une information sur les comportements élastique et plastique du matériau.
- Les essais d'indentation peuvent être fortement affectés par la complaisance du bâti, laquelle dépend aussi de plusieurs éléments de la chaine de mesure et pas seulement de la seule déformation du bâti. De la même façon, la détermination de la fonction d'aire de contact est critique pour l'estimation des propriétés, que ce soit le module d'élasticité ou la dureté.
- L'essai d'indentation est affecté par plusieurs sources d'incertitude. Pour avoir des résultats fiables, il est nécessaire d'estimer les incertitudes et de faire la corrélation avec la dispersion des résultats.
- Les cartographies en nanoindentation dans le patin de frein ont montré qu'il est possible, en utilisant une analyse statistique, de remonter aux propriétés intrinsèques de chaque composant, même si le matériau possède de nombreuses phases. Néanmoins, il est nécessaire d'effectuer l'analyse à de faibles profondeurs, ceci étant d'autant plus important que la différence entre les propriétés des différentes phases est élevée. Le choix de la profondeur et de l'espacement entre les empreintes dépend de la microstructure du matériau mais aussi de ses propriétés.
- Il est important d'étudier simultanément le module d'élasticité et la dureté dans les essais de nanoindentation sur le patin de frein pour pouvoir distinguer plus facilement les différents composants.
- La caractérisation du patin de frein par indentation en mode CSM permet d'obtenir la variation du module d'élasticité et de la dureté en fonction de la profondeur. Ensuite, les modèles multicouches permettent d'obtenir les propriétés des différentes phases superposées et des interfaces. Cette approche est intéressante car elle permet d'avoir une distribution des propriétés dans le matériau, ce qui permet de mieux comprendre son comportement.
- Les essais de macroindentation sur le patin de frein permettent d'avoir une réponse plus globale, cependant même à cette échelle avec l'indenteur Vickers, la dispersion

peut être importante. Ainsi, nous devons compiler suffisamment de données pour pouvoir donner une réponse globale et fiable. Au contraire, une réponse homogène est plus facile à atteindre avec un indenteur sphérique car la surface impactée est plus grande. Par ailleurs, le module d'élasticité trouvé par macroindentation est comparable avec le module obtenu par le modèle de Reuss (loi de mélange) estimé à partir des propriétés intrinsèques de chaque phase obtenue par analyse statistique en nanoindentation, et aussi avec les valeurs obtenues en compression uniaxiale. Le comportement global du patin de frein est principalement géré par les phases de graphite.

- Les propriétés mécaniques obtenues pour le patin de frein aux différentes échelles vont permettre de mieux comprendre son comportement au frottement et expliquer le phénomène de crissement. Nous constatons que la caractérisation par indentation multi-échelles est adaptée pour ce type de matériau et permet d'estimer les ordres de grandeurs des propriétés de manière relativement simple.

Perspectives

À partir de notre étude, nous avons constaté qu'il devenait nécessaire de déterminer de manière rigoureuse les incertitudes pour l'essai d'indentation. Couramment, dans la littérature, les incertitudes données sont seulement représentatives de la partie stochastique, c'est-à-dire de la dispersion purement expérimentale des résultats. Néanmoins, nous savons que plusieurs sources interviennent. C'est pourquoi, nous souhaitons faire une étude exhaustive en utilisant une notion bien connue pour les machines à mesurer 3D, cette notion fait appel à la notion de machine virtuelle ou de gémeau numérique. Pour cela, nous utiliserons d'abord un diagramme d'Ishikawa (5M) où sont montrées les principales sources d'incertitudes et ensuite en utilisant les caractéristiques des instruments à l'aide de simulations par la méthode de Monte Carlo, nous pouvons estimer l'ordre de grandeurs des incertitudes.

Références

[1] W. C. Oliver and G. M. Pharr, "An improved technique for determining hardness and elastic modulus using load and displacement sensing indentation experiments," *J. Mater. Res.*, vol. 7, pp. 1564–1583, Jun. 1992.

[2] D. Chicot, M. Yetna N'Jock, E. S. Puchi-Cabrera, A. Iost, M. H. Staia, G. Louis, G. Bouscarrat, and R. Aumaitre, "A contact area function for Berkovich nanoindentation: Application to hardness determination of a TiHfCN thin film," *Thin Solid Films*, vol. 558, pp. 259–266, May 2014.

[3] M. Troyon and L. Huang, "Correction factor for contact area in nanoindentation measurements," *J. Mater. Res.*, vol. 20, pp. 610–617, Mar. 2005.

[4] W. C. Oliver and G. M. Pharr, "Measurement of hardness and elastic modulus by instrumented indentation: Advances in understanding and refinements to methodology," *J. Mater. Res.*, vol. 19, pp. 3–20, 2004.

[5] M. Griepentrog, C. Ullner, and A. Duck, "Instrumented indentation test for hardness and materials parameter from millinewtons to kilonewtons," in Proceedings of the International Conference on

Force, Mass, Torque, Hardness and Civil Engineering Metrology in the Age Globalization, Celle, Germany, 2002, vol. 1685, pp. 105–112.

[6] M. Cabibbo, P. Ricci, R. Cecchini, Z. Rymuza, J. Sullivan, S. Dub, and S. Cohen, “An international round-robin calibration protocol for nanoindentation measurements,” *Micron*, vol. 43, pp. 215–222, Feb. 2012.

[7] R. Cagliero, “Macro instrumented indentation test for structural materials: experimental and numerical methods,” Doctoral thesis, *Politecnico di Torino*, 2016.

[8] T. Chudoba and M. Griepentrog, “Comparison between conventional Vickers hardness and indentation hardness obtained with different instruments,” *Z. Für Met.*, vol. 96, pp. 1242–1246, Nov. 2005.

[9] K. Herrmann, D. A. Lucca, M. J. Klopfstein, and F. Menelao, “CIRP sponsored international comparison on nanoindentation,” *Metrologia*, vol. 47, pp. S50–S58, Apr. 2010.

[10] L. Qian, M. Li, Z. Zhou, H. Yang, and X. Shi, “Comparison of nano-indentation hardness to microhardness,” *Surf. Coat. Technol.*, vol. 195, pp. 264–271, May 2005.

[11] M. F. Ashby, *Materials selection in mechanical design*, 2nd ed. Oxford; Boston, MA: Butterworth-Heinemann, 1999.

[12] J. R. Davis, *Concise Metals Engineering Data Book*. ASM International, 1997.

[13] Application note: “Properties and characteristics of graphite for industrial applications,” Entegris, Inc, Massachusetts, USA, 2015.

[14] V. V. Bannikov, I. R. Shein, and A. L. Ivanovskii, “Mechanical properties and electronic structure of zircon: Ab inito FLAPW-GGA calculations,” *Inorg. Mater. Appl. Res.*, vol. 3, pp. 7–10, Jan. 2012.

[15] B. C. Chakoumakos, W. C. Oliver, G. R. Lumpkin, and R. C. Ewing, “Hardness and elastic modulus of zircon as a function of heavy-particle irradiation dose: I. *In situ*-decay event damage,” *Radiat. Eff. Defects Solids*, vol. 118, pp. 393–403, Nov. 1991.

[16] D. B. Sirdeshmukh and K. G. Subhadra, “Note on the elastic properties of zircon,” *J. Appl. Phys.*, vol. 46, pp. 3681–3682, Aug. 1975.

[17] W. C. Oliver, J. C. McCallum, B. C. Chakoumakos, and L. A. Boatner, “Hardness and elastic modulus of zircon as a function of heavy-particle irradiation dose: II. Pb-ion implantation damage,” *Radiat. Eff. Defects Solids*, vol. 132, pp. 131–141, Oct. 1994.

[18] H. Xiang, Z. Feng, Z. Li, and Y. Zhou, “Theoretical investigations on mechanical and thermal properties of MSiO4 (M = Zr, Hf),” *J. Mater. Res.*, vol. 30, pp. 2030–2039, Jul. 2015.

[19] N. M. Rendtorff, S. Grasso, C. Hu, G. Suarez, E. F. Aglietti, and Y. Sakka, “Dense zircon (ZrSiO4) ceramics by high energy ball milling and spark plasma sintering,” *Ceram. Int.*, vol. 38, pp. 1793–1799, Apr. 2012.

[20] D. Mercier, J.-F. Vanhumbeeck, M. Caruso, and X. V. Eyndes, “Caractérisation mécanique par nanoindentation d'un revêtement composite ? matrice nickel électrodéposé ?” *Matériaux Tech.*, vol. 105, pp. 106, Feb. 2017.

[21] R. G. Munro, “Materials properties of a sintered α-SiC,” *J. Phys. Chem. Ref. Data*, vol. 26, pp. 1195–1203, May 1997.

[22] “CRC Materials Science and Engineering Handbook, Third Edition,” *CRC Press*, 26-Dec-2000. [Online]. Available: https://www.crcpress.com/CRC-Materials-Science-and-Engineering-.

[23] K. Rahmoun, A. Iost, V. Keryvin, G. Guillemot, and N. E. C. Sari, “A multilayer model for describing hardness variations of aged porous silicon low-dielectric-constant thin films,” *Thin Solid Films*, vol. 518, pp. 213–221, Nov. 2009.

[24] I. Serrano, "Microsctructural and mechanical characterization of G36S". Internal communication, 2017, Polytech Lille.